

HYDRODYNAMICS AND HEAT TRANSFER
OF LAMINAR PULSATING FLOW IN A
RECTANGULAR CHANNEL

RICHARD BLYTHMAN

Department of Mechanical & Manufacturing Engineering

Parsons Building

University of Dublin, Trinity College

Dublin 2

Ireland

October 2017

A confirmation report submitted to the University of Dublin in
partial fulfillment of the requirements for the degree of Ph.D.

Declaration

I declare that this thesis has not been submitted as an exercise for a degree at this or any other university and it is entirely my own work.

I agree to deposit this thesis in the University's open access institutional repository or allow the library to do so on my behalf, subject to Irish Copyright Legislation and Trinity College Library conditions of use and acknowledgement.

Richard Blythman, October 2017

Abstract

The exploitation of flow pulsation is a potentially useful technique for enhanced cooling in single-phase cooling systems. This thesis contains parametric analyses of the hydrodynamics and heat transfer of a laminar hydrodynamically- and thermally-developed sinusoidally-pulsating flow in a rectangular channel using experimental measurements, novel analytical solutions and numerical CFD simulations. The pulsating velocity profiles over two bisecting planes of the channel cross-section are taken using particle image velocimetry (PIV). The pulsating wall temperature and convective heat flux profiles are measured using infrared thermography (IRT). To the best of the author's knowledge, the velocity measurements constitute the first experimental verification of theory over two dimensions of a rectangular channel, while the local time-dependent temperature measurements are the first in a heated pipe or channel. It is found that the temperature profile is formed primarily by fluid displacement against the axial temperature gradient, although appreciable thermal diffusion occurs for low Prandtl numbers and long pulsation time scales. As a result, the local displacement gradient at the wall is approximately proportional to the local temperature gradient for the ideal constant temperature boundary condition. For realistic boundary conditions, the increased instantaneous near-wall velocity gradients of pulsating flow act to increase the heat flux at the wall. However, the velocity and temperature fields also interact through the non-obvious second order effect of oscillation-induced diffusivity that moves heat towards the channel entrance and reduces advective heat transfer with respect to steady flow. The time-averaged change in Nusselt number is universally negative, although intervals and local regions of heat transfer enhancement exist. The results are subject to the assumptions of a unidirectional, hydrodynamically- and thermally-developed flow with flow reversal precluded and negligible axial temperature gradient fluctuations, axial conduction and viscous heating.

Acknowledgements

This work would not have been possible without the help and support of the following people. Not many Ph.D. students have the privilege of learning from three supervisors. I would like to thank Prof. Darina Murray for her continual mentoring and eye for detail. Dr. Tim Persoons is a world-class experimentalist, whose input into rig design and technical issues has been invaluable. Dr. Nick Jeffers is a truly inventive engineer. As every researcher knows, testing often fails to go to plan and Nick's lateral thinking has saved many a round of testing.

The opportunity to work in industry for such a long period of time has been a hugely enriching experience. I would like to give an enormous thank you to Ollie Burns who, despite his monumental workload, has always found time to resolve major issues with my rigs. Thanks to Dr. Kevin Nolan for teaching me how to perform PIV and trying to teach me how to code (properly). I'd also like to give special mentions to Dr. Domhnaill Herson, Dr. Brian Donnelly, Dr. Jason Stafford, Dr. Akshat Agarwal, Dr. Rayhaan Farrelly, Dr. James Howard and Dr. Diarmuid O'Connell who have each given their unique expertise in some way.

In the thermal research group in Trinity, I would like to thank Gerry Byrne for the experience he has offered in thermal testing and for trusting me to smuggle his lab equipment off to Bell Labs in the boot of the Volvo. Thanks to Mick Reilly for accommodating my demanding time schedules in the workshop. While perhaps a little bit distracting at times, I've been lucky to find so many friendships in the office with Rudi, Ger, Greg, Michael, Diarmuid, Stephen, Guibing, Melika, Kian, Shi and Maxime. Even if their offices are sub-par, thanks also to Sajad, David, Eleonora, Richard and Jaakko.

Finally I would like to thank my friends and family, especially my parents who have always encouraged my thirst for knowledge from a young age. Words simply cannot describe my appreciation for everything that you've done to support me.

Contents

Acknowledgements	iii
Abstract	iii
List of Figures	viii
List of Tables	xii
Nomenclature	xiii
1 Introduction	2
1.1 Research Motivation	2
1.1.1 Thermal Challenges in Electronics and Photonics Devices	2
1.1.2 Microfluidic Liquid-Cooling	3
1.1.3 Applications of Unsteady Flow	5
1.2 Research Objectives	7
1.3 Outline of Thesis	8
Publications	2
2 Literature Review	9
2.1 Hydrodynamics of Unsteady Flow	10
2.1.1 Dimensionless Hydrodynamic Parameters	12
2.1.2 Velocity Profiles, Flow Rate and Pressure Gradient	13
2.1.3 Wall Shear Stress	19
2.1.4 Momentum Balance	23

2.1.5	Summary of Unsteady Hydrodynamics Review	24
2.2	Heat Transfer of Unsteady Flow	29
2.2.1	Dimensionless Thermal Parameters	29
2.2.2	Mechanisms	30
2.2.2.1	Mechanism 1: Enhanced Axial Diffusivity	31
2.2.2.2	Mechanism 2: Enhanced Wall Shear Stress Analogy	42
2.2.2.3	Further Mechanisms: Bulk-mean Flow Reversal	46
2.2.3	Summary of Unsteady Heat Transfer Review	50
2.3	Implications for Research Objectives	52
3	Analytical Theory	55
3.1	Description of Flow and Governing Equations	56
3.1.1	x-Momentum Balance	57
3.1.2	Vorticity and Stokes Boundary Layer Thickness	58
3.1.3	Non-dimensionalisation of Principal Parameters	59
3.1.4	Linearisation	59
3.1.5	Boundary Conditions	60
3.2	Solution for Velocity Field	62
3.3	Solution for Temperature Field	64
3.3.1	Bulk Temperature and Nusselt Number	66
4	Experimental Methods, Analysis and Uncertainty	70
4.1	Experimental Methods	70
4.1.1	Hydrodynamic Testing	71
4.1.1.1	Experimental Apparatus	71
4.1.1.2	System Calibration	77
4.1.1.3	Experimental Procedure	78
4.1.2	Heat Transfer Testing	79
4.1.2.1	Experimental Apparatus	80
4.1.2.2	System Calibration	87
4.1.2.3	Experimental Procedure	91
4.2	Experimental Analysis	92

4.2.1	Velocity Data Analysis	92
4.2.1.1	Vector Field Processing	93
4.2.2	Thermal Data Analysis	95
4.2.2.1	Thermal Image Processing	96
4.2.2.2	Element Energy Balance	97
4.3	Experimental Uncertainty	105
4.3.1	Uncertainty of Velocity Measurements	105
4.3.1.1	PIV Uncertainty	106
4.3.1.2	Verification and Validation Method	109
4.3.2	Uncertainty in Temperature Measurements	112
4.3.3	Uncertainty in Heat Flux	114
5	Numerical Methods	117
5.1	Geometry and Boundary Conditions	118
5.2	Solver Settings	120
5.3	Numerical Procedure	121
5.4	Numerical Analysis	122
6	Hydrodynamics of Laminar Pulsatile Flow in a Rectangular Channel	123
6.1	Introduction	123
6.2	Parametric Analysis of Flow Hydrodynamics	125
6.2.1	Velocity Profiles	125
6.2.1.1	Local Flow Reversal	130
6.2.1.2	Vorticity and the Velocity Overshoot Mechanism	131
6.2.2	Wall Shear Stress and Pressure Drop	134
6.2.3	x -Momentum Balance	140
6.3	Conclusions	143
7	Idealised Heat Transfer of Laminar Pulsatile Flow in a Rectangular Channel	145
7.1	Introduction	145
7.2	Mechanism 1: Enhanced Axial Diffusivity	147
7.2.1	Transverse Temperature Profiles	147

7.2.2	Axial Temperature Profiles	153
7.2.3	Time-averaged Heat Transfer	157
7.2.4	Time-dependent Heat Transfer	160
7.3	Mechanism 2: Enhanced Wall Shear Stress Analogy	165
7.3.1	Transverse Temperature Profiles	165
7.3.2	Nusselt number	168
7.4	Conclusions	170
8	Experimental Heat Transfer of Laminar Pulsatile Flow in a Rectangular Channel	173
8.1	Introduction	173
8.2	Wall Temperature and Convective Heat Flux Profiles	175
8.3	Conclusions	181
9	Discussion	183
10	Conclusions	187
10.1	Future Work	189
10.1.1	Flow Rate Pulsations	189
10.1.2	Channel Geometry and Developing Flow	191
	Bibliography	193
	Appendix A	210
A.1	Solutions for Flow Rate and Wall Shear Stress	210
A.2	Solution for Steady Temperature Profile	210
A.3	1-D Parallel Plates Solution for Oscillatory Temperature Profile	211

List of Figures

1.1	Microchannels integrated with photonics integrated circuits (PICs) [5]	3
1.2	Schematic of microfluidic flow loop [3]	4
1.3	Structure and operating principle of diaphragm micropump [15]	5
2.1	Stokes' second problem [37]	11
2.2	Near-wall velocity overshoot in a square section [42]	14
2.3	Oscillating velocity profiles in a narrow rectangular duct [31]	16
2.4	Amplitude and phase of flow rate with frequency in a pipe [32]	17
2.5	Amplitude and phase of pressure gradient with frequency in a pipe [55]	19
2.6	Amplitude and phase of wall shear stress with frequency in a pipe [32]	20
2.7	Pulsating velocity profiles, flow rate, and wall shear rate in a pipe [57]	20
2.8	Effect of near-wall resolution on the wall shear rate estimate in a pipe [57]	22
2.9	Pulsating flow rate, centreline velocity and wall shear stress [58]	22
2.10	Pulsating viscous and inertial stress contributions in a pipe [32]	23
2.11	Inertial and viscous stress contributions with frequency in a pipe [60]	24
2.12	Parameter spaces of the reviewed and current hydrodynamic experiments	25
2.13	The augmented diffusion mechanism in steady flow [63]	32
2.14	Enhanced diffusivity relative to molecular conduction with frequency [67]	33
2.15	Pulsating axial temperature profiles in oscillating pipe flow [70]	35
2.16	Visualised temperature field in an insulated square channel [71]	36
2.17	Time-dependent axial temperature profiles at the wall [34]	38
2.18	Mechanism for developing spatial periodicity in axial temperature profile [29]	41
2.19	Flow rate pulsations found to enhance heat transfer [30]	42

2.20	Oscillating temperature field of an air flow between parallel plates [80] . . .	45
2.21	Oscillating temperature profiles of an air flow between parallel plates [80] .	46
2.22	Pulsating mass transfer rate and pressure drop in a pipe [88]	48
2.23	Pulsating mass transfer rate and pressure drop in a pipe [88]	49
2.24	Heat transfer enhancement of pulsating flow with flow rate amplitude [16] .	50
3.1	Coordinate system of rectangular channel	56
3.2	Steady temperature profiles in a channel for various boundary conditions [97]	61
3.3	Steady wall temperature profiles with lateral conduction in the wall [99] . .	65
4.1	Model of the hydrodynamic test rig	72
4.2	Orientation of camera, laser optics and channel	73
4.3	Model of the optical setup	75
4.4	Single burst of the lasers on laser alignment paper	77
4.5	Pump calibration curve	78
4.6	Exploded view of test section	81
4.7	Cross-section showing of test section	83
4.8	Model of heat transfer test rig	84
4.9	Transmissivity of IR light with wavelength for sapphire glass [121]	85
4.10	Thermocouple calibration curves	88
4.11	Temperature calibration curve for the thermal camera	89
4.12	Radiation detected by thermal camera [122]	90
4.13	Energy balance in a single heater element	98
4.14	Oscillating lateral conduction term	100
4.15	Oscillating capacitance term	102
4.16	Oscillating conduction term	104
4.17	Oscillating radiation term	104
4.18	Raw PIV image over channel width	107
4.19	Uncertainty as a function of displacement gradient	108
5.1	Schematic of the 3-D numerical model	118
5.2	Structured non-uniform mesh	119

6.1	Flow rate and wall shear stress amplitudes with pressure gradient amplitude	126
6.2	Steady velocity profiles	127
6.3	Normalised steady velocity profiles	127
6.4	Oscillating velocity profiles	128
6.5	Velocity amplitude and phase profiles	129
6.6	Pulsating velocity profiles	131
6.7	Acceleration profiles	133
6.8	Oscillating flow rate, wall shear stresses and pressure gradient	134
6.9	Amplitude and phase of pressure gradient and wall shear stress	135
6.10	Amplification of pressure gradient relative to wall shear stress and flow rate	136
6.11	Oscillating wall shear stress profiles	138
6.12	Wall shear stress amplification of oscillating flow	139
6.13	Oscillating viscous and inertial stress contributions to the pressure drop . .	140
6.14	Phasors of viscous and inertial contributions to the pressure drop	142
6.15	Amplitudes of viscous and inertial stress contributions to the pressure drop .	142
7.1	Steady temperature profile	148
7.2	Oscillating temperature profiles compared to the 1-D solution [69]	148
7.3	Oscillating temperature and displacement profiles for $Pr = 5.6$	149
7.4	Pulsating temperature profiles	151
7.5	Temperature and displacement amplitude and phase profiles	151
7.6	Oscillating temperature and displacement profiles for $Pr = 1$	152
7.7	Pulsating axial temperature profiles	154
7.8	Oscillating axial temperature profiles	155
7.9	Axial temperature amplitudes and axial temperature gradient	156
7.10	Nusselt number reduction with frequency compared to pipes [29]	157
7.11	Nusselt number reduction with frequency in a rectangular channel	158
7.12	Nusselt number reduction with frequency at constant dimensionless amplitudes	159
7.13	Pulsating bulk temperature and driving temperature difference	160
7.14	Network showing generalised impedance for constant heat flux	162
7.15	Similarity of temperature and displacement profiles in a parallel plate channel	164

7.16	Oscillating heat flux and wall displacement gradient in a parallel plate channel	166
7.17	Amplitude of heat flux and wall displacement gradient with frequency . . .	166
7.18	Oscillating heat flux profiles for $Pr = 5.6$	168
7.19	Oscillating wall temperature gradient and temperature difference in a parallel plate channel	169
7.20	Nusselt number enhancement with frequency at flow rate amplitude	170
8.1	Steady temperature profiles with and without buoyancy	176
8.2	Oscillating wall temperature profiles	177
8.3	Oscillating mean wall temperature and flow rate	178
8.4	Oscillating fluid and wall temperature profiles in normal direction	179
8.5	Oscillating convective heat flux profiles	180
10.1	Model of the piston pump	191

List of Tables

2.1	Details of reviewed and current hydrodynamic experiments	28
2.2	Details of reviewed and current heat/mass transfer experiments	54
3.1	Nomenclature for boundary conditions [92]	60
3.2	Nomenclature for combination of heated and adiabatic walls [96]	61
3.3	Constants of analytical solution for unique version of heating [98]	62
4.1	Hydrodynamic channel dimensions	73
4.2	Experimental parameter space	79
4.3	Heated channel dimensions	82
4.4	Foil and paint properties [114, 118, 119]	82
4.5	Water properties at 30°C [104].	86
4.6	Specifications of infrared camera	87
4.7	Space-averaged heat flux components of the energy balance	99
4.8	Expanded uncertainty of heat flux components	116
5.1	Numerical parameter space for large adiabatic channel	121
5.2	Numerical parameter space for large heated channel	121
5.3	Numerical parameter space for small heated channel	121
7.1	Comparison of time-averaged Nusselt number definitions	162

Nomenclature

\hat{a}, \hat{b}	Channel width, height	[<i>m</i>]
\hat{L}	Channel length	[<i>m</i>]
\hat{p}	Pressure	[<i>Pa</i>]
\hat{q}	Heat flux	[<i>W/m²</i>]
\hat{q}_{cap}	Capacitive heat flux component	[<i>W/m²</i>]
\hat{q}_{cond}	Air gap conduction heat flux component	[<i>W/m²</i>]
\hat{q}_{conv}	Convective heat flux component	[<i>W/m²</i>]
\hat{q}_{gen}	Generated heat flux component	[<i>W/m²</i>]
\hat{q}_{lc}	Lateral conduction heat flux component	[<i>W/m²</i>]
\hat{q}_{rad}	Radiation heat flux component	[<i>W/m²</i>]
\hat{t}	Time	[<i>s</i>]
\hat{u}	Velocity in the axial direction	[<i>m/s</i>]
\hat{w}	Thickness	[<i>m</i>]
\hat{x}	Axial flow coordinate	[<i>m</i>]
\hat{y}, \hat{z}	Coordinates normal to flow direction	[<i>m</i>]
\Im	Imaginary part of complex number	
\Re	Real part of complex number	
c	Heated fraction of cross-sectional perimeter	
c_p	Specific heat capacity	[<i>J/(kg.K)</i>]
d	Binary constants defined by Table 3.3	
D_h	Hydraulic diameter of channel	[<i>m</i>]

f	Oscillation frequency	[Hz]
g	Gravitational acceleration	[m/s ²]
G_u	Green function for velocity	
h	Heat transfer coefficient	[W/(m ² K)]
i	Imaginary unit, $i = \sqrt{-1}$	
j, k	Summation indices	
k	Thermal conductivity	[W/(mK)]
L_e	Hydrodynamic entry length	[m]
m, n	Summation indices	
Q	Flow rate	[m ³ /s]
T	Temperature	[°C]

Dimensionless Numbers

A_0	Dimensionless amplitude, $A_0 = 2\langle\hat{\chi}_A\rangle/D_h$	
Bi	Biot number, $Bi = h\hat{w}_s/k_s$	
Fo	Fourier number, $Fo = \alpha_s/(\omega\hat{w}_s^2)$	
Gr	Grashof number, $Gr = g\beta_f(T_w - T_f)D_h^3/\nu^2$	
Nu	Nusselt number, $Nu = 1/(\theta_w - \theta_b)$	
Pe	Péclet number, $Pe = Re \cdot Pr$	
Pr	Prandtl number, $Pr = \nu/\alpha_f$	
Q_A/Q_0	Flow rate amplitude	
Ra	Rayleigh number, $Ra = g\beta_a(T_w - T_a)L_c^3/(\nu_a\alpha_a)$	
Re_{δ_v}	Reynolds number based on the Stokes layer thickness, $Re = \hat{u}\delta_v/\nu$	
Re	Reynolds number, $Re = \hat{u}D_h/\nu$	
Wo	Womersley number, $Wo = (D_h/2)(\omega/\nu)^{1/2}$	

Greek Symbols

α	Thermal diffusivity	[m ² /s]
β	Coefficient of thermal expansion	[1/K]
β_{jk}, β_{mn}	Functions defined by Equations 3.13b and 3.23	

ω	Vorticity	[rad/s]
δ	Dirac delta function	
$\hat{\chi}$	Axial displacement	[m]
$\hat{\delta}_v$	Stokes layer thickness	[m]
$\hat{\tau}$	Wall shear stress	[Pa]
μ	Viscosity	[kg/ms]
ν	Kinematic viscosity	[m ² /s]
ω	Angular oscillation frequency	[rad/s]
$\partial\tau$	Wall shear stress enhancement relative to steady flow	
∂Nu	Heat transfer enhancement, $\partial Nu = (\overline{Nu} - Nu_0)/Nu_0$	
Φ	Functions defined by Equations 3.13a and 3.21	
ϕ	Phase of oscillating parameter	[rad]
ψ	Complex functions defined by Equations 1b and 3.20	
ρ	Density	[kg/m ³]
θ	Dimensionless Temperature	
Superscripts		
'	Phase relative to $\nabla p' = \Re[\nabla p_A e^{i\omega t}]$	
''	Phase relative to $Q'' = \Re[\psi_Q e^{i(\omega t - \phi_Q - \pi/2)}]$	
'''	Phase relative to Q'' , bulk mean phase removed	
Subscripts		
∞	Ambient property	
0	Steady flow component	
A	Oscillating flow amplitude	
a	Air property	
b	Bulk fluid temperature property	
f	Water property	
p	Paint property	
s	Foil property	

w	Wall temperature property
y	Acting about \hat{y} axis
yx	Component with normal \hat{y}
z	Acting about \hat{z} axis
zx	Component with normal \hat{z}

Other Symbols

ΔA	Difference in variable A
\hat{A}	Dimensional variable A
$\langle A \rangle$	Space-average of variable A
∇A	Gradient of variable A , $\nabla = [\partial A/\partial x, \partial A/\partial y, \partial A/\partial z]$
\bar{A}	Time-average of variable A

Publications

The author has published in journals and conference proceedings as follows:

- R. Blythman, T. Persoons, N. Jeffers, K. P. Nolan, and D. B. Murray, “Localised dynamics of laminar pulsatile flow in a rectangular channel,” *International Journal of Heat and Fluid Flow*, vol. 66, pp. 8-17, 2017.
- R. Blythman, S. Alimohammadi, T. Persoons, N. Jeffers, and D. B. Murray, “Parametric analysis of laminar pulsating flow in a rectangular channel,” *Heat and Mass Transfer, In press*, 2017.
- R. Blythman, N. Jeffers, T. Persoons, and D. B. Murray, “Idealised heat transfer of laminar pulsatile flow in a rectangular channel,” *International Journal of Heat and Mass Transfer, In review*, 2017.
- R. Blythman, N. Jeffers, T. Persoons, and D. B. Murray, “Wall temperature of laminar pulsating flow in a channel,” in *9th World Conference on Experimental Heat Transfer, Fluid Mechanics and Thermodynamics, Iguazu Falls, Brazil*, 2017.
- R. Blythman, T. Persoons, N. Jeffers, and D. B. Murray, “Effect of oscillation frequency on wall shear stress and pressure drop in a rectangular channel for heat transfer applications,” *Journal of Physics: Conference Series*, vol. 745, p. 032044, 2016.
- R. Blythman, N. Jeffers, T. Persoons, and D. B. Murray, “Localized and time-resolved velocity measurements of pulsatile flow in a rectangular channel,” in *18th International Conference on Fluid Mechanics and Thermodynamics, Rio de Janeiro, Brazil*, 2016.
- N. Jeffers, J. Stafford, K. Nolan, B. Donnelly, R. Enright, J. Punch, A. Waddell, L. Erlich, J. O’Connor, A. Sexton, R. Blythman, D. Hernon, “Microfluidic cooling of photonic integrated circuits (PICs),” in *4th European Conference on Microfluidics, Limerick, Ireland*, 2014.

Chapter 1

Introduction

1.1 Research Motivation

The background to this research is a collaboration between the Fluids and Heat Transfer Research Group of Trinity College Dublin and the Thermal Management Research Group of Bell Labs Ireland. Thus, the motivations primarily concern advances in the thermal management of telecommunications technology. This chapter briefly explores the background, practical benefits and applications of the research work.

1.1.1 Thermal Challenges in Electronics and Photonics Devices

Modern technological innovation in the ICT sector remains continually dependent on the removal of the significant amounts of heat generated by electronic and photonic components. In computing applications, the persistent size and cost reduction of semiconductor discretises has enabled the integration of hundreds of millions of transistors in three-dimensional architectures within microprocessors [1]. Although this spatial optimisation reduces physical distances and communication times between cores and memory, the increased power densities and thermal fluxes require the integration of smart thermal solutions at the design stage [2]. In telecommunications, the demand for global mobile connectivity imposed by online utilities such as cloud computing and the Internet of Things (IoT) is causing network requirements to grow exponentially, surpassing 1 Pb/s by 2020 according to projections [3]. It is widely accepted that network traffic is outgrowing system capacity with the present rate of evolution

[4], meaning that a transformation in network architecture must accommodate these advances in web-based consumer technology. While a transition from the use of copper to fibre optics to transfer information is already underway, the current photonics integrated circuits (PICs) which integrate multiple optical devices are expensive, not scalable and thermally inefficient. While the lasers used dissipate just 100 mW each, their small volume results in very high localized heat fluxes of the order of 1 kW/cm^2 [5]. The enhanced functionality and continued miniaturisation of these packages are causing traditional cooling solutions to approach their upper limit and new thermal solutions must be developed.

1.1.2 Microfluidic Liquid-Cooling

Since the early work of Tuckerman and Pease [6], liquid-cooling systems involving microchannel ($10\text{ }\mu\text{m} < D_h \leq 200\text{ }\mu\text{m}$) heat sinks have been commonly cited as a solution to the high heat fluxes that result from the sustained miniaturisation of electronics packages [7]. While the high heat transfer rate of two-phase flow boiling in these architectures has been widely acclaimed as the most promising technique, it is still a number of years away from becoming a plausible solution due to the stability problems with which it is associated [8]. Hence, heat transfer augmentation in single-phase flow remains an entirely active research area. Thermal technologies involving microchannel heat sinks have been implemented by Fujitsu in high-end servers [9] and by IBM for cooling high power chips [10]. Similarly, the use of microchannels embedded in a submount has been suggested to

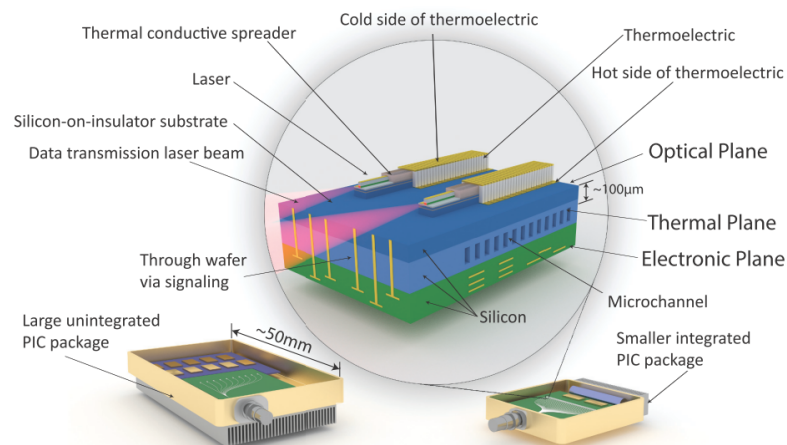


Figure 1.1: Microchannels integrated with photonics integrated circuits (PICs), Jeffers et al. [5].

facilitate the integration of electrical and photonic components [5], as illustrated in Figure 1.1. The self-contained flow loop depicted in Figure 1.2 is driven by a fluid micropump integrated within the optoelectronic package, which must be compact, reliable and energy efficient. Microscale pumping solutions were originally proposed about thirty years ago [11] and remain an active area of research due to the demanding pumping requirements and space constraints in electronics packages [12]. Most systems use large external pumps, though the ideal solution involves the integration of the micropump directly into the microchannel heat sink, since the size, channel length and pressure drop are reduced [13]. For example, pumps and channels have been integrated into self-cooled printed circuit boards (PCBs) [14]. A common structure of micropumps involves a deflectable membrane that vibrates in a pumping chamber, with one or more valves to direct the flow, as depicted in Figure 1.3. Actuation methods include piezoelectric, electrostatic, peristaltic, thermo-pneumatic and liquid-vapour phase change techniques. The flow rate and pressure drop of the inherently unsteady flow generated depend on features of the pump including the actuator type and chamber geometry. The type and number of valves affects the rectification of the flow and shape of the overall flow rate pulsations.

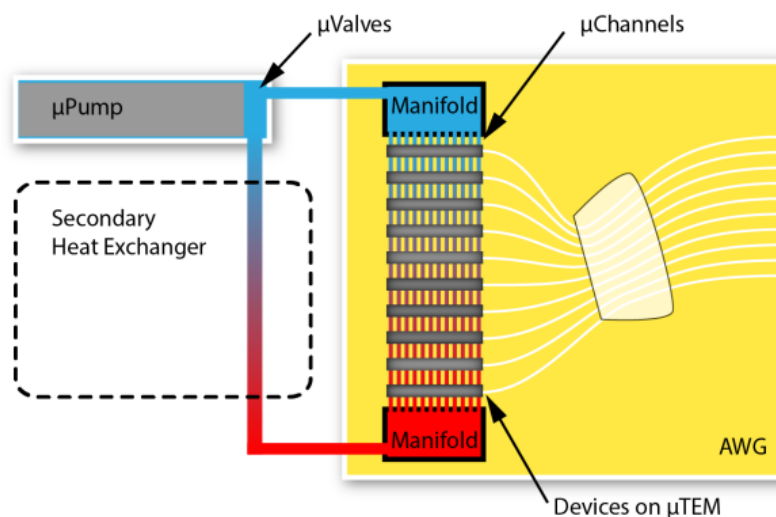


Figure 1.2: Schematic of microfluidic flow loop, Enright et al. [3].

1.1.3 Applications of Unsteady Flow

Interestingly, the inherent pulsations generated using a piezoelectric element and vibrating membrane have been found to enhance heat transfer by as much as 40% in minichannel heat sinks at low Reynolds numbers [16]. Also, the diaphragm of an integrated micropump has been found to enhance heat transfer in channels, with large heat fluxes expected using larger diaphragms [17]. While Poiseuille flow velocity profiles are self-similar – and therefore bound the Nusselt number – it is thought that pulsation alters the thickness of the hydrodynamic and thermal boundary layers, the near-wall gradients and the overall thermal resistance to heat transfer. Single-phase pulsating (non-zero mean) and oscillating (zero mean) flows have been successfully implemented in a variety of applications. Wälchli et al. [18] exploited this mechanism to spread heat to a large area in the primary liquid cooling loop of a thin form factor solution for blade server modules, with heat being exchanged to a secondary cooling

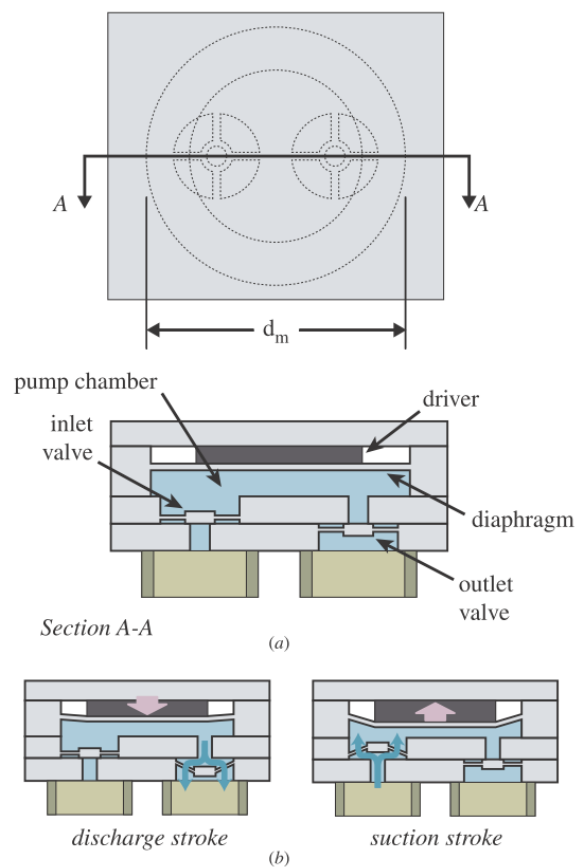


Figure 1.3: Structure and operating principle of diaphragm micropump that may be driven by piezoelectric element, Laser and Santiago [15].

loop of oscillating air flow. With moderately high frequencies, a peak cooling performance of 180 W/cm^2 was achieved using a pumping power of 1 W [19]. Walsh et al. [20] employed an oscillatory flow device in a microelectronic PC cabinet to reduce component operating temperature by as much as 40% from steady flow temperatures. Kurzweg and Zhao [21] patented a capillary tube bundle that uses oscillatory flow to transport heat from a hot to a cold reservoir without accompanying net mass transport [22], with applications including heat removal from radioactive fluids and heat transfer in zero gravity.

At the macroscale of industrial processes, Keil and Baird [23] demonstrated heat transfer enhancement of up to 31% compared to steady flow in a shell and tube heat exchanger. However since space restrictions aren't necessarily strict, the low additional cost of a unit with a larger footprint with sufficient capacity may limit adoption of the technology on the basis of thermal performance alone. More significant in such applications may be the capability of flow unsteadiness to mitigate fouling [24], the global cost of which has been estimated at greater than \$4.13 billion in the petrochemical industry, due to increased capital expenditure, maintenance costs, and productivity losses [25]. Fouling increases the thermal resistance, causes local hotspots by maldistribution of fluid in parallel channels, and demands additional pumping power because of the diminished cross-sectional area. The high near-wall velocity gradients of pulsating flow break up deposits at the heat exchanger surface, as demonstrated in the removal of bacteria from stainless steel equipment [26] and in the prevention of deposits in biomaterials processing [27]. Also, utilisation of the mechanical and thermal effects of fluid flow, rather than the chemistry of cleaning agents, may reduce the toxicity and environmental impact of chemicals required in retrospective cleaning applications. Gillham et al. [28] found that the cleaning rates of whey protein agglomerates, deposited in the thermal treatment of milk and dairy products, were especially sensitive to pulse amplitude and the presence of reverse flow. Enhanced cleaning and heat transfer rates of 250% and 100%, respectively, were measured using low-frequency, large amplitude pulsations.

Hence, pulsating flow may improve the performance of heat exchangers by enhancing heat transfer, preventing fouling and aiding cleaning with applications in the electronics cooling, food processing and petrochemical industries. The practical benefits depend on the input frequency and amplitude variables but, more specifically, on the influence of these

parameters on features of the flow such as near-wall velocity gradients and flow reversal.

1.2 Research Objectives

A multitude of applied studies have successfully demonstrated the feasibility of unsteady cooling solutions; however, the top-down or black box approach to system design has failed to identify the underlying physical mechanisms. To this day, the literature continues to assert that the results of existing studies are contradictory or inconsistent [29, 30]. This owes in part to high variability in a large parameter space, which contains geometric dissimilarities, differing material properties, varying unsteady characteristics, and disagreements in the definition of heat transfer enhancement. For example, the heat transfer characteristics for even the simplest cases of pulsating flow in two-dimensional channels are not well understood. The primary aim of this PhD thesis is simple:

- to investigate whether a hydrodynamically- and thermally-developed sinusoidally-pulsating flow enhances heat transfer in a rectangular channel geometry.

Since pulsating flow is of primary interest, heat transfer enhancement is defined relative to a steady flow with a flow rate equal to the time-average of the pulsating flow rate. Although the mechanical and thermal problems are inextricably linked, decoupling of the local instantaneous parameters provides insight into underlying physical mechanisms. The principal objective may hence be split into secondary objectives:

- to investigate and characterise the fluid mechanics of pulsatile flow using complementary analytical, numerical and experimental analyses.
- to investigate and characterise the heat transfer of pulsatile flow using similar analyses.
- to couple the hydrodynamic and thermal problems on a local time-dependent basis to understand any underlying mechanisms and exploit and optimise any potential heat transfer enhancement.

The variation of the pertinent parameters with channel aspect ratio is beyond the scope of this thesis. Since local verification of the hydrodynamic and thermal models is desired, the

research is focused on a macro-scale channel, with the hope that future work might validate the theory at the microscale. While this bottom-up approach is further removed from the implementation of unsteady cooling solutions at an applications level, it is hoped that such an investigation can facilitate the understanding and optimisation of future heat removal systems. Finally, it is hoped that this fundamental problem can act as a general case study, which can identify the manner in which the hydrodynamic and thermal problems are coupled, and how they are affected by superimposed unsteadiness on a local time-dependent basis.

1.3 Outline of Thesis

The chapters of this thesis are structured to achieve the primary and secondary research objectives in a logical systematic manner. Initially, the hydrodynamic and heat transfer problems are discussed in isolation before being consolidated in the final chapters. **Chapter 2** performs a review of the literature, addressing any contradictions and inconsistencies found with respect to the question of heat transfer enhancement. Sections 2.1 and 2.2 overview the relevant hydrodynamic and thermal studies, respectively. **Chapter 3** develops an analytical framework for modelling pulsating flow. Section 3.2 expands an existing analytical solution to the hydrodynamic problem, while Section 3.3 derives a novel solution to the thermal problem. **Chapter 4** overviews the design and analysis of separate hydrodynamic (Section 4.1.1) and thermal (Section 4.1.2) test facilities for measuring the local time-dependent velocities and temperatures of pulsating flow. **Chapter 5** develops a computational fluid dynamics (CFD) model for the hydrodynamic and thermal characteristics of pulsating flow. **Chapter 6** validates the hydrodynamic models using particle image velocimetry (PIV) measurements, and investigates any underlying hydrodynamic mechanisms using the complete data provided by the theoretical solutions. **Chapter 7** investigates any underlying thermal mechanisms using the complete data provided by the theoretical models. **Chapter 8** assesses the validity of assumptions made in the idealised analytical thermal model, especially in the near-wall region, using infrared thermography (IRT). **Chapter 10** provides an overview of the work done and summarises the main findings from the research.

Chapter 2

Literature Review

As stated in Chapter 1, the current research is concerned with a laminar incompressible hydrodynamically- and thermally-developed sinusoidally-pulsating flow in a rectangular channel geometry. As expected, this flow is fundamentally similar to flow in a circular pipe [31] and a flat plate boundary layer (as discussed in Section 2.1), but also contains physical similarities to acoustically-excited compressible flows (as discussed in Section 2.2.2.2). In contrast, pulsating and synthetic jet flows are quite different, owing to vortices and turbulence. By definition, pulsating or modulating flow has a non-zero mean flow rate while oscillating, reciprocating, or periodically-reversing flow has zero-mean advection. However, since the governing momentum and energy equations are linearised (this is developed rigorously in Chapter 3), the flows are superposable and are discussed interchangeably throughout this thesis.

The complexity of the unsteady internal flow problem necessitates a detailed review of the interdependence of the fundamental flow variables on a parametric basis. While the mechanical and thermal fields are inextricably linked, it is useful to temporarily decouple the respective problems to give insight into underlying physical mechanisms that may effect a change in heat transfer. Many aspects of the hydrodynamic problem are well understood. A multitude of analytical studies have analysed the interdependence of the velocity, wall shear stress and pressure gradient with time and frequency, using mathematical solution techniques including Fourier expansion [32], Laplace transform [33] and Green's function [31] methods. Moreover, confirmatory experimental works have measured the

time-dependent velocity profiles in a pipe using experimental techniques including hot wire anemometry, laser Doppler velocimetry and flow visualisation. The heat transfer problem is less developed in comparison. Early analytical solutions were highly idealised, using the slug flow assumption [34] or focusing on the behaviour of slowly pulsating flows [35]. Comprehensive analytical solutions in pipes have only become available in recent times using the method of undetermined coefficients [29] and the Laplace transform technique [30]. Furthermore, the literature contains a comparative lack of experimental data, especially with respect to local time-dependent measurements. The handful of studies that do exist have used a thermo-sensitive liquid-crystal tracer technique and planar laser-induced fluorescence (PLIF).

2.1 Hydrodynamics of Unsteady Flow

Unsteady flow was treated mathematically as early as 1851 with Stokes' second problem [36], which considers the one-dimensional shear flow of a viscous fluid near a flat plate vibrating in a direction parallel to its length. The flow is laminar and propagation in the transverse direction is solely as a result of viscosity in a phenomenon that is essentially a diffusion of vorticity and momentum by molecular action. Figure 2.1(a) presents the velocity oscillations for the flow, which models the spreading of transverse velocity oscillations from the boundary. The amplitudes of the velocity oscillations decay exponentially with distance from the wall and the phase lag increases. The region affected by oscillations is constrained since gradients in the flow are repeatedly annulled by those with opposite sign and a finite layer of vorticity forms close to the surface called the Stokes boundary layer. The extent of this layer may be arbitrarily defined based on the relative size of the near-wall and free stream velocity amplitudes. Typically, the Stokes layer thickness is chosen as the distance at which fluid elements experience 1% of the effects of the boundary oscillations.

The linearity of the governing momentum equation (discussed further in Chapter 3) imposes an inherent similarity between wall-driven fluid oscillations and those resulting from a harmonically-oscillating pressure gradient acting over the cross-sectional area of the fluid. Hence, the latter may be constructed by superposition of solutions. To realise the no-slip boundary condition at the wall, the solution can be subtracted from a globally

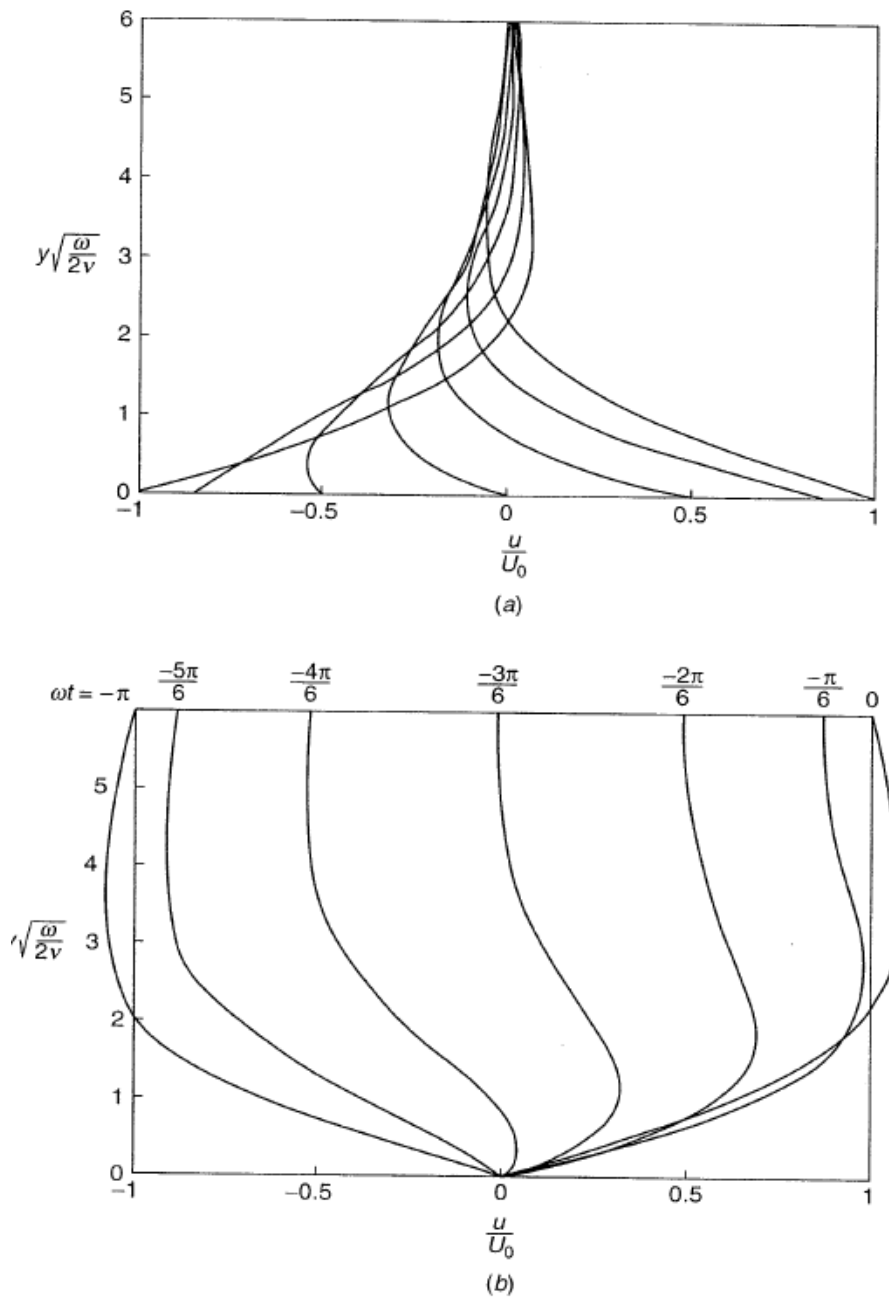


Figure 2.1: Stokes' second problem (a) flow above an oscillating infinite plate (b) an oscillating stream above a fixed plate, White [37].

uniform velocity oscillation imposed by an oscillating pressure gradient applied uniformly in the transverse direction. Figure 2.1 illustrates the similarity of these flows with entirely different driving forces. Despite its convenient construction from Stokes' second problem, the similarly-shaped velocity profiles of a quickly oscillating body of fluid are not a consequence of viscous lag between fluid layers. Viscous stresses reduce the momentum of fluid layers

near the wall, which are inclined to reverse quickly when the pressure gradient reverses. A steady flow may also be added to simulate a pulsating flow. Furthermore, the boundary layer problem is a generalisation of the internal flow in an enclosed vessel and the behaviour of the pertinent parameters is characteristically similar.

2.1.1 Dimensionless Hydrodynamic Parameters

A sinusoidal pulsation is characterised by its mean, amplitude and frequency. The dimensionless parameter for the steady component of the flow is the Reynolds number Re_0 , which gives the prominence of viscous forces relative to inertial forces:

$$Re_0 = \frac{\langle \hat{u}_0 \rangle D_h}{\nu} = \frac{\langle \hat{u}_0 \rangle / D_h}{\nu / D_h^2} \quad (2.1)$$

where $\langle \hat{u}_0 \rangle$ is the spatially-averaged dimensional velocity, ν is the kinematic viscosity, and the hydraulic diameter D_h is a measure of the cross-sectional size of the vessel. Square and circular ducts with the same D_h have the same pressure gradient per unit length. Alternatively, the equivalent diameter is used where the cross-sectional area is kept constant [31]. The Reynolds number also conveys the ratio of convective and diffusive time scales. In contrast, the behaviour of an unsteady flow is described by the Womersley number [38], which measures the ratio of oscillatory and diffusive time scales:

$$Wo = \frac{D_h}{2} \sqrt{\frac{\omega}{\nu}} \quad (2.2)$$

where ω is the angular frequency. Wo equivalently defines the relative size of the duct in comparison with the Stokes layer thickness. Alternatively, the kinetic Reynolds number $Re_\omega = 4Wo^2$ is used, so-called because the dimensionless frequency plays the same role as the Reynolds number does in uni-directional steady flow. Analogous to the study of laminar/turbulent flow transition the frequency-dependent evolution of the interaction between viscous and inertial forces governs transition between characteristic regimes of unsteadiness. In an oscillatory flow, the magnitude of oscillations may be measured by the dimensionless amplitude parameter:

$$A_0 = \frac{2\langle\hat{\chi}_A\rangle}{D_h} \quad (2.3)$$

where $\langle\hat{\chi}_A\rangle$ is the amplitude of the spatially-averaged dimensional displacement (equal to half of the tidal displacement). A_0 measures the length over which a fluid element is displaced during a cycle, compared with the hydraulic diameter. Often in pulsating flows, the flow rate amplitude Q_A/Q_0 is used instead.

Interestingly, the steady component has no effect on the characteristic behaviour of a pulsating flow (assuming that it is not high enough to trigger turbulence) and only the oscillating components of the flow need generally be considered. Furthermore, the amplitudes of the pertinent parameters are found to be directly proportional to the driving pressure gradients [39], such that the hydrodynamics of pulsating and oscillating flows are completely characterised by the frequency parameter alone. The evolving relationships between the time-dependent velocity profiles, flow rate, wall shear stress and pressure gradient with varying pulsation parameters are conveniently captured by the historical development of analytical solutions and subsequent experimental confirmation.

2.1.2 Velocity Profiles, Flow Rate and Pressure Gradient

Holmes and Vermeulen [40] measured the velocity profiles of rectangular ducts with aspect ratios of 1, 0.25, 0.15 and 0.1 using a flow visualisation technique, finding the results to be in excellent agreement with theory. In the narrower channels, the measurements – which appear to have been taken over the longer dimension only – have a maximum error near the wall. This is attributed to the high near-wall velocity gradients associated with ducts of this form factor that generate a high percentage error for a relatively small discrepancy in slope.

In acoustical studies on Helmholtz resonator tubes, Richardson [41] became the first to observe the near-wall velocity maximum that is uniquely characteristic of oscillating flow. Velocity measurements were taken by traversing a hot wire anemometer across the mouth of the orifice with a compressible reciprocating flow generated by the motion of a piston coupled to an electric motor by a long crank. While the phenomenon has come to be known as Richardson's annular effect, it is actually not related to geometry and was correctly attributed to the lesser inertia of the viscously-damped outer annuli of the tube. In

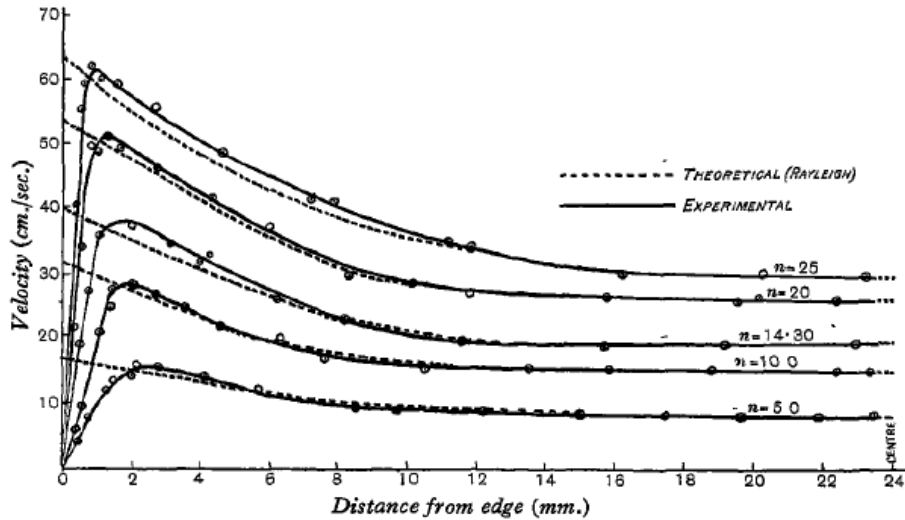


Figure 2.2: Near-wall velocity overshoot in a square section for $Wo = 34.6, 48.9, 58.5, 69.2$ and 77.4 , Richardson and Tyler [42].

a subsequent confirmatory work, Richardson and Tyler [42] measured the effect in ducts with alternative shapes, such as that shown for a square section in Figure 2.2. Ironically, it seems that the latter pioneering work – which precedes even the mathematical solutions – contains the only published experimental velocity data in a channel other than that of the current authors. However, the results differ significantly from the theory of Chapter 3, away from the phenomenon of interest for the solitary phase values investigated. While the magnitude and location of the overshoot were captured reasonably well for the slower oscillations, an error in magnitude of as much as 23% at higher frequencies has been estimated using a plot digitiser. Furthermore, the accuracy of the centreline velocity was poor, differing by as much as a factor of 2.5 at the high frequencies. It is likely that much of this error originates from the measurement technique. The hot-wire probe causes a blockage that disturbs the flow field. Hence, non-intrusive techniques have more recently been utilised.

Understanding of the behaviour over the complete oscillation cycle followed from analytical theory, beginning with Sexl [43] who solved the Navier-Stokes equations for velocity in a pipe geometry. Uchida [32] extended the solution to study its relationship with the flow rate, pressure gradient and wall shear stress in a comprehensive parametric study. Fan and Chao [31] developed analytical solutions for steady, oscillating and pulsating flows in a two-dimensional channel using the method of Green's functions. Figure 2.3 presents the oscillating velocity profiles for a fixed cosine wave pressure gradient in a narrow rectangular

duct for low and high frequencies. At very low frequencies, the velocity profiles are parabolic – each resembling a steady laminar profile at that instantaneous flow rate oscillating in phase with the flow rate and pressure gradient. At large frequencies, the velocity profiles become flatter near the centre of the pipe with a maximum flow velocity that is offset from the centre-line and the phase difference between the pressure gradient and flow rate is $\pi/2$. The study also found that the minimum pressure gradient occurred for a square duct. The method of Fourier analysis pioneered by Uchida lends itself well to the analysis of amplitude and phase alterations experienced by the important flow variables, as a function of frequency. Figure 2.4 plots the behaviour of the amplitude and phase of flow rate, for fixed pressure gradient oscillations. As expected, less flow is induced owing to an increase in work input required to maintain harmonic motion, and the phase delay approaches $\pi/2$ at high frequencies.

With a series of predictive equations developed, a series of experimental works set about confirming the relationships between the important variables using various flow measurement techniques. By introducing a thin filament of black ink into a pulsating pipe flow, Linford and Ryan [44] performed a frame-by-frame analysis of the velocity at various radial positions to within 2.5 mm of the wall, observing the behaviour of the near-wall overshoot with time. Measurements were performed over the range $1.83 \leq Wo \leq 21$, though the sinusoidal pulsations contained higher harmonics at high frequencies, probably due to turbulence. Also, the flow rate was calculated as a function of pressure gradient measurements, with the error in pressure measurements less than 5% of the amplitude. As predicted by theoretical solutions and partially shown by the experimental results of Hershey and Song [45], the pressure drops associated with higher values of Wo were larger.

With a view to developing a technique for measuring the rheological properties of viscoelastic fluids, Harris et al. [46] generated oscillatory motion in a Newtonian mixture of glycerol and propane using a bellows coupled to a gear box which allowed the frequency to be varied over $4.4 \leq Wo \leq 11.6$. Cams with differing eccentricities allowed the volumetric displacement to be varied to $A_0 = 0.98$ and 1.43. The velocity profiles were estimated using a flow visualisation technique where the tracks of suspended 250 μm polystyrene spheres were photographed by a camera operating a long exposure. Results were found to be in excellent agreement with the theoretical solution adjusted in terms of track length of the particles. Muto and Nakane [47] used a similar visualisation technique to investigate oscillating ($1.3 \leq Wo \leq$

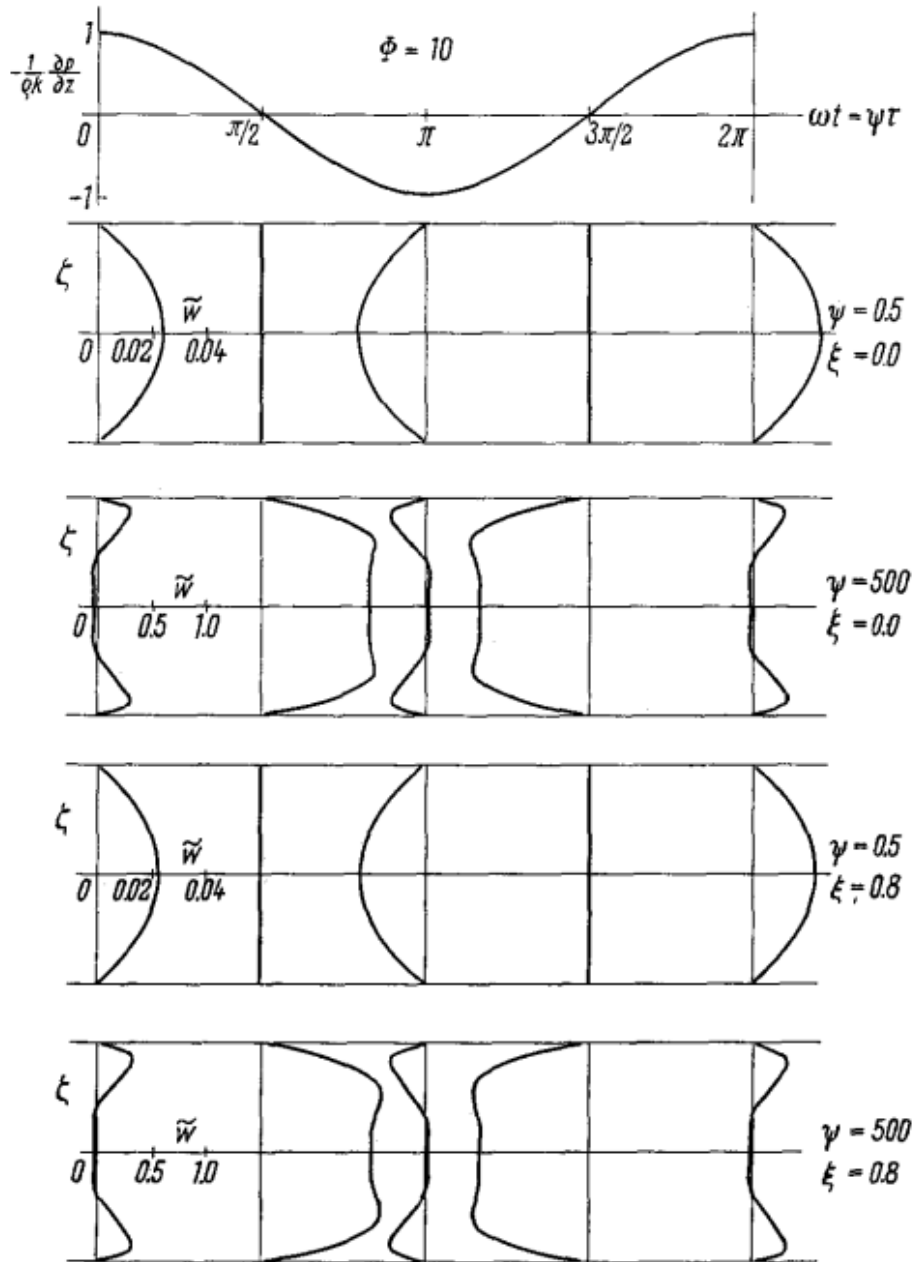


Figure 2.3: Oscillating velocity profiles in a narrow rectangular duct with an aspect ratio of 10 for $Wo = 0.4$ ($\psi = 0.5$) and $Wo = 12.9$ ($\psi = 500$) at duct centre ($\xi = 0$) and near the wall ($\xi = 0.8$), Fan and Chao [31].

23) and pulsating ($2 \leq Wo \leq 12$, $0.5 \leq Q_A/Q_0 \leq 2$) flows in a circular tube. Oscillatory motion was induced by a reciprocating piston with the dimensionless amplitude kept approximately constant $A_0 = 0.53 - 0.64$, while the optional mean flow was superimposed using a pump. $250 \mu m$ diameter aluminium particles suspended in a viscous glycerin-water solution were illuminated using a light source concentrated into a thin sheet using a pair of slits. The tracks

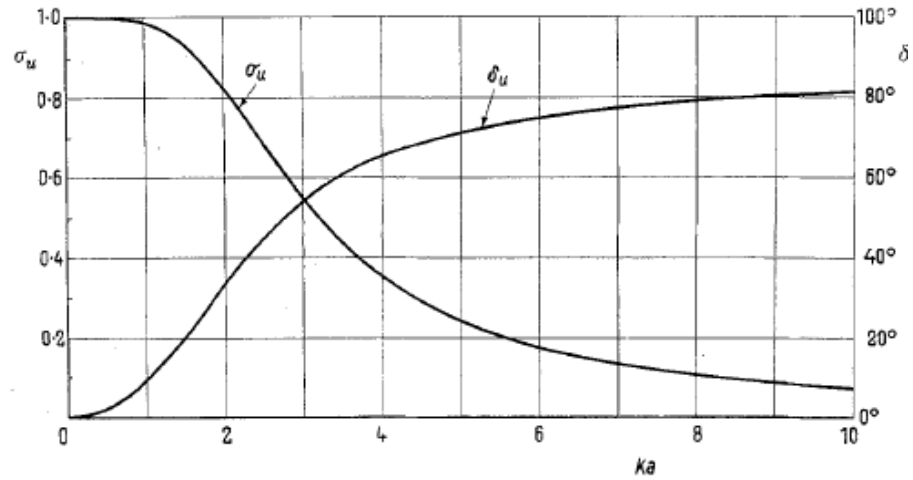


Figure 2.4: Amplitude ($= \sigma_u$) and phase ($= \delta_u$) of flow rate with frequency $Wo (= ka)$ for constant pressure gradient oscillations in a pipe, Uchida [32].

were photographed using a camera triggered by motion of the piston and exposed for a time interval. The velocity could therefore be calculated by measuring the length of the particle tracks. The results were found to coincide well with theory.

Laser Doppler velocimetry was used by Denison and Stevenson [48] to measure oscillating flows ($1.71 \leq Wo \leq 14.1$) in a pipe. The directionally-sensitive laser velocimeter operates by detecting the Doppler frequency shift produced when coherent light is scattered from small moving particles seeded in the flow. Oscillations between two water tanks were generated by controlling pressure fluctuations in the enclosed air space at one side. Theoretical velocity profiles were computed from the instantaneous pressure gradient measurements and compared to the experimental distributions. The maximum velocity at the centreline was found to be in agreement to within 1.4% and the RMS error across the profile did not exceed 2% for any of the profiles. In a subsequent work, Denison et al. [49] investigated pulsatile flow in developing and fully-developed flows using the same technique. Oscillations were generated using a piston driven by a Scotch yoke, and superimposed on a mean flow with $Q_A/Q_0 = 0.16$. For the range of frequencies tested ($4 \leq Wo \leq 6$), the results were found to corroborate theory. Similarly, Einav and Lee [50] used laser Doppler velocimetry to study oscillating flows ($1.12 \leq Wo \leq 8.23$) in a tube between a pair of pistons coupled to a motor, finding agreement to within 1.1% of the results of Denison and Stevenson and theory.

In their carefully-controlled experiments on transition to turbulence, Eckmann and Grot-

berg [51] constructed a sinusoidal drive mechanism to generate an oscillatory flow in a straight circular tube. A variable-speed electric motor and speed reduction gear were used to generate rotational motion over a high range of frequencies, $9 \leq Wo \leq 33$. A gradation of eccentric tapped holes on the drive wheel of the Scotch yoke allowed the oscillation amplitude to vary between $2.4 \leq A_0 \leq 21.6$. Measurements of the laminar velocity profiles made using laser-Doppler velocimetry were generally found to be within 1-2% of theoretical prediction. To the same end, Clamen and Minton [52] used the hydrogen bubble technique to validate laminar velocity distributions over the range $11.2 \leq Wo \leq 26.7$. The oscillatory flow of water was generated by a Scotch-yoke mechanism.

More recently, Ünsal et al. [53] measured velocity profiles over the range $0.8 \leq Wo \leq 6.6$ using a hot-wire probe at the end of a tube. The pulsating air flow was generated using a purpose-built mass flow rate PID control system designed by Durst et al. [54]. Using the same experimental setup, Ray et al. [55] synchronised the system with a distribution of low time-scale transducers to measure the amplitude and phase of the pressure gradient over a range of frequencies between $Wo = 0.15$ and 21 (varying the amplitude of flow rate pulsations was found to have no effect on the timing). The experimental results were found to be in very close agreement with the analytic solution based on the Fourier analysis method of Uchida [32], reorganised in terms of a prescribed flow rate. Now the behaviour of the parameters could be analysed for constant flow rate amplitude pulsations. In the low-frequency range, the instantaneous pressure gradient values were found to be approximately equal those of similar steady flows. At intermediate frequencies, the amplitude of the pressure gradient increased compared to the corresponding steady flow value and at high frequencies the ratio of the pulsating to steady pressure drop was seen to approach zero along with the known phase shift. The behaviour of the amplitude and phase of pressure with frequency, plotted in Figure 2.5, clearly suggests the existence of three unique oscillation regimes, which will be classified on a quantitative basis presently (see Section 2.1.4). Haddad et al. [56] expanded their analytical solution for a parallel plate channel, though using twice the hydraulic diameter of the pipe. The study found that there is both a larger pressure gradient amplitude and a larger phase shift for channel flow than pipe flow at the same frequency. The relative difference is negligible in the low-frequency regime, grows quickly in the mid-frequency regime and levels off in the high-frequency regime. The study also performed a comprehensive analysis of parameters

predicting and quantifying the phenomenon of flow reversal.

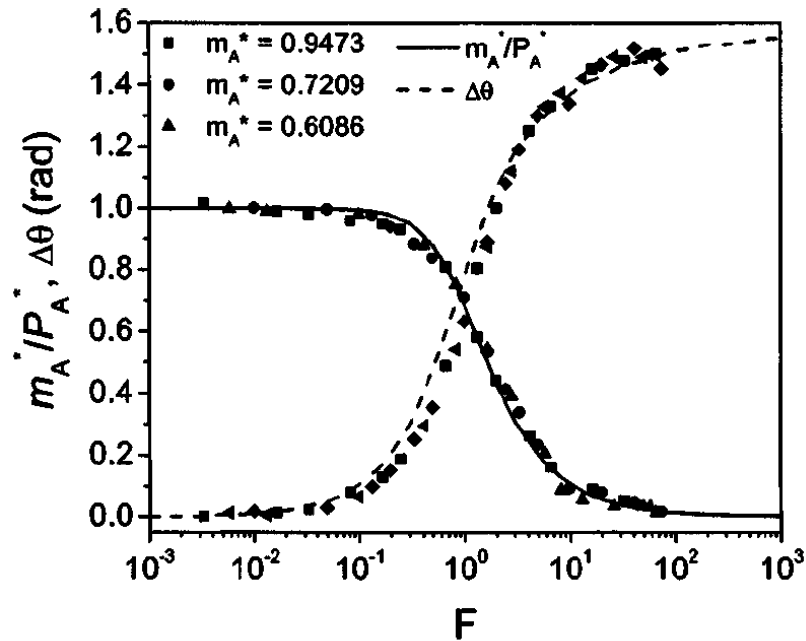


Figure 2.5: Amplitude ($= P_A^*$) and phase ($= \Delta\theta$) of pressure gradient with frequency $Wo (= \sqrt{2\pi F})$ for constant flow rate amplitude ($= m_A^*$) in a pipe, Ray et al. [55].

2.1.3 Wall Shear Stress

The analytical solution of Uchida [32] predicts the behaviour of the amplitude and phase of wall shear stress with varying frequency. Figure 2.6 indicates that the magnitude of the wall shear stress decreases, since the flow rate amplitude decreases with increasing frequency at constant driving pressure. However, the reducing flow rate conceals the augmented near-wall velocity gradients experienced at high frequencies, which result from a thinning Stokes boundary layer. Haddad et al. [56] investigated the frequency-dependent behaviour for constant flow rate pulsations in a pipe and a parallel plate channel, finding the amplitude of the wall shear stress to increase with frequency with the magnitude higher for the channel geometry. The phase delay relative to the pressure gradient tends to $\pi/4$ for both vessels, though the phase lag is higher for the non-circular geometry in the mid-frequency range. Since the cross-section of a pipe is one-dimensional, the wall shear stress profile is uniform at the perimeter. Experimental verification of the wall shear stress in a tube at a given frequency thus requires a single estimation of the slope of the velocity profile at the wall. Nonetheless,

only a handful of studies have estimated this parameter, despite a multitude of experimental studies measuring the instantaneous velocity profiles.

In a biomechanical study, Hughes and How [57] measured pulsating velocity profiles in a tube using an ultrasound Doppler velocimeter, chosen for its potential applicability to

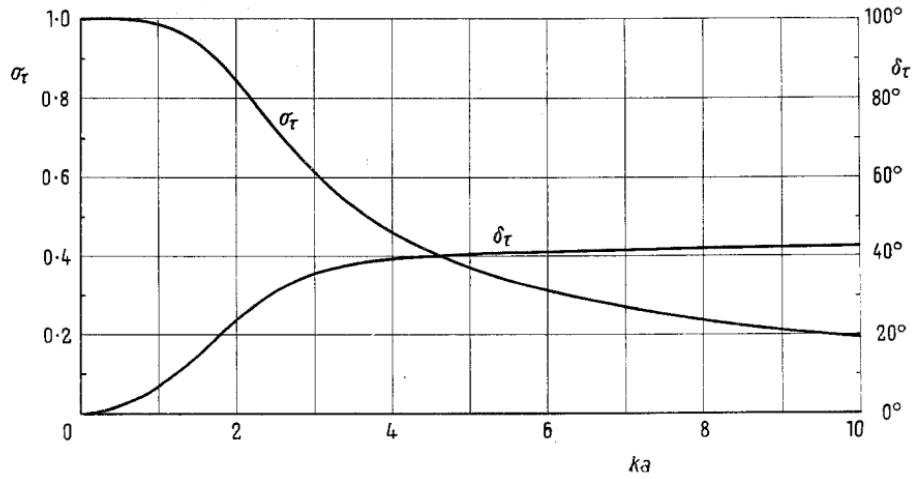


Figure 2.6: Amplitude ($= \sigma_\tau$) and phase ($= \delta_\tau$) of wall shear stress with frequency $Wo (= ka)$ for constant pressure gradient oscillations in a pipe, Uchida [32].

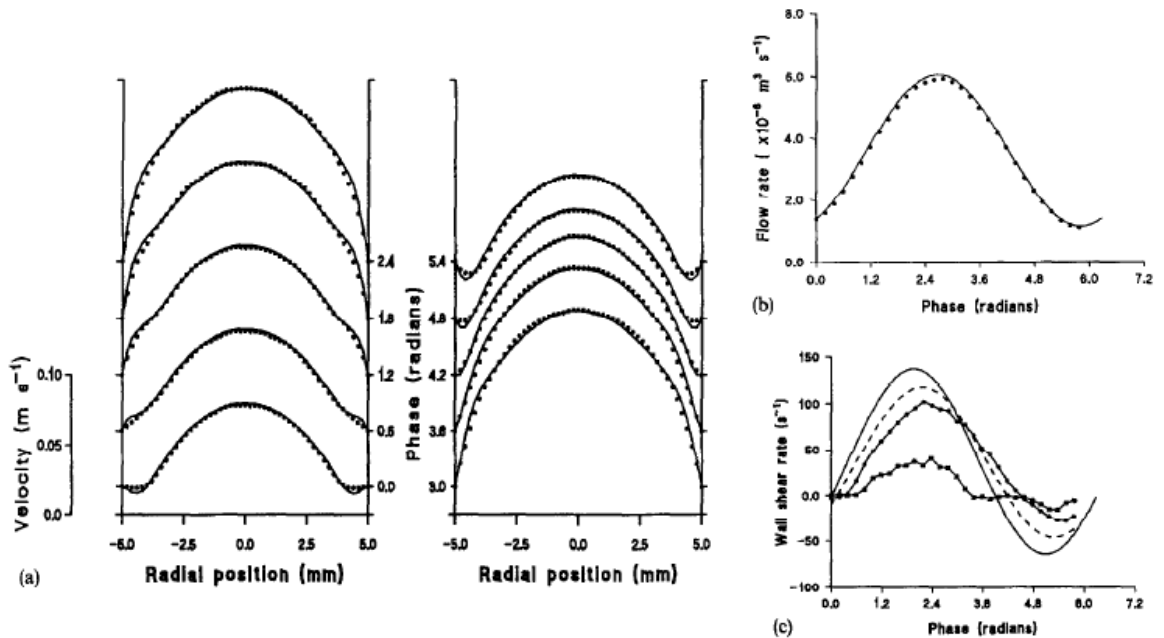


Figure 2.7: The pulsatile behaviour of (a) the pulsating velocity profiles, (b) the flow rate, and (c) the wall shear rate for $Wo = 15$ and $Q_A/Q_0 = 0.7$ in a pipe. Solid lines and markers represent analytical solutions and experimental measurements, respectively. The dashed line of (c) represents the linear fit to the theoretical velocity profile as discussed in the text, Hughes and How [57].

opaque liquids. Synchronised measurements of the velocity profile and pressure gradient were achieved using an external trigger signal from the modulating piston pump for $9.6 \leq Wo \leq 15$. Figure 2.7(a) depicts the accuracy of the reproduced pulsating velocity profiles, which contain flow reversal despite an invariably positive pulsating flow rate. Maximum error in the centreline velocity and over the entire profile were 11% and 8.8% respectively, relative to the mean flow velocity. The largest discrepancies were observed during intervals of reversed flow, at maximum acceleration or at times when inflection points exist in the profile. The flow rate waveforms, again achieved by integration, were found to agree well in both magnitude and phase with a maximum error of 6.4% relative to the mean (see Figure 2.7(b)). Experimental wall shear rates – computed using a single velocity point closest to the wall (0.2 mm from the wall) – are compared to a pair of theoretical values in Figure 2.7(c): (i) the true magnitude at the wall, and (ii) a linear fit between the velocity at 0 and 0.2 mm on the theoretical velocity profile. The latter, plotted in Figure 2.8 for different proximities to the wall, quantifies the under-estimation introduced by the limited near-wall resolution of the technique. It is clear that the amplitude and mean value of the wall shear rate decrease and the phase lag increases as the fit is extended to points farther from the wall. This explains a certain amount of the attenuation and lag found in the experimental values compared to theory. With respect to the true shear rate, the maximum errors of the mean and peak to peak wall shear rates were 14% and 35%. The latter reduced to 21% when compared to the linear-fitted theoretical value. Of course, the under-estimate increases with frequency as the Stokes layer becomes thinner. A data point a given distance from the wall attempts to approximate a larger percentage of the boundary layer, and a velocity distribution which is hence less linear. For example at $Wo = 9.6$ and 15, the regions between the wall and the nearest data point cover 9.6% and 15% of the Stokes boundary layer, respectively.

Ojha et al. [58] created a pulsating flow ($Wo = 7.52$, $Q_A/Q_0 = 0.6$) in a pipe by superimposing the steady flow of a gear pump on that from a cam-driven piston pump. Flow visualisation was performed using a tracer technique, which makes use of the photochromic properties of a normally colourless indicator in the working fluid. A pulsed UV laser beam changes the indicator to a coloured dye, producing a trace in the laser plane direction that may be photographed a short time after its creation. The flow rates may be determined through integration of the velocity profiles. By fitting a sine wave to the data (see Figure 2.9(a)) the

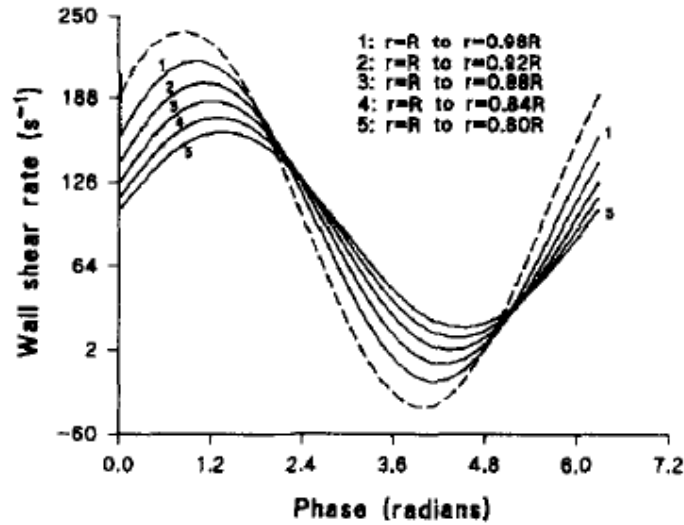


Figure 2.8: Effect of near-wall resolution on the wall shear rate estimate in a pipe. Curve 1 corresponds to a data point nearest the wall at 0.2 mm in the experiment. The true value is given by the dashed line, Hughes and How [57].

values of Q_0 and Q_A are determined and the corresponding predicted velocity profiles may be compared to experiment. Furthermore, the shear stress at opposing sides of the tube was computed by evaluating the derivative of a fitted polynomial to the near wall velocity data. The results, plotted in Figure 2.9(c), were accurate to within 7% of the theoretical value with the phase error less than 9° . While a slight asymmetry between the walls is present, the accuracy of the near-wall shear stress measurements illustrates well the superior spatial resolution of the technique compared to LDA.

Zhao and Cheng [59] used an indirect technique to compute frictional stresses in a pipe

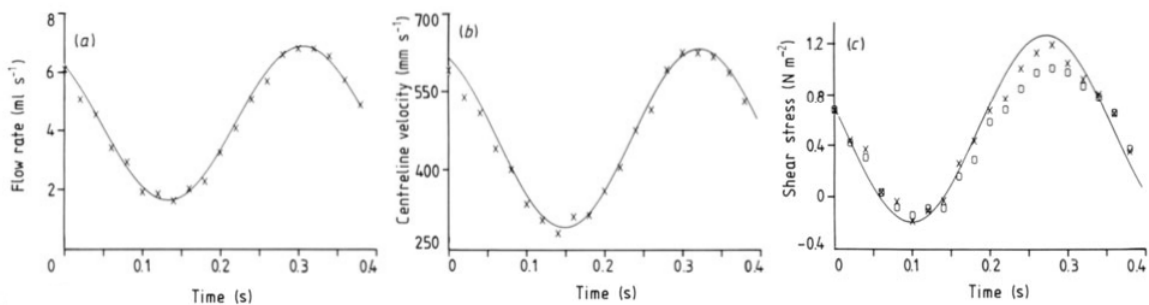


Figure 2.9: (a) Pulsating flow rate, (b) centreline velocity and (c) wall shear stress for $Wo = 7.52$ and $Q_A/Q_0 = 0.6$. Solid lines and markers represent analytical solutions and experimental measurements, respectively, with the differing markers indicating behaviour at opposing sides of the tube, Ojha et al. [58].

flow of air, using calculations based on the momentum integral balance (see Section 2.1.4). Reciprocating flow was generated using a double-acting pump connected to a crank shaft and yoke sinusoidal mechanism. The velocity and axial pressure gradient were measured using a hot wire anemometer and differential pressure transducer, respectively, with phase accurately measured using an angular position encoder. The experimental values of the friction factor magnitude were found to be in good agreement with theory for a range of values $2.4 \leq Wo \leq 9.9$ and $16.5 \leq A_0 \leq 26.4$. The corresponding phase was not estimated. The cycle-averaged friction factor of the measured data had a maximum deviation of 14.8% from the analytic solution.

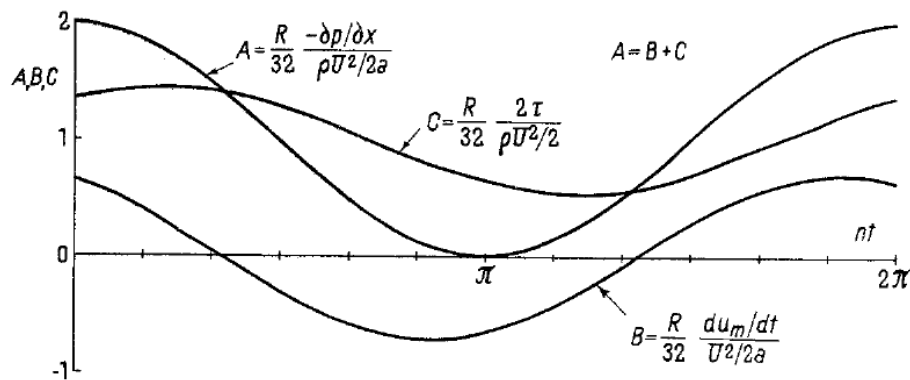


Figure 2.10: Pulsating contributions of viscous (= C) and inertial (= B) stresses to the pressure drop (= A) in a pipe for $Wo = 4$ and $Q_A/Q_0 = 1$, Uchida [32].

2.1.4 Momentum Balance

Uchida [32] went on to investigate the contributions of viscous and inertial stresses to the overall pressure drop through the momentum balance equation (developed mathematically in Chapter 3). The relative contributions of the individual losses vary periodically as a function of time, as displayed graphically in Figure 2.10. Ohmi et al. [60] investigated the behaviour of these contributions with frequency to define boundaries to the characteristic regimes. The behaviour of four parameters was analysed: a couple measuring the relative contributions of the viscous and inertia terms, as well as the phases of the flow rate and wall shear stress. Figure 2.11 presents the contributions of the inertial and viscous stresses with frequency, indicating that behaviour tends to asymptotic regimes at the limit of low and high frequency. The low-frequency regime is characterised by predominantly viscous stresses

and negligible phase delay. Further, the rate of change of these values is small. Conversely, inertial stresses – and associated phase delays – dominate the high-frequency regime. The momentum distribution cannot follow the changes in the flow rate without retarding. At mid-frequencies, the frequency-dependent behaviour is characterised by rapid changes in the momentum contributions and phase. The boundaries for the pipe geometry were arbitrarily defined at frequencies where the viscous and inertia terms comprised 95% of the overall pressure gradient. Below $Wo = 2.36$, frictional losses result largely from viscosity. The quasi-steady approximation is valid and the flow rate and shear stress are in phase with driving pressure gradient. Above $Wo = 28$, the flow is dominated by inertia and the assumption of inviscid flow holds throughout the channel. Hence, the boundaries to the regimes are defined based on adherence to certain mathematical approximations, and also by the flow's dominant characteristics.

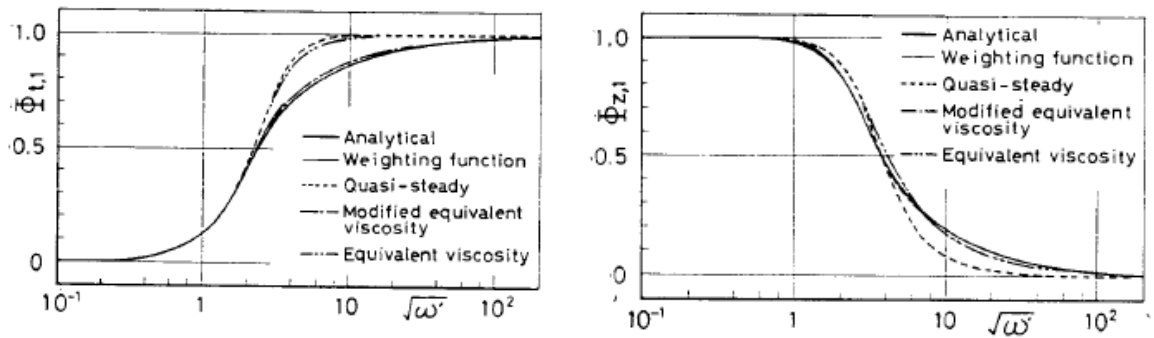


Figure 2.11: Contributions of (a) inertial stresses and (b) viscous stresses to the pressure drop with frequency $Wo (= \sqrt{\omega'})$, Ohmi et al. [60].

2.1.5 Summary of Unsteady Hydrodynamics Review

It is clear that oscillating flow involves complex relationships between the hydrodynamic variables that require a comprehensive parametric analysis on a local- and frequency-dependent basis. Analytical models are hence invaluable, offering complete information of the flow field, which is difficult to obtain experimentally. Solutions that decompose parameters into amplitude and phase values [32] allow convenient manipulation while those that study behaviour relative to a prescribed flow rate rather than pressure gradient [55] are perhaps more intuitive.

Of course, experimental works are of vital importance in the validation of theory. Heuristically, the analytical predictions for velocity and wall shear stress profiles and the pressure gradient should be verified experimentally in each of the three behavioural regimes [60] for a given geometry. A review of experimental works on the fluid mechanics of pulsating and oscillating flows indicates that the complete set of instantaneous velocity profiles in a pipe have been validated experimentally over a large range of frequencies ($0.8 \leq Wo \leq 33$) spanning the quasi-steady, transitional and inertia-dominated regimes. Synchronised measurements of the flow rate and pressure gradient have confirmed the evolving ratio of amplitudes and phase predicted by theory up to a moderate frequency ($0.25 \leq Wo \leq 15$) for flow in a pipe with high precision. The accuracies of available wall shear stress measurements in a pipe are comparably poor and span only a portion of the transitional frequency

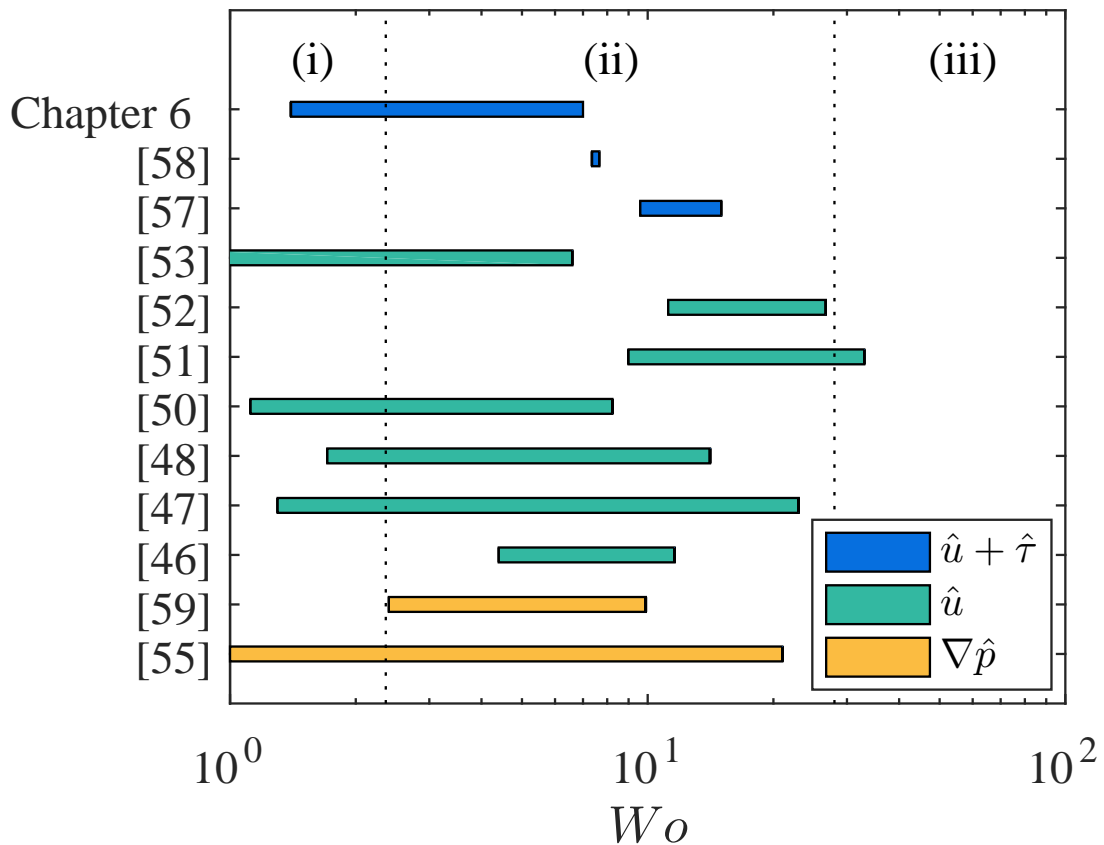


Figure 2.12: Parameter spaces covered by the reviewed hydrodynamic experiments in pipes, and the experiments of Chapter 6 in a rectangular channel. The legend indicates the hydrodynamic parameters measured in each case – velocity \hat{u} , wall shear stress $\hat{\tau}$ and pressure gradient $\nabla \hat{p}$. Dotted lines partition the characteristic regimes: (i) quasi-steady, (ii) intermediate, and (iii) inertia-dominated.

regime ($7.52 \leq Wo \leq 15$). The apparent gaps reflect the practical difficulties associated with generating rapidly-oscillating flows experimentally and with measuring the near-wall area with high resolution and precision. Furthermore, the Stokes layer narrows at intermediate to high frequencies, and measurement of the spatial gradients in the near-wall area becomes increasingly difficult. Experiments in rectangular channels are conspicuously absent from the literature, apart from the very early work of Richardson and Tyler whose limitations have been previously outlined. This is probably attributable to a velocity profile containing an extra spatial dimension, as well as wall shear stress distributions that are non-constant over the cross sectional perimeter. Paradoxically, thermal studies in channel heat sink geometries are common owing to their relative ease of manufacture.

The parameter spaces covered by the hydrodynamic experiments are displayed graphically in Figure 2.12, with the different colours indicating the type of variable measured. The measurements of the current research alone, presented in Chapter 6, were performed in a non-circular two-dimensional channel. The hydraulic diameter of the rectangular channel (described in Chapter 4) is small compared with those reviewed, as presented in Table 2.1. Experiments that achieved higher values of Womersley number used larger hydraulic diameters, which reduces the requisite dimensional frequency of oscillation.

As discussed in Chapter 1, the proposed photonics application involves single-phase liquid-cooling flow in a micro- ($10\mu m < D_h \leq 200\mu m$) or mini- ($200\mu m < D_h \leq 3mm$) channel heat sink, driven by a pulsating micropump. The influence of Wo is of vital importance to the thermal problem since the shear stress at the wall and thickness of the hydrodynamic boundary layer are expected to affect the heat flux at the wall and thermal boundary layer thickness. The high frequency regime achieves the highest increase in wall shear stress. However, to achieve non-quasi-steady flow in microchannels, very high frequency pulsations (to the order of kHz) are required to overcome the strong viscous effects brought about by the small hydraulic diameters. For example, the 60 Hz maximum operating frequency of a commercially-available micropump [61], driving a pulsating flow of water through a large microchannel with $D_h = 200 \mu m$ gives a Womersley number of just 2.2. In contrast, Persoons et al. [16] achieved Womersley numbers between 6 and 17 using a larger minichannel. The requisite work input is higher for pumps that are inherently unsteady for a fixed delivered flow rate, with the pressure drop increasing with increasing frequency of the vibrating diaphragm.

The augmented pressure losses are due to a combination of increased inertial losses and steeper near-wall velocity gradients caused by changes in the transverse velocity distribution. This adds to a work input that is already high in small-scale channels, owing to a pressure drop that scales inversely with the fourth power of hydraulic diameter in the laminar regime. The pulsations incur further losses pumping through an array of channels rather than pipes for a given flow rate.

Table 2.1: Details of reviewed hydrodynamic experiments, and of the current experimental setup of Chapter 4.

Reference	Flow	Geom.	D_h [mm]	Fluid	Measurement Technique	Var.	Wo	A_0
Richardson [41]	Osc	○	35, 60	Air	Hot Wire Anemometry	\hat{u}	5-35	
Richardson & Tyler [42]	Osc	○ □	62, 48	Air	Hot Wire Anemometry	\hat{u}	5-25	
Linford & Ryan [44]	Puls	○	25	Newtonian	Flow Visualisation	$\hat{u}, \nabla \hat{p}$	1.83-21	
Harris et al. [46]	Osc	○	25	Newtonian	Flow Visualisation	\hat{u}	4.4-11.6	
Muto & Nakane [47]	Both	○	60	Newtonian	Flow Visualisation	\hat{u}	2-12	0.53-0.64
Denison & Stevenson [48]	Osc	○	19	Newtonian	Laser Doppler Velocimetry	$\hat{u}, \nabla \hat{p}$	1.71-14.1	
Denison et al. [49]	Puls	○	19	Newtonian	Laser Doppler Velocimetry	$\hat{u}, \nabla \hat{p}$	4-6	
Einav & Lee [50]	Osc	○	25	Water	Laser Doppler Velocimetry	\hat{u}	1.12-8.23	
Eckmann & Grotberg [51]	Osc	○	32	Newtonian	Laser Doppler Velocimetry	\hat{u}	9-33	2.4-21.6
Clamen & Minton [52]	Osc	○	51	Water	Hydrogen Bubble	\hat{u}	11.2-26.7	
Ünsal et al. [53]	Puls	○	15	Air	Hot Wire Anemometry	\hat{u}	0.8-6.6	
Ray et al. [55]	Puls	○	14	Air	Pressure Transducer	$\nabla \hat{p}$	0.15-21	
Hughes & How [57]	Puls	○	10	Newtonian	Ultrasound Doppler Velocimetry	$\hat{u}, \hat{\tau}$	9.6-15	
Ojha et al. [58]	Puls	○	5	Newtonian	Flow Visualisation	$\hat{u}, \hat{\tau}$	7.52	
Zhao & Cheng [59]	Osc	○	13.5	Air	Pressure Transducer	$\nabla \hat{p}$	2.4-9.9	16.5-26.4
Current Research	Puls	○ □	7.1	Water	Particle Image Velocimetry	$\hat{u}, \hat{\tau}$	1.4-7.0	0.36 - 8.9

Variable(s) Measured

\hat{u} , local time-dependent velocity and time-dependent flow rate

$\nabla \hat{p}$, time-dependent pressure gradient and time-dependent flow rate

$\hat{\tau}$, time-dependent wall shear stress

2.2 Heat Transfer of Unsteady Flow

As described by Stokes' second problem, unsteadiness causes time-dependent velocity gradients to diffuse from the wall in a single well-defined manner resulting from the no-slip boundary condition. In contrast, the characteristics of heat diffusion vary depending on the properties of the wall, which affect the manner of heating. For example, a thick-walled copper tube approximates the constant temperature boundary condition, while a thin stainless steel foil approximates the constant heat flux boundary condition. Since solutions to the energy equation may be obtained using either of these idealisations or by some more realistic hybrid, the underlying theory of the thermal problem is more complex and the heat transfer mechanisms are not well understood. The larger parameter space may explain why less attention has been paid to the behaviour of the local time-dependent temperature field and its derivatives, to which solutions exist in a pipe geometry. Also, unlike the hydrodynamic theory – which has been reasonably well characterised over the parameter space in a pipe – analytical theory for heat transfer has not been linked to confirmatory experimental measurements. Most importantly, the focus on time- and space-averaged heat transfer fails to distinguish between underlying mechanisms of enhancement. It is thus vital to build on the local time-dependent theory of the fluid mechanics, focusing particularly on the interplay of hydrodynamic and thermal parameters, in order to optimise the unsteady heat transfer problem.

2.2.1 Dimensionless Thermal Parameters

The flow of heat is interwoven with the hydrodynamics of the fluid, and thus the dimensionless hydrodynamic parameters of Section 2.1.1 remain key indicators of heat transfer behaviour. The Prandtl number Pr quantifies the rate of viscous diffusion relative to the thermal diffusion:

$$Pr = \frac{\nu}{\alpha_f} \quad (2.4)$$

where the thermal diffusivity is given by $\alpha_f = k_f / \rho_f c_{p,f}$ (where k_f and $c_{p,f}$ are the thermal conductivity and specific heat capacity of the fluid). Newton's law of cooling states that heat flux \hat{q} is proportional to the difference between the wall temperature $T_{w,0}$ and the representative fluid temperature $T_{f,0}$ for steady forced convection. The constant of proportionality is

the dimensional heat transfer coefficient $h_0 = \hat{q}/(T_{w,0} - T_{f,0})$. At the wall, heat is diffused solely by conduction and the heat flux is proportional to the temperature gradient as captured by Fourier's law $\hat{q} = k_f(\partial T/\partial \hat{y})$. The dimensionless Nusselt number Nu_0 expresses the convective heat transfer of a steady flow with respect to that of conductive heat transfer in the same quiescent fluid:

$$Nu_0 = \frac{h_0 D_h}{k_f} = \frac{(\partial T/\partial \hat{y}) D_h}{(T_{w,0} - T_{f,0})} \quad (2.5)$$

Within this thesis, heat transfer enhancement is defined relative to a steady flow with a flow rate equal to the time-average of the pulsating flow rate:

$$\partial Nu = \frac{\overline{Nu} - Nu_0}{Nu_0} \quad (2.6)$$

where \overline{Nu} is the time-averaged Nusselt number of a pulsating flow.

2.2.2 Mechanisms

The velocity and temperature profiles of steady flow are self-similar and therefore bound the Nusselt number. Equivalently, the driving temperature difference increases in proportion to any rise in heat flux. However, the proportionality is not fixed in a time-dependent flow and hence the physical meaning of a time-dependent heat transfer coefficient is ambiguous (this is discussed further in Chapter 7). This can result from a phase difference (at high frequencies) or a difference in the frequency of oscillation of each of the temperature parameters, for example. Furthermore, the heat flux is fixed while the bulk temperature may vary with time under the isoflux boundary condition.

By inspection of Equation 2.5, the non-steady Nusselt number may be enhanced by increasing the temperature gradient at the wall, or by reducing the driving temperature difference. In theory, it is possible that certain hydrodynamic features of the flow act favourably with respect to one method of enhancement and adversely with respect to the other. Hence, this section considers the effect of oscillations on thermal behaviour in terms of individual mechanisms: (i) those that act on the bulk temperature, and (ii) those acting on the wall temperature gradient. Unfortunately, the mathematical toolkit used in theoretical analyses

turns out to be restrictive and ideal boundary conditions may obscure the effect of these underlying mechanisms. For example, the constant heat flux boundary condition fixes the numerator of Equation 2.5, while the constant wall temperature boundary condition heavily biases the denominator. As a final consideration, the effect of localised flow reversal is likely to lead to non-linear effects on heat transfer, which are distinct from the linear mechanisms discussed. However, no satisfactory theory exists for dealing with bidirectional flow, highlighting the importance of experiment.

2.2.2.1 Mechanism 1: Enhanced Axial Diffusivity

Mass Transfer Much of the initial progress was made in the analogous problem of mass transfer in tubes with impermeable walls. In a steady flow, Taylor [62] analysed specific fundamental cases of the dispersion of a volume of contaminant, including the diffusion of a cylindrical volume of a solute with a constant initial concentration, and solute of constant concentration entering a tube of zero concentration. It was determined that the axial concentration distribution spreads symmetrically from a plane that travels with the mean velocity of the flow, in spite of the velocity profile's asymmetry. Furthermore, the axial diffusion was enhanced compared to longitudinal molecular diffusion alone. Taylor was so surprised by the predicted behaviour that he set up an apparatus to validate the theoretical concentration profiles of these fundamental cases, finding good agreement with his analytical solution. The mechanism is explained with the aid of Figure 2.13. Consider the diffusion of an initially cylindrical volume of a solute with a constant initial concentration. Advection according to the velocity profile causes the initial volume at the line B to be distorted into the shape of a paraboloid. While not intuitive, the concentration is now symmetrical in the axial dimension between lines A and C, owing to the intrinsic nature of the paraboloid geometry. Subsequently, the variation in the transverse concentration profile causes transverse diffusion to occur. Hence, the enhanced diffusion mechanism results from the combined effect of axial convection and transverse diffusion. In applications where efficient removal of the concentrate is desired, such diffusion acts against the advective transport of the fluid.

Chatwin [64], Watson [65] and Smith [66] determined analytically that a similar mechanism exists in unsteady flow; however, the effect is lessened since the process cannot establish

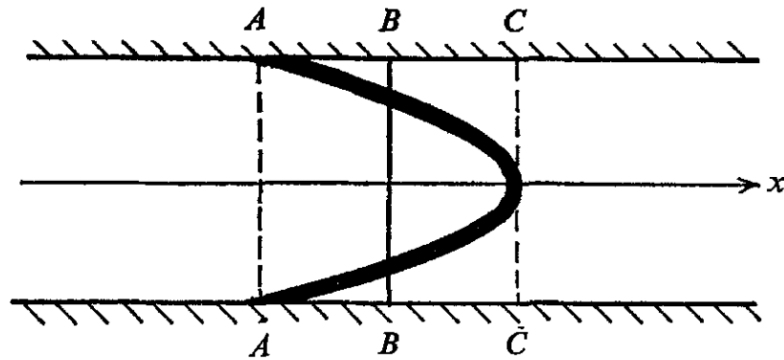


Figure 2.13: The augmented diffusion mechanism in steady flow, Chatwin [63].

itself fully before the flow conditions are changed. At large oscillation periods for example, the effects of the negative velocity profile cancel those of the corresponding positive velocity profile. The cloud of contaminant expands during one half-cycle and contracts during the second half-cycle, with the net effect of the full cycle being a slight overall increase in length. The theoretical results were corroborated by the experiments of Joshi et al. [67], who measured augmented diffusion in a pulsating pipe flow with $1.6 \leq Wo \leq 7.8$ and flow rate amplitude $600 \leq Q_A/Q_0 \leq 3000$ ¹. At low amplitudes and frequencies, a quasi-steady situation results with diffusion similar to the steady value [62]. Axial mass diffusion is enhanced with the square of A_0 due to the fluid being displaced over larger axial distances with higher temperature differences. For constant frequency, diffusivity increases with tidal displacement. For constant dimensionless amplitudes $9.2 \leq A_0 \leq 39.6$, enhanced diffusivity increases in proportion to Wo at high frequencies and approaches 1 at the limit of low frequency, with the limiting behaviours connected by a transition region (see Figure 2.14). At constant flow rate amplitude, diffusivity decreases with increasing frequency. Experiments of Jaeger and Kurzweg [68] in a pulsating flow ($3.5 \leq Wo \leq 9.1$) of oxygen gas have also confirmed the square power law relationship between the enhanced dispersion and dimensionless amplitude, and the proportionality between the dispersion coefficient and frequency. The values of diffusivity ranged from 300 to over 8000 times that predicted by molecular diffusion.

¹This very large flow rate amplitude owes to a minuscule steady component, used to offset the axial diffusion of the concentrate and create a steady-state exchange process. The steady component was found to have no effect.

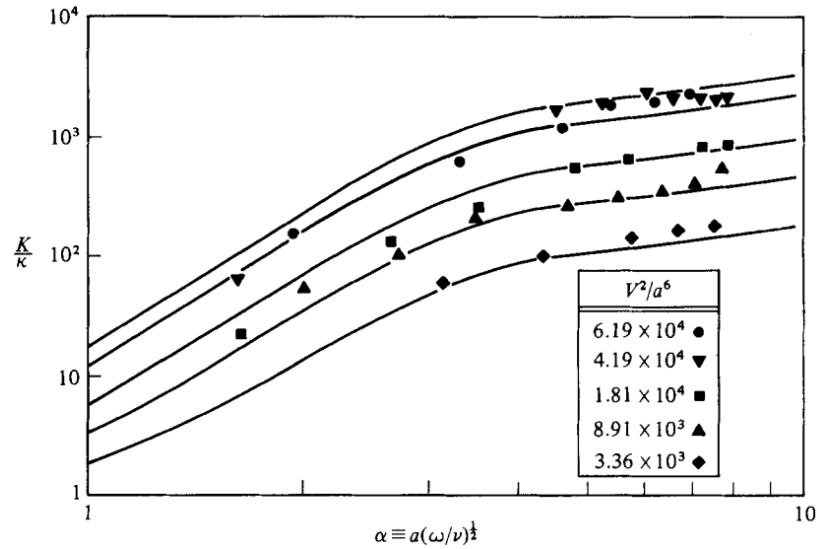


Figure 2.14: Enhanced diffusivity ($= K/\kappa$) relative to molecular conduction with frequency $Wo (= \alpha)$ for constant dimensionless amplitudes $A_0 (= \sqrt{(V^2/a^6)}/4\pi^2)$, Joshi et al. [67].

Heat Transfer The mass diffusion problem may be viewed as a generalisation of the corresponding thermal problem, which generally deals with concentration (i.e. temperature) gradients rather than finite volumes of concentration. Kurzweg [69] predicted that an equivalent thermal mechanism exists and developed a comprehensive theory for a parallel plate geometry with linear axial temperature gradient. By analogy, the non-porous walls of the former studies became thermally-insulated walls with no heat addition. It was determined that enhanced axial thermal diffusivities four orders of magnitude higher than those due to molecular diffusion could be achieved. For example, an axial heat transport of 1.8×10^6 W/cm^2 was achievable using pressurised water, which was two orders of magnitude higher than liquid-metal heat pipe technology at the time. While input of power is required, the ratio of power consumption to heat transferred is commonly less than 1% for typical operating conditions [70]. As before [65], the enhanced thermal diffusivity increases with the square of tidal displacement. Also, thermal diffusivity increased with frequency with behaviour differing at low and high frequencies. With such alternative limiting forms, the study identified that the parameters could be tuned to maximise heat transfer. By plotting 'tuning curves', it was found that optimal axial heat transfer was achieved when the time taken for heat to diffuse from the centre of the channel to the wall was equal to one half of the oscillation period.

The predicted axial heat transfer was validated to within a factor of a half (as explained by the change from a tube to a parallel plates geometry) by the experiments of Kurzweg and Zhao [21], who implemented an oscillatory flow ($25 \leq Wo \leq 50$, $3 \leq A_0 \leq 20$) in a bundle of capillary tubes between a pair of fluid reservoirs maintained at different temperatures. Effective axial conduction was enhanced by a factor of 1.79×10^4 compared with the molecular thermal diffusion value of water without accompanying net mass transport. The axial heat flux value of 292 W/cm^2 is comparable with heat pipes. A numerical study by Zhang and Kurzweg [70] solved the energy equation in an oscillating pipe flow numerically without prior assumptions, finding their simulated tuning curves to be in good agreement with the earlier analytical predictions [69]. Furthermore, the time-dependent axial temperature distributions remained approximately linear as low as $Wo = 1$, as depicted in Figure 2.15. However, the second power relationship between enhanced thermal diffusivity and tidal displacement declined at large displacements, which reduced the axial temperature gradient and the resulting axial diffusion. The numerical study also investigated the effect of wall parameters in detail, finding that a wall thickness about 10% of the pipe diameter was optimal. Since conducting walls increase heat capacity, conducting walls enhance the axial heat transfer process.

Ozawa and Kawamoto [71] used a thermo-sensitive liquid-crystal tracer technique to qualitatively measure the 2-D temperature field of an oscillatory liquid flow in an insulated square channel between constant temperature hot and cold reservoirs at $Wo = 4.4$ and $Wo = 12.2$. Figure 2.16 presents the raw images at the higher frequency. Moving from hot to cold, the colour changes through blue, green, yellow, red and brown. The unprocessed images were in qualitative agreement with the upward and downward peaks of isotherms, generated using a complementary two-dimensional numerical model. Further analysis of the model indicated that, over the range $2 \leq Pr \leq 100$, the thickness of the thermal boundary layer coincided with the Stokes layer thickness. This suggests that the transverse temperature gradient is formed primarily as a result of the velocity profile. While the study by Kurzweg [69] is referenced in the paper, the results are not compared with their 1-D analytical model, perhaps since the geometry of the channel was square. Finally, being primarily concerned with axial heat transfer, the authors used a lumped-parameter model in conjunction with axial temperature measurements to estimate the effective thermal diffusivity over a range of

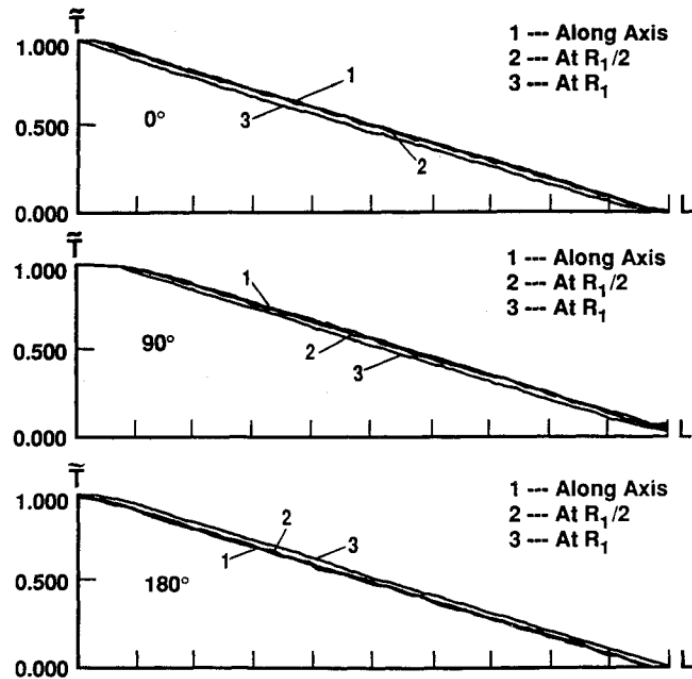


Figure 2.15: Pulsating axial temperature profiles in oscillating pipe flow for $Wo = 1$, Zhang and Kurzweg [70].

frequencies $7.1 \leq Wo \leq 23.3$ and amplitudes $9 \leq A_0 \leq 36.1$.

The analytical study of Faghri et al. [35] laid the groundwork to improving our understanding of the principal mechanisms in pulsating flow. Similar to the oscillating case, the velocity and temperature oscillations interact to give a non-zero mean heat flux in the axial direction. An axial advective term – involving the fluctuations of the two transient components – was retained in the time-averaged equation to incorporate any non-linearities inherent to the problem which may have been removed by linearisation of the time-dependent energy equation. This simplification is typically applicable to situations where the wall temperature distribution can be linearly approximated or the swept length of the oscillating flow is much shorter than the characteristic length [72]. Heat transfer was found to increase by up to 6% above the steady state value with increasing velocity amplitude and decreasing Prandtl number. It was suggested that the approximations made in the study suppressed any dependency on frequency and axial periodicity in the wall temperature and Nusselt number, which were observed previously in an analytical study by Siegel and Perlmutter [34] in the thermal entrance and thermally-developed region of a parallel plate channel. For the case of constant wall temperature, the heat flux was found to oscillate with downstream distance.

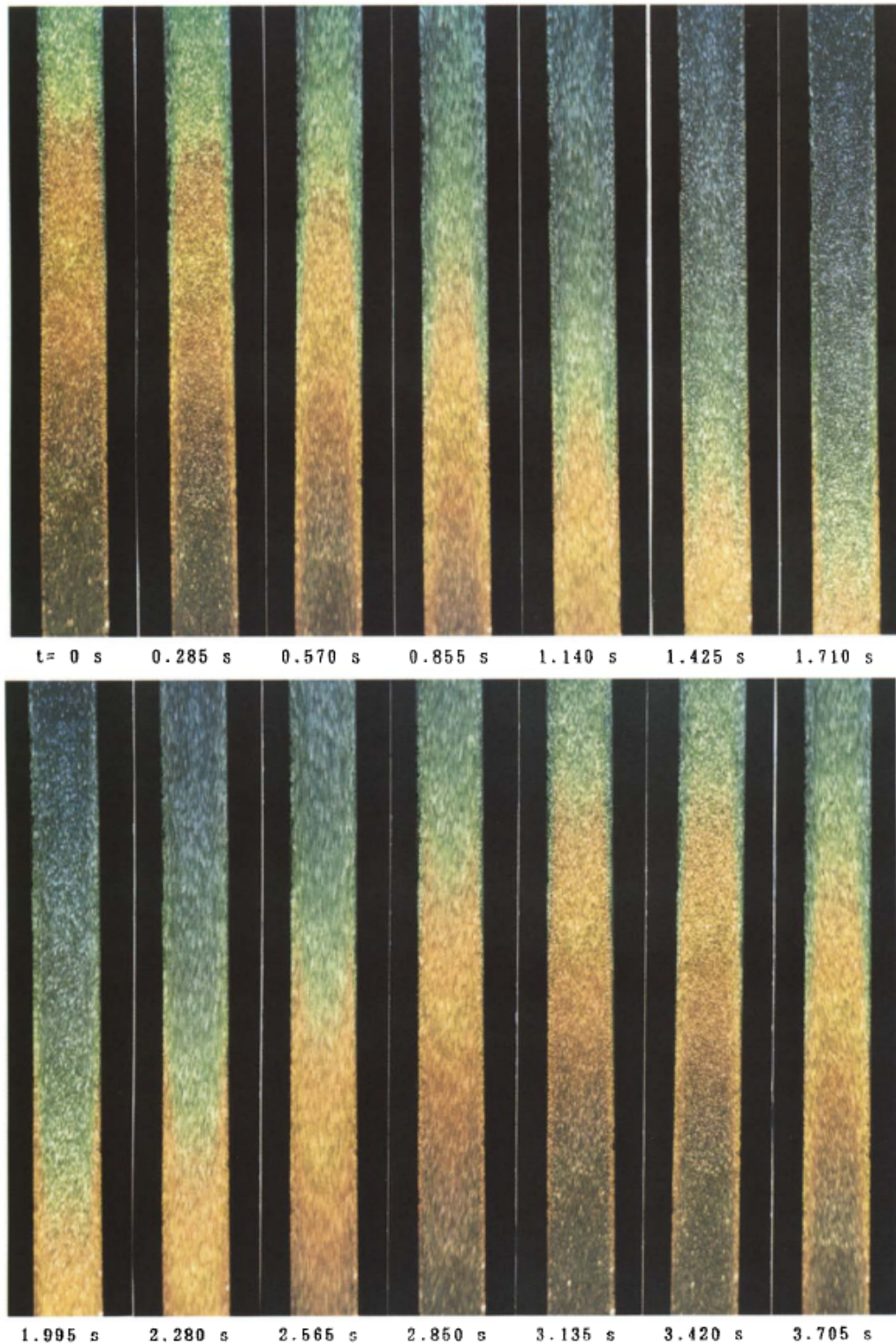


Figure 2.16: Visualised temperature field in an insulated square channel using liquid-crystal tracer for $Wo = 12.2$, $A_0 = 5$, $Pr = 7.9$, $\partial T / \partial \hat{x} = 13.5$ [K/m], Ozawa and Kawamoto [71].

Conversely, the wall temperature oscillations were found to contain spatial periodicity in the axial dimension for the case of constant heat flux. Figure 2.17 plots the axial temperature distributions for $Wo = 0.28, 2.8$ and 5.6 for constant flow rate amplitude. Figure 2.17(a) depicts the pulsating axial temperature distributions at the lowest frequency. The oscillating axial temperature distributions – which are computed by subtracting the steady component (which corresponds to the curve at 90°) from the pulsating components – are approximately parallel and are well-predicted using the quasi-steady assumption. In the time taken to complete a cycle, a pulsating fluid element and a steady fluid element are displaced by the same distance. Hence, the nodes of Figure 2.17 – where the oscillating component of temperature is zero – correspond to the locations in the channel where the steady and unsteady fluid elements have received the same level of heating for the same time duration. At the lowest frequency, the distance travelled during a pulsation (and hence the distance at which the curves converge towards the steady profile) is much longer than the channel length. The amplitudes of the temperature fluctuations are found to decrease with increasing frequency (at constant pressure gradient amplitude) and increasing Prandtl number. It was found that the presence of pulsations only slightly altered total heat transfer over a wide range of amplitudes and frequencies.

Siegel [73] argued that the enhanced axial diffusion mechanism inhibited the heat transfer process in pulsating flow owing to the sign of the temperature gradient. In a steady flow, the uniform heat flux along a channel wall induces a linearly increasing axial fluid temperature profile in the fully developed region. The overall energy balance dictates that the mean temperature gradient stays the same in a pulsating flow. Hence, the flow oscillations interacting with this positive temperature gradient will induce an increased axial heat flow towards the channel inlet, raising the temperature level within the channel and increasing the wall temperature required to transfer the same amount of heat.

Kim et al. [74] conducted numerical simulations in a parallel plate channel to assess the suitability of the simplifying assumptions and approximations in earlier analytical works in a less-restricted parameter space, $Wo \leq 28$ and $0 \leq Q_A/Q_0 \leq 0.75$ under the constant temperature boundary condition. In contradiction with the analytical work, the study found that the oscillatory component of the axial temperature gradient was an order of magnitude smaller in the downstream region. While some heat transfer enhancement was found near

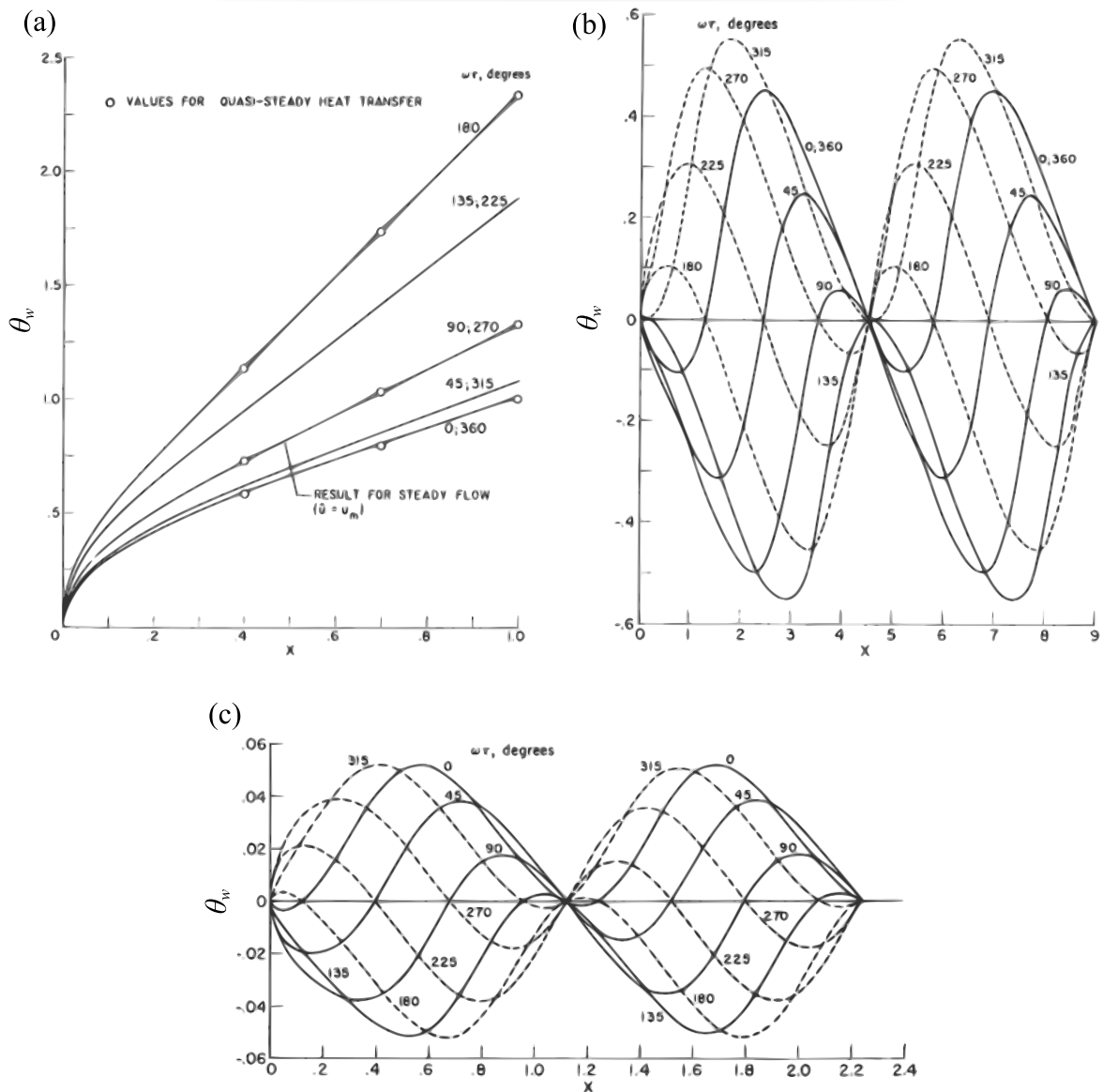


Figure 2.17: Time-dependent axial temperature profiles at the wall θ_w for $Pr = 0.7$ and (a) $Wo = 0.28$, (b) $Wo = 2.8$, and (c) $Wo = 5.6$, Siegel and Perlmutter [34].

the entrance of the channel, little change in Nu was found in the thermally-developed region. The effects of pulsation were more significant at low frequencies and high amplitudes. The numerical simulations of Cho and Hyun [75] investigated the effect of pulsations in a pipe ($0 < Q_A/Q_0 \leq 0.3$) with a constant wall temperature, finding that the time-averaged Nusselt number generally decreased (to the order of 1%) compared to the steady value, away from the entrance region. The alteration in heat transfer increased with increasing amplitude and decreasing Prandtl number. Oscillations were contained to a narrow region near the wall at the entrance of the pipe before spreading further into the bulk of the flow with increasing

downstream distance. Thus, annular effects are present in the pulsating temperature profiles. The amplitudes decreased with frequency as expected. For high frequencies in the fully developed region the oscillating part of temperature was found to lag the inlet flow by 90° in accordance with a previous numerical work on the flow over a flat plate [76].

Moschandreou and Zamir [77] obtained an analytical solution for the Nusselt number in fully developed pipe flow that showed a maximum point at moderate frequencies at which heat transfer would be enhanced by up to 20% with pulsation. Hemida et al. [29] commented that their results showed unrealistically that the Nusselt number continued to change at large values of frequency, since any inertial system should have a cut-off beyond which it should not respond to external excitations. A new analytical solution was provided using a Green's function method, which predicted that the difference in Nusselt number tends to zero as frequency tends to infinity. Their solution showed that the time-averaged Nusselt number was reduced relative to the steady flow value. The reduction was highest at low frequencies for constant flow rate amplitudes, in qualitative agreement with earlier mass transfer studies.

Hemida et al. went on to explore the physical mechanisms underlying the selective behaviour of local heat transfer enhancement or reduction in the thermally developing region. It was found that heat transfer enhancement varied sinusoidally as a function of downstream displacement and frequency, damping out as thermally-developed conditions were approached. As previously noted by Siegel and Perlmutter [34], the spatial wavelength was found to depend on the frequency of pulsation and it was suggested that the origin of the oscillations is related to the convection of upstream conditions along the pipe length. This mechanism is depicted in Figure 2.18 for a square wave pulsating flow with a flat velocity profile that starts after a long steady period. Figure 2.18(b) plots the slope of the axial temperature rise in the pipe during the high and low cycle velocities, along with the average. Initially, the temperature distribution corresponds to the average slope. During the first half-period, the velocity is high and each particle undergoes a rise in temperature along the low slope, resulting in the axial temperature distribution of Figure 2.18(c). Each particle starts from this temperature distribution at the start of the second half period and experiences a temperature rise along the high slope, corresponding to a low velocity. This results in the temperature distribution as shown in Figure 2.18(d). Continuing this trend, we obtain a spatial wave with wavelength proportional to the mean velocity and the oscillation

period. The oscillations damp out as we move along the duct, as a result of axial mixing. In reality, the velocity profile is not one-dimensional and is characteristically dissimilar during each half-period. The decelerating half-cycle contains steeper near-wall velocity gradients compared to the accelerating half-cycle, as discussed in Section 2.1. With a non-fixed heat flux at the wall, the transverse temperature gradient at the wall, and hence the heat transfer coefficient, may also be higher as a result (this is developed in Section 2.2.2.2). Hence, the fluid temperature and driving temperature difference oscillate with axial length and time, such that different axial locations experience differing amplitudes of temperature oscillation. Furthermore, these temperature oscillations have different phase with respect to the velocity oscillations, and thus to the phase of the heat transfer coefficient. The time-averaged heat transfer coefficient will be higher than the steady value at a given axial location if the velocity profile associated with a high heat transfer coefficient occurs when the driving temperature difference is a maximum, and vice versa.

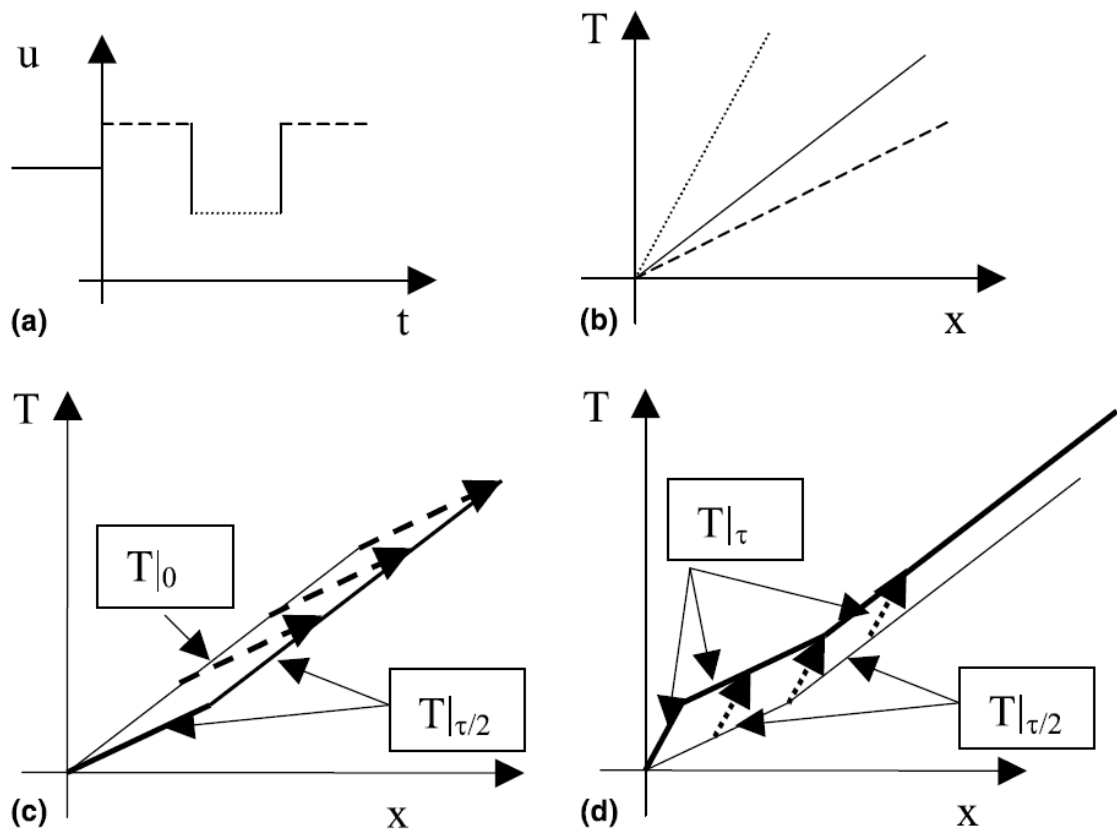


Figure 2.18: Mechanism for the development of spatial periodicity in the axial temperature profile: (a) time variation of velocity; (b) slope of spatial variation of T ; (c) situation after the first half cycle; (d) situation after one cycle, Hemida et al. [29].

Brereton and Jiang [30] used an alternative method based on the Laplace transform to develop an analytical expression for the thermal field. Using this representation, the driving temperature difference is expressed in the physical domain in terms of a convolution with flow rate. This explicitly demonstrates that the instantaneous heat transfer depends on the complete history of the transient flow rate (with weighting functions effectively representing the memory of the flow), in contradiction with the quasi-steady assumption. The theoretical study found that a pseudo-sine wave pulsation – involving modulation of the flow rate above and below its initial value – produced a slight overall reduction of the order of that found by Hemida et al. It was suggested that the effect of positive and negative excursions about the mean flow rate on the Nusselt number effectively cancel each other out. Interestingly, it was found that modulation of the flow rate either above or below its initial value (see Figure 2.19) leads to opposing effects on time-averaged heat transfer. Heat transfer was diminished with variation above the mean and enhanced (by as much as 40%) with variation below the mean. Larger amplitudes, especially those where flow reversal took place, were found to lead to greater augmentations over the range of Womersley number shown. Further, while the rest period between pulsations was arbitrarily chosen as the same length as the transient the effect of shortening the rest period was to increase the enhancement. These flow rate pulsations – which resemble truncated sine waves – could be generated using a number of check valves. In fact, commercially-available micropumps generate flow using an oscillating diaphragm and valves and could possibly be used to enhance heat transfer in microfluidic systems using existing technology.

Nield and Kuznetsov [78] used a perturbation approach to develop an analytical solution for the velocity and temperature distribution in a pipe and parallel plate channel under constant heat flux. The Nusselt number was found to contain a fluctuating component whose magnitude and phase changed with frequency, although no time-averaged change in value was found. At low and high frequencies, the amplitude was zero while a peak was observed at moderate frequencies, that decreases as Pr increases. No dependence of the transient component on Pr was found at low and high frequencies.

The enhanced axial diffusion mechanism acts on a local time-dependent basis, causing a net transport of a substance from high to low concentration without net advective transport. The time-averaged effect – which is detrimental in the case of pulsating flow – increases

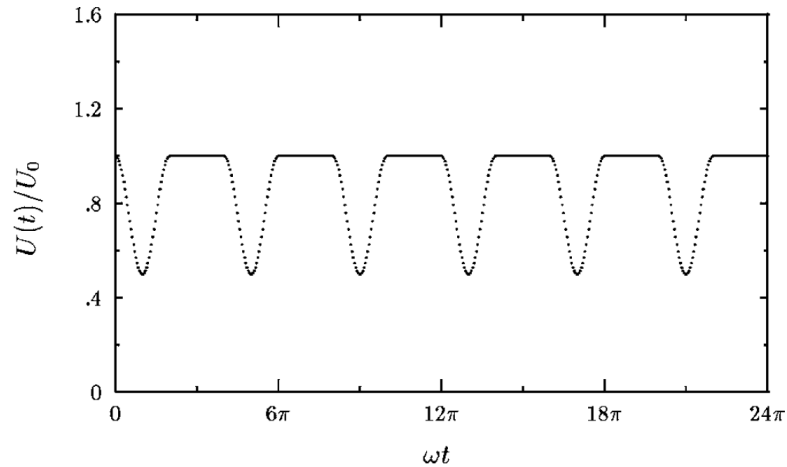


Figure 2.19: Pulsations of the flow rate below its initial value found to enhance heat transfer, Brereton and Jiang [30].

with increasing Wo , increasing A_0 and decreasing Pr . Studies have typically measured the effect relative to molecular diffusion, which is a weak method of heat transfer. Hence, enhancement relative to a steady flow would be a more informative metric. While the analytical models capture this principal mechanism, Hemida et al. [29] argued that the constant heat flux condition is too restrictive – tying the heat transfer process and reducing the effect of pulsation – and showed that the approximation reduced the effect of pulsations in the thermally-developing region. Studies that incorporate conduction in the walls (i.e. a finite wall thermal resistance) may be less restrictive.

2.2.2.2 Mechanism 2: Enhanced Wall Shear Stress Analogy

While the work of Kurzweg [69] focused primarily on axial heat transfer, the theory permits normal conduction in the thick walls of the channel array. The value of wall conductivity is varied between $k_w = 0$ (corresponding to the constant heat flux boundary condition) and $k_w = \infty$ (the constant temperature boundary condition). For the case of a finite wall thermal resistance $0 < k_w < \infty$, a finite amount of heat conduction takes place at the boundary between the fluid and solid, though the time-average must be zero. The outer boundary of the wall is adiabatic. Gedeon [79] developed a similar solution (though not allowing for variable wall thickness), focusing on transverse heat transfer at the walls. Similar to the phase shift that may exist between wall shear stress and velocity in the hydrodynamic

problem, a phase shift develops between the transverse temperature gradient at the wall and the driving temperature difference with increasing frequency. At low frequencies, the heat flux and driving temperature difference are in phase, and hence have a ratio that is universally constant. However, at high frequencies a phase difference exists such that the instantaneous heat flux is not dependent on the instantaneous temperature difference. This contradicts the quasi-steady assumption and indicates that flow history has a strong impact, as noted by a number of other studies [30, 80]. To deal with this phase discrepancy (and with a temperature difference in the denominator that became zero instantaneously), a complex Nusselt number was defined, which used the cross-sectional mean temperature as the representative fluid temperature, rather than the bulk temperature. As a result, the theory fails to capture the effect of the enhanced axial diffusion mechanism of Section 2.2.2.1. However, the magnitude of the temperature gradient at the wall, and hence the magnitude of the Nusselt number, are found to increase with increasing frequency. The largest increases are found for the case of a constant temperature wall, though substantial augmentations of the heat transfer coefficient can be achieved at high frequencies for realistic wall resistances. Liao et al. [81] incorporated an oscillating heat flux (with a time-average of zero) at the outer edge of the thick bottom wall to simulate cooling of electronic components on printed circuit boards (PCBs). The average Nusselt number increased with frequency and tidal displacement with a maximum enhancement of 200% compared to the steady flow case at the highest frequency investigated. The phase of the oscillatory heat flux appears to have been kept constant with respect to the pressure gradient, though any analysis performed on a non-time-averaged basis is highly involved and beyond the scope of the current research. Furthermore, the equations required to solve a geometrically-asymmetrical conjugate heat transfer problem are quite lengthy.

Shi et al. [82] developed the technique of planar laser-induced fluorescence (PLIF) to measure unsteady heat transfer processes in an acoustically-excited compressible air flow. The plates forming a parallel plate channel, like those in heat exchangers of thermoacoustic devices, were heated at one end and cooled at the other, introducing a non-linear step-like change in temperature gradient near the joint. The frequency was maintained at $Wo = 11.3 \pm 2.1$ (with the discrepancy deriving from the temperature-dependent kinematic viscosity) while low ($A_0 = 1.3$) and high ($A_0 = 3.8$) amplitudes were investigated. The latter had a more significant effect on the temperature field, though the tidal displacement was

larger than the length of the channel itself. A sinusoidal variation of Nusselt number was determined from the slope of temperature profiles at the wall whose amplitude increased with displacement. However, the Nusselt number was defined using a fluid reference temperature at the junction of the hot and cold heat exchangers rather than the mean or bulk temperature, the physical meaning of which is not clear. Yu et al. [80] used the same setup to complement thermal results with particle image velocimetry (PIV). Figure 2.20 presents the processed transverse/axial temperature profiles for 20 phase values. Also, a numerical study was conducted to investigate a higher range of frequencies $9.2 \leq Wo \leq 26.3$ and amplitudes $0.4 \leq A_0 \leq 4.2$. The study qualitatively described the characteristic overshoots and undershoots of temperature, and briefly noted their apparent similarity with the overshoots of the Lagrangian displacement profile of the fluid. The annular effects increased with increasing temperature gradient.

Experiments by Persoons et al. [16] found that pulsating thermal behaviour in their short aluminium minichannel heat sink was well modelled by a constant temperature boundary condition at the four walls on a time-averaged basis. The enhancement (as high as 40% at large amplitudes) was approximated well using Reynolds analogy of momentum and heat transfer. In Chapter 7, an argument is presented that some proportionality also exists in a long channel; however, it should be noted that heat transfer in the thermally-developing region is more susceptible to heat transfer enhancement [29]. Furthermore, it was noted that the flow inlet and outlet configuration – that forced the flow to enter and exit abruptly at 90° angles – may also have contributed to higher enhancement.

Interestingly, while a large number of problems with various boundary conditions exist, models that are seemingly quite different may still capture the same physical characteristics of oscillatory flow. For example, a series of numerical studies have investigated the problem of a fluid flow oscillating between two cold reservoirs with the tidal displacement longer than the short isothermal- or isoflux-heated tube length [83, 84, 85]. Zhao and Cheng [84] validated their numerical model (over $2.40 \leq Wo \leq 10.77$ and $8.5 \leq A_0 \leq 35$) using measurements of the time-dependent axial temperatures at the wall and centre line of a thick-walled copper tube heated by an insulated flexible heater. The transverse temperature profiles were seen to contain annular effects, resulting in steeper temperature profiles at the heated surface at high frequencies. The entry region contained the largest overshoots, since the absence of

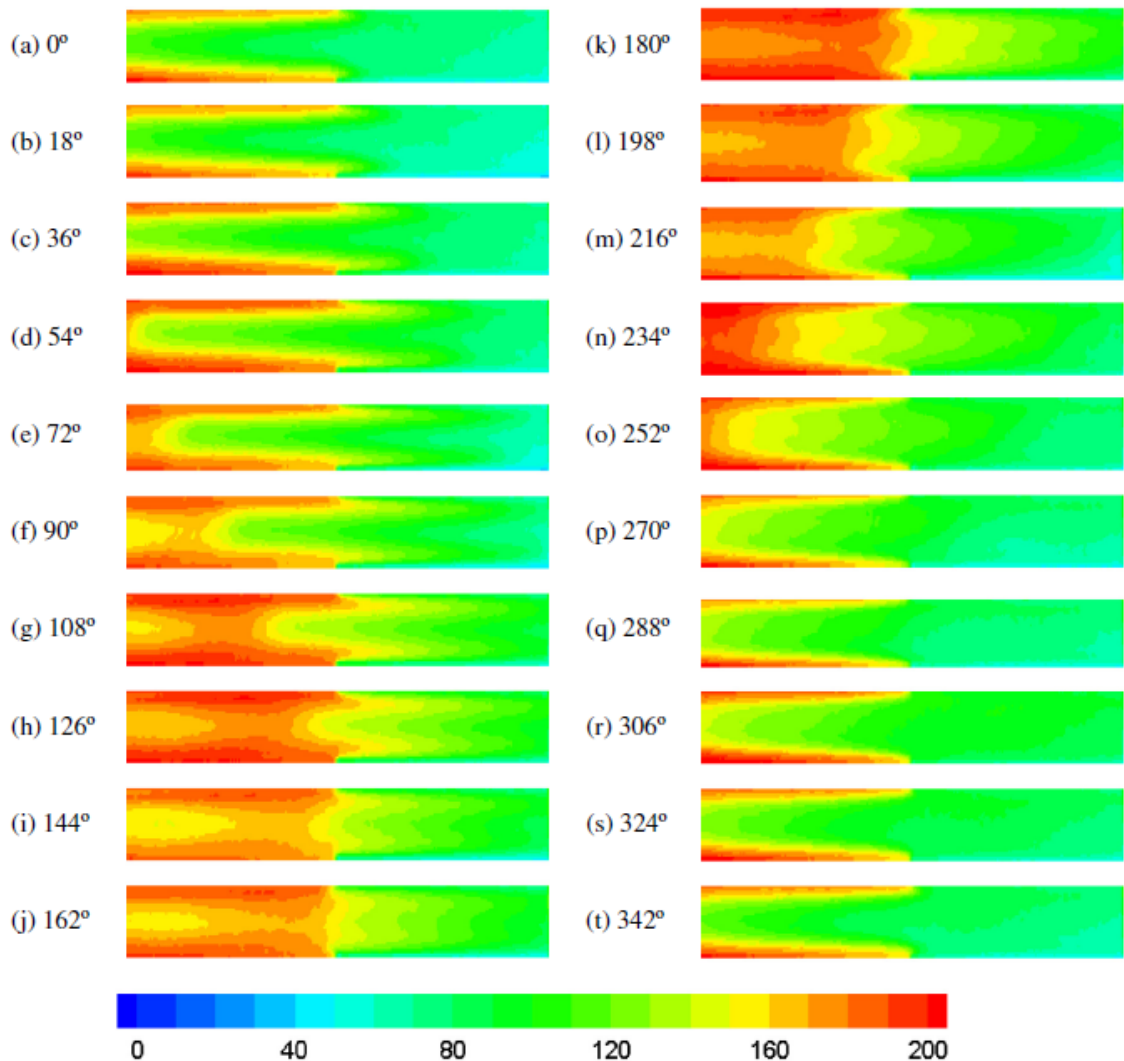


Figure 2.20: Oscillating temperature field (in $^{\circ}\text{C}$) of a compressible air flow in a parallel plate channel for $Wo = 11.3$, $A_0 = 3.7$, Yu et al. [80].

a temperature gradient at the mid-length reduces the effect of displacement. The Nusselt number was defined with a fluid temperature at the reservoir, such that it represents the thermal potential from the heated wall of the pipe to the cold fluid at the entrance and exit of the pipe rather than local instantaneous heat transfer at the wall. As expected from the temperature profiles, the time and space averaged Nu was dominated by the entrance region, reaching its smallest value near the middle of the pipe. Moreover, heat transfer increased with Wo and A_0 due to the reduced thickness of thermal boundary layer and larger displacements respectively. On a time-dependent basis, heat transfer was found to reach a maximum corresponding to the time of maximum velocity [84].

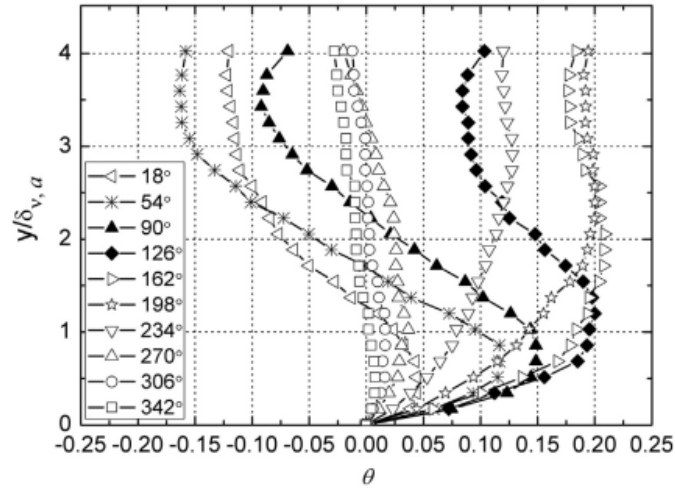


Figure 2.21: Oscillating temperature profiles of a compressible air flow in a parallel plate channel for $Wo = 11.3$, $A_0 = 3.7$, Yu et al. [80].

By permitting variation of the transverse temperature gradient at the wall, theoretical and experimental studies have typically found that heat transfer at the wall is augmented, with the performance increasing with Wo and A_0 . This matches the behaviour of the wall shear stress, whose magnitude similarly increases with frequency and amplitude (as reviewed in Section 2.1). Interestingly, the enhancement through heat flux at the wall is not necessarily in contradiction with the deterioration through the bulk temperature found in Section 2.2.2.1. In fact, the mechanisms are distinct and could operate simultaneously, in theory. It is clear that the relationship between heat flux and driving temperature difference is more complex than the simple proportionality experienced by steady flows, and this leads to problems with the definition of Nusselt number. While a definition using the mean temperature is mathematically convenient, the effect on the bulk temperature must be manually accounted for.

2.2.2.3 Further Mechanisms: Bulk-mean Flow Reversal

Small changes of the time-averaged heat or mass transfer rate are typically found for small amplitude oscillations. Conversely, experiments have demonstrated that significant heat transfer enhancement may be achieved where bulk mean flow reversal occurs. The differing effects are well-illustrated by a series of mass transfer experiments measuring the wall mass transfer of a pulsating pipe flow using the diffusion-controlled electrode technique. The

concentration boundary layers were developing due to the length of the short transfer surface. Patel et al. [86] investigated small amplitude oscillations such that reverse flow did not occur ($Q_A/Q_0 < 0.2$) over the range $1.86 \leq Wo \leq 8.57$. At constant pressure head, the amplitude of the wall mass transfer coefficient decreased and phase lag increased with increasing frequency. While values are not actually presented, the alteration of the time-averaged mass transfer rate compared to the steady case is apparently small. The results were compared with an early low-frequency boundary layer heat transfer solution [87]. Agreement was poor, likely due to discrepancies in test parameters between experiment and theory including the frequency range, geometry and boundary conditions. Gupta et al. [88] focused primarily on large amplitude fluctuations ($0.06 \leq Q_A/Q_0 \leq 4$ for $2.29 \leq Wo \leq 3.79$). The time and space-averaged transfer rate was found to tend to the steady value with increasing frequency. Little to no change was found for very small amplitudes $Q_A/Q_0 = 0.06 - 0.12$, in agreement with Patel et al. [86]. For $Q_A/Q_0 = 1.15 - 1.5$, a slight decrease in the transfer rate was found, with a reduction of as much as 6% at low frequencies. Over $Q_A/Q_0 = 1.5 - 2$, mass transfer was unchanged. For high amplitudes $Q_A/Q_0 > 2.5$, there was a relative increase in the transfer rate compared to steady flow with a maximum enhancement of about 21% recorded. The trend with amplitude was explained using the developing length. Steady flows experience a reduction in heat transfer as the flow becomes thermally developed. As the amplitude is increased, heat transfer is reduced for some unexplained reason. For $Q_A/Q_0 > 1$, heat transfer rates continue to fall at the upstream end, but start growing at the downstream end due to flow reversal. Initially, this increase is too small to offset any decrease at the upstream end. However, at very large amplitudes, the enhancement at the downstream end compensates for the reduction at the upstream end and the overall time- and space-averaged rate is augmented.

By studying the instantaneous wall transfer rates, it was demonstrated that non-linear effects were significant at the higher flow rate amplitudes under bulk-mean flow reversal conditions. Also, pressure gradient measurements were taken to infer the instantaneous behaviour of hydrodynamic parameters such as the wall shear stress from existing analytical solutions. At low amplitudes ($Q_A/Q_0 = 0.404$), the time-dependent mass transfer was approximately sinusoidal as shown in Figure 2.22(a). As the amplitude ratio was increased to $Q_A/Q_0 = 0.94$, the second harmonic became significant at low frequencies (Figure 2.22(b)),

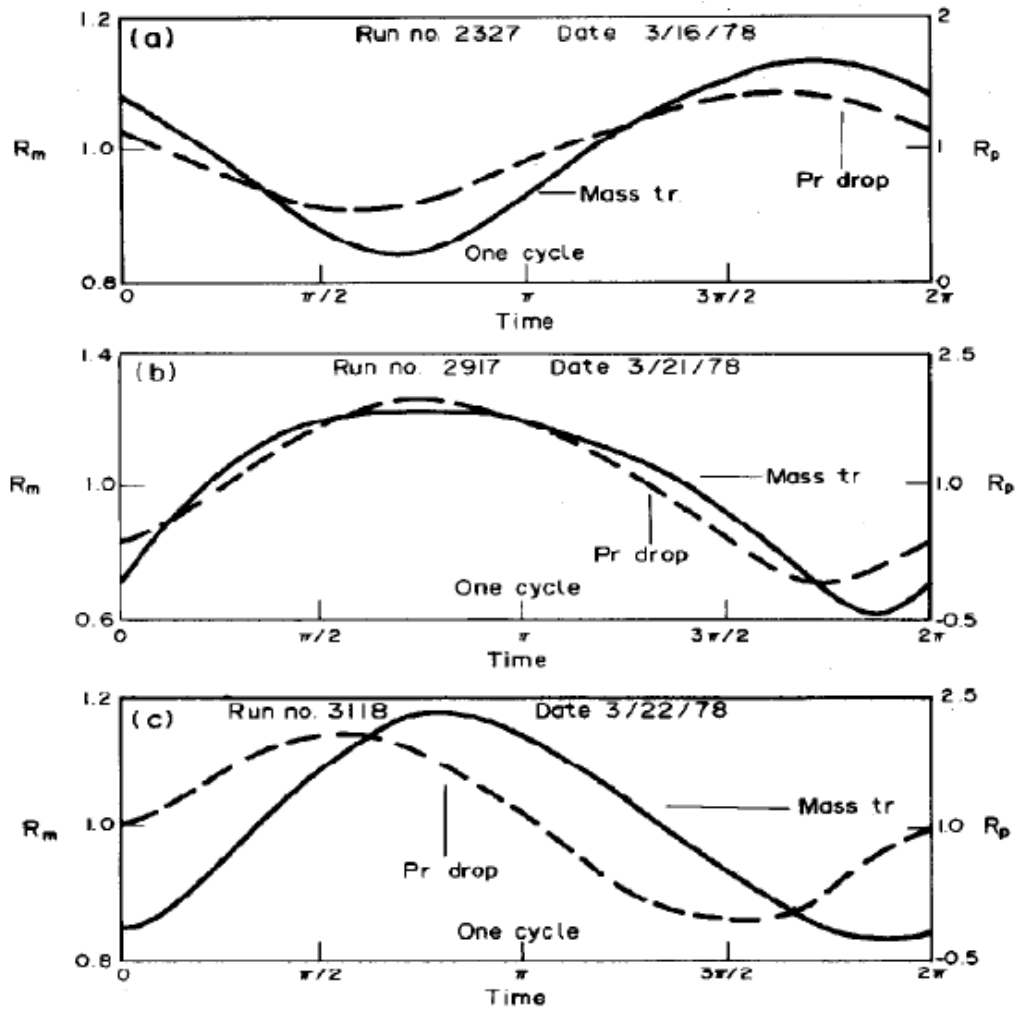


Figure 2.22: Pulsating mass transfer rate and pressure drop in a pipe for (a) $Q_A/Q_0 = 0.4$ and low frequency, (b) $Q_A/Q_0 = 0.94$ and low frequency, (c) $Q_A/Q_0 = 0.96$ and high frequency, Gupta et al. [88].

and less so at high frequencies (Figure 2.22(c)). For $Q_A/Q_0 > 1$, the flow experienced bulk-mean reversal. Since the upstream and downstream developing lengths now alternate, a second maximum appeared during an oscillation cycle corresponding to the maximum velocity in the negative direction (see Figure 2.23). The amplitude of the mass transfer signature was in agreement with theory up to $Q_A/Q_0 = 0.44$ for all frequencies. For $Q_A/Q_0 = 0.85 - 0.95$, experimental values were in agreement for large frequencies but fell below theoretical predictions for small frequencies. The agreement of phase lag was not good for $Q_A/Q_0 = 0.3 - 0.95$ at low to moderate values of frequency. Hence, the second harmonic of Nusselt number must not be neglected at high amplitudes, as it is by theory. Mass transfer

is partially governed by second harmonics and the location and size of transfer maxima are dependent on both frequency and amplitude. Unlike the momentum problem, it is likely that amplitude innately affects characteristic thermal behaviour over a certain threshold. Large amplitudes and small frequencies portray the most complex behaviour.

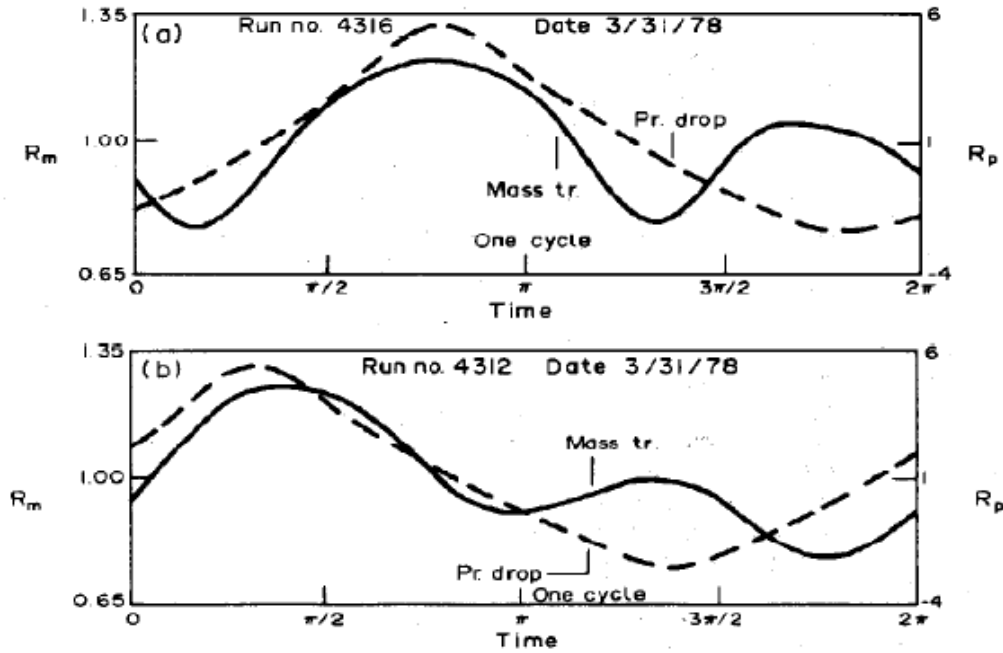


Figure 2.23: Pulsating mass transfer rate and pressure drop in a pipe for (a) $Q_A/Q_0 = 3.37$ and low frequency, (b) $Q_A/Q_0 = 3.37$ and high frequency, Gupta et al. [88].

Persoons et al. [16] investigated the effect of flow pulsation on the heat transfer performance of a minichannel in an aluminium heat sink for $6 \leq Wo \leq 17$, $0.002 \leq Q_A/Q_0 \leq 3$. While no consistent dependence with frequency was found, regimes of slight reduction and significant enhancement were observed with changing pulsation amplitude separated by a critical value of $Q_A/Q_0 = 0.23$, as shown in Figure 2.24. At low pulsation amplitudes, the heat transfer from the heat sink is reduced by less than 1%. At higher pulsation amplitudes, heat transfer enhancement increased with pulsation amplitude up to a maximum of about 40% at $Q_A/Q_0 = 2.25$. The enhancement found at higher pulsation amplitudes is comparable to the numerical results of Craciunescu and Clegg [89] in their modelling of blood flow in human arteries at constant wall temperature. For the overlap in parameter space ($20 \leq Re_0 \leq 120$, $0.6 \leq Wo \leq 4$, $Q_A/Q_0 = 1$), the numerical endeavour recorded positive heat transfer enhancements of between 6.3% and 11%; slightly lower than the experimental

study. The trends with flow rate amplitude are also qualitatively similar to the experiments of Gupta et al. [88], though the mass transfer study found that frequency did have an effect with higher transfer rates observed at lower frequencies.

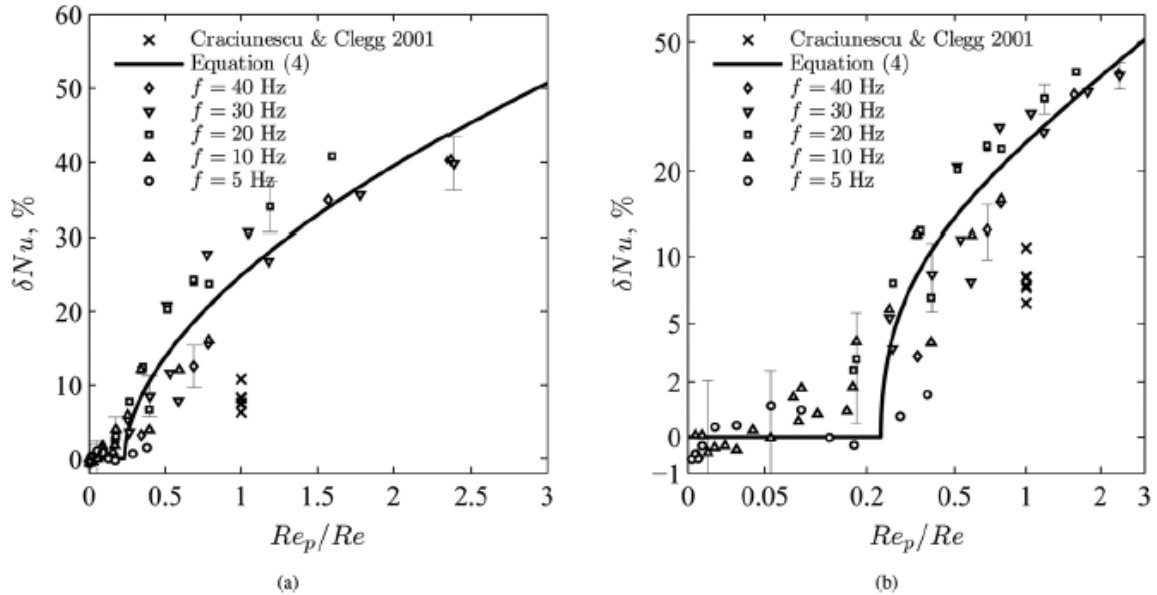


Figure 2.24: Heat transfer enhancement δNu of pulsating flow with flow rate amplitude Q_A/Q_0 ($=Re_p/Re$) for frequencies $6 \leq Wo \leq 17$ with (a) linear and (b) nonlinear axis scales, Persoons et al. [16].

Unlike the momentum problem, the relationship with amplitude is apparently non-linear above a certain threshold. Such conditions are difficult to replicate analytically or numerically, and a satisfactory theory has not been developed that can predict this form of enhancement. The features of flow reversal are reasonably complex, and details such as its location, magnitude and duration have been derived analytically in a pipe and parallel plate channel by Haddad et al. [56]. The parameters investigated in this study could prove useful when the heat transfer associated with bulk-mean reversal is characterised.

2.2.3 Summary of Unsteady Heat Transfer Review

The commonly-asked question of whether unsteadiness enhances heat transfer is mostly likely conditional on the parameters of the problem and the definition of enhancement. Theoretical works typically find negligible or slight alterations in heat transfer, while experimental studies are more likely to predict larger enhancements. Some of this conflict is likely explained by

the practical difficulties of generating a thermally-developed flow experimentally. It is also possible that experimental uncertainty in the measurement of the miniscule changes in heat flux, wall temperature or bulk temperature that occur with superimposed unsteadiness is to blame. For example, theory predicts that a 1% change in Nusselt number corresponds to a change in bulk temperature of 0.034 °C, using the experimental parameters of Chapter 4.

A review of the literature suggests that unsteadiness acts to (i) induce an enhanced axial heat flux towards the entrance of the vessel and (ii) augment the temperature gradient at the wall. Table 2.2 compiles the heat and mass transfer experiments performed on pulsating and oscillating flows. Analytical studies have consistently shown that oscillation causes a time-averaged enhanced axial heat flow against the temperature gradient, which is an adverse effect with respect to heat removal in pulsating flow. This second order effect is a non-obvious result of the interactions of the hydrodynamic and thermal fields and has the potential to remove heat without accompanying net mass transport. While experiments measuring time-dependent temperature profiles are lacking as a whole, the enhanced axial diffusivity mechanism has been reasonably characterised on a time-averaged basis by heat and mass transfer experiments over a high range of frequencies ($1.6 \leq Wo \leq 50$). This owes largely to a movement attempting to commercialise a technology that exploited the phenomenon in the 1980s [22]. However, the local time-dependent profiles have been visualised by a single qualitative experiment [71] at a pair of frequencies $Wo = 4.4$ and 12.2 . Furthermore, the time-dependent behaviour of the axial heat flux, which oscillates with twice the oscillation frequency, has only been studied theoretically.

The adverse effect of the enhanced axial diffusion mechanism on pulsating flows gives a plausible explanation for the lack of experimental measurements of any accompanying wall heat flux enhancement. The more intuitive mechanism of enhanced wall temperature gradient has been suppressed in the majority of analytical studies owing to the ideal constant heat flux boundary condition. The local time-dependent profiles – with sinusoidally-varying temperature gradient at the wall – have been measured in a couple of experiments [80, 82] for a compressible flow with a step change in axial temperature gradient at a single frequency $Wo = 11.3$. Also, evidence for the existence of the mechanism has been found in the relationship between flow rate amplitude and time- and space-averaged heat transfer, which was well-approximated by the Reynolds analogy of momentum and heat transfer for a

thermally-developing pulsating flow ($6 \leq Wo \leq 17$) heated at a constant temperature [16]. To the best of the author's knowledge, no experiments have been performed for the common flow condition of an incompressible flow in a heated vessel.

As a whole, thermal studies have tended to restrict their focus to time- and space-averaged heat transfer. However, averaging ultimately results in a loss of information and any potential optimisation requires the understanding of the instantaneous interplay of competing mechanisms. For example, the effect of each mechanism may vary in both space and time, such that certain time intervals or locations experience an overall net favourable outcome. Also, comparatively few experiments have measured the more complex thermal problem, compared with Section 2.1, probably since temperature visualisation and measurement techniques are less developed than their velocimetry counterparts. Furthermore, many of the experiments are in the thermally-developing region, use compressible fluids or are concerned with mass transfer. Heat transfer experiments have been performed predominantly in two-dimensional channels; however, the results have been compared solely to numerical models since an analytical solution does not appear to exist.

2.3 Implications for Research Objectives

In this chapter, an overview of the studies relating to pulsating and oscillating flows in pipes and channels has been performed. The gaps in the literature are significant in terms of both theory and experiment:

- An existing 2-D analytical solution to the momentum equation has not been validated experimentally.
- Thermal measurements in channel geometries have only been compared to numerical solutions, since a 2-D analytical solution to the energy equation does not exist.
- Local time-dependent temperature measurements have not been performed for the common flow condition of an incompressible flow in a heated vessel of any geometry.
- The intricate coupling between the localised instantaneous fluid dynamics and heat transfer has not been studied with a view to potential optimisation.

These gaps create problems in characterising the heat transfer performance of a photonics-cooling solution involving pulsating flow in a channel heat sink. This research aims to build a theoretical framework of understanding, by developing analytical solutions and numerical models for the hydrodynamic and thermal problems. The theory will be validated using hydrodynamic and thermal experiments that approximate any idealisations in the theory. In particular, the interdependence of the hydrodynamic and thermal fields will be considered in order to exploit any potential optimisation.

Table 2.2: Details of reviewed heat and mass transfer experiments, and of the current experimental setup of Chapter 4.

Reference	Flow	Type	\hat{q}	Geom.	D_h [mm]	Fluid	Measurement Technique	Var.	Wo	A_0
Joshi et al. [67]	Puls	Mass	0	○	10	Methane	Infrared-absorption	\bar{T}'_b	1.6-7.8	9.2-39.6
Jaeger & Kurzweg [68]	Puls	Mass	0	○	63, 79	Oxygen	Concentration Detector	\bar{T}'_b	3.5-9.1	
Kurzweg & Zhao [21]	Osc	Heat	0	○	12.7	Water	Thermometer	\bar{T}'_b	25-50	3 – 20
Ozawa & Kawamoto [71]	Osc	Heat	0	□	9	Water	Thermo-sensitive Tracer	T	4.4-12.2	
Yu et al. [80]	Osc	Heat	> 0	□	12	Air*	PLIF	T	11.3	
Shi et al. [82]	Osc	Heat	> 0	□	12	Air*	PLIF	T	11.3	1.3-3.8
Persoons et al. [16]	Puls	Heat	> 0	□ [†]	1.9	Water	Thermocouple	∂Nu	6-17	
Zhao & Cheng [84]	Osc	Heat	> 0	○ [†]	15.7	Water	Thermocouple	∂Nu	2.4 - 10.8	8.5-35
Patel et al. [86]	Puls	Mass	> 0	○ [†]	14.3	Electrolyte	Diff. Contr. Electrode	\hat{q}	1.86-8.57	
Gupta et al. [88]	Puls	Mass	> 0	○ [†]	12.7	Electrolyte	Diff. Contr. Electrode	\hat{q}	2.3 - 3.8	8.5-35
Current Research	Puls	Heat	> 0	□	3.6	Water	Infrared Thermography	T_w	1.75	4.6

Wall Heat/Mass Transfer

$\hat{q} = 0$, *adiabatic/impermeable wall*

$\hat{q} > 0$, *heated/permeable wall*

Geometry

[†]*thermally – developing*

Working Fluid

**compressible*

Variable Measured

\bar{T}'_b , *space- and time-averaged enhanced axial diffusivity mechanism*

T , *local time-dependent fluid temperature*

T_w , *local time-dependent wall temperature*

∂Nu , *space- and time-averaged heat transfer enhancement*

\hat{q} , *time-dependent wall heat/mass transfer*

Chapter 3

Analytical Theory

As reviewed in Chapter 2, several methods of solving the unsteady Navier-Stokes equations have been used in previous works. The Fourier series approach [32] involves decomposition of the complex pressure signal into individual modes in order to exploit the linearity of the governing momentum equation. The general solution is constructed from a summation taken over the individual harmonic frequencies and can handle any arbitrary time-periodic pressure fluctuation. The resulting equations are reorganised to represent the different physical quantities as an amplitude and phase lag. In existing solutions in rectangular channels [31], the amplitudes and phases of the principal flow variables are not immediately discernible since the parameters are given as an infinite sum of sinusoidal functions. As a result, the parameters need to be computed at numerous time steps – rather than a single instant – adding to the computational expense. Also, the time-dependent behaviour of the parameters is given relative to a prescribed pressure gradient rather than a positively-displaced flow rate, and difficulties arise in shifting to a flow rate-fixed model. In another work by the author [90], an existing solution in real coordinates is reorganised in terms of a single sine wave with an explicit amplitude and phase (which yields a 24-fold computation time improvement over 20 time intervals). In this thesis, complex coordinates are preferred for consistency with the newly-derived solution to the energy equation in a rectangular channel, which is solved using the method of undetermined coefficients. To the best of the author’s knowledge, an analytical heat transfer model is not currently available for a two-dimensional geometry. The solution uses simplifying assumptions similar to those of recent analytical solutions in pipes [29, 30].

Hence, the aim of the current chapter is to advance the state-of-the-art in thermo-fluidic analytical models of pulsating flow in a rectangular channel.

3.1 Description of Flow and Governing Equations

The laminar pulsating flow of interest has localised and time-dependent velocity $\hat{u}(\hat{y}, \hat{z}, \hat{t})$ in the \hat{x} direction and temperature $T(\hat{x}, \hat{y}, \hat{z}, \hat{t})$, where hat symbols represent dimensional quantities. The assumptions of a unidirectionality and hydrodynamic development of the velocity field impose linearity on the hydrodynamic problem. Similarly, the temperature field in the channel is assumed to be thermally-developed. The flow has high Péclet number $Pe > 100$ such that axial conduction is negligible [91] and viscous heating is neglected, since high Prandtl number fluids like oils are not considered [70]. Thermophysical properties are approximated as constant to focus on the principal mechanisms without non-linear secondary effects. The remaining non-linearities – contained within the advective term of the energy equation – are dealt with in Section 3.1.4. The unsteady Navier-Stokes and energy equations

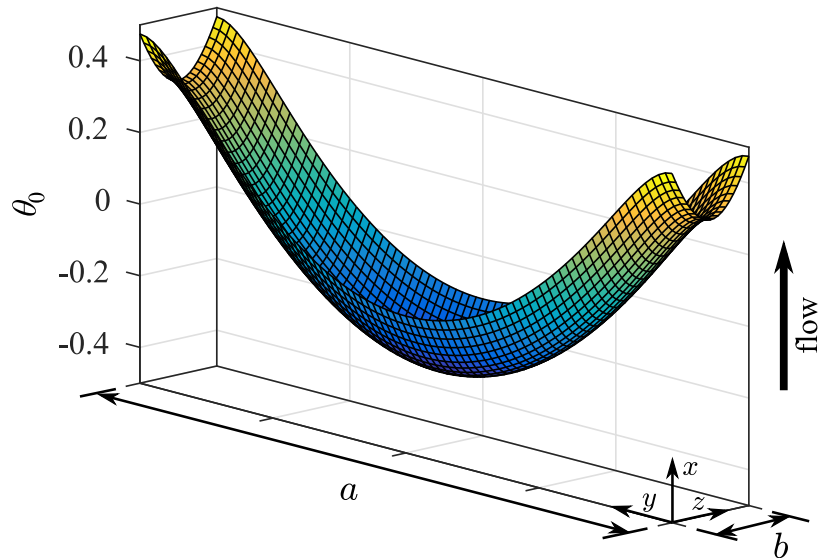


Figure 3.1: Coordinate system of rectangular channel, and temperature profile of a steady flow with two heated long walls H2(2L).

in Cartesian coordinates are simplified to [92]:

$$\nu \left(\frac{\partial^2 \hat{u}}{\partial \hat{y}^2} + \frac{\partial^2 \hat{u}}{\partial \hat{z}^2} \right) - \frac{\partial \hat{u}}{\partial \hat{t}} = \frac{1}{\rho_f} \nabla \hat{p} \quad (3.1a)$$

$$\alpha_f \left(\frac{\partial^2 T}{\partial \hat{y}^2} + \frac{\partial^2 T}{\partial \hat{z}^2} \right) - \frac{\partial T}{\partial \hat{t}} = \hat{u} \frac{\partial T}{\partial \hat{x}} \quad (3.1b)$$

where ρ_f , ν and α_f are the density, kinematic viscosity and thermal diffusivity of the fluid respectively. As is typical in unidirectional flow, the unsteady pressure gradient $\nabla \hat{p}(t) = d\hat{p}/d\hat{x}$ acts in the direction of the streamlines. Since the flow is incompressible, any change in the gradient is instantaneous throughout the system. For mathematical convenience, the origin is set at the corner of the channel such that $0 \leq \hat{y} \leq \hat{a}$ and $0 \leq \hat{z} \leq \hat{b}$, as illustrated in Figure 3.1.

3.1.1 x-Momentum Balance

The attributes of the various flow regimes are well-illuminated by inspection of the balance between individual terms. In the force balance of Equation 3.1a for example, the flow rate varies slowly at low frequencies and the $\partial \hat{u} / \partial \hat{t}$ inertia term can be neglected everywhere. Thus, the Laplacian term is balanced by the imposed pressure term and the velocity and flow rate vary periodically in the same phase as the pressure gradient. At large values of Wo , the Laplacian term in the momentum equations can be neglected everywhere except in the very narrow Stokes layer. In the inviscid part of the flow, the unsteady inertia term is balanced by the sinusoidally-varying pressure gradient, and the velocity lags the pressure gradient by $\pi/2$. The interaction of these terms may be investigated using the momentum balance equation. Equation 3.1a is integrated over the cross-section to give:

$$-\frac{4\langle \hat{\tau} \rangle}{D_h} - \rho \left\langle \frac{\partial \hat{u}}{\partial \hat{t}} \right\rangle = \nabla \hat{p} \quad (3.2)$$

where D_h is the hydraulic diameter, $\hat{\tau}$ is the wall shear stress and angled brackets denote spatial averaging. Equation 3.5a quantifies the pressure drop in a channel, resulting from viscous and inertial contributions.

3.1.2 Vorticity and Stokes Boundary Layer Thickness

The viscous term – equivalently written as $\nu(-\partial\hat{\omega}_z/\partial\hat{y} + \partial\hat{\omega}_y/\partial\hat{z})$ where $\hat{\omega}$ is vorticity, e.g. $\hat{\omega}_y = \partial\hat{u}/\partial\hat{z}$ – describes vorticity gradients in the channel, or the rate of change of normal and tangential stresses acting on fluid elements in a manner analogous to applied forces and torques in rigid body dynamics. For a steady developing flow, vorticity created at the wall diffuses into the flow and slows it through the development of a boundary layer. This layer consumes the entire cross-section in the fully-developed region, effectively halting the generation of vorticity. For a fully-developed steady flow, the term $\nu\nabla\hat{\omega}_z = 0$ at walls $\hat{z} = [0, \hat{b}]$, and the flow of positive vorticity away from the wall is given by $\nu\nabla\hat{\omega}_{y,0} = (1/\rho)\nabla\hat{p}_0$, where the latter term is a measure of the vorticity source strength per unit area [93]. Hence, vorticity diffuses steadily from the boundary before reaching the opposing wall. For the oscillating case, the accelerations involved in oscillatory flow instigate the continuous generation of vorticity [94]. The flow of positive vorticity away from the wall (at walls $\hat{z} = [0, \hat{b}]$) has magnitude $\nu\nabla\hat{\omega}_y'' = (1/\rho)\nabla\hat{p}''$ and is in phase with the pressure gradient $\phi_{\nabla\hat{\omega}_y} = \pi/2$.

Stokes' second problem (plotted in Figure 2.1(a)) models the spreading of transverse velocity oscillations from the boundary with normal velocity $\sqrt{2\nu\omega}$, an oscillation amplitude that decays exponentially with displacement from the plate and a phase lag proportional to the distance from the wall. From the diffusion equation, the time for a property to diffuse a distance $\hat{\delta}_\nu$ is given by $\hat{\delta}_\nu^2/\nu$ where ν is the constant of diffusion (see for example the denominator of Equation 2.1 quantifying the convective time scale). For time scales of the same order $\hat{t} \propto \hat{\delta}_\nu^2/\nu$, it follows that the thickness of the Stokes' boundary layer must be of the order $\sqrt{\nu/(1/\hat{t})}$. The distance at which fluid elements experience 1% of the effects of viscous diffusion in Stokes flow, given by:

$$\hat{\delta}_\nu \approx 4.6\sqrt{2\nu/\omega} \quad (3.3)$$

is similarly used to quantify the Stokes layer thickness in a rectangular channel.

3.1.3 Non-dimensionalisation of Principal Parameters

The parameters are non-dimensionalised according to:

$$u = \frac{\hat{u}}{\langle \hat{u}_0 \rangle}; \theta = \frac{k_f(T - T_{in})}{\hat{q}D_h}; t = \frac{4v\hat{t}}{D_h^2}; p = \frac{\hat{p}}{\rho \langle \hat{u}_0 \rangle^2}; x = \frac{4\hat{x}}{D_h Re_0}; y = \frac{2\hat{y}}{D_h}; z = \frac{2\hat{z}}{D_h} \quad (3.4)$$

where k_f is the fluid's thermal conductivity, \hat{q} is the heat flux at the boundary of the channel, D_h is the hydraulic diameter, $\langle \hat{u}_0 \rangle$ is the space-averaged velocity, θ is the dimensionless temperature and $Re_0 = \langle \hat{u}_0 \rangle D_h / \nu$ is the Reynolds number. The dimensionless frequency and amplitude parameters were defined in Section 2.1.1. In dimensionless form, Equations 3.1a and 3.1b become:

$$\left(\frac{\partial^2 u}{\partial y^2} + \frac{\partial^2 u}{\partial z^2} \right) - \frac{\partial u}{\partial t} = \nabla p \quad (3.5a)$$

$$\frac{1}{Pr} \left(\frac{\partial^2 \theta}{\partial y^2} + \frac{\partial^2 \theta}{\partial z^2} \right) - \frac{\partial \theta}{\partial t} = u \frac{\partial \theta}{\partial x} \quad (3.5b)$$

3.1.4 Linearisation

The linearity of Equation 3.5a permits decoupling of the mean and unsteady equations of motion such that the pertinent parameters are composed of steady and oscillating flow parts e.g. $u(y, z, t) = u_0(y, z) + u'(y, z, t)$. The mean flow is essentially irrelevant as long as the added inertia does not trigger turbulence. Equation 3.5b is non-linear owing to the axial advective term:

$$u \frac{\partial \theta}{\partial x} = u_0 \frac{\partial \theta_0}{\partial x} + u_0 \frac{\partial \theta'}{\partial x} + u' \frac{\partial \theta'}{\partial x} + u' \frac{\partial \theta_0}{\partial x} \quad (3.6)$$

In a steady flow, the uniform heat flux along a channel wall induces a linearly increasing axial fluid temperature profile in the fully developed region. In a pulsatile flow, the overall energy balance dictates that the time-averaged temperature gradient stays the same. Equation 3.5b is linearised by assuming that the time-dependent component of the axial temperature gradient in Equation 3.6 is small compared with the steady component $|\partial \theta' / \partial x| \ll \partial \theta_0 / \partial x$,

following recent analytical studies in pipes [29, 30, 69, 79]. Zhang and Kurzweg [70] found that the so-called Chatwin approximation has proven accurate for frequencies as low as $Wo = 1$ if Equation 3.5b is solved numerically without prior assumptions. Similarly, Kim et al. [74] found that the fluctuating component of temperature gradient was relatively small in the downstream region of a parallel plate channel with a constant wall temperature. In contrast, Siegel and Perlmutter [34] used the slug-flow assumption, which approximates the velocity distribution as uniform across the channel, to simplify the equation rather than negating the oscillatory temperature gradients. The hydrodynamics are effectively one-dimensional though allowed to vary with time which has been found to lead to the essential physical behaviour of the systems considered [95]. The study found that the wall temperature oscillated with axial distance for the case of constant heat flux, even in the thermally-developed region. In other words, the oscillating component of axial temperature gradient was not negligible. The suitability of this idealised model will be assessed in Chapter 7. By negating the fluctuating component of the axial temperature gradient, the oscillating component of the temperature field is independent of x and the energy equation may be decoupled $\theta(x, y, z, t) = \theta_0(x, y, z) + \theta'(y, z, t)$ to give the steady relation:

$$\frac{1}{Pr} \nabla^2 \theta_0 = u_0 \frac{\partial \theta_0}{\partial x} \quad (3.7)$$

and the oscillating expression:

$$\frac{1}{Pr} \nabla^2 \theta' - \frac{\partial \theta'}{\partial t} = u' \frac{\partial \theta_0}{\partial x} \quad (3.8)$$

3.1.5 Boundary Conditions

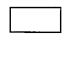
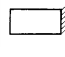
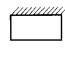
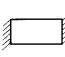


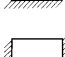

Table 3.1: Nomenclature for boundary conditions, Shah and London [92].

T	<i>temperature constant both peripherally and axially</i>
H1	<i>temperature constant peripherally, and heat flux constant axially</i>
H2	<i>heat flux constant both peripherally and axially</i>

Solutions to Equation 3.7 may be sought for a variety of boundary conditions [92] – summarised in Table 3.1 – which are more numerous for a 2-D geometry. The T condition is the classical constant temperature boundary condition, which considers temperature constant

3.1. DESCRIPTION OF FLOW AND GOVERNING EQUATIONS

Table 3.2: Nomenclature for combination of heated (symbolised by solid lines) and adiabatic (symbolised by solid lines with diagonal hatching) walls, Gao and Hartnett [96].

4	<i>four heated sides</i>	
3L	<i>three heated sides and one insulated short side</i>	
3S	<i>three heated sides and one insulated long side</i>	
2L	<i>two heated long sides and two insulated short sides</i>	
2S	<i>two heated short sides and two insulated long sides</i>	
2C	<i>one heated long side, one heated short side, and two insulated sides</i>	
1L	<i>one heated long side, three insulated sides</i>	
1S	<i>one heated short side, three insulated sides</i>	

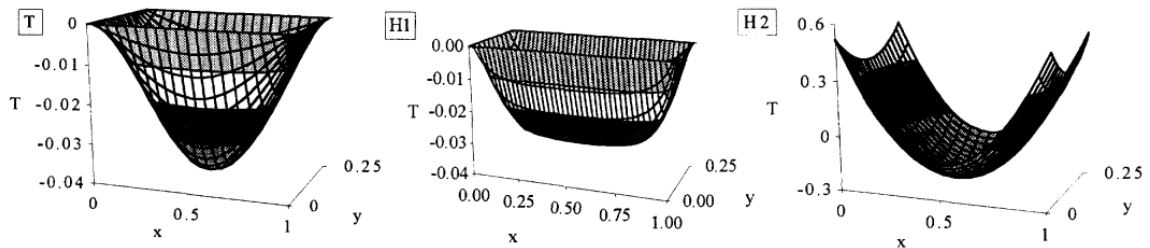


Figure 3.2: Comparison of steady temperature profiles in a rectangular channel with $b/a = 4$ for the T(4), H1(4) and H2(4) boundary conditions, Morini [97].

both peripherally and axially. The H2 condition is the classical constant heat flux boundary condition, considering heat flux constant both peripherally and axially. In a 1-D pipe, the H2 condition results in a temperature that is naturally uniform at the perimeter. In contrast, the wall temperature varies peripherally under the same condition in a 2-D channel. Hence, a hybrid type boundary condition – the H1 condition – exists in a 2-D geometry where a constant temperature at the perimeter is imposed, while a constant heat flux is imposed in the axial direction (i.e. the temperature increases linearly). In a pipe, the H1 condition and H2 condition are equivalent. Furthermore, these heating conditions may be imposed on a combination of the four wetted walls, as listed in Table 3.2. Morini [97] presents an overview of the heat transfer of steady flows heated under the T, H1 and H2 boundary conditions for the case of four heated walls. The differences in temperature profiles may be inspected from Figure 3.2. In the current research, a heat flux constant in the transverse and axial dimensions (i.e. the H2 boundary condition) is of interest, in order to match the experimental

conditions of thin-foil infrared thermography, described in Chapter 4. Spiga and Morini [98] give a rigorous analysis of different versions of heating for the H2 boundary condition. The boundary condition is formulated as:

$$\left(\frac{\partial\theta_0}{\partial y}\right)_{y=0,a} = -\frac{d_1}{2}, \frac{d_2}{2}; \left(\frac{\partial\theta_0}{\partial z}\right)_{z=0,b} = -\frac{d_3}{2}, \frac{d_4}{2} \quad (3.9)$$

where the values of the binary constants d indicate the unique version of heating (see Table 3.3). An energy balance gives $\partial\theta_0/\partial x = c/Pr$ where $c = L/(2a + 2b)$ is the heated fraction of the cross-sectional perimeter.

The boundary conditions for Equation 3.8 are zero since heat addition is accounted for in the steady equation:

$$\left(\frac{\partial\theta'}{\partial y}\right)_{y=0,a} = 0; \left(\frac{\partial\theta'}{\partial z}\right)_{z=0,b} = 0 \quad (3.10)$$

3.2 Solution for Velocity Field

Solution to Equation 3.5a is achieved using the method of Green's functions described by Fan and Chao [31], adjusted for complex coordinates and the non-dimensionalised form. The ∇p term is replaced by an impulsive pressure gradient $-\delta(t)$, where $\delta(t)$ is the Dirac delta function. The fluid is at rest in the time leading up to $t = 0$ and the momentum equation reduces to $\partial u/\partial t = \delta(t)$. Immediately after the impulse is applied, the velocity is $u(y, z, 0^+) = \int_0^\varepsilon \delta(t) dt = 1, \varepsilon \rightarrow 0^+$ and there is no driving force acting on the flow. Hence, the governing equation becomes homogeneous:

$$\nabla^2 u - \frac{\partial u}{\partial t} = 0 \quad (3.11)$$

Table 3.3: Values of binary constants d of analytical solution for unique version of heating, Spiga and Morini [98].

Version	1L	1S	2L	2S	2C	3L	3S	4
d_1	0	0	0	1	0	0	1	1
d_2	0	1	0	1	1	1	1	1
d_3	0	0	1	0	0	1	0	1
d_4	1	1	1	0	1	1	1	1

but with an inhomogeneous initial condition $u(y, z, 0^+) = 1$. The solution to Equation 3.11 is defined as the Green's function for velocity of the system:

$$G_u(y, z, t) = \frac{16}{\pi^2} \sum_{m=1,3,\dots}^{\infty} \sum_{n=1,3,\dots}^{\infty} \frac{e^{-\beta_{mn}t} \Phi_1}{mn} \quad (3.12)$$

with:

$$\Phi_1 = \sin\left(\frac{m\pi y}{a}\right) \sin\left(\frac{n\pi z}{b}\right) \quad (3.13a)$$

$$\beta_{mn} = \pi^2 \left(\frac{m^2}{a^2} + \frac{n^2}{b^2} \right) \quad (3.13b)$$

By convolving the Green's function with an arbitrary time-dependent accelerative function $f(t) = \nabla p'$ the solution for the induced velocity profile is determined:

$$u(y, z, t) = - \int_0^t f(\lambda) G_u(y, z, t - \lambda) d\lambda \quad (3.14)$$

The convolution is performed with an oscillating pressure gradient $\nabla p' = \nabla p_A e^{iWo^2t}$ to determine the pulsating velocity field:

$$u'(y, z) = \Re(\psi_u e^{iWo^2t}) \quad (3.15a)$$

$$\psi_u = - \frac{16 \nabla p_A}{\pi^2} \sum_{m=1,3,\dots}^{\infty} \sum_{n=1,3,\dots}^{\infty} \frac{\Phi_1}{mn} \frac{1}{\beta_{mn} + iWo^2} \quad (3.15b)$$

where the behaviour during the rise time, governed by the $e^{-\nu\beta_{mn}t}$ term, has been negated. If $Wo = 0$, Equation 3.15b represents the steady solution with $\psi_u = u_0$ and $\nabla p_A = \nabla p_0$. The local amplitudes and phases may be easily obtained from the length and angle of the complex vector:

$$u_A = |\psi_u| \quad (3.16a)$$

$$\phi_u = \tan^{-1} \left[\frac{\Im(\psi_u)}{\Re(\psi_u)} \right] \quad (3.16b)$$

The expressions for flow rate $\psi_Q = \int_0^a \int_0^b \psi_u dy dz$ and local wall shear stress $\psi_{\hat{t}_{zx}}(y) = \mu(\partial \psi_{\hat{u}} / \partial \hat{z})|_{\hat{z}=0}$ are reported in the Appendix. The acceleration profiles are $\partial \hat{u} / \partial \hat{t} = \Re[\psi_{\partial \hat{u} / \partial \hat{t}} e^{i\omega \hat{t}}]$ with $\psi_{\partial \hat{u} / \partial \hat{t}} = i\omega \psi_{\hat{u}}$. The mean acceleration is $\langle \psi_{\partial \hat{u} / \partial \hat{t}} \rangle$. The displacement profiles are given by $\chi' = \Re[\psi_{\chi} e^{iWo^2 t}]$ with $\psi_{\chi} = \psi_u / iWo^2$. The mean displacement amplitude (equal to half of the tidal displacement) is $\langle \chi_A \rangle = |\langle \psi_{\chi} \rangle|$ where the angled brackets denote averaging over the cross-section. Equation 1a gives the velocity data relative to a cosine wave pressure gradient. The time-dependent values relative to a fixed sinusoidal flow rate are found using a phase shift:

$$u'' = \Re[\psi_u e^{i(Wo^2 t - \phi_Q - \pi/2)}] \quad (3.17)$$

The calculation time of Equation 3.15b for the first 100 terms of each sum at 10^6 nodes is 28.2 minutes on a PC with Intel Core i7-4771 3.5 GHz processor and 32 GB RAM.

3.3 Solution for Temperature Field

The steady solution [98], reorganised in terms of the non-dimensionalised parameters of Equation 3.4, is detailed in the Appendix. Siegel and Savino [99] and Savino and Siegel [100] give the solution for the steady flow conjugate problem in a rectangular channel. The change in wall temperature profile with lateral conduction in the wall is depicted in Figure 3.3. The conjugate analytical solution for the oscillating temperature profile in a parallel plate channel [69] adjusted to the same non-dimensionalised form as Section 3.1.3 is also given in the Appendix. Currently a solution for the oscillatory component in a two-dimensional channel is not available in the literature. A solution is sought in the form:

$$\theta'(y, z, t) = \Re \left(\frac{\partial \theta_0}{\partial x} \psi_{\theta} e^{iWo^2 t} \right) \quad (3.18)$$

where $\psi_{\theta}(y, z)$ is the spatial distribution of the oscillating temperature profile. It should be noted that θ' is not necessarily in phase with u' since ψ_u and ψ_{θ} are both complex quantities. Substituting into Equation 3.8 gives:

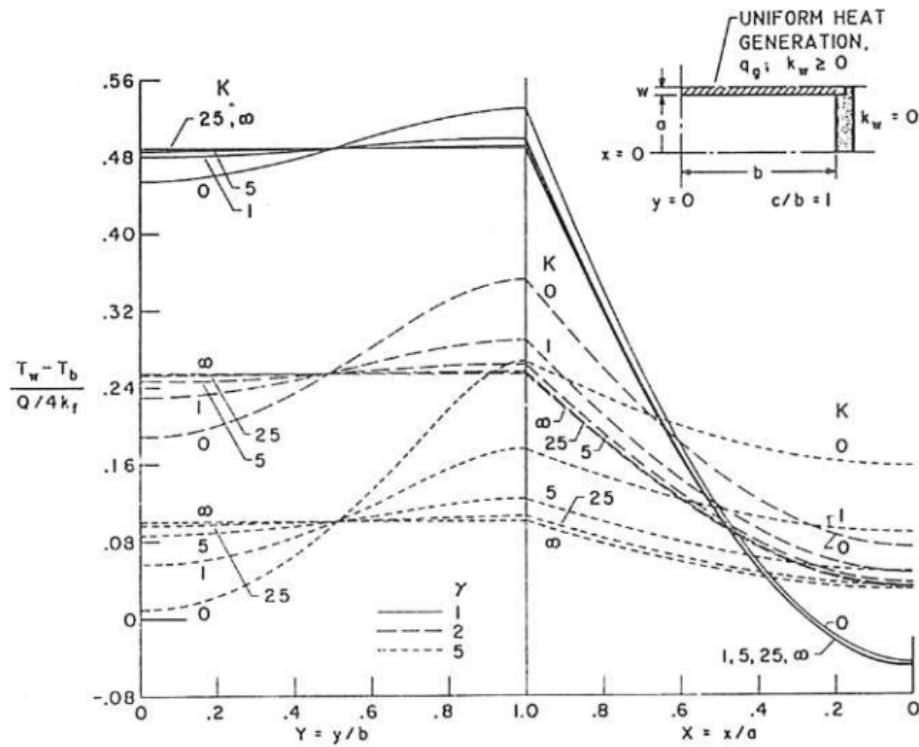


Figure 3.3: Steady wall temperature profiles with lateral conduction in the wall for aspect ratios $b/a = 1, 2$ and 5 . The case of $K = 0$ corresponds to the constant heat flux boundary condition. The experimental geometry of Section 4 corresponds to $K = 0.42$, Siegel and Savino [99].

$$\frac{1}{Pr} \nabla^2 \psi_\theta - iWo^2 \psi_\theta = \psi_u \quad (3.19)$$

Hence, a periodic time-dependent problem in the real domain is transformed into a steady-state problem in the complex domain. A general solution to the homogeneous equation is given by:

$$\psi_\theta = \sum_{j=0}^{\infty} \sum_{k=0}^{\infty} A_{jk} \Phi_2 \quad (3.20)$$

where the Neumann boundary conditions at the walls instead require cosinusoidal eigenfunctions:

$$\Phi_2 = \cos\left(\frac{j\pi y}{a}\right) \cos\left(\frac{k\pi z}{b}\right) \quad (3.21)$$

Using the method of undetermined coefficients, Equations 3.20 and 3.21 are substituted into Equation 3.19 to give:

$$A_{jk} = -\frac{(4/ab)Pr}{\beta_{jk} + iWo^2Pr} \int_0^a \int_0^b \psi_u \Phi_2 dy dz \quad (3.22)$$

$$\beta_{jk} = \pi^2 \left(\frac{j^2}{a^2} + \frac{k^2}{b^2} \right) \quad (3.23)$$

The orthogonality of the eigenfunctions in Φ_1 and Φ_2 ensures that integrals involving odd values of j and k disappear, such that:

$$\psi_\theta(y, z) = \frac{64\nabla p_A Pr}{\pi^4} \sum_{j=0,2,\dots}^{\infty} \sum_{k=0,2,\dots}^{\infty} \sum_{m=1,3,\dots}^{\infty} \sum_{n=1,3,\dots}^{\infty} \frac{a_{jk} \Phi_2}{(\beta_{mn} + iWo^2)(\beta_{jk} + iWo^2Pr)(j^2 - m^2)(k^2 - n^2)} \quad (3.24)$$

with:

$$a_{jk} = \begin{cases} 1 & j = 0, k = 0 \\ 2 & j = 0, k \neq 0 \text{ or } j \neq 0, k = 0 \\ 4 & j \neq 0, k \neq 0 \end{cases} \quad (3.25)$$

The oscillating temperature profiles are hence obtained using Equations 3.18, 3.24 and 3.25. The local amplitudes and phases of temperature are $\theta_A = (\partial\theta_0/\partial x)|\psi_\theta|$ and $\phi_\theta = \tan^{-1}[\Im(\psi_\theta)/\Re(\psi_\theta)]$. The rate of change of the temperature profile is $\partial\theta/\partial t = \Re[\psi_{\partial\theta/\partial t} e^{iWo^2t}]$ with $\psi_{\partial\theta/\partial t} = iWo^2\psi_\theta$. With $j = k = 0$, Equation 3.24 is uniform over the cross section and proportional to the mean cross-sectional displacement. Conveniently, no singularity exists at $Pr = 1$ like in the existing solution in a parallel plate channel [69]. The time-dependent values relative to a fixed sinusoidal flow rate are found using a phase shift:

$$\theta'' = \Re \left[\frac{\partial\theta_0}{\partial x} \psi_\theta e^{i(Wo^2t - \phi_\theta - \pi/2)} \right] \quad (3.26)$$

3.3.1 Bulk Temperature and Nusselt Number

Steady Case Newton's law of cooling states that heat flux is proportional to the temperature difference for steady forced convection. The constant of proportionality is the dimensional

heat transfer coefficient $h_0 = \hat{q}/(\langle T_{w,0} \rangle - T_{b,0})$, where $\langle T_{w,0} \rangle$ is the mean temperature of the heated walls only. In steady unidirectional flow in a vessel, it is conventional to use the flow rate weighted average of the fluid temperature called the bulk temperature to describe the thermal energy state of the fluid:

$$T_{b,0} = \frac{\int_0^{\hat{a}} \int_0^{\hat{b}} \hat{u}_0 T_0 d\hat{y} d\hat{z}}{\int_0^{\hat{a}} \int_0^{\hat{b}} \hat{u}_0 d\hat{y} d\hat{z}} \quad (3.27)$$

The Nusselt number expresses the convective heat transfer of a steady flow with respect to that of conductive heat transfer in the same quiescent fluid:

$$Nu_0 = \frac{h_0 D_h}{k_f} = \frac{1}{\langle \theta_{w,0} \rangle - \theta_{b,0}} \quad (3.28)$$

where the mean wall temperature corresponds to heated walls only. For steady laminar fully-developed flow in a pipe with uniform surface heat flux, it is found that the Nusselt number is a constant, independent of the Reynolds number, Prandtl number and axial location. The H2 condition exhibits the lowest Nusselt numbers of all boundary conditions owing to higher corner temperatures [97]. Figure 3.2 depicts the temperature profile for the case of four heated walls case H2(4) in a square channel (with $Nu_0 = 3.09$), which is most similar to the constant heat flux condition in a steady pipe flow (where $Nu_0 = 4.36$). The heat transfer performance decreases as the channel narrows. The highest heat transfer coefficients are found for the case of two heated long walls H2(2L) – depicted graphically in the schematic of Figure 3.1 – which appear to approach the well-known planar channel value of $Nu_0 = 8.235$ with decreasing aspect ratio. The opposing relationships between heat transfer and aspect ratio for the 2L and 4 cases may be explained by the concentration of energy in regions of poor convection [101]. For the case of plug flows, Gao and Hartnett [96] and Morini [97] found a geometry-independent value of $Nu_0 = 6$, illustrating the influence of the velocity profile.

Time-averaged Case The definition of bulk temperature and Nusselt number is not a trivial matter in unsteady flow. Guo and Sung [102] showed that alternative definitions of Nusselt

number could indicate either enhancement or reduction in heat transfer. Similarly in the field of dropwise condensation [103] (where heat flux and temperature difference are not proportional), the error bounds of calculating h from ΔT could yield contradictory results, and the concept of a mean heat-transfer coefficient is not considered helpful.

Hemida et al. [29] performed a rigorous analysis of the correct definition of bulk temperature, concluding that, to allow its use in a steady flow thermal energy balance $Q_w = \dot{m}c_p(T_{b,out} - T_{b,in})$ [104], it should be defined as:

$$\theta_b = \frac{\int_0^{\lambda} \int_0^a \int_0^b u \theta \, dy \, dz \, dt}{\int_0^{\lambda} \int_0^a \int_0^b u \, dy \, dz \, dt} \quad (3.29)$$

where λ is the dimensionless oscillation period. The overall bulk temperature contains four components resulting from the product of the decoupled velocity and temperature $u\theta = (u_0 + u')(\theta_0 + \theta')$, of which only two remain after the integration with respect to time. The time-averaged change in the bulk temperature due to unsteadiness is dependent on the interactions between the fluctuating components of velocity and temperature:

$$\bar{\theta}'_b = 1/\lambda \int_0^{\lambda} \theta'_b \, dt \quad (3.30)$$

where the overbar denotes averaging with respect to time and:

$$\theta'_b = \frac{\int_0^a \int_0^b \Re(\psi_u e^{iW_o^2 t}) \Re\left(\frac{\partial \theta_0}{\partial x} \psi_\theta e^{iW_o^2 t}\right) \, dy \, dz}{Q_0} \quad (3.31)$$

This term is related to the enhanced axial diffusion term of heat and mass transfer studies reviewed in Chapter 2. The heat transfer is independent of x and does not affect $\partial \theta_0 / \partial x$. Equation 3.31 is compatible with the first definition of time-averaged Nusselt number proposed by Guo and Sung:

$$\overline{Nu} = \frac{1}{\langle \theta_{w,0} \rangle - (\theta_{b,0} + \bar{\theta}'_b)} \quad (3.32)$$

The bulk temperature has been time-averaged prior to division in Equation 3.32. This so-called quotient of the mean \overline{Nu}_{qm} must be used to analyse whether heat transfer has been

enhanced or diminished relative to a steady flow [30]. The conclusion results from an analysis of the enthalpy at the outlet, relative to that at the inlet for a fixed time-averaged flow rate (see also the discussion of convected energy flux in [105]). The corresponding heat transfer coefficient is $\bar{h}_{qm} = \bar{\hat{q}}/\overline{\Delta T}$. However, the above definition gives no information on time-dependent heat transfer and the mean of the quotient $\bar{h}_{mq} = \overline{\hat{q}/(\langle T_w \rangle - T_b)}$ is sometimes used. Calculating instantaneous values effectively changes the order of averaging and division. However, $\bar{\hat{q}}$ does not always have the same value as $\bar{h}_{mq}\overline{\Delta T}$ as a result of coupling effects. For example, the instantaneous and time-averaged problems may be described as [106]:

$$\bar{\hat{q}} + q' = (\bar{h}_{mq} + h')(\overline{\Delta T} + \Delta T') \quad (3.33a)$$

$$\bar{\hat{q}} = \bar{h}_{mq}\overline{\Delta T} + \overline{h'\Delta T'} \quad (3.33b)$$

where the $\overline{h'\Delta T'}$ term captures non-linearities in the heat transfer problem. Zudin [107] called \bar{h}_{qm} the "experimental heat transfer coefficient" (EHTC) and \bar{h}_{mq} the "averaged true heat transfer coefficient" (ATHTC), with respect to semi-analytical analyses of conjugate problems. It is found that $\bar{h}_{mq} = \bar{h}_{qm}$ for the constant temperature boundary condition, \bar{h}_{mq} is virtually independent of wall properties, and that \bar{h}_{qm} is always less than or equal to \bar{h}_{mq} in the thermally-developed region [107]. Mathie and Markides [106] showed that \bar{h}_{mq} may be greater in the thermally-developing region, and used the non-linearity to quantify a heat transfer augmentation ratio $A = 1 + \overline{h'\Delta T'}/\bar{h}\overline{\Delta T}$ where the heat transfer is compared to a "steady equivalent", rather than a literal steady flow.

Chapter 4

Experimental Methods, Analysis and Uncertainty

In Chapter 3, an analytical model was developed for the velocity and temperature profiles of an incompressible pulsating flow in a rectangular channel heated under constant heat flux. As concluded by the literature review of Chapter 2, none of the hydrodynamic and thermal parameters have received any form of quantitative experimental validation under these specific conditions. This chapter relays the design of the experimental apparatus and testing procedure, as well as techniques used in data analysis and the evaluation of experimental uncertainty.

4.1 Experimental Methods

This section describes the design of two separate experimental rigs, constructed to measure the local time-dependent velocities and wall temperatures, respectively. The experimental setup should isolate the heat transfer enhancement due to pulsation alone, by ensuring that the flow is hydrodynamically and thermally-developed and devoid of secondary flow effects. Also, the simplest case of sinusoidal pulsations in the periodic steady-state are of interest. Since the velocity and temperature field are identical in each subsequent period, the harmonic flow pattern is exploited to decouple the experimental testing procedures and simplify the test facilities. It is expected that the construction of separate rigs to facilitate hydrodynamic and

thermal measurements will reduce the experimental error. For example, the channel tailored for hydrodynamic measurements will adhere to a smooth-walled rectangular geometry more accurately, since no cutout is required to facilitate infrared (IR) camera access of the heater using materials transparent in these wavelengths. Furthermore, the momentum and heat transfer problems contain unique design considerations and a compromise within practical constraints is difficult. A larger channel is desirable to facilitate particle image velocimetry (PIV) in two separate planes while a slightly smaller channel ensures a shorter thermal development length. Dimensional analysis may subsequently be used to recouple the problems.

4.1.1 Hydrodynamic Testing

The velocity is the principal hydrodynamic parameter from which many other parameters such as wall shear stress and vorticity derive. Table 2.1 summarises the techniques used by the reviewed studies of Section 2 to measure the velocity field. The measurement technique of particle image velocimetry (PIV) is considered a mature technology and has been implemented previously to measure the unsteady velocity profiles of a compressible flow around parallel-plate structures of thermoacoustic devices [108, 109].

4.1.1.1 Experimental Apparatus

Test Section Figure 4.1 depicts a model of the hydrodynamic test facility. The test section consists of a rectangular channel bound by four 10 *mm* thick optically transparent acrylic walls, which are bonded and sealed using chloroform. The pieces are orientated as illustrated in Figure 4.2, so that the body of water within is visible through unmachined surfaces of the material, preventing the need for polishing. The dimensions – reported in Table 4.1 – are small compared with experiments in the reviewed literature of Section 2.1 (see Table 2.1). The vertical orientation in which the test section is mounted enables the easy evacuation of air bubbles. It also ensures that the laser and camera are traversed in a plane parallel to the floor. Furthermore, the laser never shines vertically and can be maintained below waist height. The inlet and outlet are oriented at 90° to the channel axis and a conservative length of at least $50 \times D_h$ has been maintained upstream of the testing window to ensure hydrodynamic

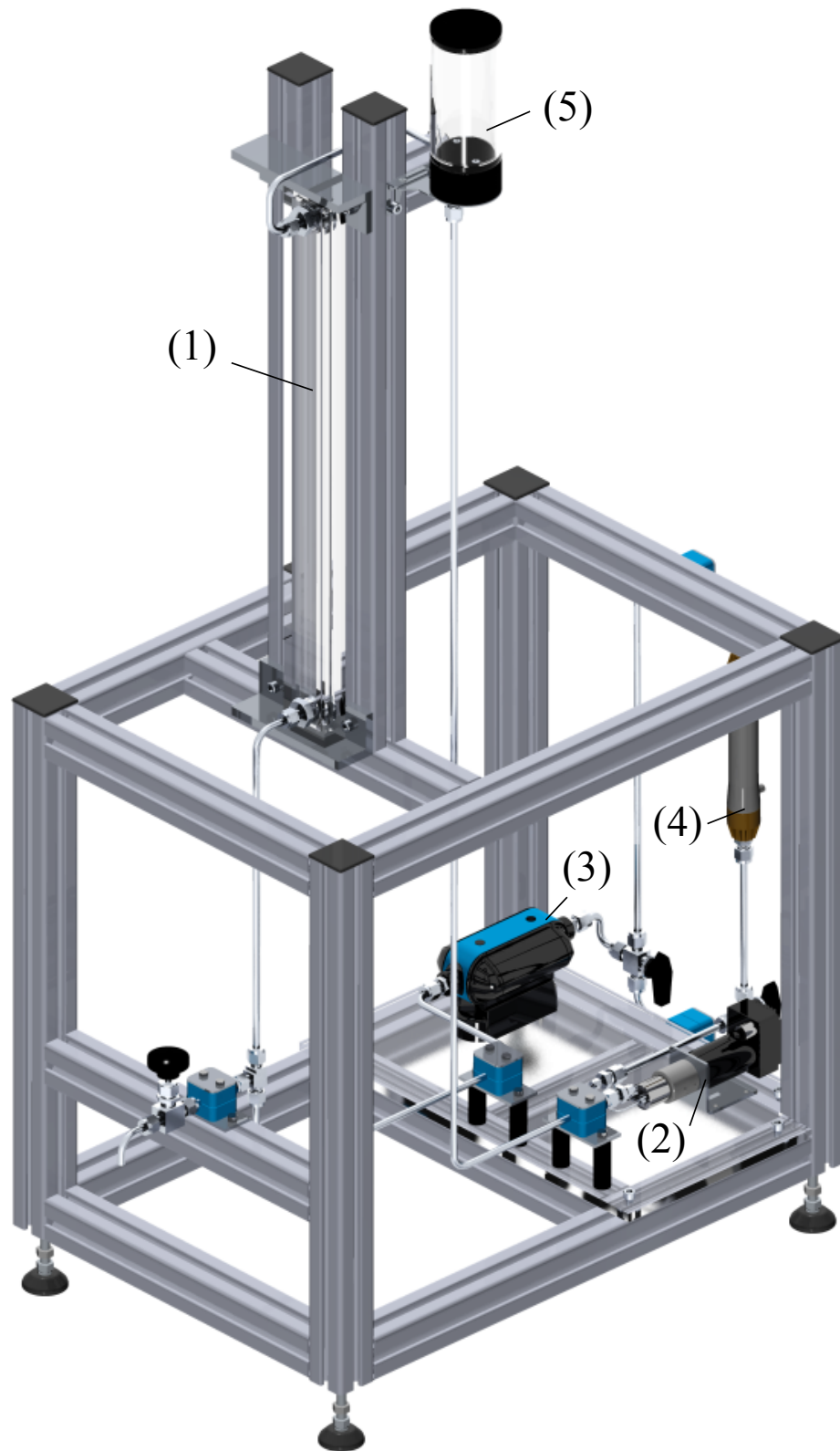


Figure 4.1: Model of the hydrodynamic test rig, containing (1) channel test section, (2) gear pump, (3) flow meter, (4) degassing system and (5) fluid reservoir.

development (this is discussed further in Section 4.2). The test section is connected to the flow loop by stainless steel connections and tubing, used so that pulsation does not induce strain in the walls of the tubes.

Table 4.1: Hydrodynamic channel dimensions.

Width, \hat{a} [mm]	30
Height, \hat{b} [mm]	4
Length, \hat{L} [mm]	500
Hydraulic Diameter, D_h [mm]	7.1

Gear Pump A HNP Mikrosysteme m zr-4605 micro annular gear pump (0.012-72 mL/min) and Terminal Box S-G05 drive are used to generate steady and pulsating flows, which draw from a 236 mL Koolance reservoir. Unlike piston/diaphragm pump methods of flow oscillation, the flow rate is controlled rather than the volumetric displacement per cycle and the relevant amplitude parameter is the dimensionless flow rate amplitude Q_A/Q_0 , rather than the dimensionless amplitude A_0 . To generate pulsations, a program has been written using Matlab software with parameters that are controlled via a graphical user interface (GUI). A sinusoidal flow rate of a given mean, amplitude and frequency is discretised into a finite number of time steps. At each interval, a timer function executes and writes a motor speed to the controller based on the phase of the period. If the flow is discretised into sufficiently small intervals, the inertia of the pump causes a smooth temporal flow rate. For flow with very long time periods, a maximum interval of 0.5 s was used to ensure a wave free from step changes in flow. A counter implemented in the timer function records the phase of the output

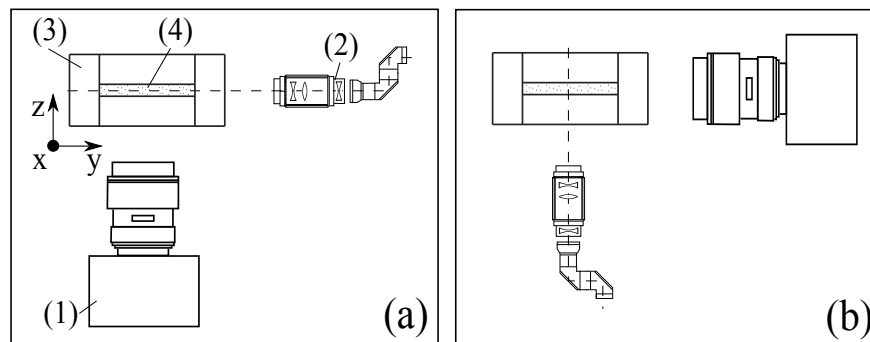


Figure 4.2: Orientation of (1) camera, (2) laser optics and (3) acrylic channel to capture the \hat{x} velocity component (out of plane) of (4) the fluid body over the (a) \hat{y} dimension and (b) \hat{z} dimension.

flow. At desired phase values ($0, 0.1\pi, 0.2\pi\dots$), the error output pin of the pump controller is set to high and sent to the imaging system to trigger image capture. The 24 V signal is ramped down to 5 V using a pair of resistors in a voltage divider circuit.

According to the manufacturer, the accuracy of the pump rotational speed is $\pm 3\text{ rpm}$, dependent on the operational conditions. Since the pump cannot achieve negative flow rate, the flow rate amplitude is limited to $Q_A/Q_0 \leq 1$. The working range of Reynolds numbers in the $30\text{ mm} \times 4\text{ mm}$ channel is $10 \leq Re_0 \leq 88$. Unknown at the time of testing, the acceleration is set to 500 rps/s by default but can be increased. Thus, pulsation speeds higher than the 0.5 Hz limit determined in Section 6 may be achievable. Interestingly, the precision of the pump has been exploited to simulate a heart beat pulsating flow of artificial blood through capillary-shaped microchannels [110].

Flow Meter The steady flow rate is measured using an Atrato 710-V00-D ultrasonic flow meter ($2 - 500\text{ mL/min}$), accurate to $\pm 1\%$ of the reading according to the manufacturer. The instrument uses the non-intrusive time of flight measuring method with symmetrical sound waves generated by the excitation of annular crystals. The up- and downstream flight times in the 1 mm diameter bore are measured to within 250 ps . The velocity of the fluid is equal to half the difference. Interestingly, the shape of the velocity profile is not important.

Degassing System A Minimodule G543 deaerater is used to remove bubbles and dissolved gases in the working fluid. This operates using 50 polypropylene hollow fibre membranes (with a lumenside inner diameter of $200\text{ }\mu\text{m}$) in polyurethane potting resin. The module is attached to an Agilent Varian SH100 single-stage dry hermetic scroll vacuum pump by polyurethane (PU) and polyamide (PA) tubing, which is stiff enough to prevent collapse in the vacuum pressure required to achieve effective degassing ($< 200\text{ mbar}$). To minimise the amount of water vapour from entering the air side, the vacuum is maintained above the 23.4 mbar vapour pressure of water (for a nominal room temperature of 20°C). Further, a water trap is utilised to prevent any water from entering the pump. To prevent any miniscule particles in the flow from clogging its pores during testing, the degasser can be cut off from the flow loop using 3-way ball valves.

Particle Image Velocimetry System The velocity field of the flow is measured using a TSI particle image velocimetry (PIV) system, composed of a laser system, an optical system, a camera and data acquisition/processing software all controlled by a dedicated computer. The fluid is seeded with $4\ \mu\text{m}$ diameter nylon-12 tracer particles (TSI P/N 10084), with a density of $1140\ \text{kg}/\text{m}^3$. The Quantel Twins Big Sky Laser system is comprised of a pair of rugged, lamp-pumped Nd:YAG, $200\ \text{mJ}$ per pulse, $1064\ \text{nm}$ lasers with a pulse repetition rate of $15\ \text{Hz}$. Mounted side-by-side, the beams of the individual lasers are combined in a single optical axis to produce collimated green light of $532\ \text{nm}$ wavelength. The beam leaves the laser with a waist diameter of $5.2\ \text{mm}$ and a divergence half-angle of $3.8\ \text{mrad}$.

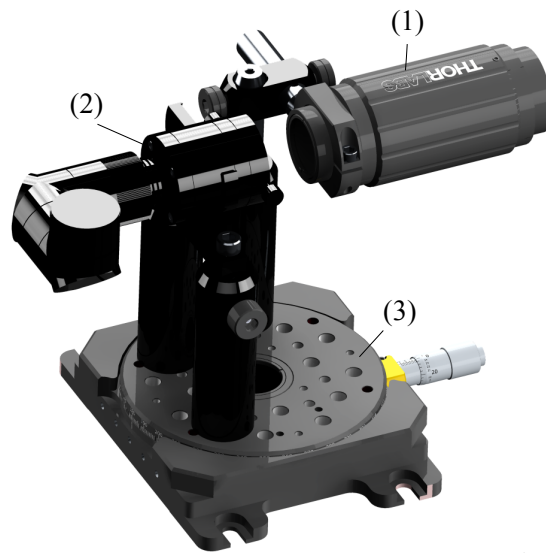


Figure 4.3: Model of the optical setup, containing (1) lens tube, (2) laser arm, and (3) rotating stage.

PIV is a volume measurement technique by nature, such that the velocity measured at a point amounts to the Gaussian-weighted average of particle velocities illuminated by the thick laser sheet. Since the channel height is $4\ \text{mm}$, an analysis is performed to determine the associated error using the analytical solution of Section 3. The error is highest when measuring the velocity profile in the \hat{y} dimension. The volume illuminated by a laser sheet with a thickness an order of magnitude smaller than the channel height contains velocities at least 1% lower than those at the mid-dimensions. Using a laser sheet thickness two orders of magnitude smaller reduces the discrepancy to 0.01%. Hence, a custom optical setup is assembled (depicted in Figure 4.3), using three lenses to achieve an adjustable focal length and laser sheet thickness. The characteristics of the laser beam such as the focal length, waist

diameter and Rayleigh range are estimated after each lens using the formulations of Self [111] for spherical Gaussian beams. A 25 mm diameter spherical plano-concave (diverging) lens with -75 mm focal length is mounted in the base of a lens tube, which stays in a fixed location. In the translating part of the lens tube are mounted a 25 mm diameter spherical plano-convex (converging) lens with 100 mm focal length and a 12.5 mm diameter cylindrical plano-concave (diverging) lens with a focal length of -12.5 mm. The focal length, beam waist diameter and Rayleigh range are varied according to the distance between the former optical pair. The lenses have wavelength ranges compatible with the collimated green light of 532 nm wavelength of laser. The minimum thickness of a single burst of the lasers on laser alignment paper placed at the theoretical focus is 266 μm , as measured using a digital microscope (see Figure 4.4). The optical setup is coupled to a rotating stage on a vertically-translating mount. Translation in the remaining dimensions is facilitated by a traversal. The cylindrical lens may be rotated to align the laser sheet to the dimensions of the channel.

The TSI 4 MP PowerView CCD camera (Model 630090) has a frame rate of up to 16 frames per second (fps) at full pixel resolution. To achieve a picture with maximum pixel density of the channel, a Nikon AF Nikkor lens with a 50 mm focal length is used in conjunction with either 12 or 48 mm of extension, dependent on the channel dimension being observed. The camera has a resolution of 2352×1768 pixels, which amounts to 34.25×25.75 mm² or 11.76×8.84 mm² in physical units, depending on the extension. The lens aperture is set to f/11 to ensure appropriate illumination of the channel. The depth of field (DOF) may be estimated using VWDOF calculator software [112]. The sensor size is 12.9 mm \times 9.7 mm and defocused points are defined as having a circle of confusion less than or equal to the 5.5 μm pixel size. The DOF varies from 2.6 mm to 257 μm dependent on the extension tubes used.

The LaserPulse Synchroniser (Model 610035) connects to all components of the imaging system and acts as the timing and control module. The timing electronics govern signal generation to the laser flash lamps and Q-switches, the camera and the frame grabber to completely automate the timing between laser pulses and camera exposure times with 1 ns time resolution. The camera is interfaced to the PC using an Xcelera frame grabber. The control unit also reads an external 800 μs TTL pulse trigger signal from the pump controller to phase-lock measurements to the sinusoidal oscillation of the flow. The time step between

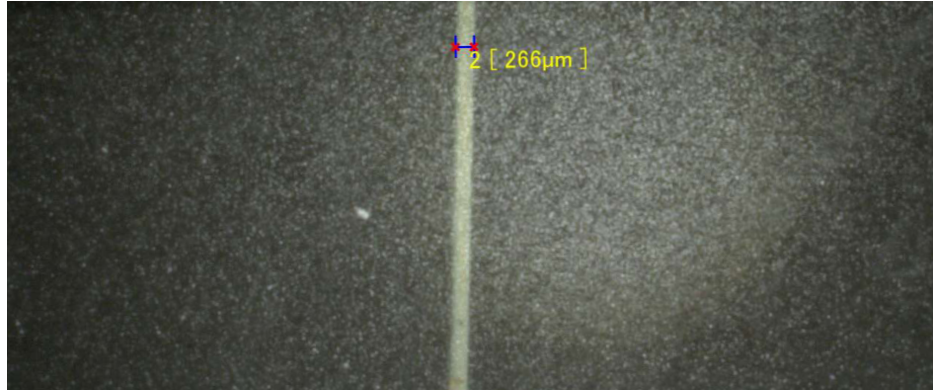


Figure 4.4: Single burst of the lasers on laser alignment paper placed at the theoretical focus measured using a digital microscope.

individual captures is kept below 0.5% of the oscillation period to minimise averaging errors resulting from the ever-changing flow field. Connected to a computer via serial interface, the entire PIV system can be completely controlled using TSI's Insight 4G (version 10.0.3.0) data acquisition software.

4.1.1.2 System Calibration

Pump The volumetric displacement per revolution of the pump is calibrated for steady flow rates using an ultrasonic flow meter (see Figure 4.5). As is typical with gear pumps, the volumetric efficiency reduces with rising differential pressure (see right of Figure 4.5). However, the changes in pressure drop with flow rate and imposed unsteadiness are assumed insignificant relative to the 10 bar pump rating. An estimate of the flow rate is hence achieved by approximating the flow as positively-displaced.

PIV System Calibration of the optical alignment is performed prior to taking measurements for each of the two perpendicular plane orientations (depicted in Figure 4.2). To calibrate the laser beam, crosshairs are attached to the end of the laser arm and aimed at a sheet of laser alignment paper. The angles of the mirrors are adjusted until a pattern symmetric in the up-down and left-right directions is achieved. The rig and traverses are leveled with a spirit level by adjusting the feet on the end of the profile. The laser arm is further mounted onto a rotating stage to enable fine rotation of the light sheet and ensure accurate alignment. A minimum and uniform sheet thickness is ensured by positioning the centre of the test window

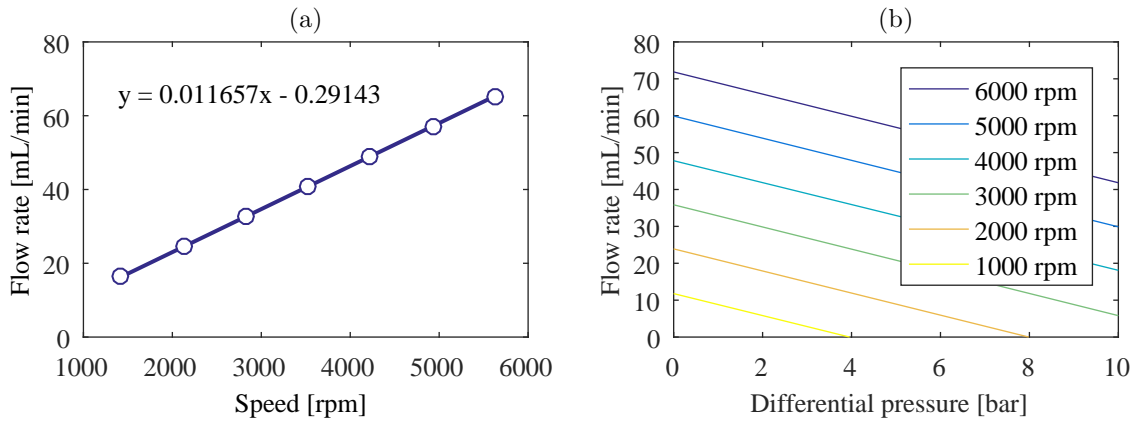


Figure 4.5: (a) Calibration curve for the pump flow rate as a function of motor speed with linear fit, (b) Manufacturer specifications for decreasing volumetric efficiency with rising differential pressure for liquid water ($\mu = 1 \text{ mPa} \cdot \text{s}$).

at the focal point of the laser's converging lens. The laser sheet is preliminarily aligned with the principal axes of the channel using a calibration target and laser alignment paper. Precise alignment is achieved using an iterative procedure involving velocity measurements in steady flow. A series of image pairs are captured for steady flows corresponding to the maximum and minimum flow rates of the pump. The angle of the laser sheet is adjusted until the ensemble-averages of the processed velocity profiles are symmetric with flat ridges. To determine the midpoint, the laser sheet is traversed between the boundaries of the channel. The processed spatial velocity distributions are processed and integrated to determine the flow rate at each increment. The maximum of the resulting curve of flow rate versus position provides the centre point of the channel. The angle of the camera traverse is finely adjusted by capturing images and ensuring vertical orientation of the channel walls. The angle of the camera is adjusted such that the particles in a flow circulated through the test section appear in focus across the entire width of the channel.

4.1.1.3 Experimental Procedure

Deionised water is added to the flow loop through the fluid reservoir and circulated for one hour through the deaerator. While the particles should be neutrally buoyant, those that settle near the middle of the solution are added to the flow using a pipette and allowed to disperse through the body of water for several minutes.

To confirm that the flow is fully-developed in the experimental setup, steady flows over

Table 4.2: Experimental parameter space.

<i>Frequency, f [Hz]</i>	0.02	0.1	0.5
<i>Womersley number, Wo</i>	1.4	3.1	7.0
<i>Flow rate amplitude, Q_A/Q_0</i>	0.9	0.9	0.9
<i>Tidal displacement, $2\hat{\chi}_A$ [mm]</i>	2.5	12.6	62.8
<i>Dimensionless amplitude, A_0</i>	0.36	1.78	8.9

the range $10 \leq Re_0 \leq 80$ are circulated through the test section. The Reynolds number of the steady component of the pulsations is $Re_0 = 40$. Since the distinct characteristics of pulsation vary solely with Wo , the pulsation speed is varied according to Table 4.2 while Q_A/Q_0 is maintained at 0.9. This high flow rate amplitude was chosen to capture the interesting effects of local flow reversal at high frequencies. The desired mean, frequency and amplitude of the flow rate for a given test are input using the Matlab GUI for the pump controller. The phase values where image capture is triggered are adjusted, depending on the pulsation speed. At lower frequencies, all required phases are captured in one cycle, while the limited repetition rate of the laser requires multiple cycles to capture the required data points at higher frequencies. The TSI Insight 4G software is set to capture an overall number of image pairs, amounting to 100 at each phase value (for ensemble-averaging). The data acquisition is set to wait for the first trigger signal, which corresponds to a zeroth phase value of the sinusoidal pump flow rate in the periodic steady-state (i.e. a number of cycles after the rise time). The images are saved in `.tif` format. As discussed in Section 4.2.1, the images are processed using Insight's in-built algorithms, and the processed vectors (in `.vec` format) are exported to Matlab for post-processing.

4.1.2 Heat Transfer Testing

Section 2.2 reviews the experimental techniques used to measure the local time-dependent temperature field of oscillating flows, as summarised by Table 2.2. While the bulk temperature is an important parameter for predicting enhancement of heat transfer in pulsating flow relative to steady flow, the behaviour of the temperature profile near the wall determines the explicit heat flux. Hence the infrared thermography (IRT) technique is preferred to planar measurement techniques that would require high resolution and precision in the near-wall region. This non-intrusive technique is proficient at resolving two-dimensional surface

temperatures with high spatial resolution [113], and has been used in the Fluids and Heat Transfer Research Group of Trinity College Dublin to measure the impacts of rising bubbles, the wakes of sliding bubbles and electrospray cooling [114, 115, 116]. To the best of the author's knowledge, IRT has not implemented with pulsating or oscillating flow in any vessel geometry. Thin foils approximate the constant heat flux boundary condition and amplify wall temperature fluctuations. For example, Mosyak et al. [117] found that the temperature fluctuations of a thin stainless steel foil were an order of magnitude higher than a thick copper plate.

4.1.2.1 Experimental Apparatus

Test Section The experimental test section consists of a channel plate and heater support plate, clamped between a pair of aluminium supports, as depicted in Figure 4.1.2.1. Sealing is achieved using a 0.2 mm silicone rubber gasket. The inlet and outlet are machined into the channel plate and are oriented at right angles to the channel axis. The support frames allow the piece to be mounted to aluminium profile and also to help to distribute the stresses on the acrylic pieces more evenly to prevent cracking. As before, stainless steel connections and tubing are used such that pulsation does not induce strain in the walls of the tubes.

Channel The channel is milled from an acrylic plate. The dimensions, reported in Table 4.3, are small compared with experiments in the reviewed literature of Section 2.2 (see Table 2.2) and have been reduced compared with the unheated channel since thermal development requires a larger axial length in water. Also, the smaller channel width reduces deformation and vibration of the unsupported thin fourth wall of the channel, as discussed below. A distance of $94 \times D_h$ has been maintained upstream of the testing window, as the inlet and outlet are at 90° to the principal axis. Since the thickness of the compressible gasket contributes to the channel height, a vernier calipers is first used to obtain ten measurements of the overall height of the clamped test section without the gasket. By performing the same measurement with the gasket in place, allows the difference (and channel height) to be determined.

Heated Foil The fourth wall of the channel is formed by a tensioned 25 μm thick annealed Inconel 625 foil (Ni61/Cr22/Mo 9/Fe 5). Inconel was chosen for its high electrical resistivity

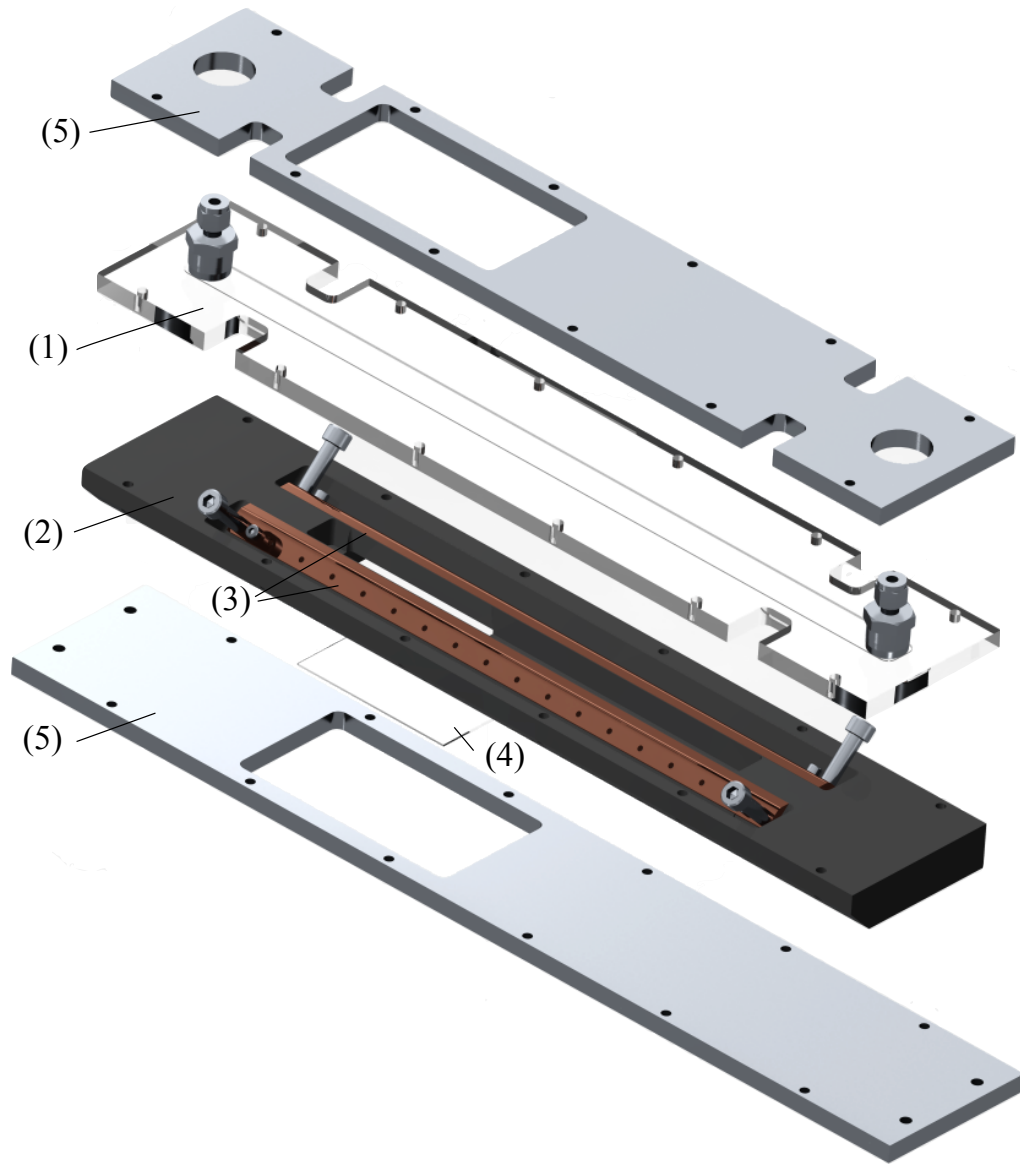


Figure 4.6: Exploded view of test section, containing (1) channel plate, (2) heater support plate, (3) electrodes, (4) IR glass, and (5) aluminium supports.

Table 4.3: Heated channel dimensions.

<i>Width, \hat{a} [mm]</i>	20
<i>Height, \hat{b} [mm]</i>	2
<i>Length, \hat{L} [mm]</i>	460
<i>Hydraulic Diameter, D_h [mm]</i>	3.6

of $129 \mu\Omega cm$ and low thermal conductivity (such that lateral conduction within the foil is reduced). Foil preparation is a delicate and time-consuming process. Since high emissivity surfaces are preferred [113] the camera-side of the foil needs to be painted black. This also acts to reduce reflections and the Narcissus effect (where the camera sees reflection of its own sensor). The foil is cut to 42 mm wide \times 700 mm long using a scalpel and cleaned using isopropanol (IPA). Ideally, the entire width would be coated with paint to negate end effects at the side walls; however, the electrodes need to contact the alloy near the channel, as depicted in Figure 4.7. Also, a long paint layer (in the axial direction) ensures consistency while the flow develops thermally. The borders around a 22 mm wide \times 350 mm long area are masked with tape, accurate to $\pm 0.5 \text{ mm}$. The matte black paint (Electrolube, RS Stock No. 374-8654) is applied using an air brush, which facilitates fine tuning of air pressure (15 psi found to be optimal) and spray angle. The properties of the foil and paint are listed in Table 4.4, where the thermal conductivity of the paint has been tested by Thermoconcept using the transient plane source (TPS) technique [114]. The density and specific heat capacity data of Raghu and Philip [118] are used. The foil properties are supplied by the manufacturer. After testing, three profile measurements of the paint thickness are taken using a Dektak surface profiler with a resolution of $\pm 0.5 \text{ nm}$. The paint has a mean thickness of $6.59 \mu m$ with a standard uncertainty of $\pm 1.12 \mu m$.

Table 4.4: Foil and paint properties [114, 118, 119].

	<i>Foil, s</i>	<i>Paint, p</i>
<i>Thickness, \hat{w} [μm]</i>	25	6.59
<i>Density, ρ [kg/m^3]</i>	8440	1162
<i>Thermal conductivity, k [$W/(m \cdot K)$]</i>	9.8	0.095
<i>Specific heat, c_p [$J/(kg \cdot K)$]</i>	410	2835
<i>Emissivity, ϵ</i>	0.13	0.95

Heater Support The foil is clamped and tensioned in the longitudinal direction, as shown in Figure 4.8. The foil wraps around rollers before being clamped between aluminium pieces with serrated inner surfaces for grip. A separate pair of longitudinal copper electrodes are used to supply current to the foil, housed in the PEEK heater support plate. The electrodes touch the foil (through a layer of silver conductive grease) near the corners of the channel, such that foil is only heated at a single wall of the channel, minimising heat leakage into the channel from the sides (see Figure 4.7). The test section design also maintains a layer of insulating PEEK between the electrodes and air gap, to minimise heat leakage into the channel from the air gap. Each pair of electrodes has two screw connections, which are connected to power via copper cables to a Lambda GENESYS GEN6-200 DC power supply, capable of 6 V and 200 A output. 59.8 A is supplied with constant current mode ensuring steady heating of the foil. An interesting analysis by Mathie [106] shows that constant current mode is optimal, since the power delivered to the foil is independent of any change in foil or cable resistance as a result of heating. Since PEEK is not infrared transparent, a section has

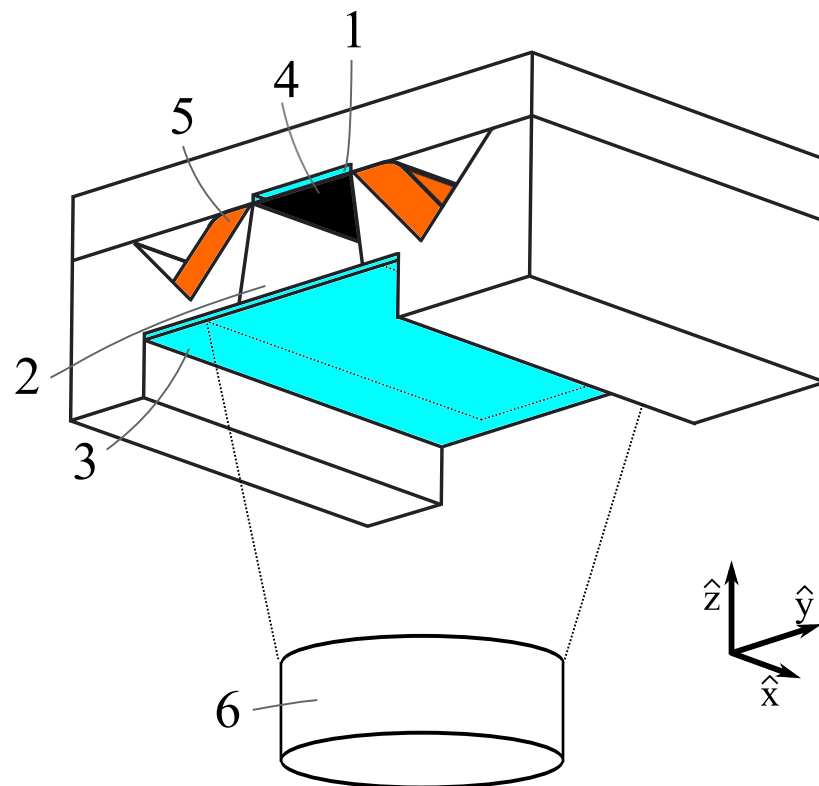


Figure 4.7: Cross-section of test section showing the (1) channel, (2) air gap, (3) IR glass, (4) heated foil, (5) electrodes and (6) camera.

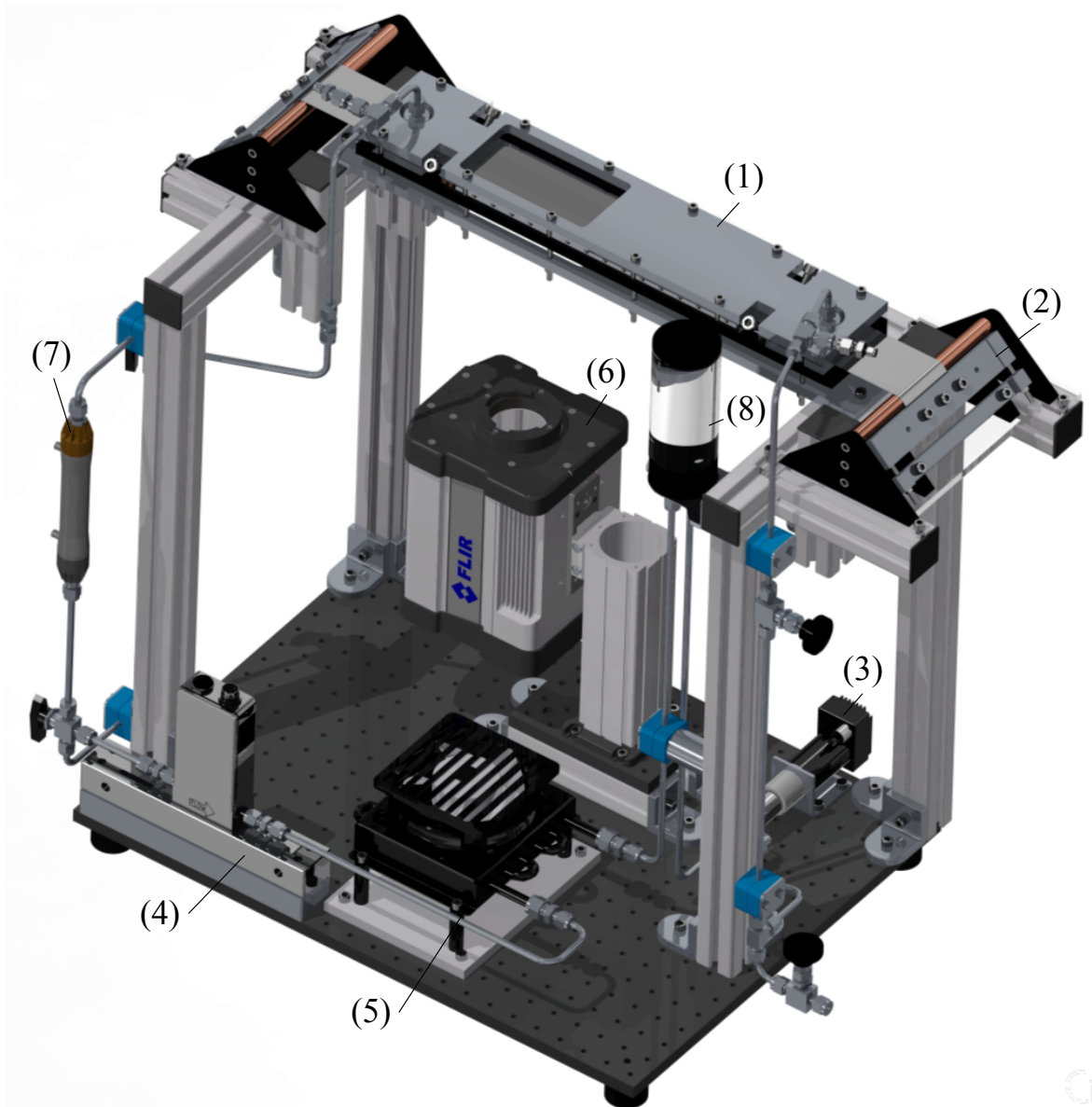


Figure 4.8: Model of heat transfer test rig, containing (1) test section, (2) tensioning system, (3) gear pump, (4) flow meter, (5) secondary heat exchanger, (6) thermal camera, (7) degassing system and (8) fluid reservoir.

been removed to allow thermal measurements of the rear face of the heated foil to be taken with an IR camera. A sapphire glass (Al_2O_3) window, $95 \times 52 \times 1 \text{ mm}^3$, is used to create a stagnant air gap, with dimensions 75 mm long \times 20 mm wide \times 15 mm high. While sapphire has a high percentage transmissibility within the $2.5 - 5.1 \mu\text{m}$ range of the infrared camera (see Figure 4.9), a temperature calibration is performed with the window in the optical path prior to testing, as detailed in Section 4.1.2.2. A heated length of $83 \times D_h$ is maintained upstream of the viewing window to ensure that the flow is thermally developed. To provide

insulation, an air gap is maintained between the foil and glass. The foil is unsupported since rigid backing supports must be transparent to the IR radiation and may contribute to the energy balance [120]. Hence, the pressure in the liquid channel flow may cause deformation and vibration of the channel boundary. The energy balance of the foil is discussed in Section 4.2.2.2.

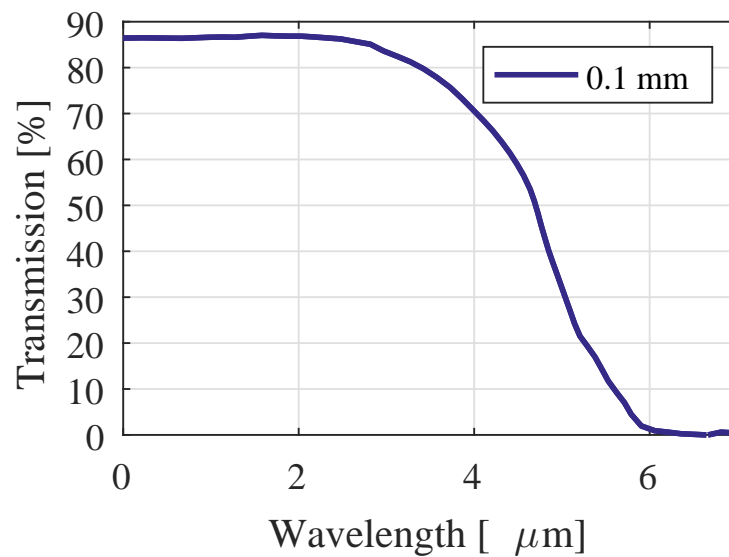


Figure 4.9: Transmissivity of IR light with wavelength for 0.1 *mm* thick sapphire (Al_2O_3) glass, Crystran [121].

Liquid-cooling Flow Loop Figure 4.8 depicts the single phase flow loop used to cool the heated channel. The hot working fluid exiting the test section is cooled by a fan-driven plate-fin heat exchanger with the circuit driven by the gear pump and drive described in Section 4.1.1.1. The 236 *mL* reservoir increases the volume of liquid to hold the bulk liquid temperature constant during operation and also to allow for easy filling and emptying of the flow loop. Deionised water – which has been degassed using the degassing system of Section 4.1.1.1 – is used as the coolant. The thermal properties of the fluid at 30°C (i.e. the temperature near the end of the heater and viewing window) are listed in Table 4.5.

Flow Meter For heat transfer testing, the steady flow rate is measured using a Bronkhorst model M14 flow meter (500 *mL/min*), which uses the Coriolis measurement technique. The instrument contains a uniquely-shaped, single-loop sensor tube which forms part of a

system oscillating at its natural frequency. As the flow passes through the vibrating tube, Coriolis forces are generated causing very small tube displacements which are detected by optimally-positioned sensors connected to an integrally mounted printed circuit board (PCB). The phase shift of the sensor signals is proportional to the mass flow rate. The meter is mounted to a vibration-free, heavy mounting block which has a mass and stiffness precisely tuned for this specific model. This ensures optimal accuracy of measurements. More than 20 pipe diameters was allowed between the instrument and any abrupt turns in connecting tubing.

Thermocouples The temperatures at the inlet and outlet, and two air gap temperatures (separated by 20 mm in \hat{x}) are taken using calibrated T-type copper-constantan thermocouples. The thermocouples are connected to a NI-9214 temperature input module, which samples up to 16 channels at a maximum combined frequency of 68 Hz in high-speed timing mode. The thermocouple card is holstered in a one-slot N-CompactDAQ-9171 chassis. Each thermocouple is programmed to take 10 measurements per second using a timer function in Matlab software.

Infrared Thermography System Thermal behaviour is measured using the infrared thermography (IRT) system, comprised of a camera, an optical system and data acquisition software run by a dedicated computer. The outer wall temperature of the heater is imaged by a high-speed FLIR SC6000 series camera, whose specifications are given in Table 4.6. The camera operates using a focal plane array (FPA) of indium antimonide (InSb) detectors, sensitive in the mid-wavelength infrared (MWIR) spectral range where the sapphire IR window is highly transmissible. The detectors are cooled to 78 K using a miniature Stirling engine to prevent the system being flooded with infrared light from its own surroundings. The camera

Table 4.5: Water properties at 30°C [104].

<i>Density, ρ_f [kg/m³]</i>	995.8
<i>Dynamic viscosity, μ_f [kg/(m · s)]</i>	8×10^{-4}
<i>Thermal conductivity, k_f [W/(m · K)]</i>	0.62
<i>Specific heat, $c_{p,f}$ [J/(kg · K)]</i>	4178.4
<i>Expansion coefficient, β_f [1/K]</i>	3×10^{-4}
<i>Prandtl number, Pr</i>	5.6

uses 14 bit signal discretisation such that each pixel detects between 0 and 16383 counts. An integration (exposure) time of 1.7 ms is chosen to maximise use of this range, while ensuring that the sensor never becomes saturated during testing. The camera is mounted to aluminium profile and views the heated surface from below, as depicted in Figure 4.8. To achieve a high spatial resolution of the channel wall, a MW G0.5 F/3.0 close up lens (L0510 LC) with a 46.12 ± 0.5 mm focal length and maximum 19.2×15.36 mm² field of view is used with an image size of 320×256 pixels (and an x offset of 160). The lens has $> 93\%$ transmission. The channel width measures 116 pixels, giving a spatial resolution of 172.4 $\mu\text{m}/\text{pixel}$. The camera is tilted at an angle of 5° to reduce reflections from the glass window, known as the Narcissus effect. Furthermore, a single axial location away from the centre of the focal array is used. The camera is instructed using FLIR ExaminIR integrated software (version 1.30.0). The camera reads external TTL pulse trigger signals from the motor drive (see Section 4.1.1.1) to phase-lock image measurements to the sinusoidal oscillation of the flow. The video files are exported to Matlab for analysis.

Table 4.6: Specifications of infrared camera.

<i>Resolution</i> [pixels]	640 × 512
<i>Wavelength Range</i> [μm]	3 – 5
<i>Full frame rate</i> [Hz]	126
<i>Thermal Sensitivity</i> [mK]	< 20

4.1.2.2 System Calibration

Thermocouples The temperatures at four locations – the inlet, outlet, near air gap and far air gap – are measured using thermocouples that are accurate to within the greater of 1°C or 0.75%, according to the manufacturer. The four probes are calibrated in a Julabo F25 constant-temperature water bath – with a maximum spatial temperature variation of 0.5°C according to the manufacturer (though variation as high as 0.8°C has been measured) – against a Stanford Research Systems calibrated thermistor and programmable temperature controller (with 0.001°C systematic uncertainty). To negate the error of bath non-uniformity, one thermocouple at a time is coupled to the thermistor probe and wrapped in insulation before immersion in the bath. With the water at the inlet and outlet unheated, the transverse temperature profiles are constant and the measured value is the average temperature at the

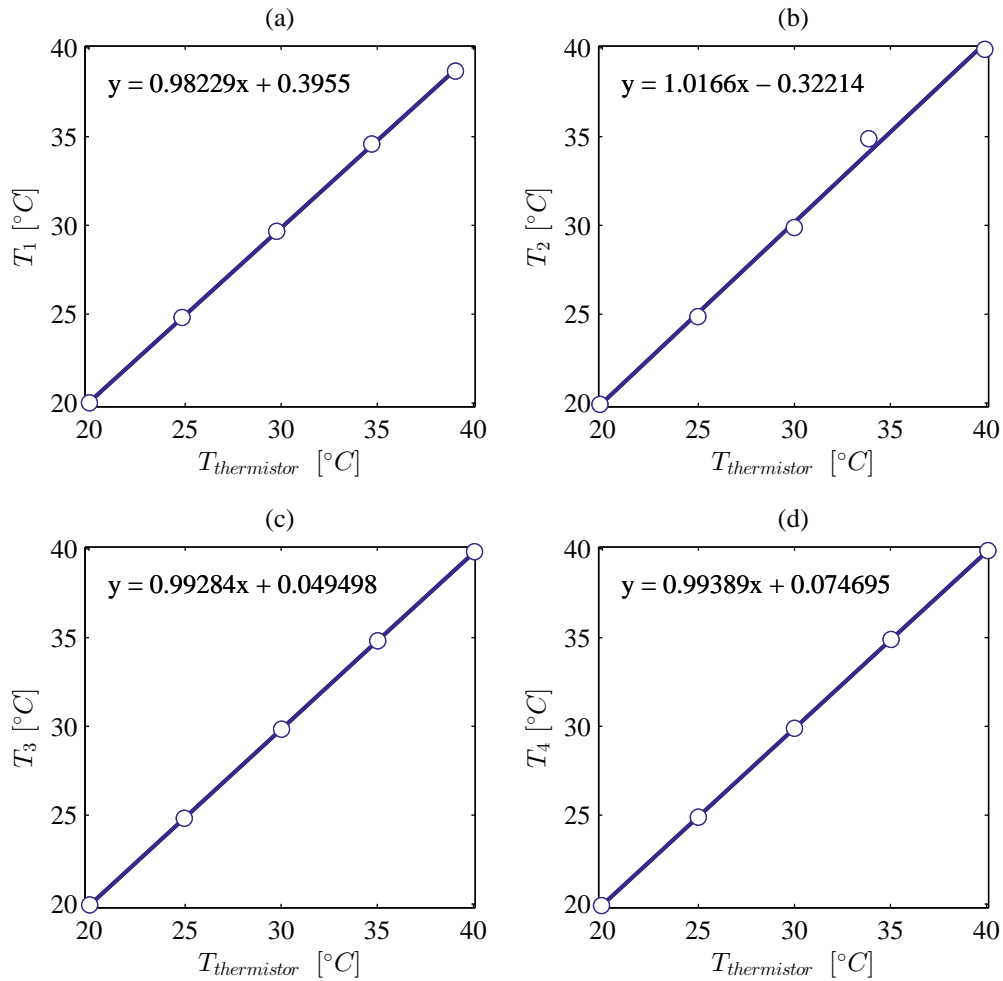


Figure 4.10: Calibration curves for the (a) inlet, (b) outlet, (c) near air gap, and (d) far air gap thermocouples with linear fits.

cross section of the tubing. The linear fits of the thermocouples are depicted in Figure 4.10.

Thermal Camera Thermal cameras are prone to fixed pattern noise, since individual detectors in the focal plane array (FPA) exhibit varying degrees of response to incoming radiation energy (i.e. they have unique gain and zero offset values). Also, inhomogeneities in the lens may distort the counts readings. A two-point non-uniformity correction (NUC) is performed prior to temperature calibration to reduce spurious temperature differences in space. The technique involves observing a constant temperature heat source at two temperatures, such that a linear fit between the two temperature/counts pairs (with a given slope and intercept) may be determined for each of the sensors. The heat source is an

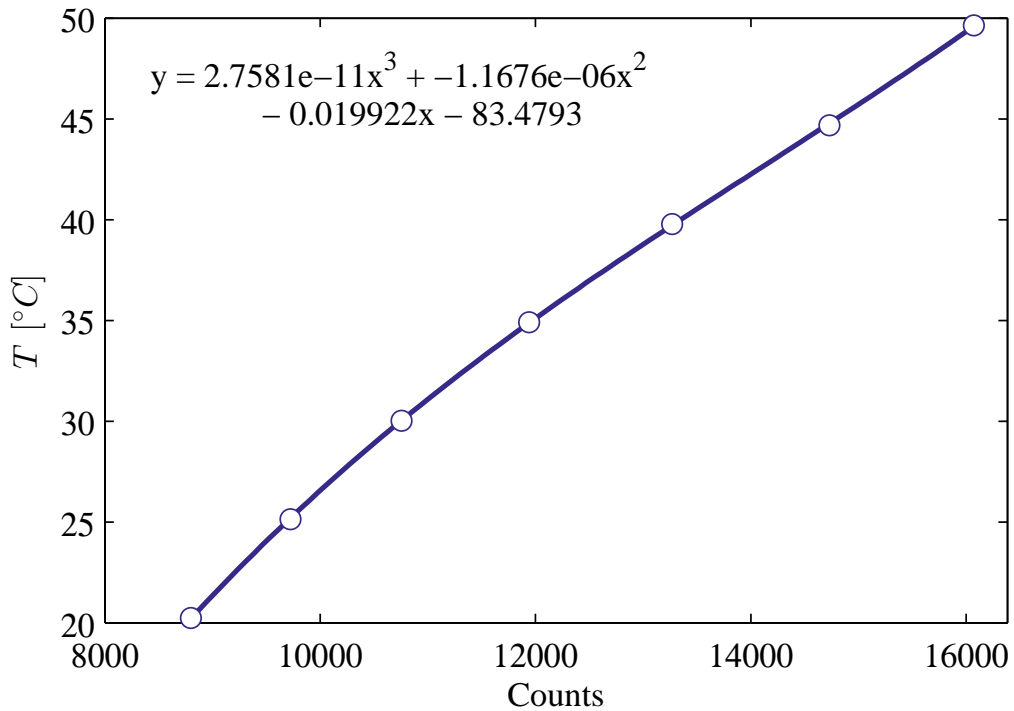


Figure 4.11: Calibration curve for the thermal camera with 3rd order polynomial fit.

Infinity Series black body generator with temperature probe and controller, manufactured by Santa Barbara Infrared (SBIR). The SBIR Model 104i precision thermometer with 0.0001°C resolution is calibrated to 0.007°C accuracy. The surface of the black body consists of an industry standard high emissivity coating with a uniform emissivity of 0.95 over 3 - 14 μm of the wavelength spectrum. The temperature is spatially uniform to the higher of $\pm 1\%$ or $\pm 0.01^{\circ}\text{C}$ over 90% of the surface area. The temperature stability is $< 1 \text{ mK}$. The black body is heated in turn to 25°C and 40°C – corresponding to room temperature and the approximate maximum temperature experienced during testing – and 50 images are recorded and averaged. The FLIR ExaminIR software outputs the gains and offsets as `.scg` and `.sco` files, and bad pixels in `.sbp` format.

Accurately mapping the relationship between temperature and radiation of an IR camera using a radiometric analysis is an arduous task, requiring detailed knowledge of the equipment and the characteristics of radiative emission, absorption and transmissivity. Figure 4.12 illustrates that the radiation energy measured by a sensor is composed of radiation emitted by the heater U_{obj} , radiation emitted by the window U_w , radiation emitted by the hot gas in the air

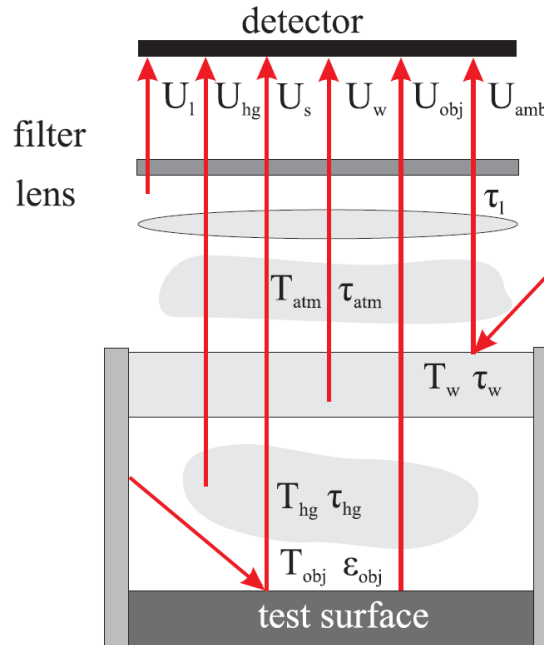


Figure 4.12: Radiation detected by thermal camera, Ochs et al. [122].

gap U_{hg} , radiation emitted by the optics U_l , and reflections of atmosphere-emitted radiation from the sapphire window U_{amb} and heater U_s . Furthermore, the radiation is attenuated according to the transmissivity of the atmosphere τ_{atm} , air gap τ_{hg} , sapphire window τ_w and camera optics τ_l . Planck's law gives the spectral distribution of radiation intensity E_b emitted from a black body. An opaque object emits radiation according to $E_{obj} = \epsilon E_b$ where ϵ is the emissivity coefficient. The calibration function is $E_D(\lambda_c, T_{obj}) = E_{obj}(\lambda_c, T_{obj}) + E_{off}(\lambda_c)$ where λ_c is the wavelength, E_D is the number of counts measured by the 14-bit detector, E_{obj} is the number of counts that were emitted by the object and E_{off} accounts for the remainder of counts. Calibration constants within the E values take into account Planck's constant, and factors dependent on the environment and the experimental setup [113].

A radiometric temperature calibration is performed in situ with the IR window in place to implicitly capture the calibration constants [122]. To shield the camera from external reflections, the path between the camera and foil is surrounded by a matte black enclosure. To reduce the Narcissus effect, the features of the camera apart from the lens are covered with black felt material. Water from a Julabo F25 chiller is circulated through the channel at 5°C intervals. The calibrated temperature range reaches beyond the minimum and maximum temperatures experienced, such that operating temperatures remain well-approximated by a

low order fitted curve. Thermal equilibrium (monitored using the inlet, outlet, two air gap temperatures and counts readings) is reached within a maximum of 1 hour and 45 minutes. The air gap is found to take much longer to stabilise than the inlet and outlet temperatures. After sufficient time, the count value is determined by averaging over a 91×18 pixel area (reaching about 5 pixels from each wall) to reduce noise. The temperature value is taken using an average of the inlet and outlet temperatures over 10 seconds at 10 Hz. The polynomial fit of the temperature calibration – calculated using the Matlab functions `polyfit` and `polyval` – is depicted in Figure 4.11.

4.1.2.3 Experimental Procedure

To set up the test section, the painted foil is first aligned with the heater support, and clamped and tensioned using the tensioning system. The electrodes are inserted into the base and silver conductive grease applied. The base is raised up to the level of the foil using the lower aluminium support and adjustable profile. The gasket and channel plate are placed on top, and the test section is clamped. As before, deionised water is added to the flow loop through the reservoir and circulated for one hour through the degassing system. It is ensured that no air bubbles are contained with the channel test section. Finally, the apparatus is levelled with a spirit level to ensure 1-D conduction in the air gap (see Section 4.1.2).

As before, the steady component of flow rate is $Re_0 = 40$. The channel geometry is characterised for a pulsating flow with frequency $Wo = 1.76$ ($f = 0.1$ Hz). At higher frequencies, the amplitudes of the temperature oscillations are too small to measure reliably. Since local flow reversal may cause non-linear effects (see Section 2.2.2.3), a pulsation amplitude $Q_A/Q_0 = 0.7$ is used. Since the frame rate of the high-speed camera is 430.8 Hz (for the 320×256 image size), thermal images are recorded at all 20 phase values in one cycle. The small transverse temperature differences involved mean that the second derivative of temperature contains high noise, even when ensemble averaged over 1000 images. Hence, the FLIR ExaminIR software is set to capture a total number of just 2000 images, or 100 at each phase value. The pulsating flow rate is input using the Matlab GUI for the pump controller and the pump turned on. The power supply is also switched on, and the system allowed to reach the periodic steady state of thermal equilibrium. After this time, the pump

flow rate is quickly reset, such that the first trigger signal (and zeroth phase value of the sinusoidal pump flow rate) can be identified by the waiting data acquisition software. This first trigger signal is sent a number of cycles after the reset, to neglect behaviour during the rise time. The images are saved as a FLIR .sfmov movie file with the temperature in counts, and exported to Matlab for processing, as discussed in Section 4.2.2.

4.2 Experimental Analysis

The analytical theory described in Chapter 3 adheres to a number of physical approximations. For example, the flow is laminar, hydrodynamically- and thermally-developed, and buoyancy effects are neglected. In this section, the compliance of the experimental rigs (outlined in Section 4.1) with these simplifications is analysed, using experimental and numerical correlations, dimensionless numbers and a lumped analysis. Also, the techniques applied in processing, post-processing and analysis of the particle image velocimetry (PIV) and infrared thermography (IRT) data are detailed.

4.2.1 Velocity Data Analysis

Hydrodynamic Development While the channel is characterised experimentally to ensure flow development in Chapter 6, the topic is discussed theoretically for completeness. Correlations for flow development with a slope but no intercept, e.g. $L_e/D_h = 0.05Re$ [104], are insufficient since they fail to account for the effect of the axial diffusion term ($\propto \partial^2 u / \partial x^2$) in developing flow. Thus, Durst et al. [123] performed numerical simulations to determine the value of the coefficients $L_e/D_h = C_0 + C_1 Re$, giving a new correlation for the entry length in a channel:

$$L_e/D_h = [(0.631)^{1.6} + (0.0442Re_0)^{1.6}]^{1/1.6} \quad (4.1)$$

where L_e is the entrance length for a uniform inlet velocity in a plane channel. At the maximum Reynolds number experienced $Re_{max} = Re_0 + Re_A = 76$, this predicts an entry length $L_e = 24.7 \text{ mm}$. Furthermore, the entry length for pulsating pipe flow has been shown numerically to vary sinusoidally with an amplitude less than or equal to the steady flow value

[124]. At low frequencies, the amplitude of the entry length is equal to the steady flow value, while the amplitude reduces with increasing frequency. Theory cannot compensate for inlet and outlet geometry of the channel which likely elongates this region. The results of Moissis [125] and Maslen [126] indicate that secondary flows do not occur in fully-developed laminar flow in a rectangular channel.

Transition to Turbulence in Pulsating Flow The steady flow Reynolds number Re_{max} is significantly less than the critical value of 2300 that is found empirically [104]. Depending on the frequency and amplitude, pulsations may induce intermittent turbulent bursts, which occur for $Re_{\delta_v} = \langle u_A \rangle \delta_v / \nu > 500$ in oscillatory flow [127] (where Re_{δ_v} is the Reynolds number based on the Stokes layer thickness). The parameters of Table 4.2 correspond to $Re_{\delta_v} = 102.6, 45.9$ and 20.5 for $Wo = 1.4, 3.1$ and 7.0 , respectively.

4.2.1.1 Vector Field Processing

Vector Processing and Post-Processing An overview of the technical background of the particle image velocimetry (PIV) method is given by Raffel et al. [128]. The image pairs in .tif format are processed using TSI Insight's in-built processing algorithms. First, the intensities of the images are normalised to reduce effects of brightness. The window cross-correlations are generated using the fast Fourier transform (FFT) technique with peaks determined by three-point fitted Gaussian curves in two dimensions to achieve sub-pixel accuracy. A multi-step interrogation scheme is used to increase spatial resolution near the wall without significantly reducing the signal-to-noise ratio. The estimated displacements of 64×32 pixel samples are used to offset a Nyquist grid of 64×16 pixel interrogation windows with respect to each other during the second pass. In physical units, the initial window sizes correspond to 0.93×0.47 and $0.32 \times 0.16 \text{ mm}^2$ in the longer and shorter dimension, respectively. Between passes the data are scanned for outliers using median tests in local neighbourhoods of 3×3 vectors and failed vectors are replaced by either of two valid secondary peaks from the cross-correlation. Post-processing involves further local vector validation, similar to before though with a less strict failure criterion. A replacement scheme fills holes created by the validation step as well as those resulting from peaks below a signal to noise ratio of 1.5 with the mean of its local neighbourhood. The files are exported

as `.vec` files.

Further Processing The text contained in the `.vec` files is parsed in Matlab. A spatial calibration is performed for each of the camera and laser orientations shown in Figure 4.2. Using the steady flow images, the spatial calibration is performed by manually identifying the pixel values of the two opposing walls of the known channel width. The phase values are ensemble-averaged over their 100 image pairs, and reordered for the quickly pulsating flows that captured the complete set of phases out of sequence. The steady velocity profile measured in a separate test is subtracted from the pulsating distribution to give the oscillating velocity profile. Since PIV struggles to resolve vectors near to solid boundaries, the accurate vectors nearest the wall are analysed manually. The experimental values of the wall shear stress at the midpoint of the channel width are computed using the slope between the velocity vector nearest to the wall and the wall itself, introducing an error that grows as the boundary layer thins. With measurements taken to within 0.3 and 0.1 *mm* of walls $\hat{y} = [0, \hat{a}]$ and $\hat{z} = [0, \hat{b}]$ respectively, the displacements of the outermost data points amount to 1.8%, 4.1% and 9.1% of the Stokes layers in the \hat{y} dimension, and 0.6%, 1.4%, 3.0% and 4.3% in the \hat{z} direction for Womersley numbers of 1.4, 3.1, 7.0 and 9.9, respectively. This is a well-documented problem in fluid mechanics and is the main reason for the poor accuracy of many existing oscillating wall shear stress measurements. Hughes and How [57] have analysed the growth of this error with proximity to the wall in detail for pulsatile flows. Accordingly, the maximum errors in the experimental data tend to be experienced at the higher frequencies.

An analytical model of the pulsating flow is computed with the input flow rate given by the gear pump calibration of Figure 4.5(a). The number of nodes is chosen to match the window size of the PIV processing algorithms, such that the error may be calculated at each grid point. The oscillation of the velocity and wall shear stress with time relative to the fixed sinusoidal flow rate is inspected at each spatial node using Matlab's inbuilt function `fitnlm` that iterates from initial values to calculate the least squares fit of the data to a non-linear regression model of the form:

$$Y = f(X, B) + \varepsilon \quad (4.2)$$

where Y and X are the response and predictor matrices, B are the unknown parameters to be estimated, ε are the error terms with mean zero and variance σ^2 . The initial guesses are taken as the theoretical values for the amplitude and phase. This is similar to the method of Eckmann and Grotberg [51]. An R^2 value is calculated to evaluate the quality of the fit.

4.2.2 Thermal Data Analysis

Thermal Development and Transition to Turbulence The hydrodynamic entry length for the smaller channel at Re_{max} is $L_e = 11.5 \text{ mm}$ using Equation 4.1 [123]. The thermal entrance length is predicted using $Pr \cdot L_e = 64.3 \text{ mm}$, which is less than one quarter of the 300 mm heated length that is maintained upstream of the viewing window. Furthermore, theory predicts the shortest thermal entrance lengths occur for high aspect ratio channels [129]. The maximum Reynolds number, based on the Stokes layer thickness, is $Re_{\delta_v} = 81$, which is low enough that intermittent turbulent bursts do not occur [127].

Natural Convection The Grashof number is the ratio of buoyancy forces to viscous forces in the velocity boundary layer:

$$Gr = \frac{g\beta_f(T_w - T_f)D_h^3}{\nu^2} \quad (4.3)$$

where g is the acceleration due to gravity, β_f is the thermal expansion coefficient of the fluid and T_f is the fluid temperature. For $Gr/Re_0^2 \ll 1$, the effects of buoyancy are negligible [104]. Using the difference between the mean wall temperature and bulk temperature, the Grashof number is $Gr = 486.4$ and $Gr/Re_0^2 \approx 0.3$ such that a mixed convection flow develops in the channel. The effect of buoyancy is quantified in Chapter 8 using a numerical model.

Lumped Thermal Capacitance The Fourier number quantifies the rate of conduction relative to the rate of storage in the solid:

$$Fo = \frac{\alpha_s}{\omega \hat{w}_s^2} \quad (4.4)$$

where α_s is the thermal diffusivity of the foil and \hat{w}_s is the foil thickness. At large $Fo \gg 1$, the second derivative of the temperature profile in the solid is small and the temperature profile

can be approximated as linear. The parameters described in Section 4.1.2.3 correspond to a Fourier number in the foil of $Fo = 7211.7$. The Biot number quantifies the ratio of the temperature gradient in the solid to the temperature difference between the wall and fluid:

$$Bi = \frac{h\hat{w}_s}{k_w} \quad (4.5)$$

where k_w is the thermal conductivity of the wall and h is the convective heat transfer coefficient. If the Biot number is much less than unity, $Bi < 0.1$, the solid domain can be neglected and the problem becomes non-conjugate [104, 130]. A channel with a single isoflux-heated long wall approximates the H2(1L) boundary condition, described in Section 3.1.5. Using analytical theory, the steady Nusselt number for the channel is $Nu_0 = 4.55$ ($h_0 = 772.4 \text{ W/m}^2 \cdot \text{K}$), which corresponds to a Biot number $Bi = 0.002$. Hence, the lumped thermal capacitance method may be used to obtain accurate results, by assuming a uniform normal solid temperature at every instant. The time constants for the wall \hat{w}_s^2/α_s and paint \hat{w}_p^2/α_p are 0.2 ms and 11.5 ms , respectively, which are significantly lower than the time constant of the pulsations of 10 s .

4.2.2.1 Thermal Image Processing

The `.sfmtov` movie files are converted to a temperature array in 2-D space and time using Matlab. The spatial calibration is performed by manually identifying the pixel values of the two opposing walls of the known channel width. Correction of perspective distortion is not required since the camera is tilted (by 5°) in a plane that lengthens the channel width equally at all axial locations. The gain and offset are applied manually using the `.scg` and `.sco` files, and the bad pixels are accounted for using the `.sbp` file, which were saved during calibration (see Section 4.1.2.2). Since the files are exported in counts, the temperature in degrees Celsius is calculated manually using the polynomial equation of the fitted temperature curve in Figure 4.11. The data are ensemble-averaged over the 100 images of each phase and the time-averaged component subtracted, to determine the oscillating wall temperature. Due to end effects near the channel walls, the accurate readings near the wall are analysed manually. An analytical solution for the pulsating flow is calculated using the experimental parameters given in Section 4.1.2.3. The case for 1 heated long wall – the H2(1L) boundary

condition – is used, which assumes an infinitely thin wall. Similarly, a solution is found for a 1-D parallel plate channel [69] with non-thin Inconel 625 walls. The amplitude and phase of the experimental temperature oscillations at each node are determined using the `fitnlm` Matlab function as before, with the initial values input as the theoretical values given by the analytical solution. The heat generated by the foil and other modes of heat transfer are calculated as discussed in Section 4.2.2.2.

4.2.2.2 Element Energy Balance

The aim of the experimental setup of Section 4.1.2 is to minimise secondary losses, such that the convective heat transfer takes up a large proportion of the heat generated within the foil. In this section, the secondary terms such as lateral conduction, radiation and conduction in the air gap are calculated using an energy balance at each pixel.

A differential control volume for the foil and paint layer with dimensions $d\hat{x} \times d\hat{y} \times (\hat{w}_s + \hat{w}_p)$ is illustrated in Figure 4.13. Heat generated in the foil is transferred between bordering foil and paint elements by lateral conduction, to the fluid by forced convection and radiation, and to the air gap by 1-D conduction and radiation. The energy may also be used to increase the temperature of the foil. The pixels of the camera are square $d\hat{y} = d\hat{z}$. The change in the thermal conductivities with temperature is assumed negligible. The material thicknesses are assumed constant, with negligible contact resistance between the foil and paint layers [118, 131]. Using the conservation of energy with the notation introduced in Figure 4.13 [104, 120]:

$$\begin{aligned}
 & [\hat{q}_x]_s + [\hat{q}_y]_s + [\hat{q}_x]_p + [\hat{q}_y]_p + \hat{q}_{gen} d\hat{x} d\hat{y} \cdot \hat{w}_s - \\
 & \quad [\hat{q}_{x+dx}]_s - [\hat{q}_{y+dy}]_s - [\hat{q}_{x+dx}]_p - [\hat{q}_{y+dy}]_p - \\
 & \quad \hat{q}_{conv} d\hat{x} d\hat{y} - \hat{q}_{cond} d\hat{x} d\hat{y} - \hat{q}_{rad} d\hat{x} d\hat{y} - \hat{q}_{cap} d\hat{x} d\hat{y} = 0 \quad (4.6)
 \end{aligned}$$

where subscripts s and p denote the foil and paint layers respectively, \hat{q}_{gen} is the heat generated per unit volume, \hat{q}_{conv} is the convective heat flux to the fluid, \hat{q}_{cond} is the heat flux to the air gap, \hat{q}_{rad} is the radiative heat flux to the surroundings from the foil and paint, and \hat{q}_{cap}

is the heat storage. The terms in square brackets are in Watts. Using Fourier's law of heat conduction $\hat{q}_x = -k \cdot \hat{w} \cdot d\hat{y}(\partial T/\partial \hat{x})$ and $\hat{q}_y = -k \cdot \hat{w} \cdot d\hat{x}(\partial T/\partial \hat{y})$ for the differential conduction terms in the foil and paint, Equation 4.6 becomes:

$$\hat{q}_{gen} = \hat{q}_{conv} + \hat{q}_{cap} + \hat{q}_{cond} + \hat{q}_{rad} - (k_s \hat{w}_s + k_p \hat{w}_p) \left(\frac{\partial^2 T}{\partial \hat{x}^2} + \frac{\partial^2 T}{\partial \hat{y}^2} \right) \quad (4.7)$$

where the last term corresponds to lateral conduction in the foil and paint layers \hat{q}_{lc} . The quantities of Equation 4.7 describe the pulsating (i.e. time-average plus time-dependent) heat fluxes. The equation may be time-averaged to give:

$$\hat{q}_{gen,0} = \hat{q}_{conv,0} + \hat{q}_{cond,0} + \hat{q}_{rad,0} + \hat{q}_{lc,0} \quad (4.8)$$

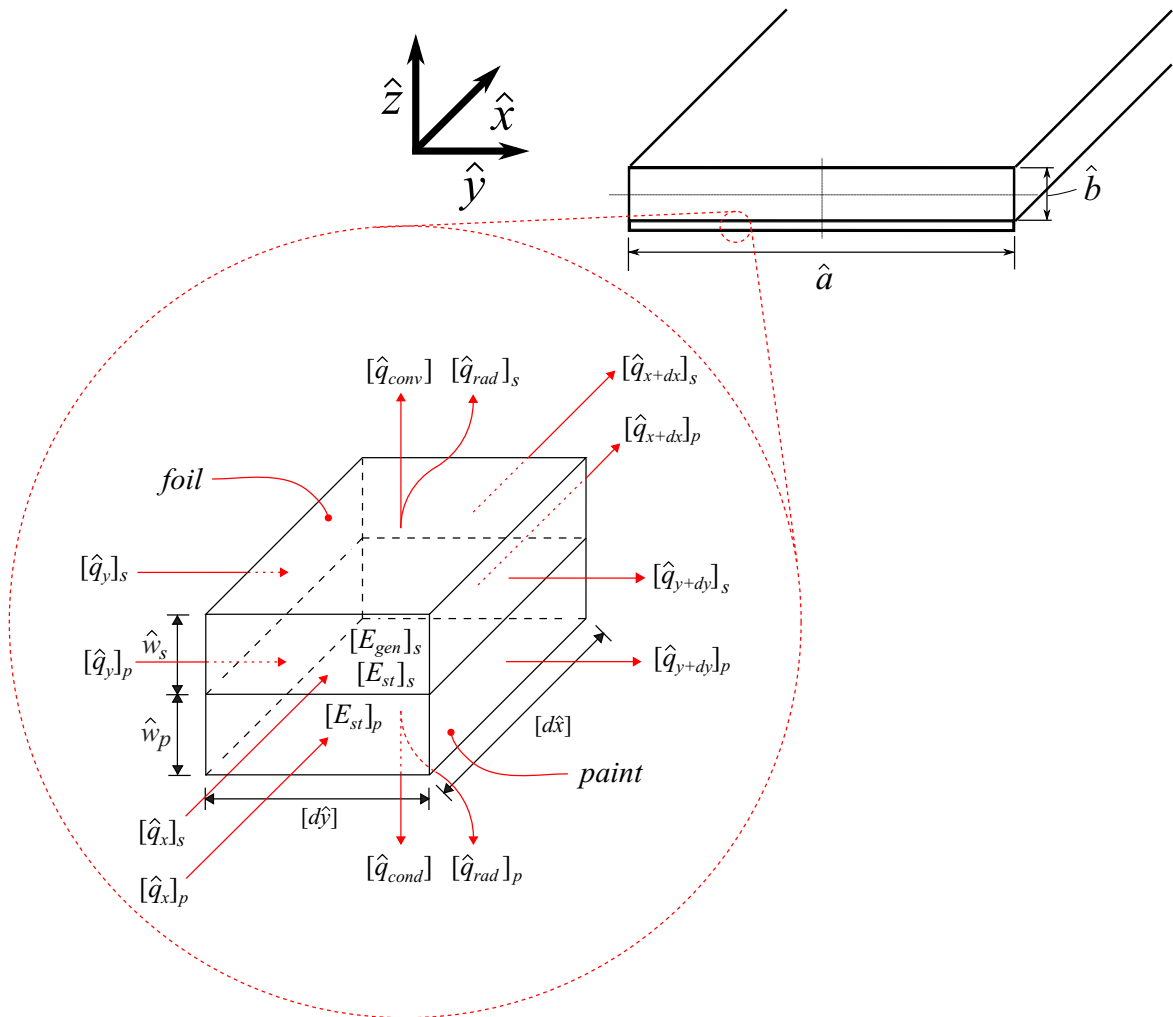


Figure 4.13: Energy balance in a single heater element with surface area $d\hat{x} \times d\hat{y}$ with foil and paint thickness, \hat{w}_f and \hat{w}_p .

where the time-average of the capacitive term is zero. The time-dependent relation is:

$$0 = \hat{q}''_{conv} + \hat{q}''_{cap} + \hat{q}''_{cond} + \hat{q}''_{rad} + \hat{q}''_{lc} \quad (4.9)$$

where the heat generation is assumed uniform in time, and the oscillating components are calculated by subtracting the mean components from the pulsating components. The convention is used that heat flow out of an element has positive sign. Hence, the generated heat in the foil is removed by forced convection of the flow, but heat transfer by lateral conduction, heat storage, conduction in the air gap and radiation must be accounted for. The space-averaged values of the steady components and the amplitudes of the fluctuating components are summarised in Table 4.7 for each of the terms in the energy balance. According to analytical theory [99, 100], thick walls should alter the steady component of the temperature profile in a rectangular channel due to augmented lateral conduction in the solid. The effect on the steady wall temperature profile in the \hat{y} direction is illustrated graphically in Figure 3.3 for aspect ratios $\hat{b}/\hat{a} = 1, 2$ and 5 , where the experimental geometry corresponds to $K = 0.42$. It is expected that a thick wall affects the oscillating temperature profiles less significantly, since the fluctuating component of the lateral conduction is smaller, has a time-average of zero and thus cannot establish itself fully before conditions are reversed. Hence, the fluctuating components – which should resemble the analytical solutions of Chapter 3 more closely – are of primary concern. Nonetheless, the trends observed in the steady components should remain qualitatively similar to the theoretical steady components.

Table 4.7: Heat fluxes of the steady components $\langle \hat{q}_0 \rangle$ and the amplitudes of oscillating components $\langle \hat{q}_A \rangle$ for terms in the energy balance (Equation 4.7), averaged over channel width.

$[W/m^2]$	$\langle \hat{q}_0 \rangle$	$\langle \hat{q}_A \rangle$
\hat{q}_{gen}	2334.8	0
\hat{q}_{lc}	-60.7	5.2
\hat{q}_{cap}	0	27.3
\hat{q}_{cond}	-15.3	-0.8
\hat{q}_{rad}	61.6	2.5

Heat Generated Assuming that electrical energy generation is uniform in the foil, the heat generated by Joule heating in each element is:

$$\hat{q}_{gen} = \frac{I^2 R}{L_s \hat{a}} \quad (4.10)$$

where I and R are the current through and resistance across the foil, and L_s is the length of the foil in the axial direction. The resistance of the foil is determined using the electrical resistivity as $R = \tilde{\rho}_s W_s / (L_s \hat{w}_s)$ where $\tilde{\rho}_s$ is the electrical resistivity of the foil, W_s is the heated length of the foil in the transverse direction and $L_s \hat{w}_s$ is the cross-sectional area of the foil in the \hat{y} dimension. As illustrated by Figure 4.7, the heated transverse length W_s is between 21 mm (the distance between the sharp tips of the electrodes) and 31 mm (which includes an added 5 mm length at either side where the foil contacts the flat surface of the electrodes through electrically conductive grease). The resultant heat flux generation varies over 1581.6 - 2334.8 W/m². Since the heat supplied to the fluid, calculated using the inlet and outlet temperatures measured by thermocouples is 2380.6 W/m², the higher estimate is used.

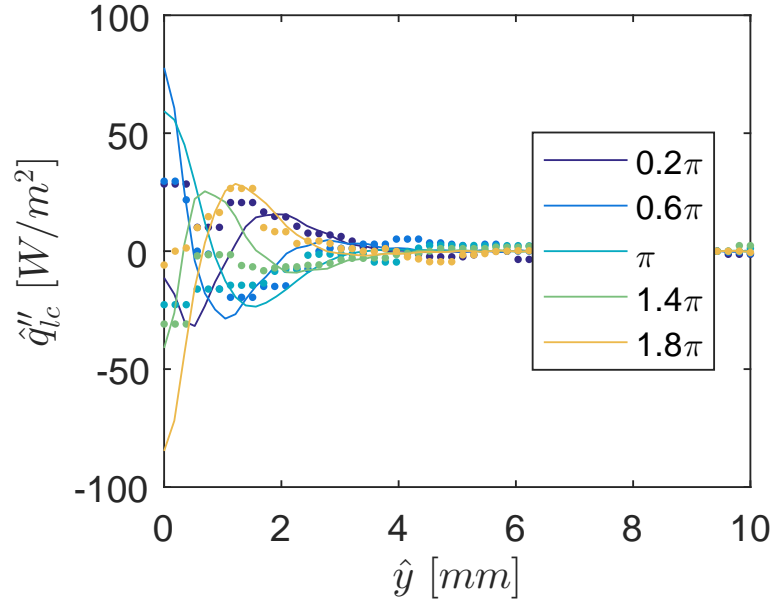


Figure 4.14: Oscillating lateral conduction term \hat{q}''_{lc} for $Wo = 1.76$, $Q_A/Q_0 = 0.7$. Solid lines and markers represent analytical solution (—) and experimental measurements (●), respectively.

Lateral Conduction The Péclet number $Pe = Pr \cdot Re_0 = 224$ measures the ratio of advective and diffusive transport rate. For $Pe > 100$, it should be possible to neglect axial conduction in the fluid and wall ($\propto \partial^2 T / \partial \hat{x}^2$) [91]. Mosyak [117] found that axial heat conduction was less than 0.5% of that normal to the wall for a thin stainless steel wall. From

the thermal data, it is found that the $\partial^2 T / \partial \hat{x}^2$ component is less than 10% of the $\partial^2 T / \partial \hat{y}^2$ component and can be neglected. The lateral conduction becomes:

$$\hat{q}_{lc} = (k_s \hat{w}_s + k_p \hat{w}_p) \cdot \frac{\partial^2 T}{\partial \hat{y}^2} \quad (4.11)$$

where the material properties of the foil and paint are presented in Table 4.4. The second derivative is calculated by using Matlab's `gradient` function twice. Since noise in the data may be amplified through differentiation, filtering procedures are often used [113]. In the current work, a median filter is applied using the `medfilt2` function before each numerical differentiation. While the analytical solution of Chapter 3 does not account for lateral conduction in the wall, Figure 4.14 compares the results to the second derivative of the temperature field at the wall $\partial^2 T_w'' / \partial \hat{y}^2$ according to theory. The space-averaged amplitude of the fluctuating component of the lateral conduction term is $\langle \hat{q}_{lc,A} \rangle = 5.2 \text{ W/m}^2$. The lateral conduction in the paint layer comprises only 0.4% of the total. The measurements follow theory quite well up to about 1 mm from the side wall. While not shown, the steady component is approximately zero and flat over the range $2 \leq \hat{y} \leq 18 \text{ mm}$ in agreement with theory. However, the term becomes highly negative near the corners $\hat{q}_{lc,0} = -600 \text{ W/m}^2$, indicating that heat is flowing into this region, in opposition with theory. This may be due to end effects or heat leakage from the electrodes. As a result the space-averaged value over the channel width is -60.7 W/m^2 , or about 2.6% of the generated heat flux.

Heat Storage Since the flow is pulsating, the $\partial T / \partial \hat{t}$ is non-zero and heat storage must be considered:

$$\hat{q}_{cap}'' = -(\rho_s c_{p,s} \hat{w}_s + \rho_p c_{p,p} \hat{w}_p) \cdot \frac{\partial T}{\partial \hat{t}} \quad (4.12)$$

According to Section 3.3, the rate of change of the temperature is $\partial T / \partial \hat{t} = \Re[i\omega \psi_T e^{i\omega \hat{t}}]$ (where the i acts only to move the phase forward by 90°), as plotted by the solid lines in Figure 4.15. Similarly, the experimental temperature measurements are multiplied by the angular frequency and phase shifted to give the experimental values, plotted by the markers. The overshoots and inflection points observed in the experimental and theoretical heat storage profile are found to be characteristically similar, although discrepancies exist in the local

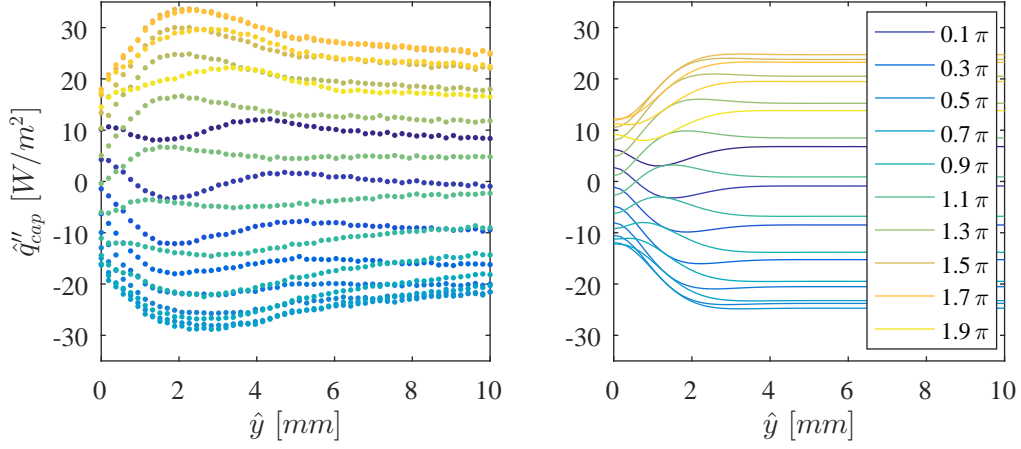


Figure 4.15: Oscillating capacitance term \hat{q}''_{cap} for $Wo = 1.76$, $Q_A/Q_0 = 0.7$. Solid lines and markers represent analytical solution (—) and experimental measurements (●), respectively. While all 20 phase values are plotted, the legend only identifies 10 for brevity.

amplitudes of oscillation near the corners. The space-averaged amplitude of the capacitance term is 27.3 W/m^2 , or 1.1% of the generated heat flux. Heat storage in the paint layer comprises only 29.2% of the total.

Heat Losses to Air Gap The design of the air gap enclosed by the sapphire window is to create stagnant air which insulates the foil at the rear side. No circulation occurs in a cavity heated directly from above and the mode of heat transfer is 1-D conduction [132]. This results in a temperature that varies linearly in \hat{z} , and according to the temperature distribution of the foil in \hat{x} and \hat{y} . Fourier's law in \hat{z} gives:

$$\hat{q}_{cond} = -k_a \frac{dT}{d\hat{z}} \quad (4.13)$$

where k_a is the thermal conductivity of air and $dT/d\hat{z}$ is the linear temperature gradient normal to the foil. The air gap temperatures are measured using a pair of thermocouples located 13.5 mm from the heater in the 15 mm high air gap (the holes were drilled by a CNC machine). Figure 4.16 plots the fluctuating component of the 1-D conduction term, which has the same shape as the oscillatory temperature profile and a space-averaged amplitude of $\langle \hat{q}_{cond,A} \rangle = -0.8 \text{ W/m}^2$. The space-averaged value of the steady conduction term is $\langle \hat{q}_{cond,0} \rangle = -15.3 \text{ W/m}^2$, which is about 0.7% of the generated heat flux. If the heated surface contains any vertical component, a thermal boundary layer forms and the temperature

field is no longer 1-D. The resultant change in heat transfer is dependent on the Rayleigh number, which measures the ratio of conductive and convective heat transfer for natural convection flows:

$$Ra = \frac{g\beta_a(T_w - T_a)L_c^3}{\nu_a\alpha_a} \quad (4.14)$$

where β_a , ν_a , α_a and T_a are the thermal expansion coefficient, kinematic viscosity, thermal diffusivity and temperature of air respectively, and L_c is a characteristic length. It has been calculated that a 1° offset causes a 3% change of the air-side Nusselt number compared to the pure conduction case [132], and hence the channel was levelled using a spirit level prior to testing. The negative value of \hat{q}_{cond} indicates that heat flows from the air gap into the foil, due to heat leakage from the electrodes (which are at about 60°C). Correlations typically exist for cavities heated at a single wall, with natural convection occurring for $Ra > 1708$ for the isothermal boundary condition. Using the channel half-width as the characteristic length (with symmetry assumed at the mid-plane) and the temperature difference between the electrodes and the mean air gap temperature, a Rayleigh number $Ra = 1625$ is estimated. Nonetheless, even large changes in the mode of heat transfer by 2-D effects or natural convection appear to contribute negligibly relative to the generated heat flux.

Radiation Losses Planck's law gives the spectral distribution of radiation intensity emitted from a black body E_b . An opaque object emits radiation according to $E_{obj} = \varepsilon E_b$ where ε is the emissivity coefficient. While radiation emitted from the foil in the 3 – 5 μm wavelength range is measured by the thermal camera, radiation is in fact emitted over the entire spectral range. The radiation losses at longer wavelengths are accounted for by the radiation losses term \hat{q}_{rad} . Inconel 625 has a low emissivity (about 14% that of the paint). Furthermore, the mean temperature of the unheated walls of the channel is about 3° lower than the mean heated wall temperature, according to theory. Hence, radiation from the water side is assumed negligible. Radiative losses on the air side are approximated as:

$$\hat{q}_{rad} = \varepsilon_p \sigma (T_w^4 - T_\infty^4) \quad (4.15)$$

where ε_p is the emissivity of the paint, σ is the Stefan-Boltzman constant, T_w is the foil and

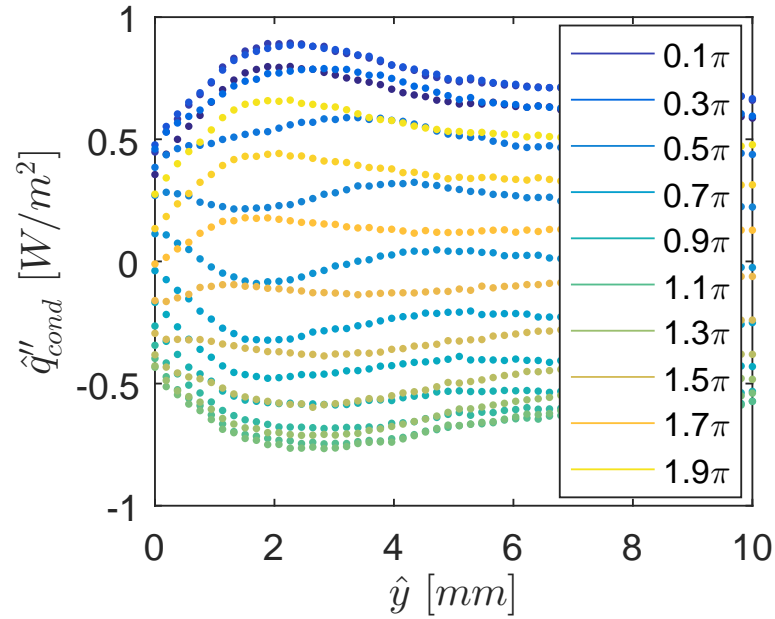


Figure 4.16: Oscillating conduction term \hat{q}''_{cond} for $Wo = 1.76$, $Q_A/Q_0 = 0.7$. Markers represent experimental measurements (\bullet). While all 20 phase values are plotted, the legend only identifies 10 for brevity.

paint temperature and T_∞ is the temperature of the surrounding walls, assumed to be at the ambient air temperature. The fluctuating component of the radiation term (plotted in Figure

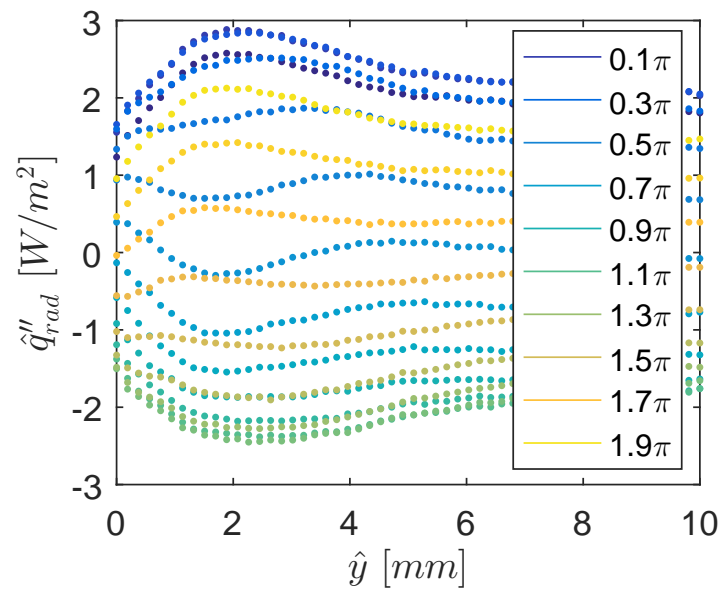


Figure 4.17: Oscillating radiation term \hat{q}''_{rad} for $Wo = 1.76$, $Q_A/Q_0 = 0.7$. Markers represent experimental measurements (\bullet). While all 20 phase values are plotted, the legend only identifies 10 for brevity.

4.17) has a spatially-averaged amplitude of $\langle \hat{q}_{rad,A} \rangle = 2.5 \text{ W/m}^2$. The steady component has $\langle \hat{q}_{rad,0} \rangle = 61.6 \text{ W/m}^2$, which constitutes about 2.6% of the generated heat flux.

4.3 Experimental Uncertainty

As discussed in Chapter 1, the fundamental aim of the current research is to perform complementary experimental, analytical and numerical analyses of the velocity and temperature fields. The experiments – with high time expense – are used to verify the theoretical models at certain points of the parameter space, with behaviour of the entire domain validated using the cheaper simulations. The aim of this section is to quantify the accuracy of the analytical model for parameters that have been both measured and modelled, using the analytical theory and experimental characterisation established in Chapter 3 and Section 4.1. Currently, quantifying the quality of the predictions in interpolated or extrapolated regions is an unresolved research area [133]. The continual advances in computing power and numerical solution algorithms have lead numerical simulations to replace a substantial amount of experimentation in thermo-fluids engineering. Nonetheless, experiment remains paramount as the most robust technique of model validation.

4.3.1 Uncertainty of Velocity Measurements

The ISO guide [134] designates two distinct types of uncertainty analysis: (i) a type A analysis estimates uncertainty by using statistical techniques on measurements such as calibration data, and (ii) a type B uncertainty analysis uses alternative techniques such as analytical modelling of the flow and its boundary conditions. As discussed below, the multitude of optical and algorithmic parameters from the initial illumination of the particle to the final analysis of the processed displacement vector greatly complicates the error analysis of the PIV measurement technique. An A-type analysis of PIV uncertainty may involve acquiring actual PIV images of a pattern of dots mounted on a translation stage that are displaced according to a known profile [135], while B-type analyses involve the generation of synthetic PIV images. Alternatively, approximate methods based on algorithms are commonly used. For example, the latest versions of Insight 4G software (unfortunately not available to the author) base their

uncertainty analysis on its correlation with image quality, or specifically, with the relative height of the secondary peak to the primary peak [136]. After many decades of research, no unified standard exists for the quantification of PIV measurement uncertainty. The following sections discuss the attempts to minimise measurement uncertainty using the general design rules for PIV developed by Keane and Adrian [137, 138], and the makeup of the components of the error between the experimental measurements and the analytical solution.

4.3.1.1 PIV Uncertainty

To illustrate the complexity of the problem, consider the popular method that uses synthetic PIV data, with the predictions compared to theory or experimental data. All parameters may be controlled to study their influence on the measurement error, which varies both locally and instantaneously. The particles are approximated as Gaussian distributions of intensity, where the magnitude of the peak is a function of the scattering efficiency of the particle and the location within the thick light sheet (which also has Gaussian intensity profile). The parameter space includes variables associated with image generation (the particle image diameter, seeding density and background noise), the underlying flow (the particle image displacement, velocity gradients, accelerations, 3-D velocity components and path curvatures), and interrogation parameters (such as the sample window size, spacing and offset). Even this substantial set of parameters often fails to capture realistic optical setups, with the errors predicted by the numerical models smaller than those experienced for real PIV images. Raffel et al. [128] have overviewed the measurement uncertainty of the major parameters using Monte Carlo simulations. The majority of the error between the true displacement and the measured displacement results from estimation of the correlation peak with sub-pixel accuracy, and the presence of velocity gradients within a single interrogation window [135].

Particle Image Diameter The particle image diameter is dependent on characteristics of the optical setup such as the camera pixel size and the size of the seeding particles, which are detailed in Section 4.1.1. Simulations show that error in velocity measurements is strongly dependent on the diameters of particle images [139]. The optimal particles have a diameter of the order of 2-3 pixels to achieve sub-pixel accuracy of peak estimators. For small particle

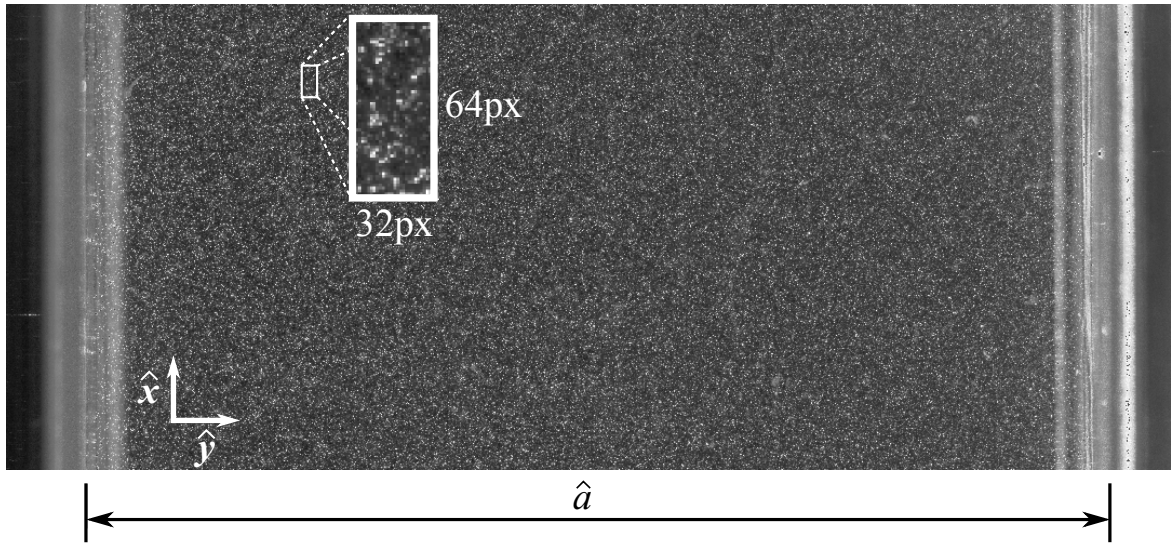


Figure 4.18: Raw PIV image over channel width illustrating particle image diameter of 2-3 pixels and particle image density of 30 per window.

images, the displacements become biased towards integer values in an effect known as peak-locking. This constitutes a systematic error predominantly caused by the sub-pixel peak estimator. Above the optimum, the uncertainty increases linearly with increasing diameter. The inset of Figure 4.18 shows a 64×32 pixel interrogation window where the particles have the optimal diameter size of between 2 and 3 pixels.

Particle Image Shift Uncertainty is approximately constant, except for displacements below 0.5 pixels where it decreases linearly. This behaviour has been observed by experiment [135] and confirmed by theory [140]. To exploit this phenomenon, the image is sampled over two interrogation windows that are offset according to the mean displacement vector, as discussed in Section 4.2.1.1. This greatly reduces the measurement uncertainty, as well as improving the detectability of correlation peaks such that a higher number of particle matches is achieved [138]. Common multi-grid PIV algorithms are typically found to have a displacement error of about ± 0.1 pixels [141].

Particle Image Density Increasing particle image density acts to (i) increase the probability of valid displacement detection and (ii) influence the measurement uncertainty directly by increasing the signal strength of the correlation peak. Keane and Adrian [138] showed that the success of image pairing is dependent on the particle image density, and the levels of

in-plane and out-of-plane displacement, as captured by the product $N_I F_I F_O$, where N_I is the effective particle image pair density in the interrogation window, F_I is a factor expressing the in-plane loss of pairs and F_O is a factor expressing the out-of-plane loss of pairs. The window offsetting technique minimises the loss of pairs in-plane, i.e. $F_I \rightarrow 1$. Furthermore, $F_O \rightarrow 1$ since the flow is unidirectional and the optical setup has been aligned with the channel axes. When $N_I F_I F_O > 8$, a 95% probability of valid detection is achieved [138]¹. The inset of Figure 4.18 indicates that about 30 particles are contained in a 64×32 interrogation window.

Displacement Gradients Displacement gradients present within an interrogation window (which is represented by a single displacement vector) cause bias in the data, since particle images in the first window disappear in the second even if the windows are offset according to the mean displacement. It is found that small interrogation windows permit higher displacement gradients (see Figure 4.19), since the spread of the correlation window scales linearly with the size of the interrogation window. In the current setup, the interrogation windows are large in the axial direction, since the flow is fully-developed and contains no velocity gradients. In the transverse dimension, the maximum displacement gradient of the data is about 0.11 pixels/pixel very near the wall. Using Figure 4.19, this corresponds to an

¹This is true for double exposure/single frame PIV, and the number is less for single exposure/double frame. Furthermore, high particle image densities (e.g. $N_I = 20$) reduce the measurement uncertainty in the presence of displacement gradients, as shown in Figure 4.19. The current PIV system uses double exposure/double frame.

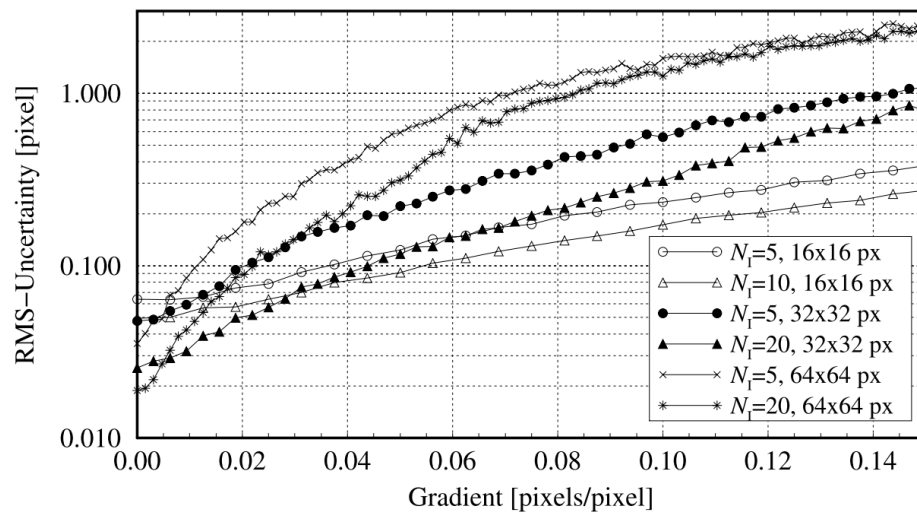


Figure 4.19: Uncertainty as a function of displacement gradient with varying particle image density and window size for a 2 pixel diameter particle size.

RMS-Uncertainty of 0.3 pixels for the 32 pixel width of the window.

4.3.1.2 Verification and Validation Method

PIV is an advanced measurement technique capable of measuring complex velocity fields – to which an analytical solution may not be known – with high spatial and temporal resolution. In contrast, the current research studies the intricate coupling of local time-dependent temperature and velocity fields of a less complex flow (e.g. laminar, unidirectional) to a level that is perhaps not possible with more complex flow fields. The need to perform vector processing on an artificial 3-D model containing a light sheet and particles is precluded, since an exact solution to the velocity field – and hence the error compared to theory – are already known.

The concepts involved with the verification and validation (V&V) technique – an actual ASME standard [142] – were originally developed for estimating the error of CFD simulations using experimental measurements [143]. The verification step involves the analysis of numerical accuracy, while the validation step assesses how accurately the model represents the real world. Of course, both the experimental measurements and model contain errors, and a simultaneous verification is in action. The technique is equally valid for estimating the experimental error from the analytical solution. Following the method and notation of Coleman and Steele [133], the validation comparison error:

$$E = S - D \quad (4.16)$$

is the difference between the analytical solution value S and the experimental measurement D . The errors in the solution δ_S and measurement δ_D values are:

$$\delta_S = S - T \quad (4.17a)$$

$$\delta_D = D - T \quad (4.17b)$$

where T is the true value. The validation error is the amalgamation of the model and experiment errors:

$$E = (T + \delta_S) - (T + \delta_D) = \delta_S - \delta_D \quad (4.18)$$

The δ_D term contains errors due to the experimental setup and processing, while δ_S consists of errors due to modelling assumptions δ_{model} , uncertainties in the input parameters δ_{input} and inaccuracies associating with the numerical calculation δ_{num} of the solution in Matlab:

$$\delta_S = \delta_{model} + \delta_{num} + \delta_{input} \quad (4.19)$$

While both δ_{input} and δ_D concern errors of the experimental instrumentation, the values are independent since the experiment measures the velocity directly. Equations 4.18 and 4.19 give:

$$E = \delta_{model} + \delta_{num} + \delta_{input} - \delta_D \quad (4.20)$$

where the terms on the right hand side are systematic errors. The standard uncertainties of the errors u estimate the standard deviations of the parent populations that the errors δ originate from. The total uncertainty u_{tot} is an estimate of the standard deviation of the parent distribution of combined errors. Assuming that the errors are independent:

$$u_{tot} = \sqrt{u_{model}^2 + u_{num}^2 + u_{input}^2 + u_D^2} \quad (4.21)$$

The expanded uncertainty is given by:

$$U = t_{95}u \quad (4.22)$$

where the interval $\pm U$ contains the true value to a given level of confidence. Typically a 95% confidence interval is used in accordance with Kim et al. [144]. t_{95} is determined using the student's t-distribution for $N - 2$ degrees of freedom using the Matlab function `tinv`. Since each local instantaneous velocity vector is ensemble averaged over 100 images, $t_{95} \approx 2$. The aim is to quantify the error between the velocity measured by experiments \hat{u}_D and the analytical velocity \hat{u}_S . From Equation 1b, the functional dependence of the analytical solution

is:

$$\hat{u}_S = f(Q, \omega, \hat{a}, \hat{b}, \rho_f, \nu) \quad (4.23)$$

where the applied flow rate Q is used to calculate the pressure gradient $\nabla \hat{p}$. The variation in ρ_f and ν may reasonably be assumed negligible. The expanded uncertainty of the input parameters U_{input} , which derive from the use of experimental conditions as inputs to the model, may be determined using the Taylor series method (TSM) for the propagation of uncertainties. Assuming that the input variables of Equation 4.23 are independent:

$$U_{input}^2 = \left(\frac{\partial \hat{u}_S}{\partial Q}\right)^2 U_Q^2 + \left(\frac{\partial \hat{u}_S}{\partial \omega}\right)^2 U_\omega^2 + \left(\frac{\partial \hat{u}_S}{\partial \hat{a}}\right)^2 U_{\hat{a}}^2 + \left(\frac{\partial \hat{u}_S}{\partial \hat{b}}\right)^2 U_{\hat{b}}^2 + \left(\frac{\partial \hat{u}_S}{\partial \rho_f}\right)^2 U_{\rho_f}^2 + \left(\frac{\partial \hat{u}_S}{\partial \nu}\right)^2 U_\nu^2 \quad (4.24)$$

The derivatives are calculated using the numerical forward finite-difference approach, for example:

$$\frac{\partial \hat{u}_S}{\partial Q} \approx \frac{\Delta \hat{u}_S}{\Delta Q} \approx \frac{\hat{u}_{Q+\Delta Q} - \hat{u}_Q}{\Delta Q} \quad (4.25)$$

For pulsations with $Q_A/Q_0 = 0.9$ and $Re_0 = 40$, the gear pump speed varies in the range 283 – 5368 *rpm*. The ± 3 *rpm* accuracy of the pump rotational speed corresponds to about 1% of the lowest value. Furthermore, the gear pump is calibrated for steady flow rates using an ultrasonic flow meter, accurate to $\pm 1\%$. The variation in angular frequency ultimately derives from the accuracy of the timing in Matlab. A `timer` object executes at defined intervals; however, the time was found to be overly sensitive to factors such as the busyness of the operating system. Hence, `tic` and `toc` are used to record the time that has elapsed since the last execution of the timer callback. From Matlab 2006b onwards, the `tic` and `toc` functions use a clock with a frequency of 10^6 *Hz* such that the resolution is 0.000001 *s* [145]. The shortest time between phase intervals is 0.1 *s* for a pulsation frequency of 0.5 *Hz*. Errors of 1% are assumed for the remainder of the parameters.

The expanded uncertainty due to the input parameters is calculated at $U_{input} = \pm 0.07$ *mm/s*. While the equations are solved analytically, the numerical uncertainty of calculating the first 100 terms of the solution has been estimated at 0.8% in the velocity at the duct

centre at the mid-dimensions such that $U_{num} = 0.01 \text{ mm/s}$. There is no robust method of quantifying δ_{model} , other than estimating the other terms in Equation 4.20 [133]. Furthermore, the evaluation of the experimental error δ_D is difficult without performing an extensive parametric analysis using synthetic PIV images. Hence, the experimental measurements give an indication of the accuracy of model assumptions and approximations in addition to the analytical theory giving an estimate of experimental uncertainty. Since the model is analytical rather than numerical, and the model assumptions (discussed in Section 4.2.1 of the experimental analysis) are reasonable, it is likely that the majority of the discrepancy between experiment and theory is due to experimental uncertainty. In Chapter 6, the relative error E/S of the velocity amplitude distributions values (see Figure 6.5) – calculated using the regression algorithm described in Section 4.2 – are within 5% at $Wo = 1.4$ and 3.1 and within 10% at $Wo = 7.0$.

4.3.2 Uncertainty in Temperature Measurements

Subsequent to the in-situ temperature calibration (see Figure 4.11), the regression model is used in place of original data, since it essentially models the relationship between the mean values of temperature T and counts X . The uncertainty of the curve fit between counts and temperature must be determined to indicate the confidence interval. Analogous to Equation 4.38, the standard error of regression estimates the standard deviation of the T_i measurements for no uncertainty in the X_i values:

$$s_T^* = \left[\frac{\sum_{i=1}^N (T_i - T)^2}{N - 4} \right]^{1/2} \quad (4.26)$$

where N is the number of temperature measurements and T is the value of the fitted curve at a given value of X . The 4 in the denominator owes to the loss of four degrees of freedom in evaluating the third order polynomial fit constants. The expanded uncertainty is (see Equation 7.17 of [133]):

$$U_T = t_{95} \left[s_T^2 \left(\frac{1}{N} + \frac{(X - \bar{X})^2}{s_{XX}} \right) \right]^{1/2} \quad (4.27)$$

where \bar{X} is the sample mean of N measurements X_i :

$$\bar{X} = \frac{1}{N} \sum_{i=1}^N X_i \quad (4.28)$$

and the term in brackets is analogous to standard uncertainty (see Equation 4.22) with:

$$s_{XX} = \sum_{i=1}^N X_i^2 - \frac{(\sum_{i=1}^N X_i)^2}{N} \quad (4.29)$$

Using Equation 4.27, it is found that the uncertainty of the fit is approximately constant over the temperature range 20 – 40°C with $U_T = \pm 0.04$ K. The analytical solution for dimensional temperature contains more input parameters. From Equations 3.4, 3.18, 3.24 and 3.25 of Chapter 3, the functional dependence is:

$$T_S = f(Q, \omega, \hat{a}, \hat{b}, \hat{q}, c, Pr, k_f) \quad (4.30)$$

where c is the fraction of the perimeter that is heated. Furthermore, the experimental uncertainty is generally higher for the thermal parameters. Neglecting errors in the heated length of the perimeter, the uncertainty in the generated heat flux is 5.1% due to accumulation of uncertainty in the variables in Equation 4.10. Also, the uncertainty in \hat{b} is higher, since the gasket contributes to the channel height. Thermophysical properties are approximated as constant, introducing an error of a few percent in the heat transfer coefficient for an unsteady liquid flow with a wall-bulk temperature differential of the order of tens of degrees [30]. The maximum value of expanded uncertainty of the input parameters over the channel cross-section is calculated at $U_{input} = \pm 0.033$ °C, which is about 17% of the mean temperature amplitude. The analytical solutions for temperature contain two more summations that greatly increases the computation time, since `for` loops are implemented in the Matlab code. Incidentally, it might be possible to vectorise the calculations to reduce the computational expense in future. As a result, only the first 30 terms of each of the infinite sums are included, which has been estimated to introduce an error of 0.00028 °C. For a 201 × 101 grid, the steady and oscillating temperature profiles take 7.8 and 170.9 minutes to calculate, respectively. Equation 4.20 may be rearranged to determine the uncertainty associated with the analytical model:

$$\delta_{model} = E - (\delta_{num} + \delta_{input} - \delta_D) \quad (4.31)$$

where δ_{model} results from assumptions made in the model derivation. A greater number of approximations have been made in solution of the energy equation in comparison with the assumptions made in the solution of the momentum equation, as discussed in Section 4.2.2 of the experimental analysis. For example, the Grashof number of the experimental setup indicates that a degree of mixed convection occurs. The validation uncertainty of the model is:

$$u_{val} = \sqrt{u_{num}^2 + u_{input}^2 + u_D^2} \quad (4.32)$$

where δ_{model} falls within the interval $E \pm u_{val}$.

4.3.3 Uncertainty in Heat Flux

From the energy equation (Equation 4.7), the expanded uncertainty in the convective heat flux is:

$$U_{\hat{q}_{conv}} = [(U_{\hat{q}_{gen}})^2 + (U_{\hat{q}_{lc}})^2 + (U_{\hat{q}_{cond}})^2 + (U_{\hat{q}_{rad}})^2]^{1/2} \quad (4.33)$$

where the uncertainty of each of the heat flux components on the right hand side is determined using the Taylor series method for the propagation of uncertainty (similar to Equation 4.24) on a pixel by pixel basis. The second derivative of the lateral conduction term is computed using the `gradient` function twice, which uses the central difference method (for interior data points). The subsequent operations may be combined into a single step as:

$$\hat{q}_{lc,s,j} \approx -(k_s \hat{w}_s) \cdot \left(\frac{T_{j+2} - 2T_j + T_{j-2}}{4\Delta y^2} \right) \quad (4.34)$$

where $\hat{q}_{lc,s,j}$ is the lateral conduction at node j and Δy is the pixel size. Using the TSM:

$$\begin{aligned}
 U_{\hat{q}_{lc,s,j}}^2 &= \left(\frac{\partial \hat{q}_{lc,s,j}}{\partial T_{j+2}} \right)^2 U_{\bar{T}}^2 + \left(\frac{\partial \hat{q}_{lc,s,j}}{\partial T_j} \right)^2 U_{\bar{T}}^2 + \left(\frac{\partial \hat{q}_{lc,s,j}}{\partial T_{j-2}} \right)^2 U_{\bar{T}}^2 \\
 &+ \left(\frac{\partial \hat{q}_{lc,s,j}}{\partial k_s} \right)^2 U_{k_s}^2 + \left(\frac{\partial \hat{q}_{lc,s,j}}{\partial \hat{w}_s} \right)^2 U_{\hat{w}_s}^2 + \left(\frac{\partial \hat{q}_{lc,s,j}}{\partial \Delta y} \right)^2 U_{\Delta y}^2 \\
 &+ \rho_2 \left(\frac{\partial \hat{q}_{lc,s,j}}{\partial T_{j+2}} \right) \left(\frac{\partial \hat{q}_{lc,s,j}}{\partial T_j} \right) U_{\bar{T}}^2 + \rho_2 \left(\frac{\partial \hat{q}_{lc,s,j}}{\partial T_j} \right) \left(\frac{\partial \hat{q}_{lc,s,j}}{\partial T_{j-2}} \right) U_{\bar{T}}^2 \\
 &+ \rho_4 \left(\frac{\partial \hat{q}_{lc,s,j}}{\partial T_{j+2}} \right) \left(\frac{\partial \hat{q}_{lc,s,j}}{\partial T_{j-2}} \right) U_{\bar{T}}^2
 \end{aligned} \tag{4.35}$$

where the final three terms account for the correlated systematic error of the nearby pixels that are used to compute a single value of the second derivative. As is typical, the correlation between the random errors of each pixel are assumed to be zero. The cross-correlation ρ_n between samples separated by a number of pixels n is [146, 147]:

$$\rho_n = \frac{\gamma_n}{s_T^2} \tag{4.36}$$

where γ_n is the cross-covariance:

$$\gamma_n = \frac{\sum_{i=1}^N (T_j - \bar{T})(T_{j+n} - \bar{T})}{N - 1} \tag{4.37}$$

and s_T^2 is the variance, or the square of the standard deviation of the sample distribution:

$$s_T = \left[\frac{\sum_{i=1}^N (T_j - \bar{T})^2}{N - 1} \right]^{1/2} \tag{4.38}$$

While the heat storage term contains a derivative with respect to time, the value is determined according to the harmonic nature of temperature (see Section 4.2.2.2) rather than temperature at two subsequent time steps. Hence, an auto-correlation term ρ_λ^* – which determines the amount of correlation between samples measured with time interval λ – is not included. The degree of auto-correlation should be considered during a temperature calibration, since it determines the optimal sampling rate. Subsequent samples become statistically independent with a time step greater than the integral time scale:

$$t^* = \int_0^\infty \rho_\lambda^* d\lambda \tag{4.39}$$

The integral time scale is estimated at 1.4 s, using steady flow data (where samples have been taken at 10 Hz).

Table 4.8 presents the maximum values of the expanded uncertainty of the heat flux components in the energy balance. While the uncertainty of the temperature measurements U_T is low, the error accumulates in determination of the lateral conduction term, as demonstrated by Equation 4.35. Interestingly, the correlation terms are found to reduce the uncertainty. The applied median filters are found to substantially reduce the maximum error of the noisy second derivative of the temperature data. This noise is a consequence of the small overall temperature difference (≈ 3 °C) between the wall and bulk fluid, compared to studies on bubble impacts, sliding bubbles and electrospray cooling [114, 115, 116].

Table 4.8: Expanded uncertainty U of measured heat flux components.

<i>Heat flux component</i>	U [W/m ²]
<i>Heat generated, \hat{q}_{gen}</i>	± 76.81
<i>Lateral conduction, \hat{q}_{lc}</i>	± 32.99
<i>Heat storage, \hat{q}_{cap}</i>	± 2.41
<i>Conduction losses, \hat{q}_{cond}</i>	± 0.22
<i>Radiation losses, \hat{q}_{rad}</i>	± 0.57
<i>Convective heat flux, \hat{q}_{conv}</i>	± 83.65

Chapter 5

Numerical Methods

The novel thermo-fluidic solution presented in Chapter 3 adds to the short list of known analytical solutions to the energy equation. Solutions obtained using exact techniques are continuous in space and time, independent of the nodes and time steps at which values are computed. As a result, mesh independency analyses are not required and divergence is not encountered. Furthermore, the relationships between the governing parameters are explicitly identified by the equations for the solved parameters. However, while solutions including the effects of lateral wall conduction in steady flow in a rectangular channel [99, 100], of natural convection in a vertical rectangular duct [148], and of the dissipation of kinetic energy (or viscous heating) in a parallel plate channel [149] have been found, known solutions are generally limited to simpler geometries with non-linear terms excluded. In contrast, solutions using numerical techniques accommodate a greater complexity of flows.

While complementary experimental and analytical treatments offer a robust verification of underlying theory, measurements in two spatial dimensions (over which velocity and wall shear stress are non-constant) and time require high amounts of raw data and computational processing power. Furthermore, pulsations become increasingly difficult to generate at high frequencies and measurement of the velocity gradients in the thin Stokes layer become increasingly inaccurate. Hence, a numerical CFD model is developed – offering complete information of the flow field – to verify analytical theory in the parameter space that is difficult to measure. Also, the numerical model will test the validity of assumptions made during solution of the momentum and energy equations, by solving the governing equations

without some of the contentious prior assumptions. The author is indebted to a colleague, Dr. Sajad Alimohammadi, for performing the CFD simulations contained within this thesis, over an extensive range of flow conditions that were not possible with the current analytical model. Alimohammadi et al. [150, 151] have previously modelled the convective heat transfer of steady, pulsating and synthetic jets. In future, it is hoped that the numerical model can be used to investigate the entry region as well as more complex geometries and flow conditions, having been validated by the analytical solution in the overlapping parameter space. Hence, the numerical model comprises a final vital component of the theoretical infrastructure of this research.

5.1 Geometry and Boundary Conditions

While the analytical model of Chapter 3 is hydrodynamically- and thermally-developed (and hence two-dimensional), the numerical model requires a 3-D geometry, as depicted in Figure 5.1. The flow is prescribed as laminar and incompressible, with fluid properties independent of temperature. The boundary conditions of no-slip and constant heat flux are imposed at the wall, and a spatially-uniform time-dependent velocity is applied at the inlet. To reduce convergence times, a pulsating cosinusoidal flow rate is used, rather than a fixed sinusoidal flow rate. To ensure that the flow is fully-developed and devoid of end effects, the transverse velocity and temperature profiles are typically tested at the mid-length of the channel.

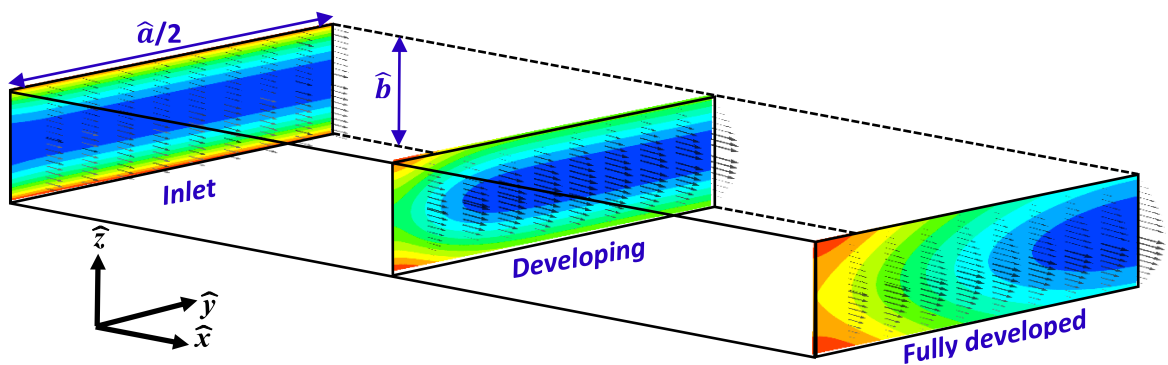


Figure 5.1: Schematic of the 3-D numerical model for Case 2 (two isoflux heated long walls). Contours and vectors depict the temperature and velocity fields, respectively.

Cases 1 and 2: Large Adiabatic and Heated Channels The first and second case studies use a rectangular channel cross-section with dimensions matching the experimental channel of the hydrodynamic test facility of Section 4.1.1.1. To permit comparison to a parallel plate geometry, the flow is heated at the two longer walls with symmetry assumed at the channel mid-planes. This also acts to increase computational efficiency by reducing the domain to one quarter of its original size. The length of the channel is 900 mm , such that the pulsating and oscillating behaviour of the axial temperature profiles can be analysed (in Chapter 7). To shorten the thermal development length, the fluid parameters are tailored to give a Prandtl number $Pr = 1$. Finally, viscous heating and buoyancy effects are precluded, though the former has been found to have no effect on the results.

Case 3: Small Heated Channel The third case uses a rectangular channel cross-section with dimensions $20\text{ mm wide} \times 2\text{ mm}$ with heat applied at a single wall, replicating the experimental conditions of the thermal test facility (see Section 4.1.2.1). Symmetry is assumed at the mid-channel width, while the flow is non-symmetrical in the z dimension. Since realistic fluid properties of water are used (see Table 4.5), the length of the channel is 4 m to allow thermal development. Also, it has been found qualitatively that a single heated wall requires a longer entry length. Solutions are found with and without natural convection and lateral conduction in the heated wall, as described in Section 5.3.

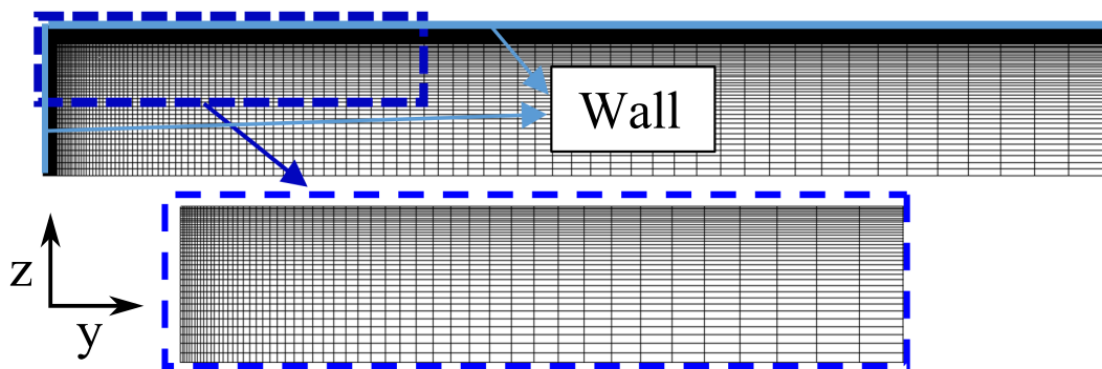


Figure 5.2: Structured non-uniform mesh with 140×75 nodes.

5.2 Solver Settings

While the parametric inputs and raw outputs of the model have been designed and processed by the author, no interaction with the CFD software itself was undertaken. For this reason, only a brief overview of the numerical solver settings is provided. The commercial CFD package ANSYS CFX 17.1 is employed to solve the governing equations numerically, using an element-based finite volume solution method [152]. A structured hexahedral mesh is used to maintain alignment with the principal channel axes. By performing a comprehensive mesh independency analysis with various grid densities ($5e4$, $1e5$, $5e5$, $1e6$, $2e6$, and $5e6$), it is found that a mesh with $140 \times 75 \times 50$ nodes provides a grid-independent solution (for Case 1). Due to high velocity gradients in the Stokes layer at high Wo , the mesh is refined in the near-wall region (to a minimum of 0.005 mm from the short wall and 0.002 mm from the long wall), as depicted in Figure 5.2. An inlet velocity is assigned by a user defined function (UDF) to define a FORTRAN based routine which integrates the sinusoidal velocity signal into the CFD model. Second order upwind discretisation schemes are used for a stable convergence. With respect to time, a second order backward Euler scheme is used to minimise the discretisation error in time which would otherwise tend to numerically diffuse steep temporal gradients. The explicit Eulerian method used here demands the maximum value of the Courant number – the characteristic flow speed ($\hat{u}\Delta\hat{t}/\Delta\hat{x}$) – to be less than 1. Accordingly, the time-step $\Delta\hat{t}$ or the number of iterations per cycle $n = 1/f\Delta\hat{t}$ are selected at certain values to attain the correct result. Theoretically speaking, this assures that the flow of data through each time step of the unsteady simulation is not propagating through more than one grid cell, guaranteeing stable convergence in the whole computational domain. The convergence criteria are 10^{-7} for the equations in the steady simulation and 10^{-5} for the unsteady cases. The unsteady simulations are considered periodic when the RMS deviations of the time-averaged velocity and pressure values between two successive cycles do not exceed 0.1%. This occurs after about 5 full cycles of flow pulsation subject to the frequency of pulsation.

5.3 Numerical Procedure

Initially, a numerical model with a 2-D geometry with matching hydraulic diameter is validated using the known analytical solutions for a parallel plate channel. For the extended 3-D geometry, the pulsation frequency and amplitude parameters match those of the respective analytical models. Each case study is run for a steady flow with $Re_0 = 40$ and for a pulsating flow with parameters described by Tables 5.1, 5.2 and 5.3. Chapter 6 presents the local time-dependent hydrodynamic parameters of the large adiabatic channel (Case 1) over the parameter space of Table 5.1. Chapter 7 presents the local time-dependent thermal parameters of the large heated channel (Case 2) over the parameter space of Table 5.2. Chapter 8 presents the local time-dependent thermal parameters of the small heated channel (Case 3) for a single frequency and amplitude. The effects of natural convection and lateral conduction in the heated wall are studied according to Table 5.3.

Table 5.1: Numerical parameter space for large adiabatic channel (Case 1) of Chapter 6.

Wo	0.1	0.3	0.7	1.4	3.1	7	9.9	19.8	31.3	54.2
Q_A/Q_0	0.9									

Table 5.2: Numerical parameter space for large heated channel (Case 2) of Chapter 7.

Wo	1.4	3.1	7	22.1
Q_A/Q_0	0.7			
A_0	8.77	1.75	0.35	0.035
Buoyancy	X			
Lateral wall conduction	X			

Table 5.3: Numerical parameter space for the small heated channel (Case 3) of Chapter 8.

Wo	1.76	
Q_A/Q_0	0.7	
A_0	5.39	
Buoyancy	X	✓
Lateral wall conduction	X	X

5.4 Numerical Analysis

The numerical model outputs velocity, wall shear stress, and temperature profiles as a three-dimensional arrays $\hat{y} \times \hat{z} \times \hat{t}$ in `.mat` format. The axial temperature gradient at the wall and centre of the channel are output as $\hat{x} \times \hat{t}$, and the pressure gradient is output as a vector with $1 \times \hat{t}$. After importing the files to Matlab for processing, the data are manually phase-shifted from the fixed cosinusoidal flow rate to a sinusoidal flow rate. The oscillatory component may be independently generated using the analytical equations, based on the rotational speed of the gear pump. In contrast, the steady component is subtracted from numerical pulsating values. The amplitude and phase values at each grid point are determined using `fitnlm`, similar to Chapter 4. Parameters such as displacement, mean wall shear stress, acceleration, viscous and inertial stresses, bulk temperature, mean temperature and time-averaged Nusselt number are calculated using numerical techniques. The parameters may also be non-dimensionalised. Finally, the hydrodynamic and thermal parameters are compared to the analytical model and experimental measurements on a local time-dependent basis.

Chapter 6

Hydrodynamics of Laminar Pulsatile Flow in a Rectangular Channel

6.1 Introduction

Chapters 6, 7 and 8 set out to resolve the primary aim of this thesis outlined in Chapter 1: to analyse the heat transfer enhancement potential of a hydrodynamically- and thermally-developed sinusoidally-pulsating flow in an empty rectangular channel. The current chapter describes a comprehensive parametric analysis of the hydrodynamics of the flow using particle image velocimetry (PIV) measurements, CFD simulations and novel representations of the analytical solutions, which conveniently decompose parameters into amplitude and phase values relative to a prescribed flow rate. Chapter 7 analyses the mechanisms of heat transfer enhancement using idealised analytical and numerical models. Chapter 8 aims to verify the local time-dependent behaviour of the models using infrared thermography (IRT) measurements, by accounting for the more realistic effects of lateral conduction, radiation and natural convection.

The interdependence of wall shear stress and heat transfer has remained underdeveloped in the literature for the case of fully-developed unsteady flow in an enclosed vessel. While Reynolds analogy does not hold in an enclosed vessel, the governing mechanical and energy equations are of a similar form (see Equations 3.1a and 3.1b). Specifically, heat and momentum are diffused in the same manner, with kinematic viscosity analogous to thermal

diffusivity. To elucidate their relationship, the wall shear stresses should be analysed on a local instantaneous basis, and coupled with spatially- and temporally-varying heat fluxes. The thermal problem is intrinsically dependent on the hydrodynamic problem, since the energy equation takes the velocity field as an input (see 3.5b). Hence, it is useful to decouple the local time-dependent parameters to study the underlying mechanisms of the velocity field independently.

It is clear from the literature review of Section 2.1 that the number of existing studies for the rectangular channel geometry is inadequate. While many of the mechanisms bear similarities to those of pipe flow, some of the geometrical features are unique to the rectangular channel. For example, the velocity profile contains two dimensions and the wall shear stress is non-uniform at the perimeter. The contributions of viscous and inertial stresses may differ owing to the corner regions, and hence the critical points of transition between the quasi-steady, intermediate and inertia-dominated regimes may occur at different frequencies. Also, a non-unity aspect ratio is likely to affect the relative magnitudes of wall shear stress at each wall, and the behaviour of the near-wall overshoot and flow reversal. Although an analytical solution exists [31], it is less mature than the corresponding pipe flow representations, where the parameters have been conveniently decomposed into amplitude and phase values relative to a prescribed flow rate. Using a pair of values rather than a single instantaneous value may give further insight into the evolution of underlying physical mechanisms and the transition between frequency-dependent regimes. Furthermore, the 2-D theory has not been subject to the same comprehensive parametric analyses, which describe the intricate relationships of pressure gradient, velocity and wall shear stress in the parameter space. For example, the frequency-dependent behaviour of the wall shear stress has not been studied satisfactorily. Confirmatory experimental works have verified the 1-D theory over much of the parameter space (however, the quality and quantity of wall shear stress measurements are relatively poor). Conversely, the velocity field of an incompressible pulsating or oscillating flow in a rectangular channel has not been measured experimentally, to the best of the author's knowledge. The unavailability of data likely owes to the extra dimension, which squares the requisite raw data and computational processing expense. In contrast, heat transfer studies in channel heat sink geometries are relatively common. This apparent gap between the thermal results and the underlying mechanics of the fluid flow means that a coupled thermo-fluidic

analysis should not proceed prior to experimental verification of the velocity field.

The new representations of the 2-D analytical solution – developed in Section 3.2 – warrant a comprehensive parametric analysis. In particular, the decomposition of parameters in terms of amplitude and phase values may give insights into the evolution of physical mechanisms. The aims of the current chapter are thus to characterise pulsating channel flow hydrodynamics to form a basis for subsequent heat transfer studies, using (i) novel representations of the analytical solution for the hydrodynamics parameters in a rectangular channel, (ii) particle image velocimetry (PIV) measurements, and (iii) numerical CFD simulations.

6.2 Parametric Analysis of Flow Hydrodynamics

The amplitudes of the flow rate, acceleration and wall shear stress parameters are directly proportional to the driving pressure gradients in the laminar flow regime, as illustrated by Figure 6.1. Hence, the characteristic behaviour of oscillatory flow is determined solely by the frequency parameter, and a constant flow rate amplitude is used during the parametric analysis. The local behaviour is compared with experimental measurements at three distinct frequencies ($Wo = 1.4, 3.1$ and 7.0). For completeness, pulsations with a very high Womersley number $Wo = 31.3$ ($f = 10$ Hz), which are unachievable with the gear pump pulsator, are studied analytically and numerically. The frequency-dependent behaviour is compared with experimental measurements at four distinct frequencies ($Wo = 1.4, 3.1, 7.0$ and 9.9) and with the numerical solution at ten frequencies over the range $0.1 \leq Wo \leq 54.2$ (see Table 5.1). While the modification of behaviour with channel aspect ratio is beyond the scope of this thesis, the trends have generally been found to be representative of rectangular geometries as a whole.

6.2.1 Velocity Profiles

Characterisation of the velocity field establishes a foundation from which to develop the theory of underlying physical mechanisms in Section 6.2.1.2. Furthermore, the wall shear stress and x -momentum balance terms of Sections 6.2.2 and 6.2.3, respectively, derive from

the velocity field.

The PIV measurements of velocity profiles of steady flows typical of microchannels with $10 \leq Re_0 \leq 80$ are depicted graphically by the symbols of Figure 6.2. To illustrate hydrodynamic development, the velocity profiles in the \hat{y} dimension are plotted at axial distances $\hat{x} = 330, 335, 340, 345$ and 350 mm . The agreement between the constant flow rate measurements and the analytical solution affirms that the flow approaches its asymptotic state prior to measurement. Hence, hydrodynamic development is confirmed beyond the maximum Reynolds number of the tested parameter space. Figure 6.3 presents the velocity profiles normalised by the mean velocity in the channel, indicating that the flow field is independent of Reynolds number in the range considered, although the lowest flow rate contains a larger relative error. The steady component used for the unsteady tests is described by the curves at $Re_0 = 40$. The steady component plays a subsidiary role – assuming that it is not high enough to trigger turbulence – and only the oscillating components of the flow are considered (except in the case of local flow reversal).

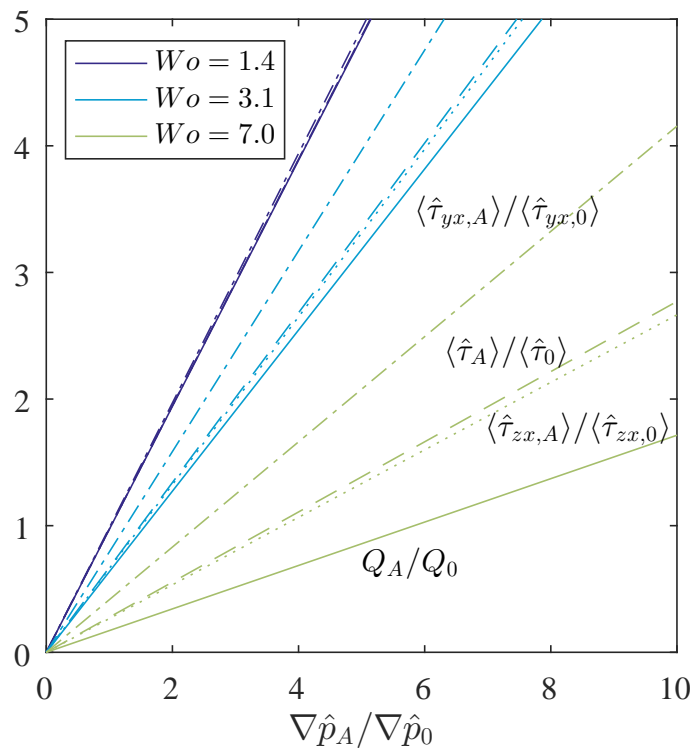


Figure 6.1: Amplitudes of flow rate (—), mean wall shear stress over long walls (···), short walls (·—) and whole perimeter (—) with pressure gradient amplitude.

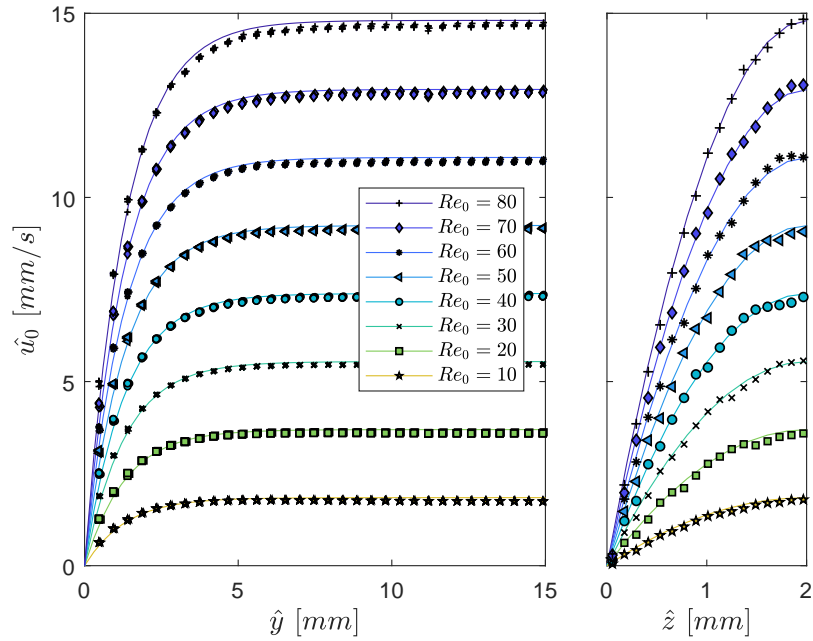


Figure 6.2: Steady velocity profiles for $Re_0 = 10 - 80$. Solid lines and symbols represent analytical solutions and experimental measurements respectively. To illustrate hydrodynamic development, velocity profiles in the \hat{y} dimension are plotted at axial distances $\hat{x} = 330, 335, 340, 345$ and 350 mm.

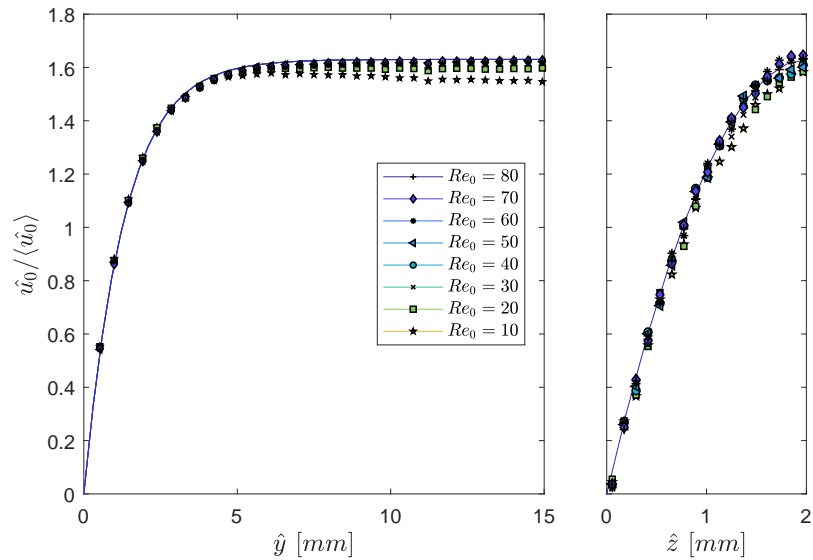


Figure 6.3: Steady velocity profiles normalised by the mean channel velocity for $Re_0 = 10 - 80$. Solid lines and symbols represent analytical solutions and experimental measurements respectively.

Figure 6.4 presents the phase-averaged experimental velocity measurements across two bisecting planes of the channel cross-section. The data are shown to accurately recover the distinct frequency-dependent features of the formerly-unverified analytical solutions

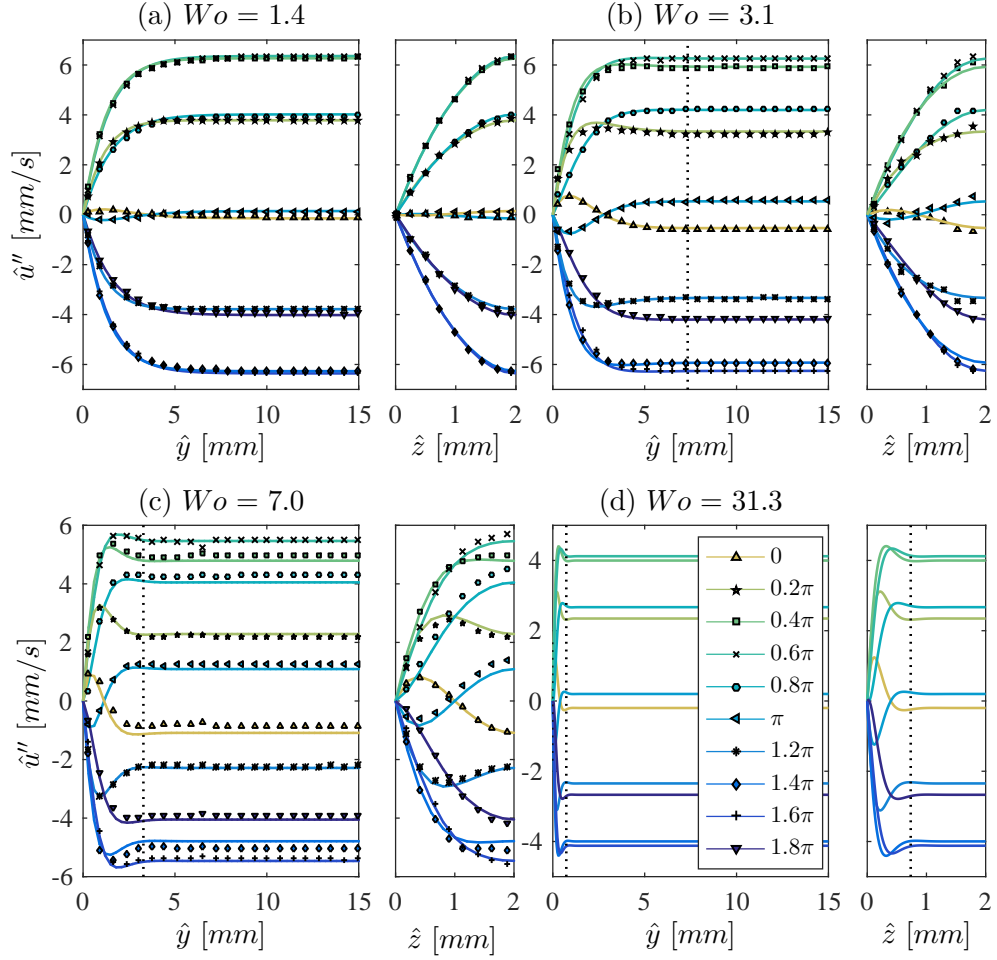


Figure 6.4: Oscillating velocity profiles for $Q_A/Q_0 = 0.9$ and (a) $Wo = 1.4$, (b) $Wo = 3.1$, (c) $Wo = 7.0$, (d) $Wo = 31.3$. Solid lines and symbols represent analytical solutions and experimental measurements respectively. Dotted lines mark the Stokes layer thickness $\hat{\delta}_v$.

(Equation 1a), which include inflection points and overshoots that result from the interplay between viscous and inertial stresses (discussed in Section 6.2.1.2). While not shown the velocity profiles generated by the numerical solution are in excellent agreement. The low and high frequencies depicted typify the limiting cases of unsteadiness where the profiles are quasi-steady and plug-like, respectively. The intermediate transition regime ($Wo = 3.1$ and 7.0) is perhaps most interesting, containing a relatively diverse range of unique velocity profiles.

The velocity data may alternatively be expressed in terms of local amplitude and phase values, as accommodated by the complex representation (see Equation 3.16). With oscillating magnitudes normalised by the local values of the steady flow component, such representa-

tions are useful for characterising the degree of unsteadiness in a quantitative and compact manner. Furthermore, decomposition may give further insight into the origin and evolution of distinguishing inertial features. Figure 6.5 shows that the regressed experimental amplitudes capture theoretical behaviour well, with magnitudes generally within about 5% of theoretical predictions based on the flow rate of the gear pump. The \hat{z} values at $Wo = 7.0$ are slightly

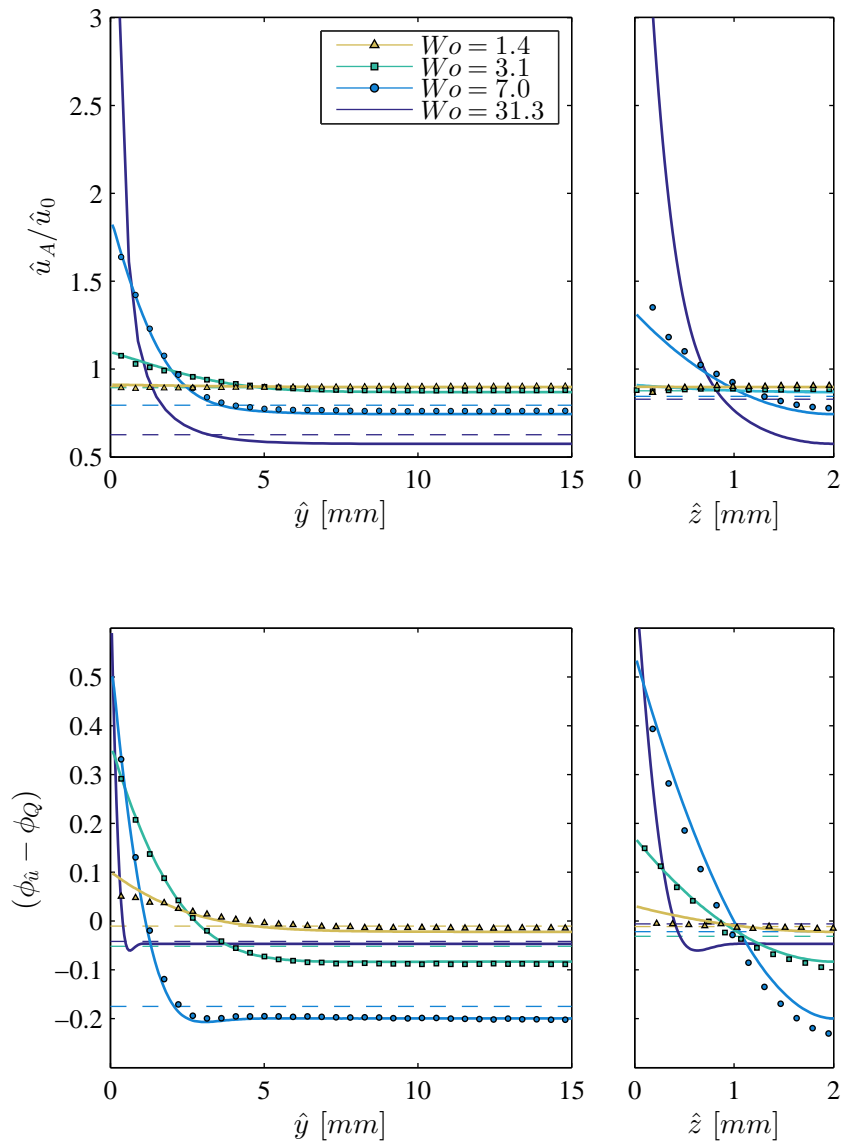


Figure 6.5: Velocity amplitude and phase profiles for $Q_A/Q_0 = 0.9$. Solid lines and symbols represent analytical solutions and experimental measurements respectively. Dashed lines plot the bulk mean values.

less accurate, deviating by a maximum of 10% from the analytical solution. As expected, the uncertainty is highest in the near-wall region where the displacement gradient is high (see Figure 4.19). The measured phase values are universally within 0.05 radians (3°) of rotation. The mean R^2 value of the fitted sine waves at each node of each frequency is 0.9978. The near-constant amplitude distribution $\hat{u}_A/\hat{u}_0 \approx 0.9$ exemplifies the quasi-steady nature of the low-frequency flow; however, some unsteady effects are observable in the near-wall region as demonstrated by the non-constant phase distribution. This positive phase shift constitutes the origin of a near-wall velocity overshoot, described in detail in Section 6.2.1.2. The phase of the outer annuli and main body are seen to vary even further with the development of an inviscid region. At $Wo = 7.0$, the bulk mean phase of the \hat{y} velocity profile at the mid-channel height lags behind the mean flow rate by 0.18 radians as marked by the lowermost dashed line of Figure 6.5. With complete inertial dominance ($Wo = 31.3$), the fluid is largely in phase but for a very narrow region near the wall. The amplitude increases further near the walls as the flow behaves largely as an irrotational plug.

6.2.1.1 Local Flow Reversal

Local flow reversal occurs in regions $\hat{u}_A/\hat{u}_0 > 1$ of Figure 6.5. At $Wo = 7.0$, inertial effects dictate near-wall behaviour and the flow is intermittently reversed near the entire perimeter, despite a mean flow rate that never drops below zero. The features of flow reversal are reasonably complex, and details such as its location, magnitude and duration have been derived analytically in a pipe and parallel plate channel by Haddad et al. [56]. That study also distinguished between wall-attached-reversal and off-wall reversal, a phenomenon of pulsatile flow alone that results from superpositioning steady and oscillating velocity distributions. This unusual profile containing a double inflection point is measured experimentally for the first time at 1.7π in Figure 6.6. In a two-dimensional channel with high aspect ratio, the feature seems only to appear near walls $\hat{y} = [0, \hat{a}]$. In fact, flow reversal is more prevalent near the shorter walls as a whole, due to the shallower near-wall gradients of the steady component in this dimension. For example, reversal occurs at lower frequencies and has a larger amplitude. At $Wo = 3.1$, Figure 6.5 indicates that local flow reversal occurs near $\hat{y} = 0$ but not near $\hat{z} = 0$. At $Wo = 7.0$, reversal occurs near both walls; however, it begins sooner

and ends later near the short wall (with a duration about twice as long). For example, Figure 6.6 indicates that the flow is reversed in the \hat{y} profile but not the \hat{z} profile at 1.6π .

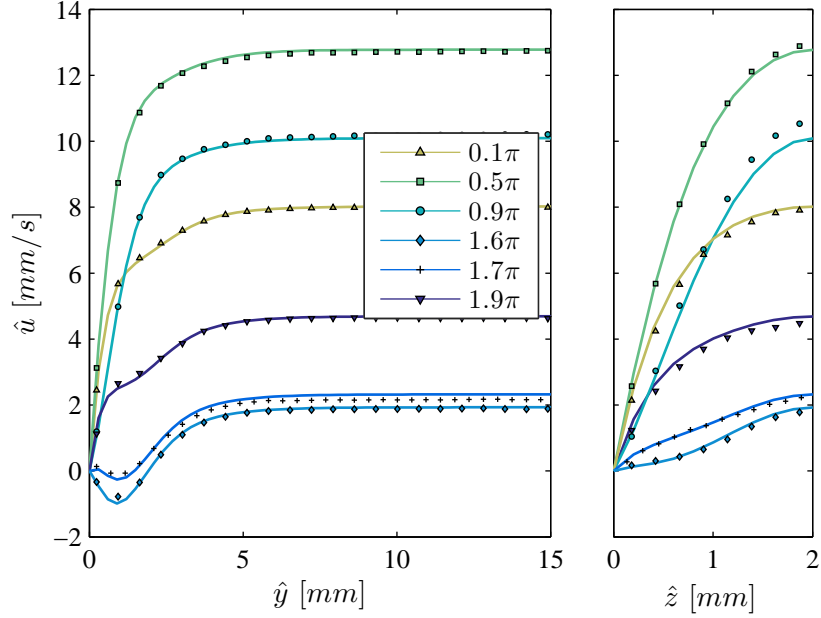


Figure 6.6: Pulsating velocity profiles for $Q_A/Q_0 = 0.9$ and $Wo = 7.0$. Solid lines and symbols represent analytical solutions and experimental measurements respectively.

In heat transfer applications, local flow reversal will act to carry hot fluid in the direction of the channel entrance, altering the temperature difference and heat flux. However, this potentially undesirable outcome emanates from augmented near-wall velocity amplitudes and local flow rates, which may also enhance heat removal from the walls of the channel. Furthermore, a mean steady flow component could easily be tailored to prevent negative flow. Even very slowly oscillating flows have been shown to display unsteady attributes in the above analysis and thermal behaviour is likely to be affected.

6.2.1.2 Vorticity and the Velocity Overshoot Mechanism

The velocity overshoot mechanism may be studied using the local stress balance given by the time-dependent Navier-Stokes equation. The local accelerations are:

$$\frac{\partial \hat{u}''}{\partial \hat{t}} = \nu \left(\frac{\partial^2 \hat{u}''}{\partial \hat{y}^2} + \frac{\partial^2 \hat{u}''}{\partial \hat{z}^2} \right) - \frac{1}{\rho_f} \nabla \hat{p}'' \quad (6.1)$$

where the viscous Laplacian term describes the local vorticity flow. The acceleration at a point is proportional to the sum of the local instantaneous viscous and pressure stress distributions. Over the period of one cycle, vorticity diffuses a finite distance before being annulled by vorticity with opposing sign. This is in contrast to steady flow, where the entire duct is consumed by viscous effects. The thickness is well-approximated by the distance at which fluid elements experience 1% of the effects of viscous diffusion in Stokes flow, since momentum is diffused perpendicular to the walls and vorticity source strength is uniform at the perimeter of the channel (see Section 3.1.2). For $Wo = 1.4, 3.1$ and 7.0 , the Stokes layer thicknesses are $16.4, 7.3$ and 3.3 mm , respectively (marked by dotted lines in Figure 6.4). Hence, the Stokes layer may be either all-encompassing or negligible, dependent on the frequency parameter. For the slowly oscillating flow, viscous stresses diffuse throughout the entire duct and their relative dominance results in steady-like profiles that are almost identical during pumping and suction. As the time scale of pulsations is reduced, the Stokes layer narrows, creating an inviscid body in the fluid's core. For both $Wo = 3.1$ and $Wo = 7.0$, $\hat{\delta}_v$ is larger than the channel height, though less than the channel half-width. As a result, viscous features permeate the entire velocity profile in the \hat{z} direction, though only some of that in \hat{y} . At the high frequency, the Stokes layer thickness is significantly less than the channel's hydraulic diameter.

The near-wall velocity overshoot is caused by slight misalignment of the phases of pressure gradient and the flow rate or, more specifically, the local vorticity flux density. In other words, the readjustment of the flow to imposed stresses is limited by the speed of viscous diffusion. In a steady flow (with $\partial\hat{u}/\partial\hat{t} = 0$), the Laplacian term is constant over the cross-section and balanced by the pressure gradient term, which acts immediately and uniformly throughout the fluid. In contrast, the phase shift resulting from a very slight unsteadiness causes non-zero, non-uniform accelerations, which are plotted in Figure 6.7(a) for phases $0 - \pi$. From $0.4\pi - \pi$, the acceleration magnitudes of the near-wall fluid layers are lower than the main body, though proportionally large enough – compared with their momentum – to reverse flow ahead of the main body. Interestingly, the phase shift is smaller near walls $\hat{z} = [0, \hat{b}]$ at lower frequencies, owing to steeper velocity gradients and higher viscous stresses, which act against the driving pressure gradient. As the discrepancy between the viscous and oscillation time scales increases, the time history of boundary-diffused

vorticity may not always produce a damping effect in a given fluid layer. Consider the acceleration at 0.6π in Figure 6.7(c) for example. The difference between this distribution and the uniform pressure term (plotted by the horizontal dashed lines) represents the local value of the vorticity term. Hence, viscous stresses act temporarily in the same direction as the pressure gradient with a magnitude largest near the wall, leading to the augmented near-wall velocity amplitudes of Figure 6.5. Specifically, the evolution of the amplitudes and phases of the near-wall velocities – resulting from local imbalances between viscous damping and imposed driving stresses – appear to enhance and degrade shear stress magnitudes at the wall. The localised instantaneous behaviour of this parameter is quantified in the following section, along with the requisite work input to induce pulsations.

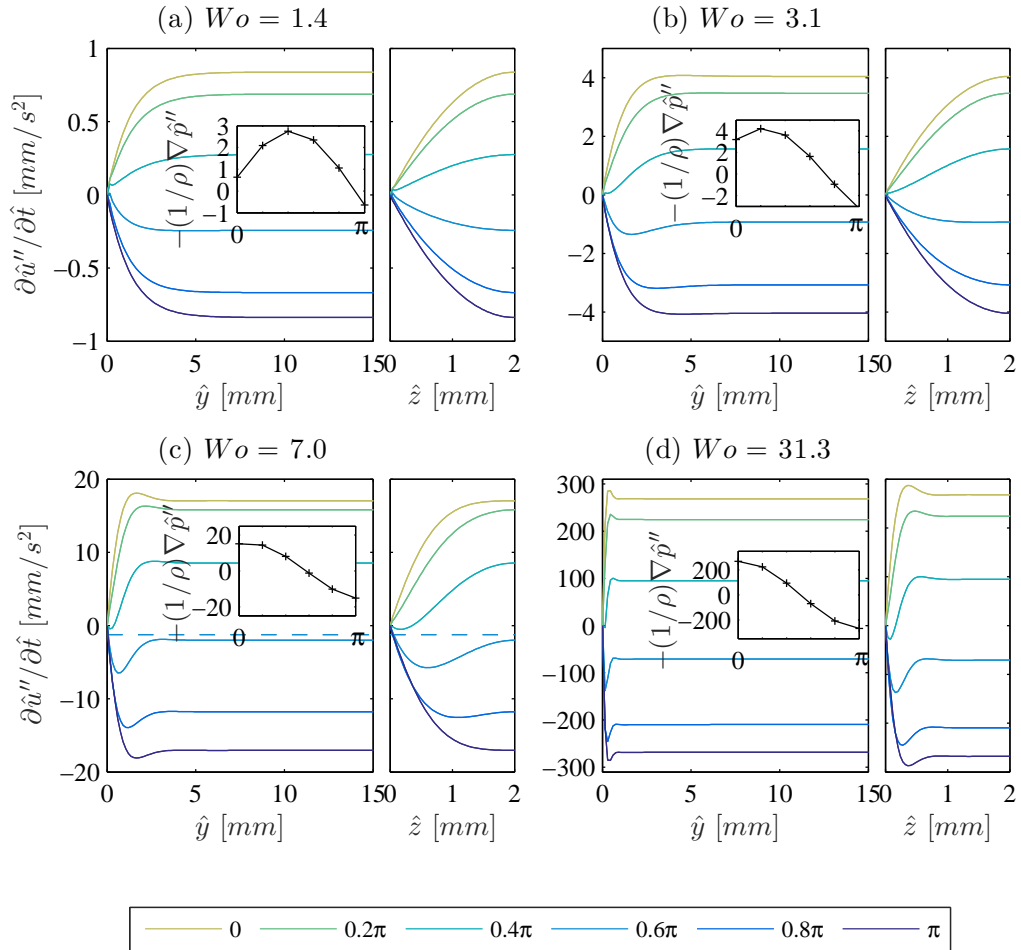


Figure 6.7: Main: Acceleration profiles $\partial \hat{u}'' / \partial \hat{t} = v(\partial^2 \hat{u}'' / \partial \hat{y}^2 + \partial^2 \hat{u}'' / \partial \hat{z}^2) - (1/\rho)\nabla \hat{p}''$ for (a) $Wo = 1.4$, (b) $Wo = 3.1$, (c) $Wo = 7.0$, (d) $Wo = 31.3$. Inset: Contribution of pressure term, which acts uniformly over the cross-section as illustrated by the dashed lines in (c) at 0.6π .

6.2.2 Wall Shear Stress and Pressure Drop

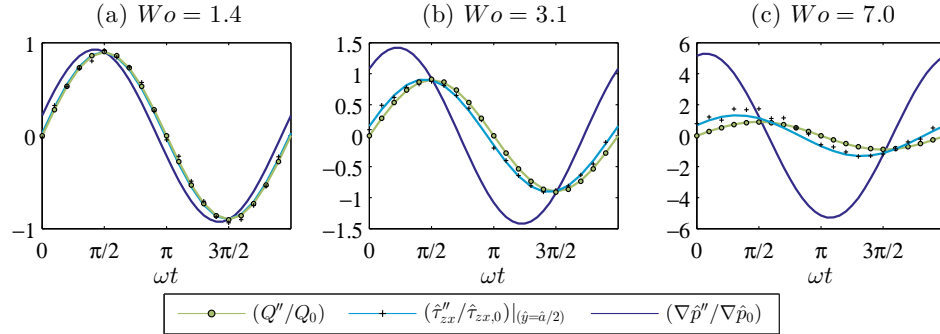


Figure 6.8: Oscillating flow rate, wall shear stresses at the mid-dimensions and pressure gradient for $Q_A/Q_0 = 0.9$ and dimensionless frequency (a) $Wo = 1.4$, (b) $Wo = 3.1$, and (c) $Wo = 7.0$. Solid lines and symbols represent exact solution and experimental measurements respectively.

The temporal behaviour of the measured shear stress at the wall in relation to the flow rate and driving pressure gradient are plotted in Figure 6.8. Experimental values of the wall shear stress at the midpoint of the channel width and height are computed using the slope between the velocity vector nearest to the wall and the wall itself, introducing an error that grows as the Stokes layer thins. With measurements taken to within 0.3 and 0.1 mm of walls $\hat{y} = [0, \hat{a}]$ and $\hat{z} = [0, \hat{b}]$, the displacements of the outermost data points amount to 1.8%, 4.1% and 9.1% of the Stokes layers in the \hat{y} dimension for $Wo = 1.4, 3.1$ and 7.0 , and 0.6%, 1.4%, 3.0% and 4.3% in the \hat{z} direction for Womersley numbers of 1.4, 3.1, 7.0 and 9.9, respectively. This is a well-documented problem in fluid mechanics and is the main reason for the poor accuracy of many existing oscillating wall shear stress measurements. Hughes and How [57] have analysed the growth of this error with proximity to the wall in detail for pulsatile flows. Accordingly, the maximum errors in the experimental data tend to be experienced at the higher frequencies.

The evolution of amplitude and phase of wall shear stress parameters with frequency has not been studied in a two-dimensional channel. The behaviour is reasonably complex, owing to the non-axisymmetric nature of the vessel that contains unique distributions at each wall (for non-square cross-sections). Figure 6.9 depicts the experimental amplitude and phase values at each wall as a function of frequency. At the wall $\hat{z} = 0$ (i.e. the zx components), the regressed amplitude and phase differ by 11.32% and 7.5° from theory at the highest frequency. The errors are 1% and 1.4° at the mid-frequency and 0.4% and 2.2° at the low frequency.

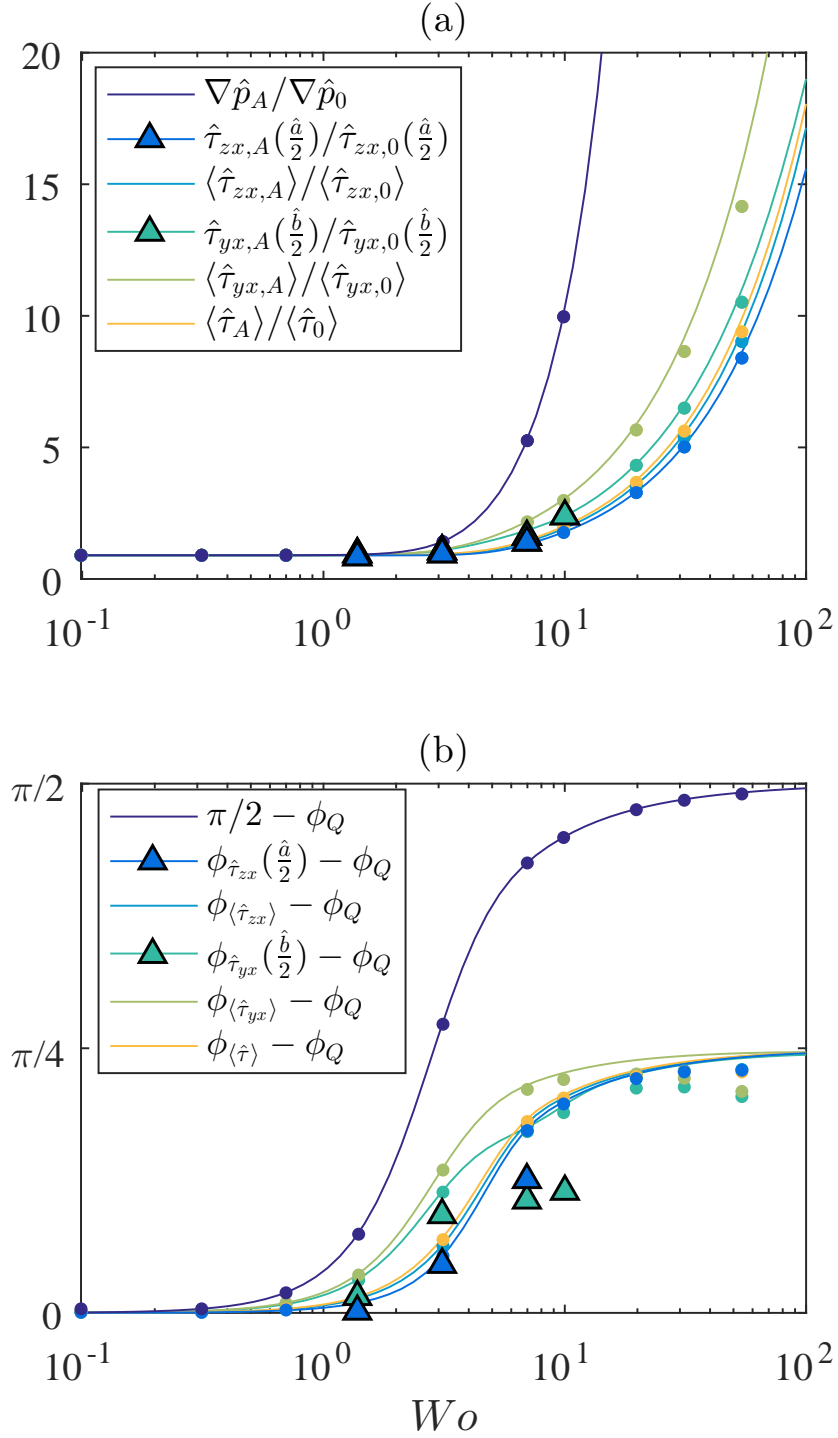


Figure 6.9: (a) Amplitude and (b) phase of pressure gradient and wall shear stress for $Q_A/Q_0 = 0.9$. Solid lines and markers represent analytical (—), numerical (●) and experimental (△) values, respectively.

Near the wall $\hat{y} = 0$, the error of the wall shear stress measurements is higher owing to the obstruction of the channel bonding. For $Wo = 1.4, 3.1, 7.0$ and 9.9 , the amplitude and phase errors are 2% and 2.8° , 0.2% and 4° , 11.9% and 12.4° , and 0.7% and 14.1° . The mean R^2 value of the sine waves fitted to the shear stress data is 0.9953. The numerical values of a collection of mean and local wall shear stress parameters and pressure gradient are plotted at a higher range of frequencies in Figure 6.9. The same values calculated from the numerical solution do not suffer from the issues associated with experimental measurement, and differ by a maximum of 2.6%, 1.9° at the long wall and 7%, 4.8° at the short wall at the highest frequency $Wo = 54.2$. Furthermore, the mean value at each wall and over the entire perimeter are shown to agree with analytical theory. The amplitudes are near-constant at low frequencies and in phase with the flow rate. The amplitudes increase gradually with increasing frequency, before a rapid increase begins at moderate to high frequencies as an inviscid core develops in the channel. The shear stress near the short wall experiences higher amplification, though this results from normalisation by its lesser steady flow value. In fact, the absolute value of the shear stress parameters at each wall equalise, resulting from a flow that is well-approximated by a Stokes boundary layer near each boundary. The high augmentation near the corners is

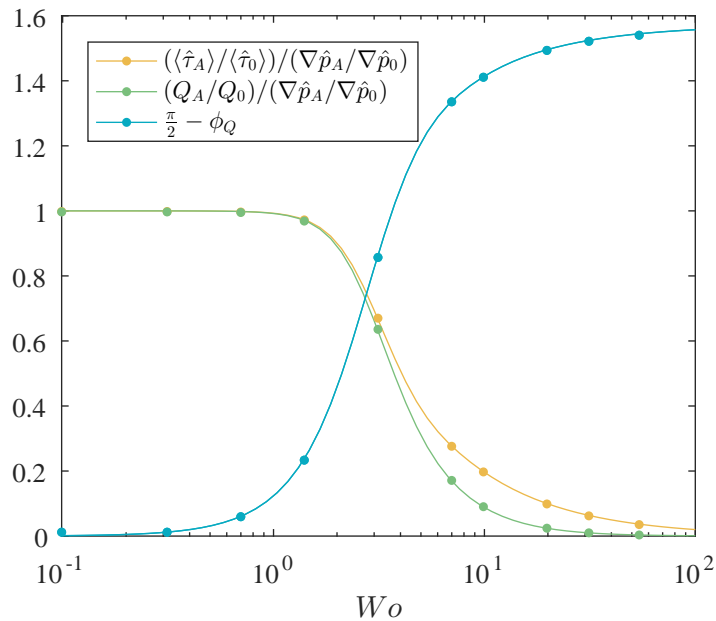


Figure 6.10: Amplification of pressure gradient relative to mean wall shear stress and flow rate for $Q_A/Q_0 = 0.9$. Solid lines and dots and represent analytical and numerical solutions, respectively.

shown by the mean values that increase more substantially relative to their steady components than the mid-dimensional values. The evolution of phase is particularly interesting, where the mid yx component leads in phase at moderate frequencies and lags behind the mid zx component at high frequencies. This relationship appears to be captured by the experimental and numerical estimates, despite error in the absolute values. The frequency at which the phase components at each wall become equal approximately coincides with that where the amplitudes become equal, suggesting that it too is correlated with the development of the inviscid core. Figure 6.10 plots the amplification of the mean wall shear stress and flow rate relative to the pressure gradient amplification with frequency. As a consequence of inertial forces associated with unsteady plug flows, the pressure gradient amplitude increases more substantially compared to the wall shear stress parameters and the phase lag tends to $\pi/2$, which is typical of first-order systems. The relationships with frequency contained within Figures 6.9 and 6.10 are fundamentally similar to those in pipes (see Figures 2.4 and 2.5), implying that the characteristic behaviour is subject to the assumptions and boundary conditions of the problem, rather than geometry.

The wall shear stress profiles are non-constant over two dimensions of the cross-sectional perimeter and experimental measurement is impractical. With all but points at the mid-dimensions of the channel unknown, local behaviour is investigated using the analytical and CFD solutions. Figure 6.11 illustrates the local behaviour of wall shear stress at distinct frequencies. The numerical data are shown to accurately recover the local behaviour of the analytical solution. Intricately related to the velocity field, the profiles have the same distinct shapes as the plots of Figure 6.4, though qualitatively similar profiles have a phase advance relative to the flow rate that increases with frequency. For slow oscillations, the wall shear stress profiles are quasi-steady with lower magnitudes at the short wall, owing to higher viscous stresses in the region. As the frequency is increased the local wall shear stresses universally increase due to higher near-wall velocity gradients. The local amplification of the wall shear stress is depicted in Figure 6.12. In the insets, the phase shifts of the mean shear stresses at each wall have been removed to facilitate direct comparison of corresponding profiles, e.g. $\hat{\tau}_{zx}'''(\hat{y}, \hat{t}) = \hat{\tau}_{zx,A}(\hat{y}) \cdot \sin(\omega\hat{t} + \phi_{\hat{\tau}_{zx}}(\hat{y}) - \phi_{\langle\hat{\tau}_{zx}\rangle})$. The dashed lines plot the equivalent behaviour of completely steady flows with matching instantaneous flow rates, $\hat{\tau}_{zx,0}''(\hat{y}, \hat{t}) = \hat{\tau}_{zx,0,A}(\hat{y}) \cdot \sin(\omega\hat{t})$. At the low-frequency, the shear rate is either augmented

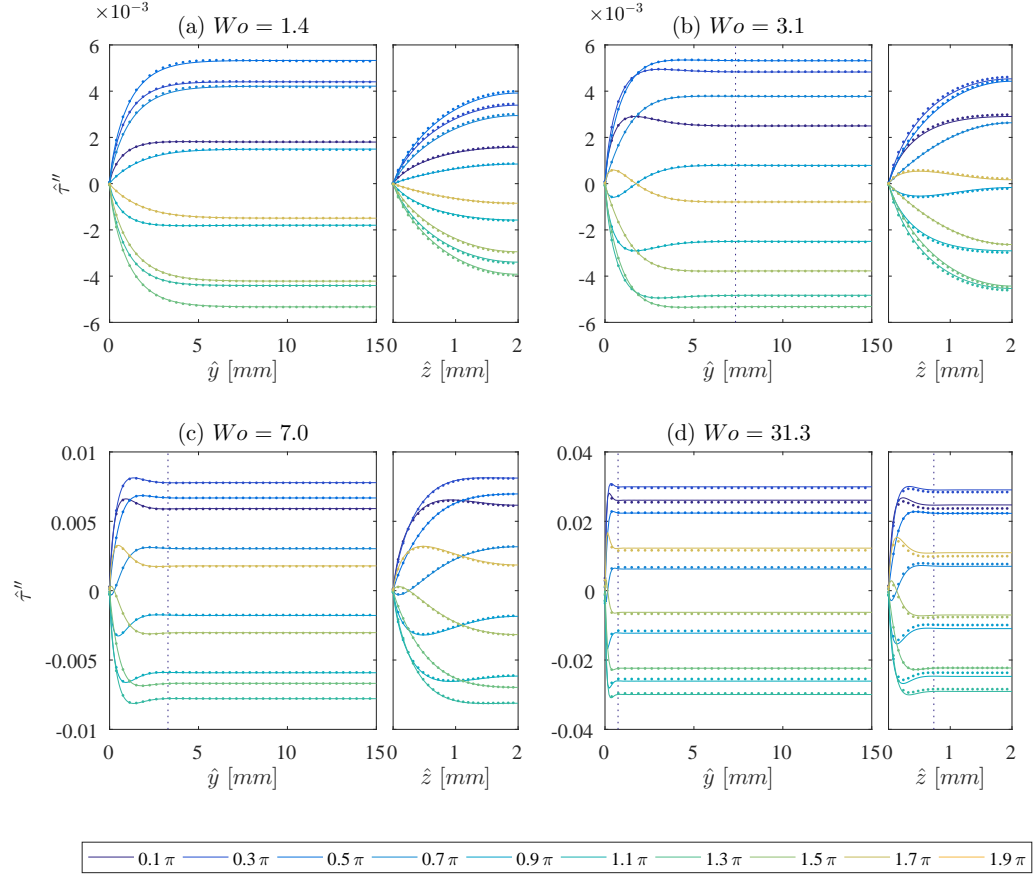


Figure 6.11: Oscillating wall shear stress profiles for $Q_A/Q_0 = 0.9$. Solid lines and markers represent analytical (–) and numerical (●) solutions, respectively.

or diminished locally as a result of the slight overshoots and undershoots in the velocity profiles of Section 6.2.1. The local time-dependent amplifications, defined along the longer wall by:

$$\partial \tau_{zx}'''(\hat{y}) = \frac{\hat{\tau}_{zx}'''(\hat{y})}{\hat{\tau}_{zx,0,A}(\hat{y})} \quad (6.2)$$

are plotted explicitly by solid lines in the main plot of Figure 6.12(a) for positive half-cycle phase values $\phi_{\hat{\tau}_{zx}}(\hat{y}) - \phi_{\langle \hat{\tau}_{zx} \rangle} = 0 - \pi$. Steady flows with matching flow rates are defined by uniform amplification over the cross-section, as shown by the dashed lines $\partial \tau_{zx,0}''(\hat{y}) = \hat{\tau}_{zx,0}''(\hat{y})/\hat{\tau}_{zx,0,A}(\hat{y})$. At the low frequency, the magnitude of the spatial gradients of $\partial \tau'''$ are similar during acceleration and deceleration and the plots are symmetric about the corresponding $\partial \tau_0''$. While the flow is nearly identical to a steady flow on average

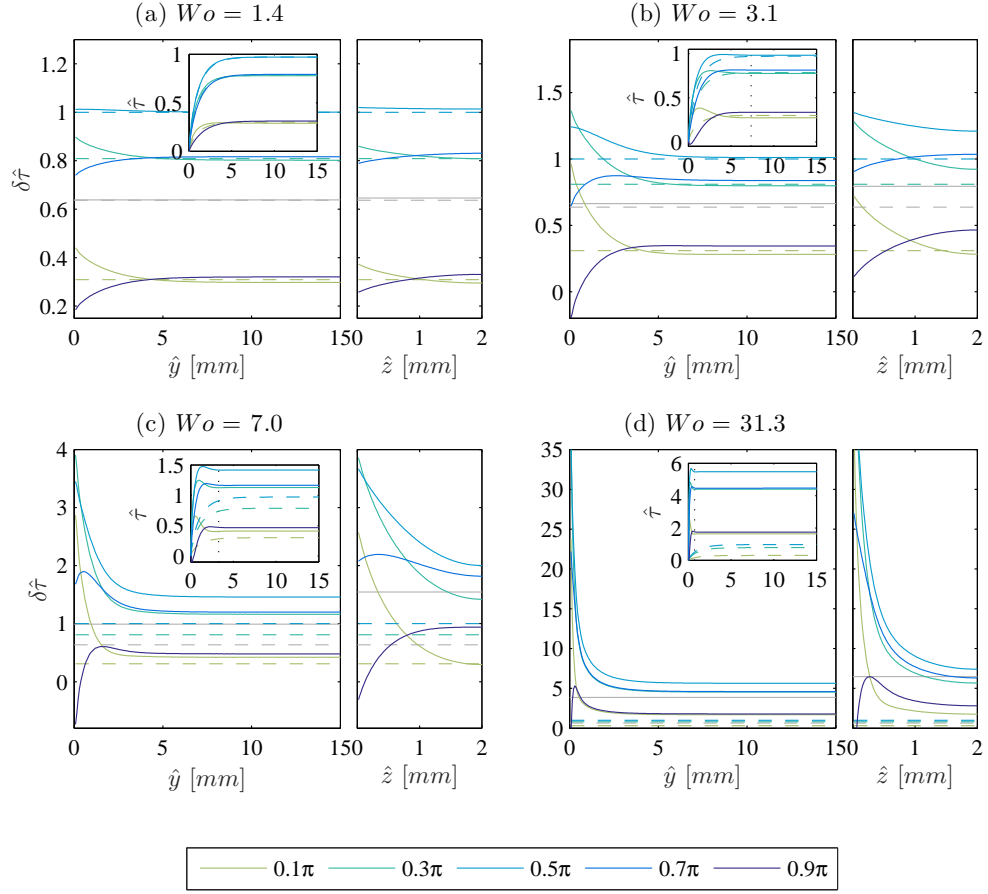


Figure 6.12: Main: Wall shear stress amplification of oscillating flows $\partial \hat{\tau}'''$ (solid lines) and steady flows with matching flow rate $\partial \hat{\tau}'''$ (dashed lines). Horizontal grey lines mark the positive half-cycle space and time average over each wall $(2/\pi)\langle \hat{\tau}_A \rangle / \langle \hat{\tau}_{0,A} \rangle$. Inset: Wall shear stress profiles of oscillating flow (solid lines) and steady flow references (dashed lines). Dotted lines mark the Stokes layer thickness $\hat{\delta}_v$. All data is generated using the analytical solution.

$\langle \tau_{zx,A} \rangle / \langle \tau_{zx,0,A} \rangle = 1.003$, the wall shear rate is greater near the corner over the interval $0 - 0.5\pi$ and smaller over $0.6\pi - \pi$, compared with the central wall. Thus, quasi-steady pulsations may be ineffective in applications concerned with time- and space-averaged augmentation, though it may be possible to alter heat transfer or particulate removal locally for portions of the cycle with very little work expense $(\nabla \hat{p}_A / \nabla \hat{p}_0) / (Q_A / Q_0) = 1.03$. During the intermediate regime, the proximity of the velocity maximum to the boundary begins to dictate near-wall behaviour and the characteristic shapes of the unsteady flows begin to differ during acceleration and deceleration. The interval of greater wall shear stress at the corner lengthens, spanning the majority of the half-period when full inertial-dominance is

achieved. Furthermore, the values near the centre of the wall tend to become higher than their similar steady flow values, as captured by the corresponding positive half-cycle space- and time-averaged values (plotted by grey lines). Along the shorter wall, the mean leads in phase and increases more substantially, mimicking the previously noted inclination for flow reversal. At the high frequencies of $Wo = 7.0$ and 31.3 , the oscillating shear-rates are much larger than their steady counterparts at the longer wall, $\langle \tau_{zx,A} \rangle / \langle \tau_{zx,0,A} \rangle = 1.55$ and 6.08 , though the pressure cost is increased 5.84 and 100 times, respectively. The total pressure drop hence grows at a faster rate than the wall shear stress. While some of this is attributed to increased frictional losses, work is also required to accelerate the flow.

6.2.3 x -Momentum Balance

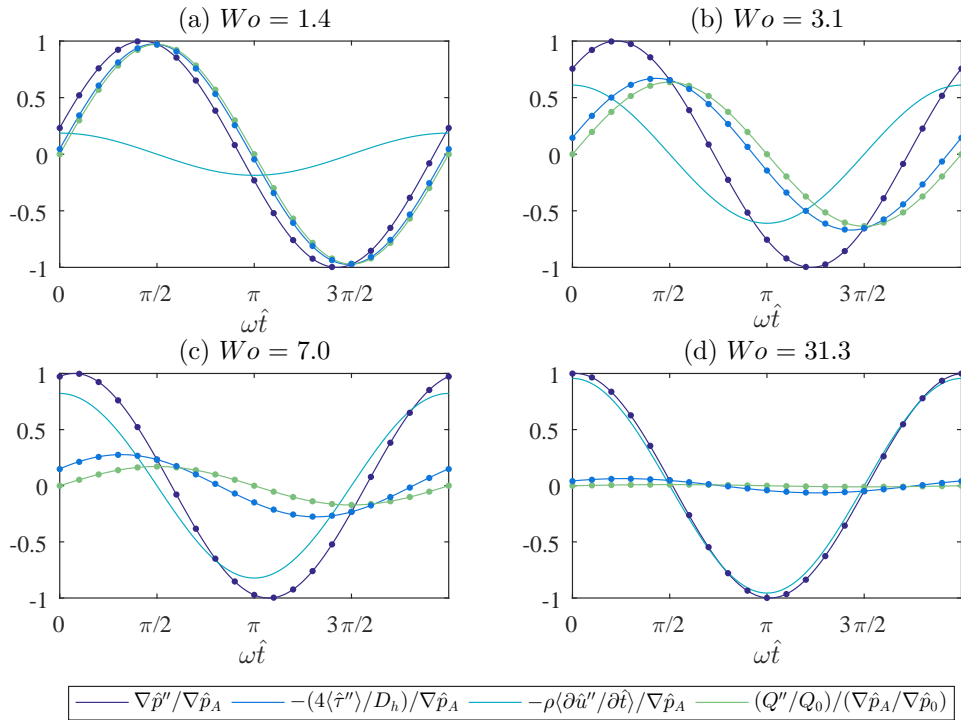


Figure 6.13: Oscillating viscous, inertial and pressure stresses relative to the pressure gradient amplitude for (a) $Wo = 1.4$, (b) $Wo = 3.1$, (c) $Wo = 7.0$ and (d) $Wo = 31.3$. Solid lines and markers represent analytical (—) and numerical (●) solutions, respectively.

The relationships of the spatially-averaged viscous, inertial and pressure stresses may be investigated through the momentum integral balance (see Section 3.1.1 of the analytical

theory chapter). Figure 6.13 tracks the time-dependent relative contributions of the individual stresses to the overall pressure drop. Also plotted are the temporal evolutions of the flow rate oscillations, normalised by the pressure gradient amplification. The instantaneous make-up of the force balance varies with time for a given frequency, based on the phases and amplitudes of the distinct terms. For a slowly oscillating flow, the acceleration of the fluid is negligible and viscous forces predominate. The flow rate and mean wall shear stress have the same amplitude as steady flows with matching flow rates and oscillate in phase with the pressure gradient. With increasing frequency, the value of the inertial term becomes appreciable, with an amplitude of the order of the frictional term. The characteristics of the flow are neither viscous nor inertial, and the resultant phase of the pressure gradient is somewhere between that of the individual contributors. A phase shift appears between the flow rate and pressure gradient, which increases more considerably. At $Wo = 7.0$, the majority (though less than 95%) of forces in the system are inertial and the phase of the pressure gradient approaches that of the acceleration. Moreover, the phase difference between the pressure gradient and the flow rate increases. At $Wo = 31.3$, the flow is dominated by inertia with nearly the entire driving pressure used to accelerate the fluid. The pressure gradient is in phase with the accelerative stresses, leading the rate of flow by $\pi/2$. It should be noted that the amplitudes of the stress contributors do not necessarily sum to one, as illustrated in Figure 6.13 for $Wo = 3.1$. Figure 6.14 plots the momentum balance in terms of phasors, as accommodated by the complex solution representations. A triangular force balance exists between the momentum terms, where the sum of the viscous and inertial vectors is equal to the pressure vector. The flow rate terms are at right angles to the inertial terms. At low frequencies, the pressure and viscous vectors are approximately unidirectional. The angle between the phasors increases with frequency, simultaneously decreasing the angle between the pressure and acceleration phasors, which become collinear at high frequencies.

Figures 6.9, 6.13 and 6.14 indicate that distinguishing behavioural characteristics are attained at the limits of low and high frequencies, with transitional behaviour observed at moderate frequencies. Boundaries to the three regimes may be defined where the value of a certain parameter reaches 5% of its asymptotic value. For example, Ohmi et al. [60] studied the behaviour of the phase of flow rate and mean wall shear stress for a pipe geometry, before defining limits at $Wo = 1.32$ and 28, based on the amplitudes of the viscous and inertial terms

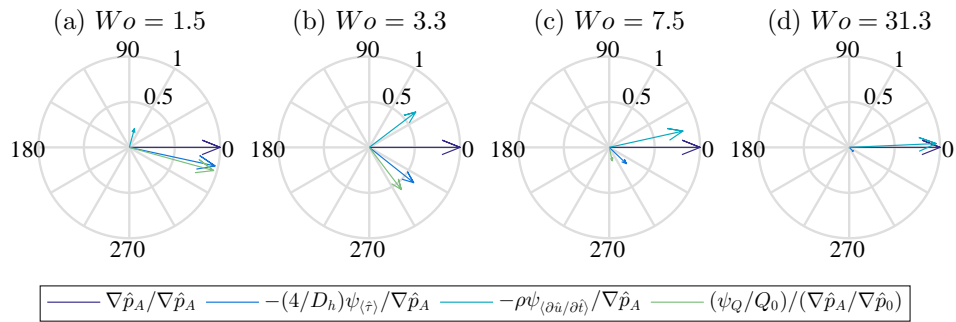


Figure 6.14: Phasors of viscous, inertial and pressure stresses relative to the pressure gradient amplitude for (a) $Wo = 1.4$, (b) $Wo = 3.1$, (c) $Wo = 7.0$ and (d) $Wo = 31.3$.

relative to the pressure gradient amplitude in the pipe geometry. This definition is useful for characterising the work input requirements of oscillations at a certain frequency, as well as reducing computation times using mathematical approximations. With few inertial losses in the system, the quasi-steady assumption is valid. When the majority of the pressure drop is due to inertia, the assumption of inviscid flow holds. Ray et al. [55] opted to use the ratio of flow rate and pressure gradient amplifications. While the choice of parameter is arbitrary, the

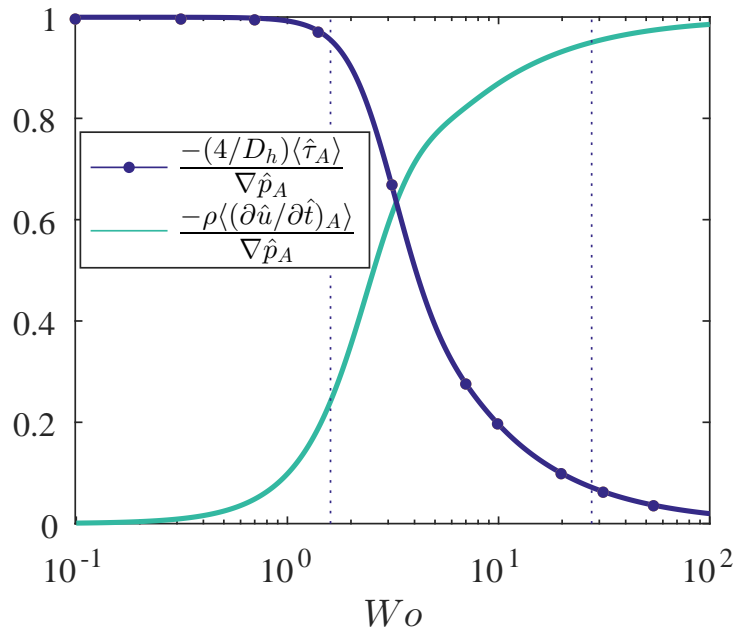


Figure 6.15: Amplitudes of viscous $\propto \langle \hat{\tau}_A \rangle$ and inertial $\propto \langle (\partial \hat{u} / \partial \hat{t})_A \rangle$ stresses relative to pressure gradient amplitude. Solid lines and markers represent analytical (—) and numerical (•) solutions, respectively. Vertical dotted lines delineate the frequency regime boundaries.

wall shear stress is a critical parameter with respect to heat transfer and the pressure gradient is an ever-present design consideration of thermal solutions. Figure 6.15 plots the amplitudes of the frictional and inertial stresses relative to the pressure gradient amplitude as a function of frequency, with vertical lines plotted where the distributions have a value of 95%. The boundaries of $Wo = 1.6$ and 27.6 for a rectangular channel are similar to the values in a tube and do not appear to vary significantly with aspect ratio. Hence, the critical points of transition are approximately geometry-independent. The ratio of viscous to pressure gradient amplitude is a pseudo-performance coefficient, equivalent to the frictional parameter plotted in Figure 6.10. The overall fluid mechanical performance of pulsating flow has analytically determined values of 0.97, 0.67, 0.27 and 0.06 at $Wo = 1.4, 3.1, 7.0$ and 31.3 respectively, demonstrating the increasing work input required to overcome inertia.

6.3 Conclusions

This chapter has described a parametric analysis of the decoupled momentum problem of laminar pulsating flow in a rectangular channel, with experiments measuring the velocity profile and wall shear stresses using particle image velocimetry (PIV). Since the amplitudes are directly proportional to pressure, local behaviour was investigated at constant flow rate amplitude over the range $1.4 \leq Wo \leq 7.0$. To the best of the author's knowledge, the results constitute the first verification of a two-dimensional rectangular analytical solution. Furthermore, the wall shear stress measurements add to the very limited number of studies that exist for any vessel geometry. The accuracy compares favourably with existing results in pipes. As an interesting aside, the phenomenon of off-wall reversal has been observed experimentally.

Analytical and numerical analyses provide complete data, such as the local wall shear stress variation, that is difficult to obtain experimentally in a 2-D geometry. The exact solution has been derived in complex notation, such that amplitudes and phases are easily calculated. This facilitates a shift to a flow rate-fixed model, reduces computational expense and provides further insight into the evolution of inertial effects. Phase alteration occurs even in the quasi-steady regime, causing slight near-wall overshoots and wall shear stresses that are amplified by varying amounts during a cycle. Amplitude augmentation occurs when

viscous and driving stresses act briefly in tandem, due to the phase discrepancy between boundary-diffused vorticity and instantly-transmitted pressure stresses, to enhance the time-averaged wall shear stress. The amplification of wall shear stress relative to steady flow is an important thermal indicator that may be coupled with future heat transfer measurements. The amplitudes and phases of local and mean wall shear stress measures are augmented with frequency compared to steady flow (especially near the short walls and corners), as a result of growing phase delays and higher amplitudes in the near-wall region of the velocity profiles. Furthermore, the local time-dependent amplification varies depending on the regime of unsteadiness: (i) For quasi-steady flows, the local values are similar during acceleration and deceleration though amplification is greater near the corners over the interval $0 - 0.5\pi$. (ii) At intermediate frequencies, local behaviour begins to differ during accelerating and decelerating periods and the interval of greater wall shear stress near the corners lengthens. (iii) Plug-like flows experience universally high amplifications, with wall shear stress greater near the corners for the majority of the positive half-cycle. The phases of wall shear stress differ at each wall at moderate frequencies – with the bulk-mean values at the short wall leading those at the long wall – and tend to $\pi/4$ in the limit of high frequency. The amplitudes of pressure gradient increase more significantly than wall shear stress magnitudes due to accelerative forces. It is useful to define boundaries to the characteristic regimes of oscillatory flow in order to (i) make computationally-efficient mathematical approximations in its modelling, and (ii) characterise its fluid mechanical performance in practical applications. Based on the relative contributions of spatially-averaged viscous and inertial stresses to the overall pressure drop [60], the critical frequencies are $Wo = 1.6$ and 27.6 in a rectangular channel. In practical heat transfer applications, a trade-off scenario exists where increases in wall shear stress are balanced by increased pressure demands.

The analytical framework for the pulsating flow hydrodynamics, developed in Section 3.2, has been validated by measurements and numerical calculations over a high range of Womersley numbers, providing a platform from which the heat transfer of the problem can be studied. Chapter 7 will analyse the coupled behaviour of the local time-dependent velocity and temperature fields to identify the mechanisms of any change in heat transfer due to pulsation.

Chapter 7

Idealised Heat Transfer of Laminar Pulsatile Flow in a Rectangular Channel

7.1 Introduction

Superimposed unsteadiness has been found to improve the heat transfer performance of cooling solutions in a number of experimental investigations. The mechanism of enhancement is commonly reasoned using analogies with the flow hydrodynamics, or the second mechanism of enhancement reviewed in Chapter 2. In Chapter 6, the fluid mechanics were characterised on a parametric basis using theory and experiment over a high range of frequencies. The Stokes boundary layer was found to narrow with increasing frequency, leading to fuller velocity profiles and augmented wall shear stresses at the boundary. It seems physically intuitive that a simultaneous reduction in the thermal boundary layer must occur, augmenting temperature gradients at the wall and enhancing heat transfer. Generally, the relationship between wall shear stress and heat transfer has remained underdeveloped in the literature for the case of a non-zero pressure gradient. While the problems are not similar in the exact mathematical sense of Reynolds analogy, heat and momentum are diffused in the same manner with kinematic viscosity analogous to thermal diffusivity. Theoretical investigations on turbulent heat transfer in steady pipe flows with $Pr = 1$ often assume similarity between the velocity and temperature profiles in a practical sense [153]. Hence, the local wall shear stress is proportional to the local heat transfer coefficient calculated using the temperature

gradient at the wall, which is the same result as Reynolds analogy. It has also been determined that this relationship holds true in the direction normal to the wall of non-circular polygonal tubes if the angles between walls are not too small [154, 155] (see also Figure 7 of [153]). However, the theory has not been established for an unsteady flow, to the best of the author's knowledge.

The field of heat transfer is often treated as a macroscopic science, using engineering correlations between large quantities of parameters in the form of dimensionless numbers. While convective heat transfer is generally unsteady and spatially non-uniform, the heat transfer is typically averaged in time and space. This is useful for characterising experiments and predicting the overall performance of thermal engineering solutions. However, the treatment may obscure the time-dependent behaviour of counteracting physical mechanisms. For example, the discrepancy between heat transfer enhancement through the bulk temperature (mechanism 1) and by the temperature gradient at the wall (mechanism 2) has not been highlighted in the literature, since enhancement is typically described using the time-averaged Nusselt number. Since the dimensionless heat transfer coefficient describes the ratio of heat flux to driving temperature difference, any change with pulsation encompasses the overall net effect of changes in the numerator and denominator. As reviewed by Adiutori [156], the origins of the heat transfer coefficient and the so-called Newton's law of cooling are usually traced to Sir Isaac Newton for his article published anonymously in Latin in 1701 [157] and Joseph Fourier's seminal treatise on heat transfer [158]. The intentions of this constant of proportionality were to tie the flow in the solid with the flow at the surface, and to identify that the heat flux and temperature differential are proportionate under steady convective heat transfer. In the analysis to follow, the heat transfer coefficient is used solely to compare the time-averaged heat transfer of pulsating flow to the steady scenario. In fact, as will be shown, time-dependent heat transfer does not work with the classical concept of the heat transfer coefficient, since the heat flow and driving thermal force are not always proportional with time. It becomes necessary to deal with the quantities independently, in a manner that conforms with Adiutori's vision for heat transfer [159], which rejected classical thermal engineering concepts including dimensionless correlations, power laws, and heat transfer coefficients in place of the explicit dimensional variables. In the case of pulsating flow heat transfer, the Nusselt number combines the characteristics of two non-proportional

quantities, such that its decomposition into a heat flux and temperature difference provides more information about the state of heat transfer. Since analytical models give complete information of the velocity and temperature field, experimental correlations are not required.

Hence, the aim of the current chapter is to build on the experimental and theoretical hydrodynamic analyses of the previous chapter by theoretically investigating the mechanisms responsible for any change in heat transfer. In particular, the local time-dependent interdependence of the mechanical and thermal fields will be inspected using a novel analytical solution to the energy equation and a numerical CFD model, to form a basis for subsequent experimental studies. The mechanisms affecting the temperature difference and heat flux are dealt with independently. In Section 7.2, a parametric analysis is performed on the novel solution in a rectangular channel, which holds the heat flux constant to analyse the behaviour of the driving temperature difference. In Section 7.3, the wall temperature is fixed to inspect the behaviour of the temperature gradient at the wall using an existing 1-D solution.

7.2 Mechanism 1: Enhanced Axial Diffusivity

The first mechanism – which occurs regardless of the boundary condition at the wall – is illuminated by the solution for a thin-walled two-dimensional channel derived in Chapter 3. Since the heat flux is fixed, any change in heat transfer with varying frequency, amplitude and Prandtl number owes to alteration of the bulk temperature. In order to inspect coupling with the velocity field, the local time-dependent behaviour of the temperature field is investigated at the same dimensionless frequencies as the previous chapter for a rectangular channel with $a/b = 7.5$ with two heated long walls H2(2L). The requisite number of terms included in the sums increases steadily with frequency, and hence $Wo = 22.1$ is the highest frequency considered (which takes over a week to compute accurately).

7.2.1 Transverse Temperature Profiles

The steady component of dimensionless temperature, which is independent of Prandtl number, is plotted in Figure 7.1 for a rectangular channel with $a/b = 7.5$ with two heated long walls H2(2L). The analytical and numerical solutions are in excellent agreement. To the best of

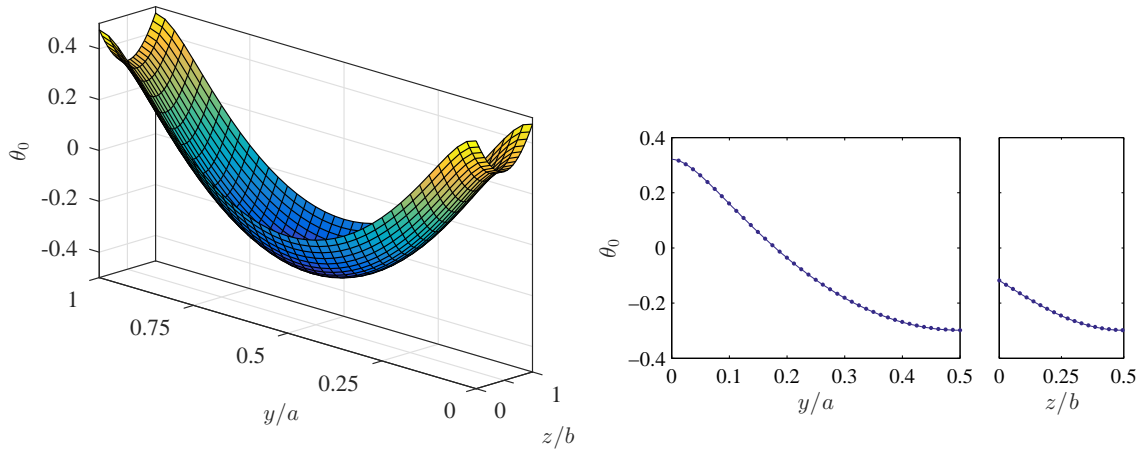


Figure 7.1: Steady temperature profile in a rectangular channel with $a/b = 7.5$ with two heated long walls H2(2L). Solid lines and markers represent analytical (—) and numerical (•) solutions, respectively.

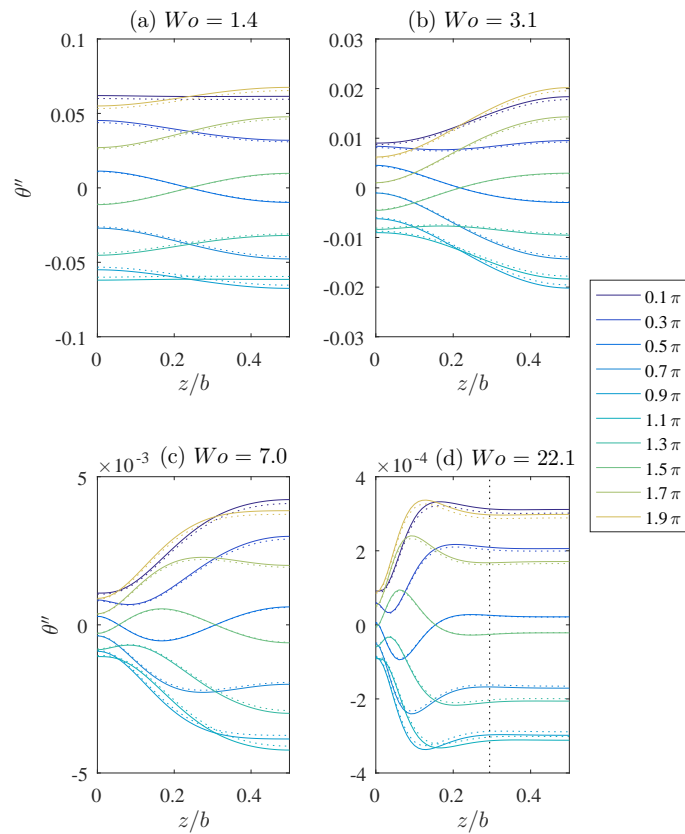


Figure 7.2: Oscillating temperature profiles for $Pr = 5.6$ and (a) $Wo = 1.4$, (b) $Wo = 3.1$, (c) $Wo = 7.0$, (d) $Wo = 22.1$ in a rectangular channel with two heated long walls H2(2L) and $a/b = \infty$ (solid lines), compared to the solution in a parallel plate channel with insulated walls $k_w = 0$ (dotted lines) [69].

the author's knowledge, no independent verification for the analytical solution for steady temperature profiles in a rectangular channel [98] has been given in the literature.

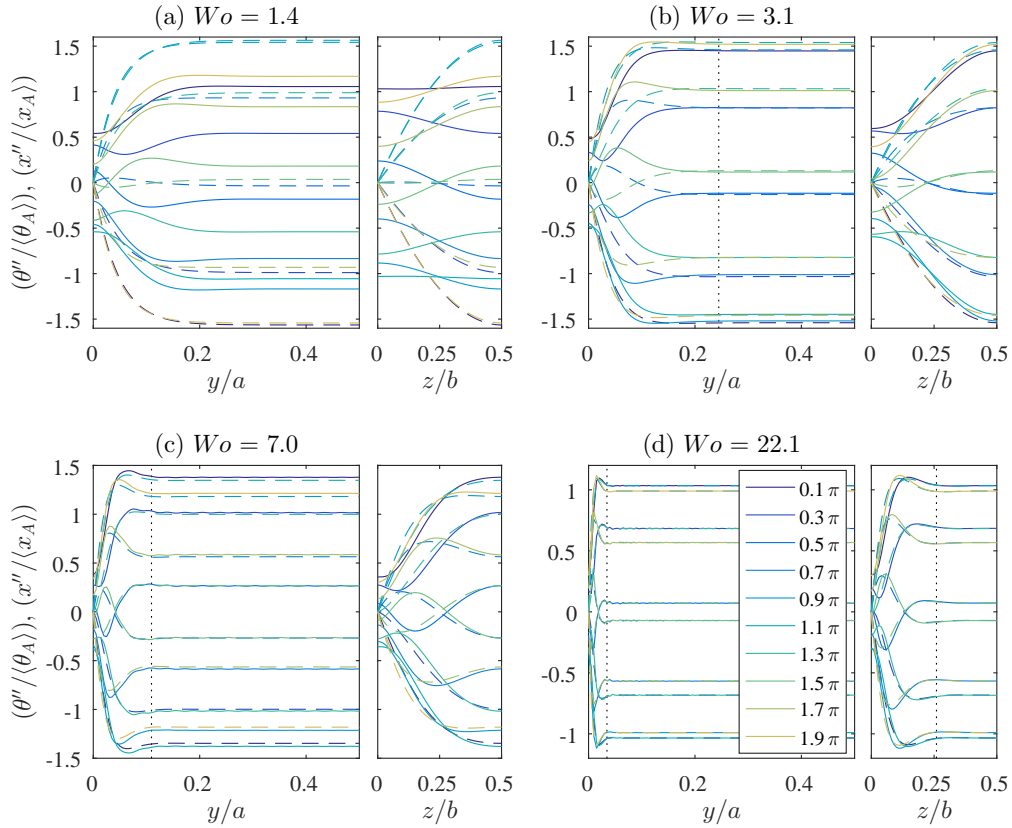


Figure 7.3: Oscillating temperature profiles (solid lines) and displacement profiles (dashed lines) for $Pr = 5.6$ and (a) $Wo = 1.4$, (b) $Wo = 3.1$, (c) $Wo = 7.0$, (d) $Wo = 22.1$ in a rectangular channel with $a/b = 7.5$ with two heated long walls H2(2L). Dotted lines mark the Stokes layer thickness δ_v .

Figure 7.2 illustrates the agreement between the temperature profiles generated by the insulated form of the existing parallel plate model [69] and the current two-dimensional solution with two isoflux heated broad walls (the H2(2L) boundary condition). As expected, the solutions coincide over a plane bisecting the 2-D channel width at very high aspect ratios. The pressure gradient and hydraulic diameter are maintained as constant, since flow rate is infinite for the parallel plate geometry.

Figure 7.3 presents the normalised temperature and displacement profiles across two bisecting planes of the channel cross-section for a realistic Prandtl number of water $Pr = 5.6$ in a channel with aspect ratio of 7.5. It is immediately apparent that the temperature distributions mimic behaviour previously observed in the velocity and wall shear stress

profiles (see Chapter 6), especially at the higher frequencies of $Wo = 7.0$ and 22.1 . In fact, these thermal profiles closely resemble those of displacement, which have the same characteristic shape as velocity though lagging in phase by $\pi/2$. Fluid displaced in the negative x direction has been carried against the positive axial temperature gradient (from a hotter region of the fluid) such that the time-dependent fluid temperature is increased. It is found that a larger temperature gradient produces larger temperature variations. This is in agreement with the mechanism of positive and negative forcing of the temperature field described by Brereton and Jiang [30]. At high frequencies, the oscillations are quick enough that the temperature field cannot readily readjust. Furthermore, no significant transverse diffusion occurs since the temperature profiles are plug-like in the fluid core. A near-wall overshoot is observed, causing high near-wall temperature gradients, except at the walls where the gradients of the oscillating temperature profiles are zero. The inflection point very near the wall appears unnatural and may relate to the restrictions imposed by the constant heat flux boundary condition as discussed in Section 2.2.2. Any coupling that exists between the wall and the fluid is precluded when the thermal behaviour at the wall is explicitly prescribed. For the more realistic case of a finite wall thermal resistance, the slope of the temperature gradient at the wall will be non-zero with the maximum experienced for the constant wall temperature boundary condition [69]. The regions containing annular effects are well-approximated by the Stokes layer thickness (marked by dotted lines). Hence, the region containing transverse temperature gradients does not actually correspond with a thermal penetration length $\delta_\alpha = \delta_v/\sqrt{Pr}$ for a pulsating flow with constant heat flux, since the heat addition to the time-dependent problem is zero and the oscillatory component of the flow is effectively insulated. At $Wo = 1.4$ and 3.1 , thermal diffusion – whose time scale is short compared with the period of oscillation – acts to differentiate the temperature profiles from the displacement profiles, especially in the near-isothermal short channel dimension.

In the hydrodynamic problem the velocity amplitudes were similar at fixed flow rate pulsations. In contrast, the amplitudes of temperature oscillations decrease further at higher frequencies, and the pulsating temperature profiles deviate less significantly from the steady temperature profile, as plotted in Figure 7.4 for the lower two frequencies. The volume displaced during a half-cycle is proportional to the area under the pulsating flow rate curve. Since the amplitude of the flow rate is constant, decreasing the wavelength of the pulsation

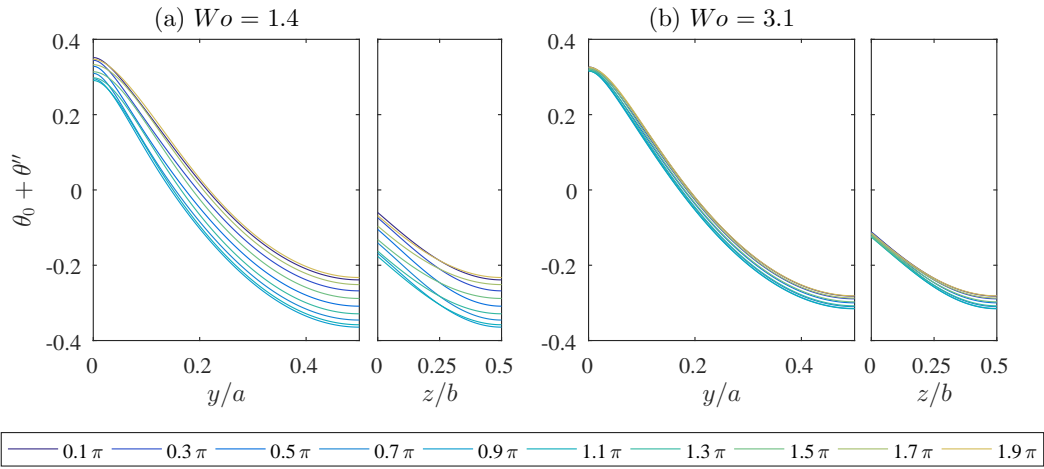


Figure 7.4: Pulsating temperature profiles for $Pr = 5.6$ and (a) $Wo = 1.4$, (b) $Wo = 3.1$ in a rectangular channel with $a/b = 7.5$ with two heated long walls H2(2L).

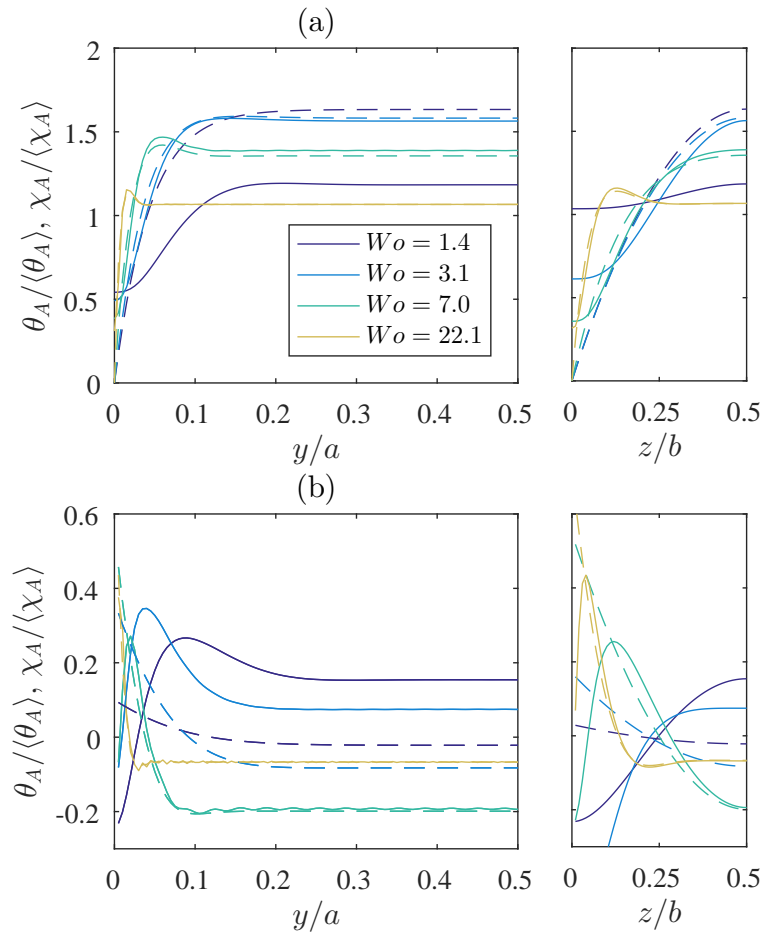


Figure 7.5: Temperature θ (solid lines) and displacement χ (dashed lines) amplitude and phase profiles for $Pr = 5.6$ in a rectangular channel with $a/b = 7.5$ with two heated long walls H2(2L).

(or increasing the frequency) decreases the volumetric displacement and hence the mean displacement amplitude. The fluid elements are displaced over smaller axial distances with smaller axial temperature differences. Since displacement is the primary driver of temperature oscillations, the amplitude is reduced. It is for this reason that the experimental parameter space of Chapter 8 contains a single low frequency.

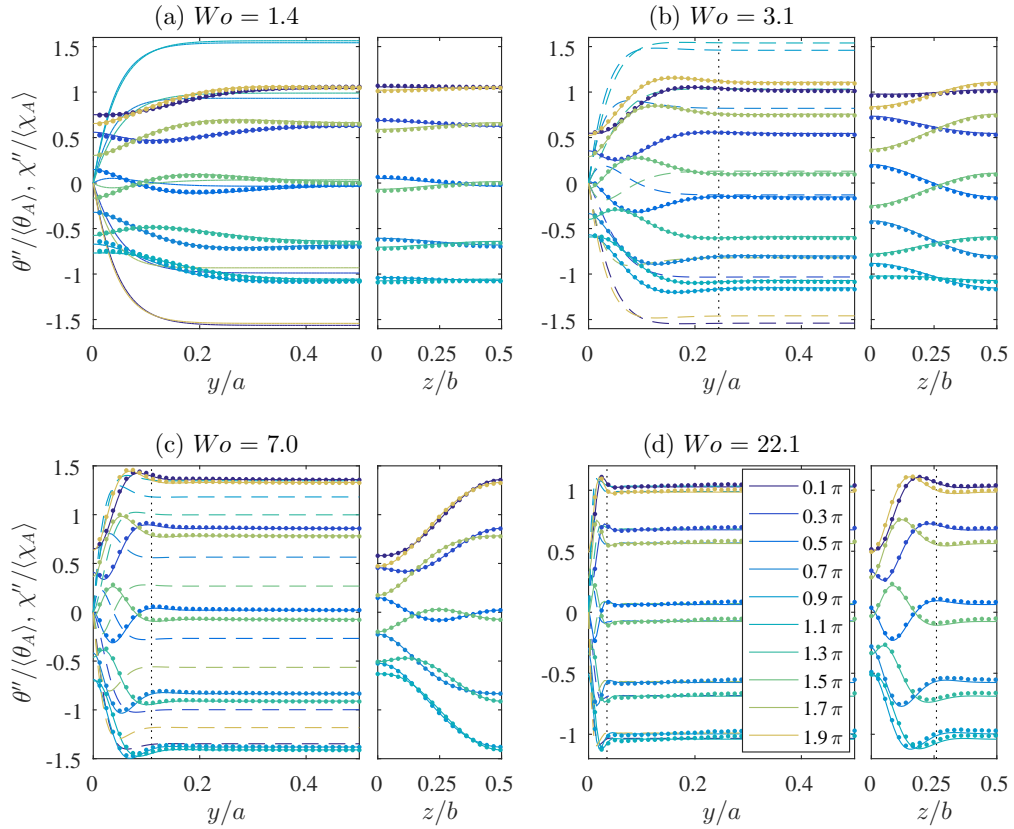


Figure 7.6: Oscillating temperature profiles (solid lines) and displacement profiles (dashed lines) for $Pr = 1$ and (a) $Wo = 1.4$, (b) $Wo = 3.1$, (c) $Wo = 7.0$, (d) $Wo = 22.1$ in a rectangular channel with $a/b = 7.5$ with two heated long walls H2(2L). Solid lines and markers represent analytical (–) and numerical (•) solutions, respectively. Vertical dotted lines mark the Stokes layer thickness δ_v .

Figure 7.5 decomposes the same data into amplitude and phase values (as accommodated by the complex solutions). The plots are normalised by their respective bulk-mean amplitudes, since the aim is to elucidate similarities between the dynamic and thermal parameters. On average, the temperature and displacement profiles are precisely out of phase, independent of frequency ($\phi_{\langle \chi \rangle} - \phi_{\langle \theta \rangle} = -\pi$), suggesting that the temperature profile is formed primarily as a result of fluid advection. At low frequencies, heat diffuses from the core to the wall

such that the near-wall region lags the main body, in contradiction with the hydrodynamic parameters. Near the corners, the phase lag is larger since the lines of heat flow from the wall to the bulk fluid are longer. At high frequencies, the temperature at the wall still lags the main body (since any change in temperature must occur by transverse diffusion alone); however, the near-wall temperature oscillations now lead in phase relative to those at the mid-channel with amplitudes that are high compared to quasi-steady oscillations in the same region.

The same parameters are plotted in Figure 7.6 for a Prandtl number $Pr = 1$. The numerical data are shown to accurately recover the local behaviour of the analytical solution. While not plotted, the numerical displacement profiles are also found to match. The temperature profiles are differentiated from their corresponding displacement profiles and the thermal boundary layer is less well predicted by the Stokes layer thickness, since thermal diffusion is appreciable with respect to viscous diffusion at low Prandtl numbers. The difference is most easily recognised between the temperature/displacement profile overlays at $Wo = 7.0$, $Pr = 1$ and $Wo = 7.0$, $Pr = 5.6$ of Figure 7.3. At the highest frequency, the time scale of the pulsations remains short enough, compared to the time scale of thermal diffusion, that the transverse spreading of heat is small.

Hence while diffusion obscures the mechanism at low frequencies and Prandtl numbers, temperature oscillations are predominantly caused by fluid displacement. Similarly, as Prandtl number is reduced, thermal diffusion becomes appreciable at higher frequencies and acts to smooth the temperature profiles. At the limit of high Prandtl number, the temperature profiles are the inverse of the displacement profiles for all frequencies.

7.2.2 Axial Temperature Profiles

Similar to the current study, more recent analytical studies have tended to neglect the fluctuating component of the axial temperature gradient [29, 30, 69, 79]. However, it appears that the early analytical study of Faghri et al. [35] permitted spatial fluctuations in the axial temperature distribution. While other idealisations were made, this study predicted heat transfer enhancement for the case of a slowly pulsating flow. By instead using the slug flow assumption, Siegel and Perlmutter [34] found that the oscillating axial temperature gradient was non-negligible. As indicated by Figure 2.17, the slopes were approximately 100%, 64%

and 14% of the mean axial temperature gradient for $Wo = 0.28, 2.8$ and 5.6 , respectively. A single numerical study [70] tested this assumption for a constant heat flux boundary condition, finding that the pulsating temperature profiles were indeed approximately linear at $Wo = 1$ (see Figure 2.15). Hence, contradictions exist in the literature and the assumptions made in the linearisation of the energy equation (see Section 3.1.4) need to be critically assessed.

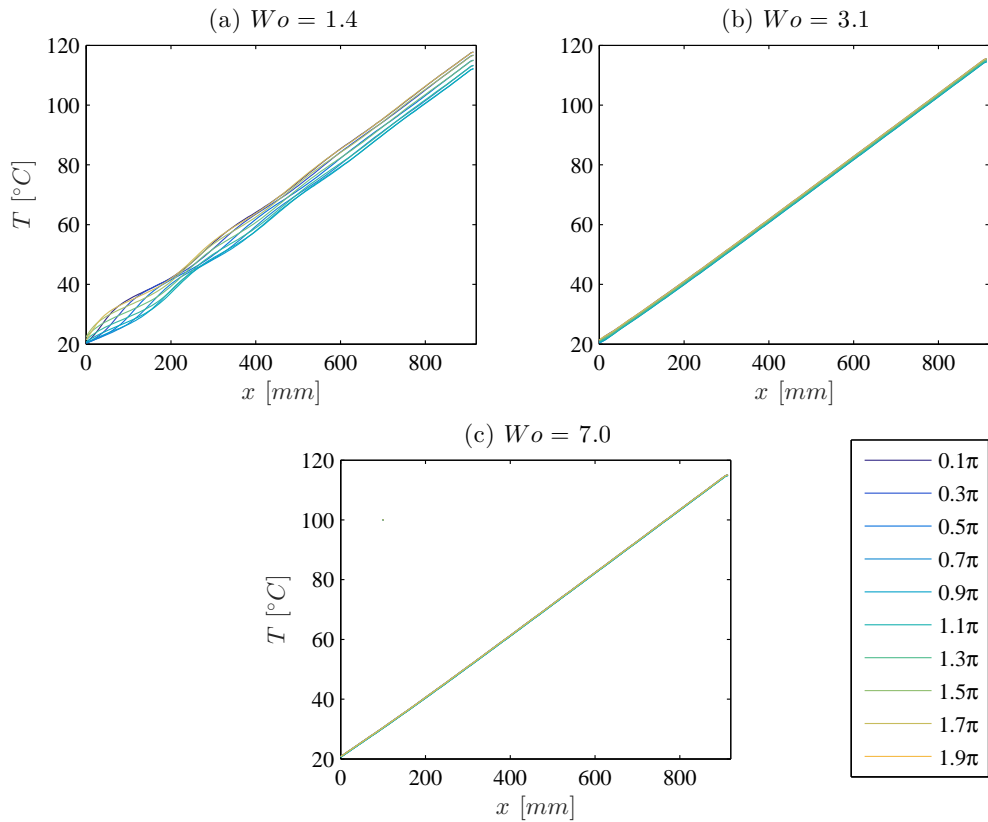


Figure 7.7: Pulsating axial temperature profiles of numerical CFD model (see Chapter 5) for $Pr = 1$ in a rectangular channel with $a/b = 7.5$ with two heated long walls H2(2L).

Figure 7.7 presents the pulsating axial temperature profiles at the centroid of the channel for $Pr = 1$. The behaviour is representative of that at the wall. For all frequencies, the temperature profiles are approximately linear at each time instant far from the channel entrance. This confirms findings in earlier numerical studies [70, 74], and validates the assumption made in the current research and earlier analytical studies [29, 30]. At $Wo = 1.4$, the linearity condition is achieved after an axial distance much greater than the thermal development length.

To the best of the author's knowledge, the oscillating component of the axial temperature

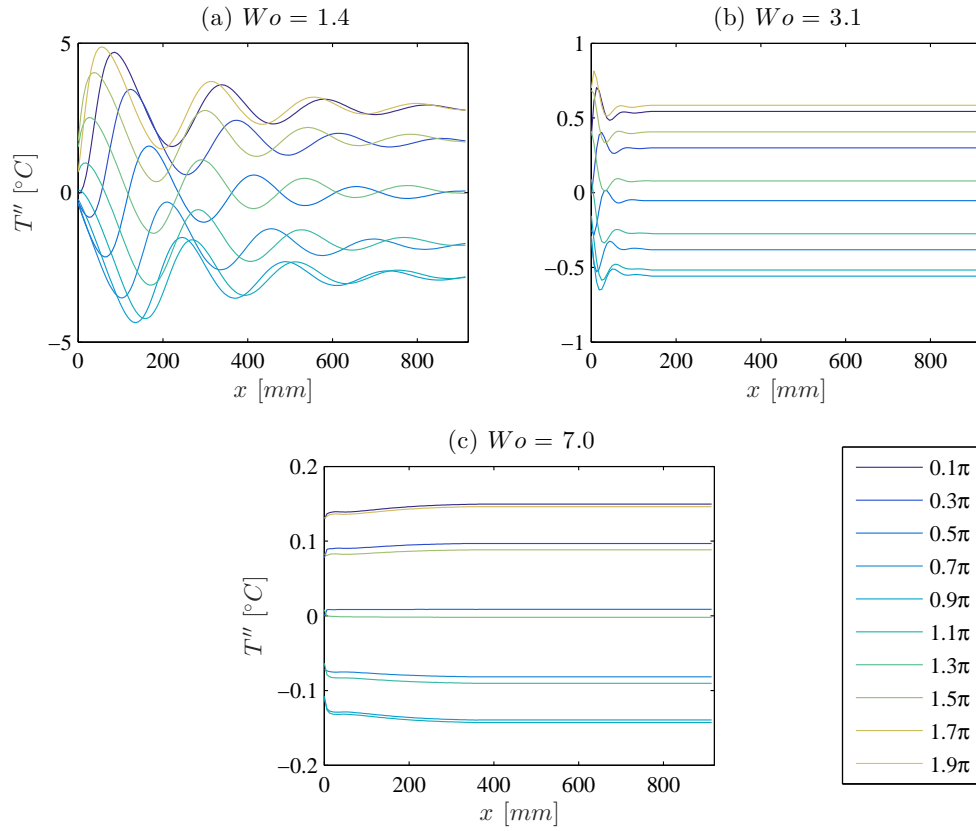


Figure 7.8: Oscillating axial temperature profiles of numerical CFD model (see Chapter 5) for $Pr = 1$ in a rectangular channel with $a/b = 7.5$ with two heated long walls H2(2L).

distribution has not been analysed since Siegel and Perlmutter [34]. Figure 7.8 presents the oscillating axial temperature profiles at the centroid of the channel. As before, behaviour is found to be qualitatively similar at the wall. The amplitudes of the axial temperature fluctuations are highest at low frequencies. In each case, the amplitude of the temperature oscillations in the linear region corresponds to the first term of the double sum (with $j = k = 0$) in the analytical expression for temperature (Equation 3.24). This term is uniform over the cross section and proportional to the mean displacement amplitude $\psi_\theta|_{j=k=0} = -\langle\psi_\chi\rangle/Pr$. The axial distributions are predominantly parallel at the higher frequencies $Wo = 3.1$ and 7.0 . In the upstream region at the lowest frequencies $Wo = 1.4$ and 3.1 , the temperature distributions are found to contain spatial periodicity that appears similar in nature to those observed in Figure 2.17. Furthermore, the spatial wavelength of the oscillations is larger at smaller frequencies, since the distance travelled during one pulsation cycle ($= \chi_0 = (1/f)\langle\hat{u}_0\rangle$) is larger. At the lowest frequencies, the distances are $\chi_0 = 226.7$ and 45.3 [mm],

respectively, which seem to correspond with the troughs of the spatial curves. Siegel and Perlmutter [34] found that the magnitude of the temperature oscillations was zero at each node χ_0 . In contradiction with that early analytical study, every axial location experiences non-zero temperature fluctuations since fluid is continuously displaced over axial temperature differences in the heated channel. Also, the oscillations are found to damp out completely with sufficient axial length. The mechanism responsible for this axial behaviour was discussed in conjunction with Figure 2.18. Since the temperature field varies in the \hat{x} dimension near the entrance of the channel, the difference between the wall and bulk temperatures is not uniform axially. Hence, Nusselt number enhancement may be experienced at some axial locations. While this region of the channel is beyond the scope of the current thesis, it is suggested as an area of future research (see Chapter 10).

The amplitude of the temperature oscillations (calculated using non-linear regression) as a function of axial distance is plotted in Figure 7.9(a). Figure 7.9(b) plots the oscillating temperature gradient normalised by the steady temperature gradient at $Wo = 1.4$ for the length of channel. Very near the channel entrance the oscillating component of the temperature gradient has approximately the same magnitude as the steady component, implying a quasi-steady nature. While not plotted, the ratio between the components is just less than 0.4 in the same region of the channel for $Wo = 3.1$. Hence, the magnitudes in the entry region are of the order of those determined from Figure 2.17, though the magnitudes become negligible downstream. Hence, the CFD model of the current research has found that the

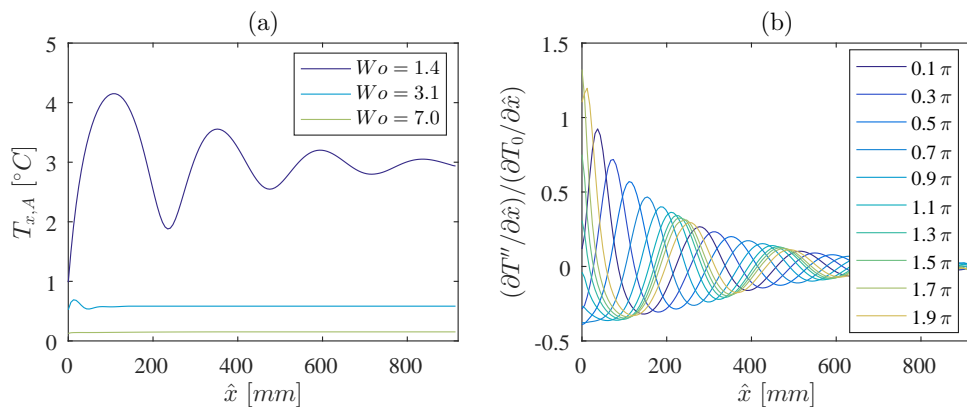


Figure 7.9: (a) Amplitude of axial temperature oscillations, (b) Relative size of axial temperature gradient compared to steady axial temperature gradient for $Wo = 1.4$, using numerical CFD model (see Chapter 5).

assumptions made in the analytical solution hold true in the far downstream region of the channel, though the spatial oscillations may extend beyond the region where the temperature profile is thermally-developing.

7.2.3 Time-averaged Heat Transfer

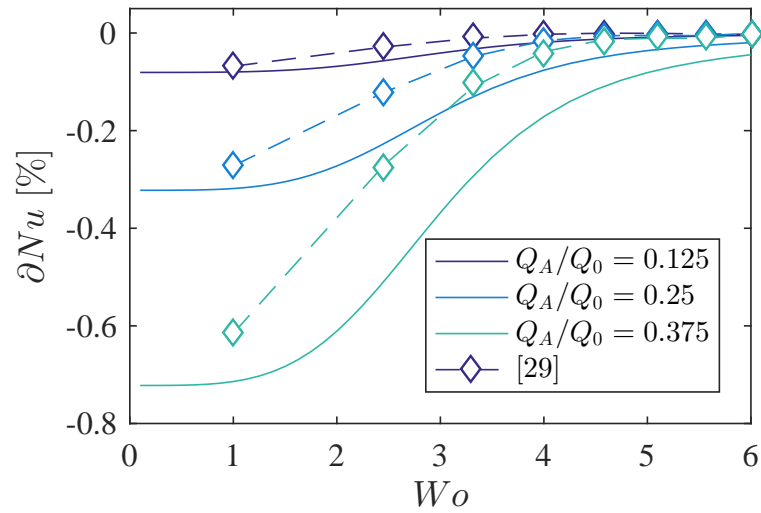


Figure 7.10: Reduction in Nusselt number with frequency Wo at constant flow rate amplitudes Q_A/Q_0 for $Pr = 1$ in a square channel with four heated walls H2(4). Symbols represent the solution of Hemida et al. in pipes [29].

Analytical theory predicts a steady flow Nusselt number of $Nu_0 = 5.9805$. The Nusselt number of the numerical solution predicts a Nusselt number $Nu_0 = 5.9293$, which represents a 0.86% error compared to the analytical solution. The effect of the temperature oscillations on the time-averaged heat transfer is presented in Figure 7.10 for pulsating flows at constant $Pr = 1$ in a square channel with 4 heated walls, which is comparable with existing studies in pipes. Enhancement is universally negative over the parameter space with the magnitude of the reduction decreasing with frequency and increasing with flow rate amplitude. The results are in qualitative agreement with the trends observed by Hemida et al. [29] in a pulsating pipe flow, though heat transfer is reduced more substantially in the non-circular conduit. For positive-leading pseudo-sine modulations in a pipe, Brereton and Jiang [30] found a reduction of 0.1% at $Wo = 2.5$, $Q_A/Q_0 = 2$ and $Pr = 7$, with the alteration increasing at higher amplitudes. The reduction increases with decreasing Prandtl number and increasing aspect

ratio. Figure 7.11 presents the effect of the temperature oscillations on the time-averaged heat transfer for pulsating flows in a rectangular channel with two heated walls at $Pr = 1$. The numerical results are in reasonable agreement with analytical theory, with the larger discrepancy at $Wo = 1.4$ likely due to the slight waviness in the axial temperature profiles throughout the channel (see Figure 7.8(a)). For reference, the temperature oscillations shown in Figure 7.3 (two heated long walls, $Pr = 5.6$) correspond to Nusselt number reductions of 0.82%, 0.21%, 0.0014% and 0.0003% at $Wo = 1.4, 3.1, 7.0$ and 22.1 , respectively. Such changes are near impossible to measure experimentally, further highlighting the importance of the complete data set provided by the theoretical solutions.

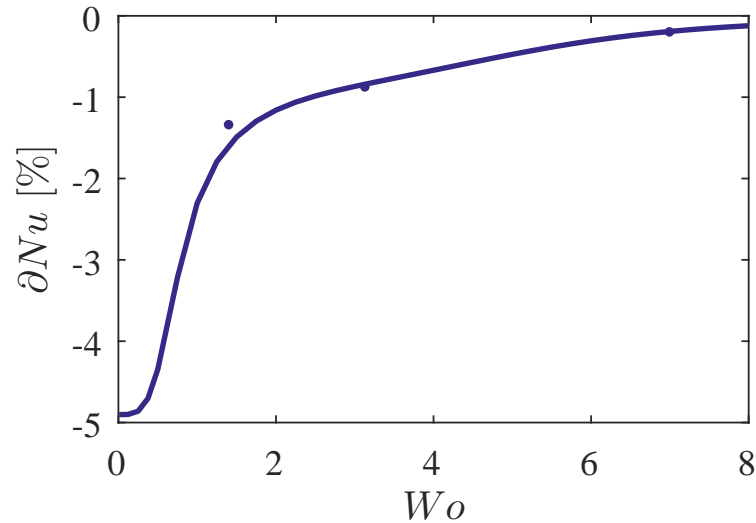


Figure 7.11: Reduction in Nusselt number with frequency Wo for $Q_A/Q_0 = 0.7$ and $Pr = 1$ in a rectangular channel with $a/b = 7.5$ with two heated long walls H2(2L). Solid lines and markers represent analytical (—) and numerical (●) solutions, respectively.

Similar to existing solutions in circular geometries, the steady flow solution is not approached as frequency is reduced at constant flow rate amplitude. This apparently counter-intuitive result is actually in agreement with the theory and measurements of the enhanced axial diffusivity phenomenon in oscillatory flows [64, 65, 67]. The mechanism may be explained by the periodic variation of the transverse temperature gradients, which interact with axial displacement to induce an effective conduction towards the channel entrance: For $\phi < 0.5\pi$ and $\phi > 1.5\pi$ in Figure 7.3, the displacement is negative and the temperatures in the fluid core are higher than those in the Stokes layer. Hence, heat is flowing to the walls of the channel when it has been displaced in the negative x direction. For $0.5\pi < \phi < 1.5\pi$, the

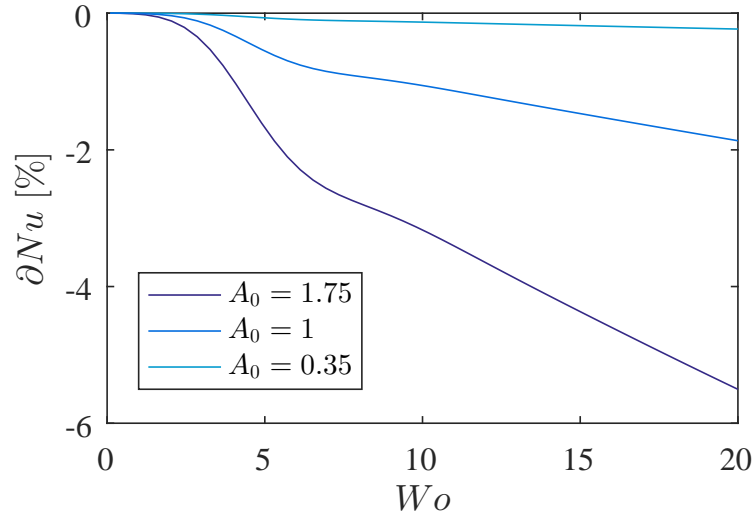


Figure 7.12: Reduction in Nusselt number with frequency Wo at constant dimensionless amplitudes A_0 for $Pr = 1$ in a square channel with four heated walls H2(4).

displacement is positive and the temperature in the core is lower than that near the wall. Heat is transported toward the core as the core is displaced positively. The early mass diffusion studies [65, 67] found that axial mass diffusion is enhanced with the square of A_0 since the fluid is displaced over larger axial distances with higher temperature differences. In contrast, the volumetric displacement and dimensionless amplitude parameter continue to rise as the frequency is reduced at constant flow rate amplitude (as quantified by Table 5.2). Hence, the combined effect of varying A_0 and Wo conceals any underlying trends. Figure 7.12 illustrates that the relative reduction in Nusselt number increases with frequency and approaches zero at low frequencies for constant A_0 . The low and high frequency behaviour appears to be connected by a transition region, similar to that observed by Joshi et al. [67] (see Figure 2.14). Similarly, Kurzweg [69] found that the behaviour of enhanced thermal diffusivity differed at low and high frequencies. The reduction increases with A_0 at constant frequency since a higher volume of heat-carrying fluid is displaced over larger axial distances with higher temperature differences. According to theory, the reduction increases indefinitely with increasing pulsation amplitude, although this will be limited in cooling applications by practical constraints in the length of channel.

The Nusselt number reduction is caused by a time-averaged decrease in the bulk temperature ($\bar{\theta}'_b < 0$ in Equation 3.32). The steady flow thermal equation may be described

as $Q_w = \dot{m}c_p(T_{b,out} - T_{b,in})$ [104], where Q_w is the rate of heat transferred in Watts. Since pulsation acts to reduce $T_{b,out}$, the temperature difference between the inlet and outlet is now smaller. While the same fixed amount of heat flux is transferred to the fluid, the axial heat flux in the negative x direction acts against the removal of heat, meaning that heat transfer has been reduced compared to a steady flow. In other words, the energy convected by the fluid through the outlet is reduced compared to that convected by the fluid through the inlet (though the time-averaged flow rate through each is fixed). Conversely, if the bulk temperature is increased, more heat has been removed and the heat transfer has been augmented. Since displacing a fluid backwards increases the bulk temperature, Brereton and Jiang [30] suggested that modulations acting to reduce the flow rate below its initial value increase Nu compared to steady flow. The effect of a time-varying bulk temperature on the Nusselt number may be studied analogously in a steady flow with time-varying inlet temperature [105].

7.2.4 Time-dependent Heat Transfer

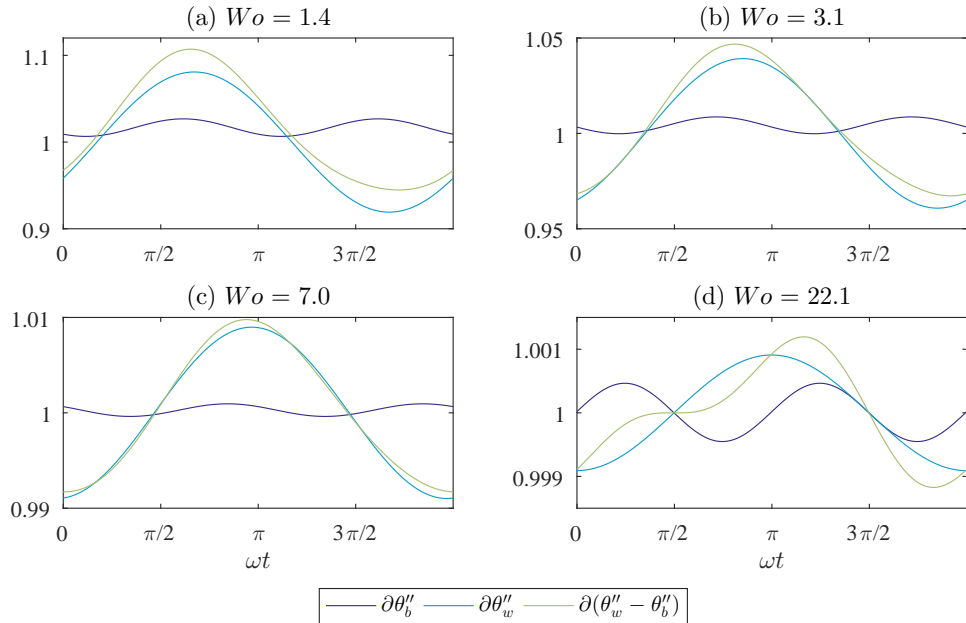


Figure 7.13: Pulsating bulk temperature $\partial\theta_b'' = [(\theta_{w,0}) - (\theta_{b,0} + \theta_b'')]/[(\theta_{w,0}) - \theta_{b,0}]$, wall temperature $\partial\theta_w'' = [(\theta_{w,0}) + \theta_w'']/[(\theta_{w,0}) - \theta_{b,0}]$ and driving temperature difference $\partial(\theta_w'' - \theta_b'') = [(\theta_{w,0}) + \theta_w'' - (\theta_{b,0} + \theta_b'')]/[(\theta_{w,0}) - \theta_{b,0}]$ for $Pr = 5.6$ and (a) $Wo = 1.4$, (b) $Wo = 3.1$, (c) $Wo = 7.0$, (d) $Wo = 22.1$ in a rectangular channel with $a/b = 7.5$ with two heated long walls H2(2L).

The axial heat flow of a pulsating flow is captured by the behaviour of the overall bulk temperature, which contains components resulting from the product of the decoupled velocity and temperature $u\theta = (u_0 + u')(\theta_0 + \theta')$. Using the 2-D analytical solution, it has been determined that $u_0\theta'$ and $u'\theta_0$ contribute equally at low frequencies, though $u_0\theta'$ doesn't contribute at high frequencies, in agreement with the analytical study of Nield and Kuznetsov [78]. The enhanced axial diffusion mechanism is captured by the product of the unsteady components that contributes to an alteration of the time-averaged value (described by Equation 3.31). Hence, the phase between the oscillating velocity and temperature profiles determines whether heat transfer is enhanced or diminished. Since the net result of both half-cycles is to move heat towards the entrance of the channel, the axial heat flow oscillates with twice the frequency of pulsation (see Figure 7.13). The phenomenon is analogous to mass diffusion studies, where the cloud of contaminant expands during one half-cycle and contracts during the second half-cycle, with the net effect of the full cycle being a slight overall increase in length [64, 65, 66]. Periodically-reversing flows, which contain a phase difference between the velocity and temperature fields, present a problem for the classical theory of bulk temperature. In order to isolate the axial heat flow induced solely by the transverse diffusion mechanism, the component relating to the one-dimensional displacement of fluid is removed. This corresponds to the first term of the double sum (with $j = k = 0$) in Equation 3.24, which is uniform over the cross section and proportional to the displacement $\psi_\theta|_{j=k=0} = -\langle\psi_\chi\rangle/Pr$. Negating this term does not affect the time-average $\bar{\theta}'_b$. For illustrative purposes, an instantaneous measure of the temperature difference is calculated using a wall temperature parameter where the same 1-D term has been removed. This is justified, since neglecting the uniform term does not affect the temperature profile's shape and any driving temperature gradients. Figure 7.13 indicates that the temperature difference is not sinusoidal in time, as the wall temperature oscillates with the fundamental pulsation frequency. The instantaneous nature of heat transfer is dependent on the amplitude and phase relations of the wall and bulk temperatures. Although the governing energy equation is linear, a non-linear coupling has arisen between the oscillating velocity and temperature components.

The physical meaning of a time-dependent heat transfer coefficient is ambiguous where heat flux and temperature difference are not proportional. In the field of dropwise condensa-

tion [103], for example, the error bounds of calculating h from ΔT can yield contradictory results, and the concept of a mean heat-transfer coefficient is not considered helpful. While the magnitudes may give some indication of heat transfer effectiveness, they should be considered approximate. Furthermore, errors in h , which is inversely proportional to ΔT , become large when the fluctuations in the temperature difference are small. Similarly, the heat flux is not proportional to the driving temperature difference for the case of constant heat flux (see Figure 7.13). It appears that non-dimensionalisation of the temperature by the driving temperature difference permitted the definition of a time-dependent Nusselt number in complex notation for Nield and Kuznetsov [78]. However, the amplitude of the flow rate pulsations was assumed small and the product of the fluctuating components $u'\theta'$ was neglected, such that no time-averaged change in the Nusselt number was found.

Table 7.1: Comparison of time-averaged Nusselt number definitions. The steady Nusselt number is $Nu_0 = 5.9805$ [98].

Wo	1.4	3.1	7.0	22.1
\overline{Nu}_{qm}	5.9311	5.9678	5.9796	5.9805
\overline{Nu}_{mq}	6.2919	6.1379	6.04	5.9883

For illustrative purposes, the mathematical problems associated with the heat transfer

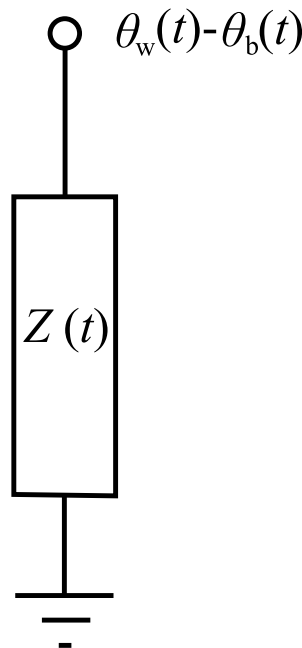


Figure 7.14: Network showing generalised impedance $Z(t) = 1/Nu(t)$ for constant heat flux $q = 1$ and generalised potential $\theta_w - \theta_b$.

coefficient are explicitly quantified for a pulsating flow under constant heat flux. As discussed in Section 3.3.1, time-averaging of the numerator and denominator of $Nu = 1/(\theta_w - \theta_b)$ should be performed prior to performing the division (\overline{Nu}_{qm}) to facilitate direct comparison to a steady flow [29, 30]. Calculating instantaneous values of the Nusselt number effectively changes the order of averaging and division (\overline{Nu}_{mq}). As a result, the time-average of any temporal plot of the dimensionless heat transfer coefficient does not agree with the time-averaged definition given in Equation 3.31 and can actually falsely predict heat transfer enhancement. Also, it is not clear whether the temperature-velocity product $u\theta$ should be divided by the time-averaged flow rate or the instantaneous flow rate, since no rigorous definition of a time-dependent bulk temperature has been established. After much analysis of both definitions, the author has opted to divide by the time-averaged flow rate since the definition achieves more accurate values of \overline{Nu}_{qm} at intermediate to high frequencies. Table 7.1 gives the values of the Nusselt number, where the order of averaging and division has been changed. For these calculations, the component relating to the one-dimensional displacement of fluid has been retained (unlike Figure 7.13). Its removal appears to give better estimates at very low frequencies (e.g. $Wo = 0.03$) where $\theta_w - \theta_b$ approaches zero during the cycle (some studies allow Nusselt number to become infinite momentarily [105]). However, the predicted \overline{Nu}_{mq} is still higher than \overline{Nu}_{qm} . Mathie and Markides [106] used this non-linearity to quantify a heat transfer augmentation ratio $A = 1 + \overline{h'\Delta T'}/\overline{h\Delta T}$ where the heat transfer is compared to a "steady equivalent", rather than a literal steady flow. Since $\overline{Nu}_{qm} < \overline{Nu}_{mq}$, the $\overline{h'\Delta T'}$ term in Equation 3.33 is negative. Hence, both the definition of enhancement used in the current work (Equation 2.6) and A become increasingly negative at low frequencies. It appears that the non-linearity of the problem does indeed relate to heat transfer reduction. For the reasons discussed in this section, a complex representation is not used and the heat transfer performance is interpreted instead as an impedance Z :

$$Z(t) = \frac{1}{Nu(t)} = \theta_w(t) - \theta_b(t) \quad (7.1)$$

where the simple relationship between Z and $\Delta\theta$ is linear (see Figure 7.14). A heat transfer coefficient is not necessary as the exact state of heat transfer has been described in terms of the unsteady axial heat flux and the driving temperature difference. Degiovanni and Remi

[160] have proposed using a generalised impedance as an alternative to the heat transfer coefficient for modelling thermal boundary conditions varying in space and time. The green line of Figure 7.13 is illustrative of the component of the time-varying impedance that effects a time-averaged change of heat transfer. However, a robust definition of the time-varying bulk temperature has not been established. Furthermore, the time-dependent behaviour of the impedance changes substantially depending on the definition. Hence, no definitive comment can be made on optimisation of heat transfer with respect to the time-varying temperature difference.

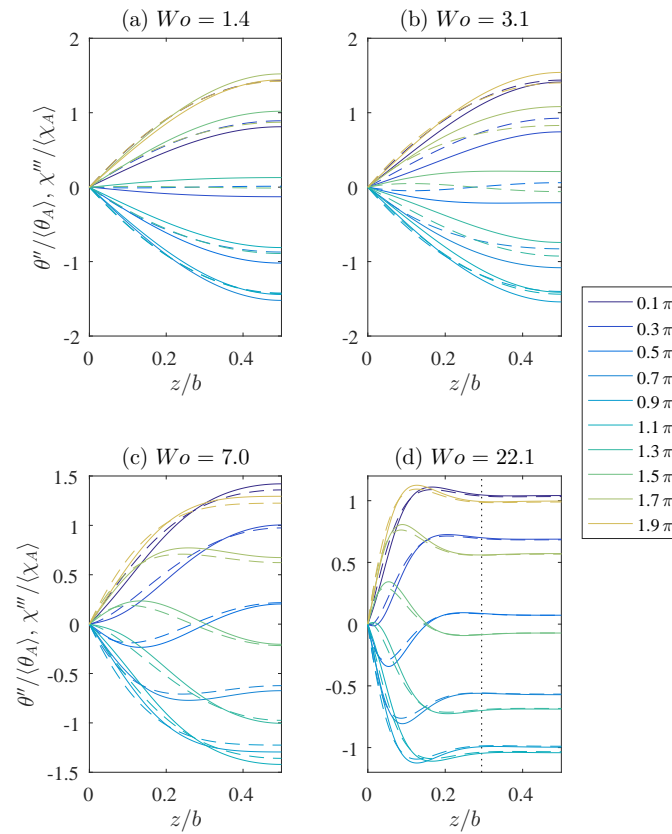


Figure 7.15: Oscillating temperature profiles (solid lines) and displacement profiles (dashed lines) for $Pr = 5.6$ and (a) $Wo = 1.4$, (b) $Wo = 3.1$, (c) $Wo = 7.0$, (d) $Wo = 22.1$ in a parallel plate channel with constant temperature walls $k_w = \infty$ and $\hat{w} = 100D_h$ [69]. Dotted lines mark the Stokes layer thickness δ_v .

7.3 Mechanism 2: Enhanced Wall Shear Stress Analogy

As discussed, the similarity between the turbulent diffusivity of momentum and heat has been identified in steady flow in a pipe for $Pr = 1$ [153], such that the temperature profile may be estimated if the velocity profile is known. Furthermore, the relationship holds true in the direction normal to the wall of non-circular polygonal tubes if the angles between walls are not too small [154, 155], although a balance of stresses and heat fluxes (through Equations 3.1a and 3.1b) will not hold true near the corners. The similarity between the velocity and temperature field has not been established for the case of unsteady flow. In the previous section, the similarity of the local time-dependent temperature and displacement profiles in the main fluid body – especially at high frequencies and Prandtl numbers – was demonstrated for the constant heat flux boundary condition (see Figure 7.3). However, the slopes of the time-dependent temperature profiles at the wall are fixed at zero such that the second mechanism of heat transfer enhancement is precluded and corresponding profiles differ significantly in the close near-wall region. The aim of this section is to address the discrepancy at the wall, showing that the difference in behaviour owes entirely to the constant heat flux boundary condition. In fact, the near-wall behaviour matches if the slope at the wall is permitted to vary at constant temperature. Previously, the agreement between the temperature profiles generated by the insulated form of the conjugate analytical solution in a parallel plate geometry [69] and the two-dimensional solution with two isoflux heated broad walls (the H2(2L) boundary condition) was illustrated (see Figure 7.2). In future, the solution of the 2-D energy equation of Section 3.3 should be modified for the case of constant wall temperature. For now, similarity is assumed to extend the 1-D solution to an approximate 2-D analysis. The conjugate 1-D solution [69] adjusted to the same non-dimensionalised form as Section 3.1.3 is detailed in the Appendix.

7.3.1 Transverse Temperature Profiles

Figure 7.15 exhibits the normalised temperature and displacement profiles in a parallel plate channel with thick constant temperature walls for a realistic Prandtl number of water. A significant improvement in similarity has been achieved compared to the z temperature distributions of Figure 7.3, particularly near the wall and at low frequencies. Since the

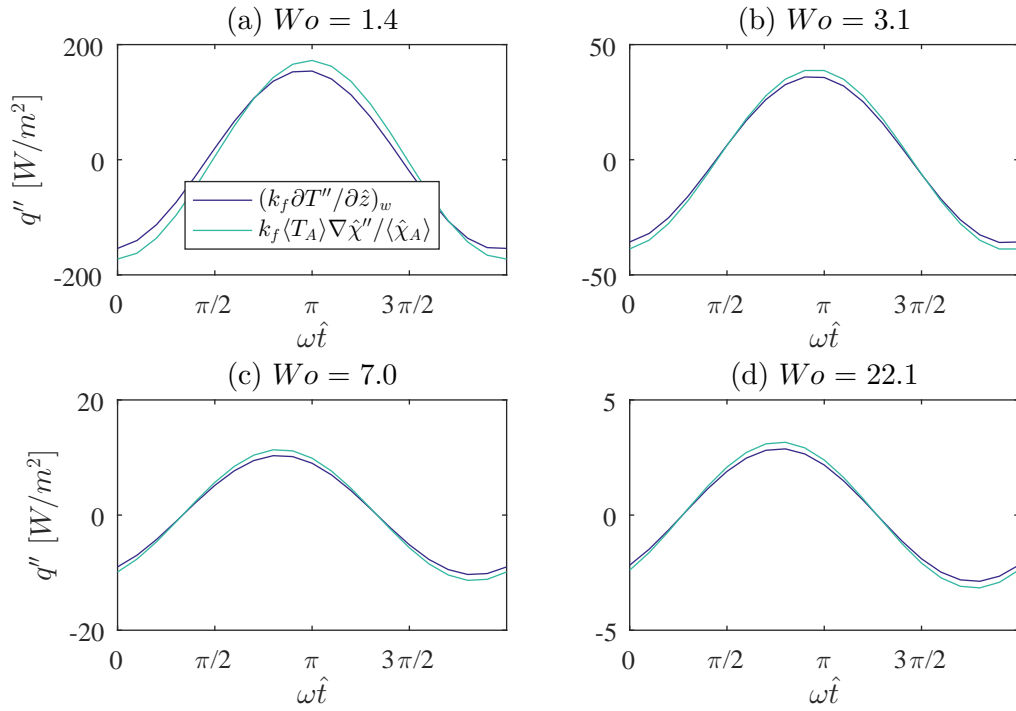


Figure 7.16: Oscillating heat flux and wall displacement gradient for $Pr = 100$ and (a) $Wo = 1.4$, (b) $Wo = 3.1$, (c) $Wo = 7.0$, (d) $Wo = 22.1$ in a parallel plate channel with constant temperature walls $k_w = \infty$ and $\hat{w} = 100D_h$.

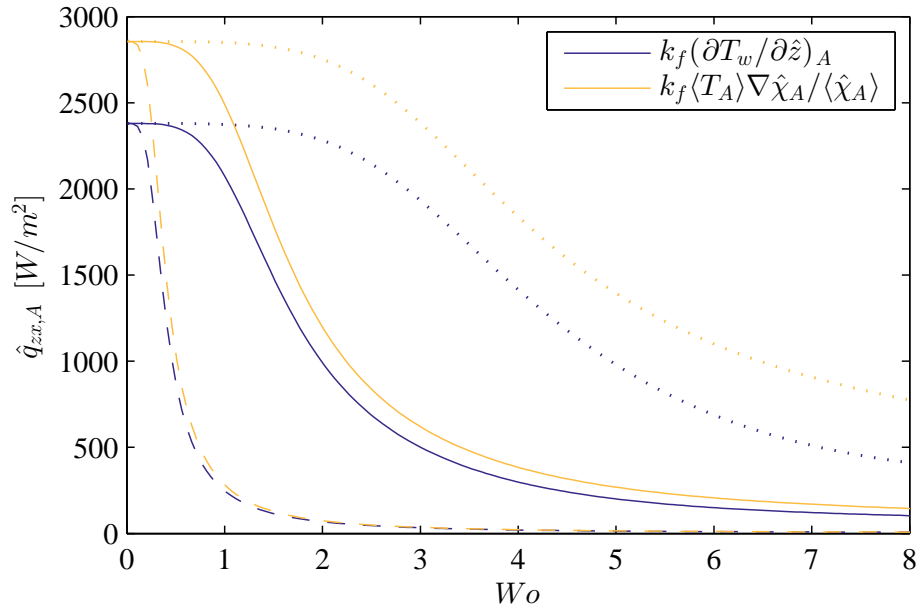


Figure 7.17: Amplitude of heat flux and wall displacement gradient with frequency Wo in a parallel plate channel with constant temperature walls $k_w = \infty$ and $\hat{w} = 100D_h$ for $Pr = 1$ (dotted lines), $Pr = 5.6$ (solid lines) and $Pr = 100$ (dashed lines).

profiles are normalised by their space-averaged values, the similarity works equally well in dimensional variables. At low frequencies, the amplitudes of temperature oscillations are well predicted, though discrepancies remain in the local phase values. At the limit of high Prandtl number, the profiles are found to become identical at all transverse locations. Figure 7.16 plots the amplitudes and phases of the time-dependent wall temperature and displacement gradients for $Pr = 100$, where a negative value means that heat is flowing to the wall (i.e. $\langle T \rangle > T_w$). The π radian phase difference between the temperature and displacement fields has been removed for clarity, $\chi''' = \Re[\psi_u e^{i(Wo^2 t - \phi_Q - \pi/2 - \pi)}]$. The similarities of the amplitudes with frequency are plotted in Figure 7.17 for various Prandtl numbers. The offset between the magnitudes at each Prandtl number is likely proportional to some measure of the thermal diffusion. Also, the magnitudes of the heat flux are independent of the steady heat flux component. Assuming sufficiently high frequency and Prandtl number, the equality of the dimensional wall heat flux and displacement gradient is thus:

$$\hat{q}_{zx}'' = -k_f \cdot \left(\frac{\partial T_w''}{\partial \hat{z}} \right) \approx -k_f \cdot \frac{\langle T_A \rangle}{\langle \hat{\chi}_A \rangle} \cdot \nabla \hat{\chi}_w''' \quad (7.2)$$

where $\nabla \hat{\chi} = \partial \chi / \partial \hat{z}$. Dimensional analysis indicates that the terms on the right of Equation 7.2 have units W/m^2 . This is equivalently given in terms of the velocity and wall shear stress parameters by:

$$\begin{aligned} \hat{q}_{zx}'' &= \Re(\psi_{\hat{q}_{zx}} e^{i(Wo^2 t - \phi_Q - \pi/2)}) \\ \psi_{\hat{q}_{zx}} &\approx -\frac{k_f}{\mu} \cdot \frac{|\Psi_{\langle T \rangle}|}{|\Psi_{\langle \hat{u} \rangle}|} \cdot \psi_{\hat{\tau}} \end{aligned} \quad (7.3)$$

Hence, the displacement profile may be used as an approximate solution for constant temperature in a parallel plate channel. The heat flux in a rectangular channel may now be estimated using the known hydrodynamic parameters with Equation 7.3. The case of four walls heated at a constant temperature is considered to illustrate the equivalent behaviour along the short wall (i.e. the yx component). Figure 7.18 depicts the local time-dependent heat fluxes, which are qualitatively similar to the wall shear stress profiles of Figure 6.11. Further processing would give local heat flux enhancements relative to equivalent steady flows, analogous to the local wall shear stress enhancement of Figure 6.12. Furthermore, heat transfer for the more realistic case of a finite wall thermal resistance (i.e. somewhere in

between isoflux and isothermal heating) could be approximated by including capacitive and lateral conduction terms (with distributions such as the solid lines of Figures 4.15 and 4.14) in an energy balance.

7.3.2 Nusselt number

Gedeon [79] developed the idea of a complex Nusselt number for an oscillatory flow in a thick-walled channel using a Nusselt number that uses the cross-sectional mean temperature and the fluid reference temperature $Nu_m = q' D_h / [k_f (T'_w - \langle T' \rangle)]$. The heat flux $q' = \Re[\psi_q \cdot e^{iWo^2 t}]$ and $\Delta T' = \Re[\psi_{\Delta T} \cdot e^{iWo^2 t}]$ oscillate with the same frequency and the exponential terms vanish. The wall of the channel is fixed at very large thickness such that the wall temperature is

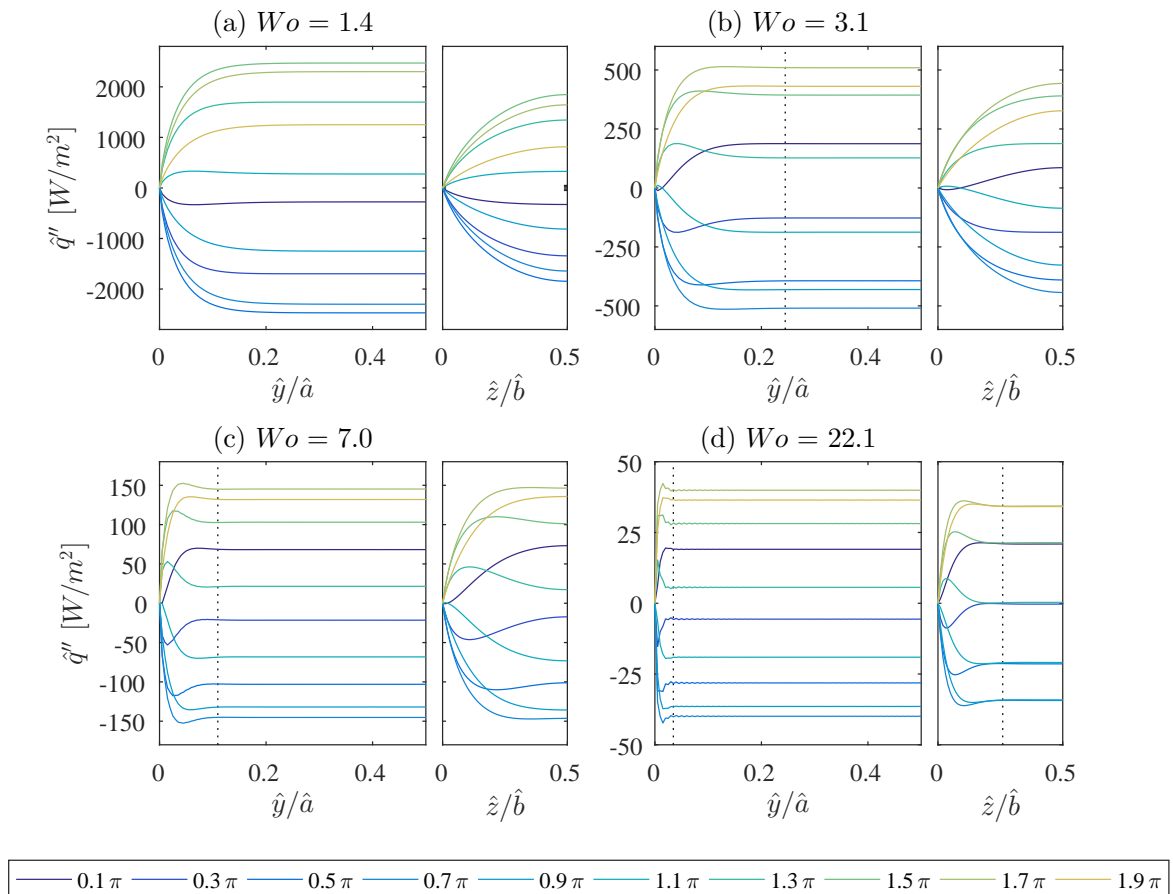


Figure 7.18: Oscillating heat flux profiles calculated using Equation 7.3 for $Pr = 5.6$ and (a) $Wo = 1.4$, (b) $Wo = 3.1$, (c) $Wo = 7.0$, (d) $Wo = 22.1$ in a rectangular channel. Dotted lines mark the Stokes layer thickness δ_v .

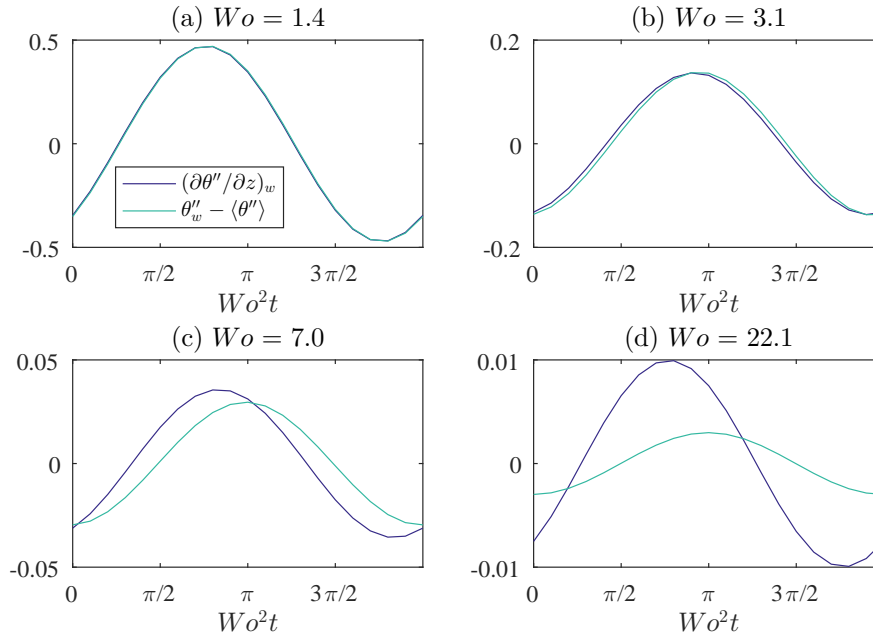


Figure 7.19: Oscillating wall temperature gradient and temperature difference for $Pr = 5.6$ and (a) $Wo = 1.4$, (b) $Wo = 3.1$, (c) $Wo = 7.0$, (d) $Wo = 22.1$ in a parallel plate channel with constant temperature walls $k_w = \infty$.

invariant in both time and space. The solution has been extended by the author for a wall with variable thickness (see Appendix). The wall may have high thermal conductivity but a low thermal mass, such that the temperature is constant in space but not time (this acts to reduce the augmentation of the temperature gradient at the wall). For a slowly oscillating flow, q' and $\Delta T'$ are in phase and the Nusselt number is constant in time since the quantities always have the same ratio (see Figure 7.19(a)). Furthermore, the phasor representation has solved the problem of division by zero by transforming to a domain where the amplitudes in the denominator are non-zero. Nu is a complex-valued coefficient that relates the relative phase difference between the heat flux and temperature difference. For higher frequencies, the heat flux and temperature difference are out of phase. Figure 7.20 indicates that the Nusselt number is enhanced with increasing frequency in a parallel plate channel. Although the amplitude of the temperature gradient at the wall decreases with increasing frequency (see Figure 7.17), the amplitude of the temperature difference decreases at a faster rate.

Since the mean temperature is used, the solution fails to capture any change in heat transfer as a result of the bulk temperature variation. Furthermore, the complex representation of single-frequency time-dependent variables requires a linear (albeit complex-valued)

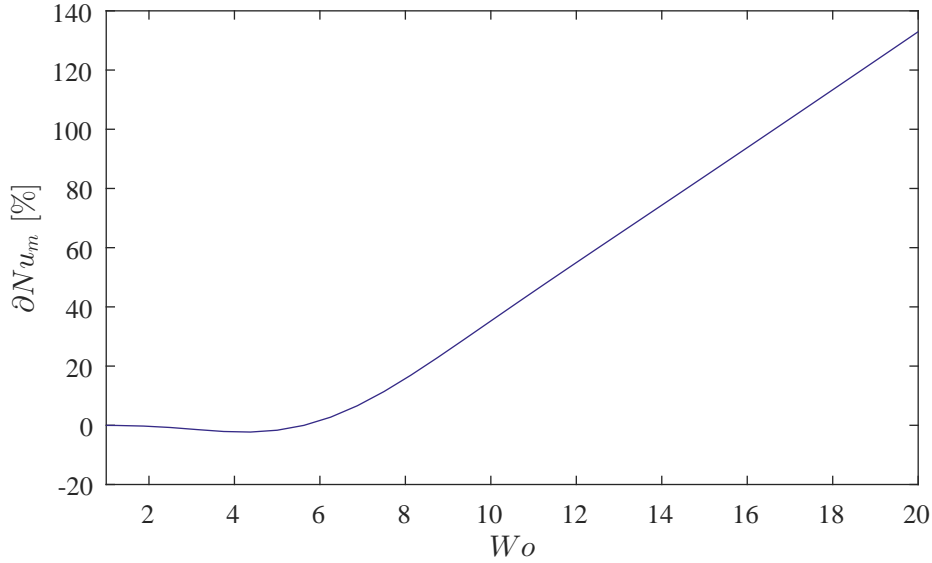


Figure 7.20: Enhancement of Nusselt number based on the mean temperature with frequency Wo at constant flow rate amplitude $Q_A/Q_0 = 0.7$ for $Pr = 5.6$ in a parallel plate channel with constant temperature walls $k_w = \infty$ and $\hat{w} = 100D_h$.

relationship between the quantities. Since the bulk temperature contains second harmonics of the pulsation frequency (see Figure 7.13), the Nusselt number based on bulk temperature varies in time such that the heat flux is $q'(t) = (k_f/Dh)Nu'(t)\delta T'(t)$. This system is not linear, i.e. it can not be treated by mapping all single-frequency temperature differences to all single-frequency heat fluxes by a matrix of constant (i.e. frequency-dependent but not time-dependent) complex coefficients. In other words, the heat flux contains spectral frequencies other than the pulsation frequency.

7.4 Conclusions

This chapter built on the results of Chapter 6 to characterise the unique mechanisms of heat transfer enhancement using (i) a novel analytical solution in a rectangular channel heated under constant heat flux and (ii) an existing analytical solution in a parallel plate channel heated by constant temperature walls [69]. The first mechanism (through bulk temperature modulation) is elucidated by the isoflux solution, while the second mechanism (through augmented near-wall temperature gradients) is illustrated by the isothermal solution. To the best of the author's knowledge, the 2-D solution for temperature constitutes the first

in a channel with a two-dimensional cross-section. The oscillatory temperature profiles, computed in a narrow channel with two heated long walls, are found to coincide well with the 1-D solution. The change in Nusselt number due to pulsations, computed in a square channel with four heated walls, is in reasonable agreement with existing solutions in pipes. Also, the solution has been verified over a portion of the parameter space using a numerical CFD model.

It is well-known that the thermal problem is heavily dependent on the hydrodynamics of the flow. However, no framework is available in the literature for extending the effect of time-varying displacements to likely effects on instantaneous heat transfer. It is found that the temperature profile is formed primarily as a result of fluid displacement against the temperature gradient, such that the normalised temperature profiles are the inverse of the displacement profiles when diffusion is negligible and the wall is at a constant temperature. In contrast to steady flow, where the problems are similar at $Pr = 1$, the oscillating velocity and temperature profiles are most similar at high Prandtl numbers. Hence, the temperature profile may be estimated if the velocity profile is known, provided that the frequency and Prandtl number are not too low (see Figure 7.17). Furthermore, the local wall shear stress may be mapped to the local wall heat flux using Equation 7.3. In a rectangular channel, the similarity may not hold near the perpendicular boundaries at the corners, since the balance of stresses and heat fluxes are less similar. In future, it may be possible to modify the similarity equation to account for the effect of thermal diffusion and the offset between the estimates of Figure 7.17. Ideally, the high accuracy achievable with velocity measurement techniques could be applied in the study of heat transfer. For example, accurate estimates of second order parameters such as vorticity typically require time-averaging over 1000 image pairs with particle image velocimetry (PIV). Local temperature measurement techniques such as planar laser-induced fluorescence (PLIF), which are less mature, cannot achieve the same estimates. This perhaps explains this reason that the theory associated with the second derivative of the temperature field has not been developed (nor has the parameter been given a name!). However, its role in the balance of local heat flow in the fluid is analogous to the role that vorticity plays in the balance of stresses (see Figure 6.7). Hence, it is useful to use analogies with the flow hydrodynamics.

The phases of temperature and velocity in the hydrodynamically- and thermally-developed

region result in a universal reduction in heat transfer by the first mechanism. Since transverse diffusion drives the mechanism, the reduction decreases with increasing frequency and Prandtl number (see Figure 7.10). The second mechanism acts to augment the heat fluxes at the wall during portions of the cycle, although the time-averaged augmentation is zero. Similarly, the Nusselt number enhancement (based on the mean temperature) increases with increasing frequency and Prandtl number (see Figure 7.20). According to the linear theory, the heat flux and temperature difference increase in proportion and hence the flow rate amplitude has no effect on the Nusselt number. Since Persoons et al. [16] found that the Nusselt number enhancement increased with flow rate amplitude (see Figure 2.24), it is expected that enhancement was due to the bulk-mean reversal mechanism.

Optimal enhancement on a time-averaged basis is hence achieved by high frequencies, high Prandtl numbers and high wall thermal conductivities. On a time-dependent basis, optimisation may be achieved through inspection of the oscillating temperature difference and heat flux. It is generally found that any heat transfer enhancement through the heat flux mechanism is offset by a heat transfer reduction through the bulk temperature mechanism. For example, Figures 7.13 and 7.16 indicate that both the temperature difference and heat flux at the wall are increased over the interval $\pi/2 - 3\pi/2$. To increase the heat flux from the wall to the fluid (or equivalently, to decrease the slope of the temperature gradient at the wall), the mean temperature must be reduced with respect to the wall temperature. However, this has the added effect of reducing the bulk temperature, which increases the temperature difference. The overall effect likely depends on parameters such as the frequency, amplitude and Prandtl number. Chapter 8 sets out to verify the predictions for the wall temperature in a rectangular channel on a local time-dependent basis using infrared thermography (IRT).

Chapter 8

Experimental Heat Transfer of Laminar Pulsatile Flow in a Rectangular Channel

8.1 Introduction

As discussed in Chapter 1, the fundamental aim of this thesis is to characterise the heat transfer enhancement potential of pulsating flow using complementary analytical, numerical and experimental analyses. Using the complete data provided by the novel analytical solution (derived in Section 3.3), the mechanisms of enhancement were investigated on a local time-dependent basis in Chapter 7. The analytical model was found to agree with the numerical CFD model at $Pr = 1$. Heat transfer is altered through either (i) the bulk temperature or (ii) the wall heat flux, though both mechanisms result from the displacement of fluid in the presence of an axial temperature gradient. Nonetheless, experimental analysis is an important step in the verification of underlying theory and should proceed in a manner similar to the hydrodynamic study of Chapter 6. Generally, the local time-dependent measurements of the velocity field were in consistent agreement with theory, as reviewed in Chapter 2. In contrast, heat transfer studies tend to find disagreement, with theory finding negligible or slight changes in heat transfer and experiment finding enhancements as high as 40% [16]. Some of this discrepancy may arise from the larger parameter space of the thermal problem – where complexity is added by parameters such as the Prandtl number and the spectrum of boundary conditions at the wall – and the difficulties in generating a thermally-developed

flow experimentally.

While experiments measuring the temperature profiles of unsteady flows are lacking as a whole, a number of heat and mass transfer experiments have characterised the overall effect of the first mechanism of heat transfer enhancement (through bulk temperature modulations). However, the time-averaged analyses employed ultimately result in a loss of information since any potential optimisation requires understanding of the instantaneous mechanism. Over the time interval $\pi/2 - 3\pi/2$ for example, an overall enhancement of heat flux at the wall appears to be observed (see Figure 7.16). While a multitude of experimental measurement techniques have been used to verify the velocity field on a local time-dependent basis, planar measurement techniques such as planar laser-induced fluorescence are less mature than their velocimetry counterparts. Oscillating temperature profiles have been visualised by a single qualitative experiment at a pair of frequencies corresponding to $Wo = 4.4$, and 12.2 for an incompressible flow [71]. The sinusoidally-varying temperature gradient at the wall has been measured in a couple of experiments [80, 82] for a compressible flow with a step change in axial temperature gradient at a single frequency $Wo = 11.3$. Furthermore, the experimental measurements were compared solely to numerical models. To the best of the author's knowledge, no experiments have been performed for the common flow condition of an incompressible flow in a heated vessel.

Since convective heat flux takes place at the wall, heat transfer enhancement is primarily dependent on the near-wall behaviour of the velocity and temperature field. In Chapter 6, it was necessary to take single measurements of the non-uniform shear stress at each wall using the planar particle image velocimetry (PIV) measurement technique. Similarly, a planar temperature measurement technique (e.g. PLIF) performs zero order heat flux measurements at the wall. Hence, the technique of infrared thermography (IRT) is used to achieve high spatial resolution of the non-uniform convective heat flux at the wall. IRT acts to approximate the constant heat flux boundary condition such that temperature variations in the flow are accentuated; however, the ideal isoflux state actually precludes any variation in convective heat flux (as discussed in Chapter 7). In contrast, constant temperature heat sources experience the highest enhancement due to unsteady effects in the flow, though the non-variation of temperature means that the heat flux enhancement can not readily be measured with good spatial and temporal resolution. For example, Mosyak [117] used a thick copper

plate and thin stainless steel foil to approximate the isothermal H1 and isoflux H2 boundary conditions, respectively, in turbulent flow, finding that the temperature fluctuations of the latter were an order of magnitude higher. While not quite Heisenberg's uncertainty principle, some accuracy in the quantification of enhancement is sacrificed to allow measurement of the thermal phenomena. For this reason, IRT is commonly viewed as a technique that is particularly good at identifying regions of local relative heat transfer enhancement.

Generally, the relationship between wall shear stress and convective heat flux has remained underdeveloped in the literature. In Figure 6.12, the local time-dependent amplification of wall shear stress with pulsation was predicted. An analysis of the similarity between the gradients of the velocity and temperature fields at the wall under various conditions was performed in Chapter 7. It has been proposed that the qualitative behaviour (and perhaps quantitative behaviour) of the wall heat flux may be approximated from the wall shear stress. Finally, using the hydrodynamic prediction tools developed in Chapter 6 and the infrastructure for quantifying similarity, the local enhancement of convective heat flux may be tested on an experimental basis. Hence, the aim of the current study is to build on the experimental hydrodynamic results to measure the local time-dependent variation in wall temperature for pulsating flow in a heated rectangular channel.

8.2 Wall Temperature and Convective Heat Flux Profiles

To permit comparison with analytical theory the flow should be thermally-developed and devoid of secondary flow effects. Theoretical predictions of the thermal development length for steady flow were discussed in the experimental analysis of the heat transfer apparatus (see Section 4.2.2). In general, it has been found by experiment and CFD that thermal development takes much longer than that predicted by $Pr \cdot L_e$. The 300 mm heated length upstream of the viewing window is just enough to ensure thermal development for $Re_0 < 80$ ($Pr \cdot L_e \approx 300$ mm for $Re_0 = 200$), which is inspected through the uniformity of the transverse temperature profiles with increasing downstream distance. The solid lines and dots of Figure 8.1 plot the steady temperature profiles predicted by the analytical and numerical models for the channel heated at a single long wall H2(1L). The idealised models assume that no lateral conduction, radiation or buoyancy take place and that the rear side of the wall is perfectly

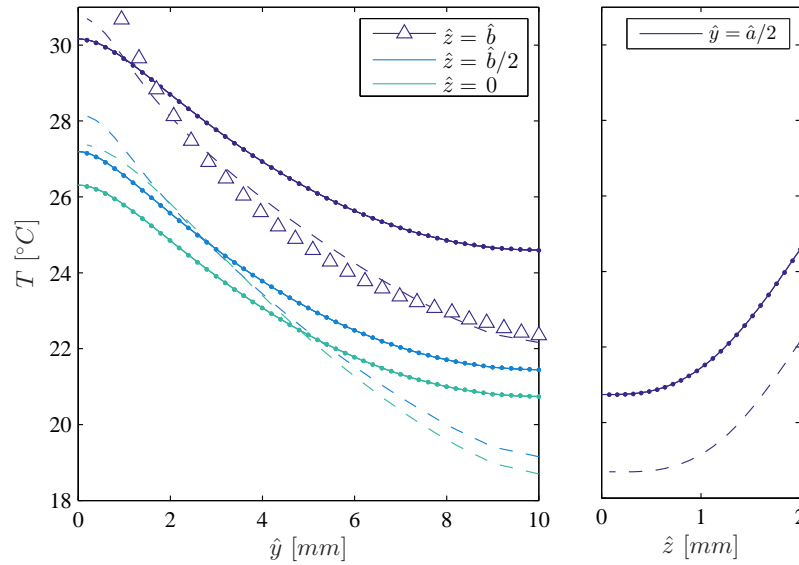


Figure 8.1: Steady temperature profiles for $Re_0 = 40$. Solid lines and dots represent analytical (–) and numerical (●) solutions, respectively, without buoyancy. Dashed lines and symbols represent the numerical solution with buoyancy (–) and the experimental measurements (Δ), respectively. The wall at $\hat{z} = \hat{b}$ is heated.

insulated. Table 4.7 indicates that the space-averaged value of lateral conduction, conduction through the insulating air gap and radiative losses are small compared with the generated heat flux. However, the heat flux by lateral conduction is appreciable near the corners owing to the steep transverse temperature gradient. This acts to equalise the temperature profile at the wall of a channel [99, 100] (see Figure 3.3). Also, the low Reynolds number flow (with $Gr/Re_0^2 \approx 0.3$) may result in heat transfer by mixed convection, as discussed in Section 4.2.2. For these reasons, the steady component of the experimental measurements (plotted by markers) differs quite substantially from the thin-walled theory. Furthermore, the non-zero slope and positive value of $\nabla^2 T$ near the corner indicate that heat is flowing to this region, rather from this region as predicted by theory. This suggests that the foil outside of the channel boundary is indeed heated. The dashed lines of Figure 8.1 model the same steady flow with buoyancy using the numerical CFD model (but without wall conduction). Much of the discrepancy between the idealised predictions and the experimental measurements appears to result from buoyancy effects in the channel. In future, it may be necessary to change the fluid to prevent mixed convection, since higher Reynolds numbers require longer development lengths. Nonetheless, the time-dependent components of lateral wall conduction

and buoyancy will be much smaller than their time-averaged counterparts, and the effects cannot establish themselves fully before conditions are reversed (the time-averaged value is zero). Hence, a lesser impact is expected on the time-dependent temperature field that is of primary concern in this research.

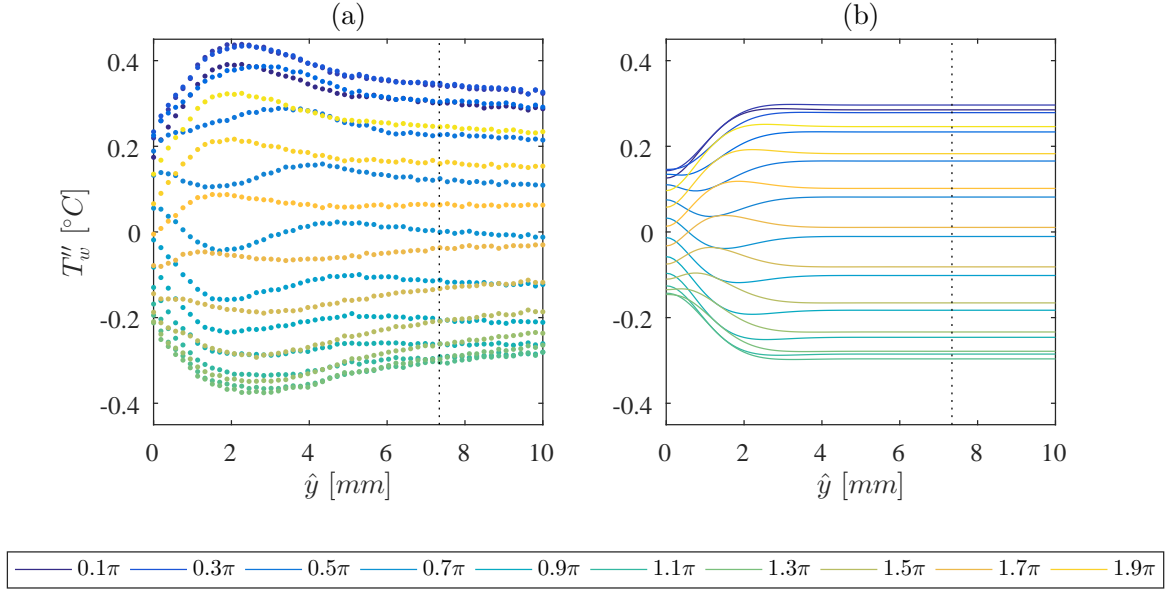


Figure 8.2: Oscillating wall temperature profiles for $Wo = 1.76$, $Q_A/Q_0 = 0.7$, $Pr = 5.6$. Solid lines and dots represent analytical solutions (—) and experimental measurements (\bullet), respectively. Dotted lines mark the Stokes layer thickness $\hat{\delta}_v$. While all 20 phase values are plotted, the legend only identifies 10 for brevity.

Figure 8.2 compares the phase-averaged oscillating temperature profiles at the heated wall of the channel for $Wo = 1.76$, $Q_A/Q_0 = 0.7$ measured using IRT, to the novel analytical solution of Section 3.3. The data are found to capture the unique frequency-dependent characteristics of the analytical solution such as inflection points and near-wall overshoots, which are similar to those observed in the experimental velocity profiles of Chapter 6. The region containing the annular effects is well-predicted by the Stokes layer thickness (marked by dotted lines) suggesting that the temperature profile is formed primarily as a result of the displacement of fluid against the axial temperature gradient. The lack of fluid motion very near the corner means that heat transfer occurs primarily by diffusion and a phase lag develops with respect to the main fluid body. Annular effects in the temperature profile have been observed previously in experiments [71, 82] and numerical models [83, 85], though not for an incompressible flow in a heated vessel. The amplitude of temperature oscillations

of $0.3\text{ }^{\circ}\text{C}$ near the mid-wall are in agreement with the analytical solution, although the amplitudes are slightly larger than predictions near the corner. This may result from the same heat leakage that affected the steady temperature profiles in this region, which causes a non-zero slope at the corners. Furthermore, the uncertainty associated with the experiment is large compared with the measured values, especially near the corners. Figure 8.3 presents the sinusoidal behaviour of the space-averaged wall temperature in relation to the flow rate. As before, the amplitude of the experimental measurements is larger than that of the analytical solution. The phase difference of 66° between the flow rate induced by the gear pump and the wall temperature measured by the thermal camera is well-predicted by the theoretical value of 74° .

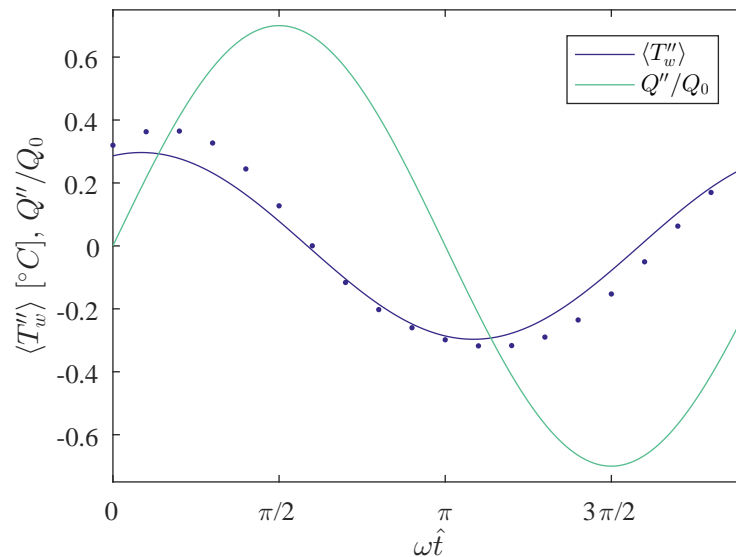


Figure 8.3: Oscillating mean wall temperature and flow rate for $Wo = 1.76$, $Q_A/Q_0 = 0.7$, $Pr = 5.6$. Solid lines and dots represent analytical solutions (—) and experimental measurements (●), respectively.

Figure 8.4 plots the normal temperature profiles in the wall and fluid according to the 1-D and 2-D analytical solutions characterised in Chapter 7. Firstly, the fluid temperature profiles of the 1-D (marked by solid lines) and 2-D (marked by dashed lines) solutions under constant heat flux are similar, with the discrepancy arising from the difference in aspect ratio between the parallel plate and rectangular ($\hat{a}/\hat{b} = 10$) geometries. Secondly, while a very slight conjugation exists due to the wall thickness, the time-dependent problem approximates the isoflux boundary condition well, according to the 1-D solution. The amplitude of temperature oscillations at the wall for the ideal boundary condition (plotted by dotted lines) is just 2.7%

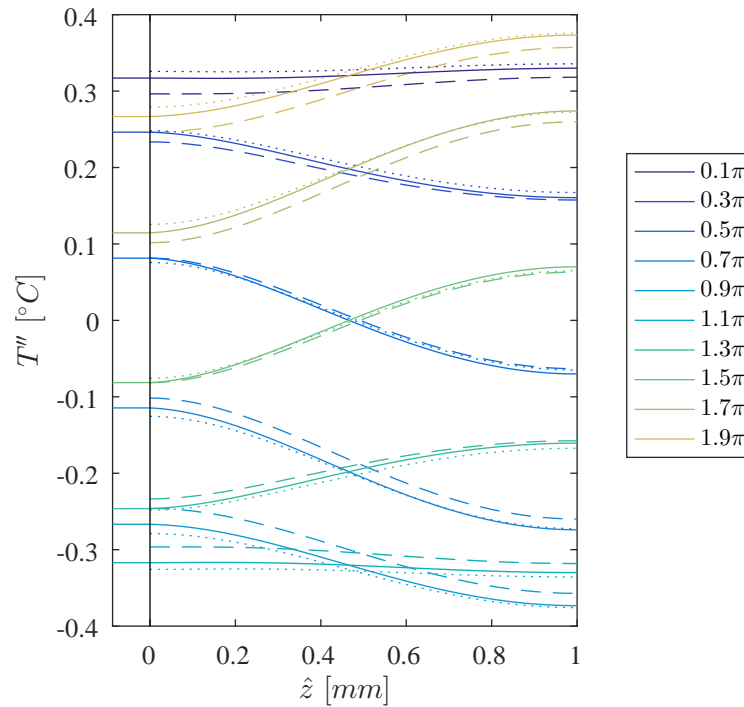


Figure 8.4: Oscillating fluid and wall temperature profiles in normal \hat{z} direction for $Wo = 1.76$, $Q_A/Q_0 = 0.7$, $Pr = 5.6$. The solid lines (—) represent the 1-D solution with conducting Inconel 625 walls with thickness $\hat{w} = 25 \mu m$. The dashed (---) and dotted (\cdots) lines represent the 2-D and 1-D constant heat flux solutions.

greater than the realistic case (plotted dashed lines), although transient lateral conduction in the walls may augment this discrepancy. The distribution within the wall (whose scale has been enhanced for clarity) is approximately uniform and clearly adheres to the lumped capacitance model, as analysed in Section 4.2.2 using the Biot number. The slowly-oscillating flow with $Wo = 1.76$ falls near the boundary of the quasi-steady and transitional regimes of unsteadiness (see Chapter 6), and the time-scale of the pulsations is long compared with that of thermal diffusion. As a result, the wall-normal temperature profiles are relatively uniform compared with the corresponding velocity profiles, which are subject to the no-slip boundary condition. As the time-scale of oscillations is decreased, less heat is diffused to the wall and the amplitudes of wall temperature oscillations drop significantly, such that wall temperature and heat flux variations are difficult to measure using IRT. The smaller wall temperature oscillations at higher frequencies may be inspected from Figure 7.3. While adherence to the isoflux condition results in larger temperature oscillations that are measurable using IRT, a price of measurement is paid in the estimate of convective heat flux enhancement.

According to 1-D theory, the enhanced heat flux at the wall of the experimental setup is just 0.0003% of that achievable using a constant temperature boundary condition. According to the analytical solution, the change in bulk temperature is $-0.0086 [K]$ which is not measurable using thermocouples. This amounts to a 0.25% reduction in the Nusselt number from its steady value of $Nu_0 = 4.52$.

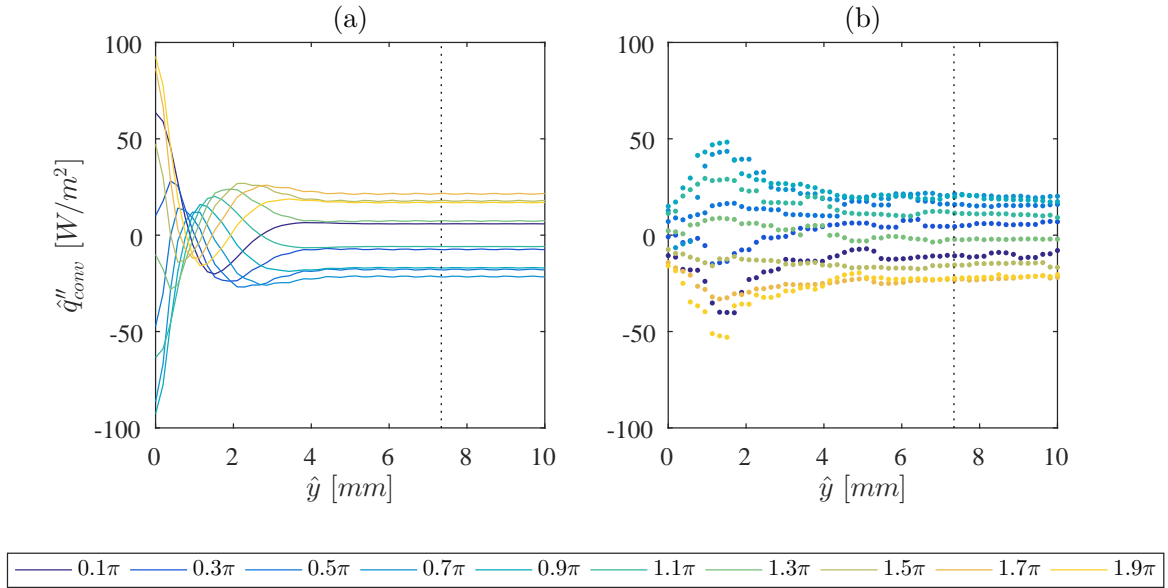


Figure 8.5: Oscillating convective heat flux profiles for $Wo = 1.76$, $Q_A/Q_0 = 0.7$, $Pr = 5.6$. Solid lines and dots represent analytical solutions (—) and experimental measurements (●), respectively. Dotted lines mark the Stokes layer thickness $\hat{\delta}_v$.

Figure 8.5(a) presents the local time-dependent convective heat flux to the fluid calculated using the energy balance of Figure 4.13. The time-dependent heat flux profiles of lateral conduction, heat storage, conduction through the air gap and radiation were analysed in Section 4.2.2.2. Figure 8.5(b) uses the analytical distributions of $\partial^2 T / \partial \hat{y}^2$ and $\partial T / \partial \hat{t}$ at the infinitely-thin wall, along with the experimental wall properties of Table 4.4, to predict the combined effect of the capacitive and lateral conduction terms for a finite wall thickness. In other words, it is assumed that lateral conduction in the wall does not affect the fluid temperature profile. The contributions of heat flux by lateral conduction and capacitance distort the heat flux profiles compared to the idealised profiles for a constant temperature that were similar to the wall shear stress profiles (see Figure 7.18). Hemida et al. [29] found numerically that wall thermal inertia damps out pulsation effects, especially at high

frequencies. For the ideal case of constant heat flux, the time-dependent component of the convective heat flux is zero since all generated heat is transferred to the fluid at all times. The convective heat flux is found to vary with an amplitude of 20 W/m^2 in the central wall region, which constitutes a maximum enhancement of less than 1% of the generated heat flux. In Chapter 6, the local time-dependent amplification of wall shear stress with pulsation was studied with Figure 6.12. Even at the lowest frequency ($Wo = 1.4$), slight enhancements and reductions were observed near the corners, which resulted from the development of a near-wall velocity overshoot. Furthermore, the wall shear stress could be both instantaneously enhanced and reduced at different locations of the wall. The same qualitative behaviour is observed in Figure 8.5. Hence, it appears that heat transfer may be slightly enhanced and diminished near the corners of a rectangular channel with very little work expense. However, it should be noted the relative uncertainty of the convective heat flux measurements is large, especially near the corners.

8.3 Conclusions

This chapter has complemented the experimental velocity measurements of Chapter 6 with thermal measurements of the oscillating wall temperatures for a pulsating flow with $Wo = 1.76$ in a rectangular channel. To the best of the author's knowledge, the results constitute the first experimental measurements of the temperature profiles of a sinusoidally-pulsating incompressible flow in a heated vessel. The low Reynolds number flows mean that the steady temperature profiles are affected quite significantly by natural convection. For a microchannel (with $D_h = 200 \mu\text{m}$) heated at a constant heat flux of 1000 W/cm^2 and cooled by water, it has been calculated that mixed convection effects are negligible for $Re_0 > 15$. The amplitude of oscillation near the centre of the wall of 0.3 K is in agreement with that predicted by the novel analytical solution in a rectangular geometry. Near the corner, the profiles contain similar frequency-dependent characteristics such as inflection points and overshoots. The annular effects are contained within a region well defined by the Stokes layer thickness. The time-dependent behaviour of the mean temperature is approximately sinusoidal and leads the flow rate, with a phase advance of 66° relative to the flow rate, in reasonable agreement with theory.

Infrared thermography (IRT) is preferred to planar measurement techniques to measure the local time-dependent variation of the convective heat flux. The time-dependent convective heat flux profile is well predicted using the behaviour of the 2-D analytical solution at the infinitely-thin wall. While heat storage and lateral conduction distort the shape of the wall heat flux profile compared to the corresponding wall shear stress profile, local enhancements and reductions are observed that are qualitatively similar to the wall shear stress amplification of Figure 6.12. As concluded in Chapter 6, pulsations may be used to enhance and reduce heat transfer near the corners of rectangular channels at low frequencies. While the local time-dependent relationship between wall shear stress and convective heat flux was developed by the theory of Chapter 7, a connection has been made using experimental measurements. The heat transfer enhancement by the second mechanism is approximately 1% of the generated heat flux. However, this is a small fraction of that achievable as the constant temperature boundary condition is approached, according to theory. While beyond the scope of the current research, an experimental quantification of the heat transfer enhancement experienced by constant heat flux and constant temperature heaters is an interesting endeavour that can give insight into the usefulness of IRT as a quantitative heat transfer measurement technique. The convective heat flux of the isothermal source would require measurements with high resolution in the near-wall region, using a planar fluid measurement technique such as PLIF. In the current thesis, thermal behaviour in the fluid has been analysed using analytical solutions.

Chapter 9

Discussion

This research has sought to improve understanding of the mechanisms of heat transfer enhancement of unsteady fluid flow pulsations using complementary analytical, experimental and numerical techniques. The velocity field is the foundation from which higher level mechanisms and heat transfer behaviour ultimately derive, such that all of the results of this thesis may be related back to the parametric analysis of the velocity problem presented in Chapter 6. Chapter 7 established the connection between the fluid mechanics and heat transfer using a novel 2-D analytical solution and an existing 1-D conjugate solution. Finally, Chapter 8 presented experimental measurements of the wall temperature and convective heat flux, to test the developed theory and measure any heat transfer enhancement by pulsation.

Since the parameter space is large, heat transfer is often treated as a macroscopic science, with engineering correlations used between dimensionless numbers and time- and space-averaged variables. A multitude of applied thermal studies have successfully demonstrated the feasibility of unsteady cooling solutions using a top-down or black box approach. However, the approach has failed to establish consensus on the question of heat transfer enhancement, as reviewed in Chapter 2. In general, a dichotomy exists between hydrodynamic and thermal experiments measuring pulsating flow. While the velocity field has been measured on a local time-dependent basis, heat transfer studies have chased time- and space-averaged heat transfer enhancement. However, convective heat transfer is often unsteady and spatially non-uniform. Hence, the thermal problem should be characterised in a manner similar to the hydrodynamic problem. Since analytical models give complete information of the velocity

and temperature field, classical engineering concepts such as correlations, regimes and the heat transfer coefficient are not actually required. Parametric analyses instead present the explicit interdependencies of the pertinent variables. This thesis set out to use a bottom up approach to the designs of liquid cooling solutions, which has involved adding layers of complexity beginning from the time-dependent velocity and temperature fields.

Compared to the steady state, transient thermal processes are useful for illuminating the underlying physics of heat transfer since complexity arises with the departure from a quasi-steady state. The simplest transients involve impulsive changes in the parameters such as heat flux or wall temperature [161], such that the response of the other flow variables may be inspected. The sinusoidal pulsation is perhaps the simplest transient that achieves a periodic steady-state. The evolution of the near-wall overshoot was traced to small local phase differences between boundary-diffused viscous stresses and instantly-transmitted pressure stresses that occur even at low frequencies. This phase alteration leads to local instantaneous amplifications and reductions of wall shear stress, which average to zero. Although in the quasi-steady state, the approximation of a regime results in a loss of information. Larger phase differences caused viscous and driving stresses to act briefly in tandem to enhance the time-averaged wall shear stress. Thus, the phases of parameters – which were neglected by existing versions of the solutions for the velocity field – may give insight into underlying hydrodynamic mechanisms. In the thermal problem, phase remains just as important. In fact, heat transfer enhancement ultimately depends on the respective phases of temperature and velocity which govern the driving temperature difference between the wall and bulk fluid temperatures.

Analogous to the time dimension, the addition of a spatial dimension adds complexity in space. In this regard, 1-D solutions in pipe are less informative than their 2-D counterparts since the local effects of physical mechanisms may not be as readily inspected. To the best of the author's knowledge, the solution for the rectangular geometry constitutes the first time-dependent solution in a two-dimensional vessel and thus gives the unique opportunity to study local time-dependent heat transfer simultaneously. For example, the local behaviour of the amplitude and phase of the shear stress at each wall was studied for the first time. While the mechanism of heat transfer enhancement by bulk-mean reversal has not been studied in detail, the results may be more illustrative in a rectangular channel, where the local behaviour

of flow reversal is more complex. The addition of a third dimension and an axial temperature gradient with spatial periodicity adds further complexity that will give further insight into the optimisation of heat transfer.

The interdependence of the velocity and temperature field is often stated, but rarely quantified. According to Reynolds analogy, the velocity and temperature profiles of a steady flow along a flat plate with no pressure gradient at $Pr = 1$ are similar, so long as similar boundary conditions exist for the hydrodynamic and thermal problems. In steady internal flow, the governing equations are not mathematically similar owing to a non-zero pressure gradient, though heat and momentum are diffused in the same manner with kinematic viscosity analogous to thermal diffusivity [153]. Practically, this means that the temperature profile can be calculated if the velocity profile and pressure gradient are known. In unsteady flow, annular effects in the temperature profile have been observed previously in experiments [71, 82] and numerical models [83, 85]. While it is known that the wall shear stress is a key indicator of thermal performance, the similarity between the time-dependent problems has not been rigorously established. The temperature profile is formed primarily as a result of fluid displacement against the temperature gradient, although appreciable thermal diffusion may occur at low Prandtl numbers and for long pulsation time periods. The local displacement gradient at the wall is proportional to the local temperature gradient for the constant temperature boundary condition, and thus local wall shear stress data may be used to estimate the local heat flux enhancement. In Figure 6.12, the local time-dependent wall shear stress amplification of pulsating flow was mapped theoretically. In Chapter 8, qualitatively similar behaviour was observed in the experimental measurements of convective heat flux enhancement for a quasi-steady flow (see Figure 8.5). As intuitively proposed in Chapter 1, the simultaneous thinning of the hydrodynamic and thermal boundary layers does indeed act to increase the temperature gradients at the wall. However, the hydrodynamic and thermal fields also interact through the less obvious second order effect of oscillation-induced diffusivity, which acts to move heat in the axial direction against the increasing temperature gradient and reduce advective heat transfer with respect to steady flow. For both mechanisms, the heat transfer performance is improved with increasing frequency and flow rate amplitude, although the pressure cost increases too. A further mechanism exists in the presence of flow reversal although the problem is non-linear and difficult to model using analytical or

numerical techniques. Nonetheless, experiments with periodically-reversing local velocities tend to find significant heat transfer enhancement.

For the case of a unidirectional, hydrodynamically- and thermally-developed flow with flow reversal precluded and negligible axial temperature gradient fluctuations, axial conduction and viscous heating, it has been shown that time-averaged heat transfer is reduced; however, it may be possible to optimise the flow rate pulsations using knowledge of the instantaneous behaviour of the bulk temperature and wall heat flux. The mechanisms are not entirely independent and enhancement of heat flux is typically offset by a reduction in bulk temperature. For example, the mean temperature must be reduced with respect to the wall temperature to increase the heat flux from the wall to the fluid (i.e. to decrease the slope of the wall temperature gradient). However, this also acts to increase the temperature difference (and reduce the Nusselt number) by reducing the bulk temperature. The concept of a heat transfer coefficient is not as meaningful on a time-dependent basis, since the heat flux and temperature difference are not proportional under constant heat flux. Furthermore, the bulk temperature oscillates with twice the pulsation frequency. Hence, a time-dependent impedance may be preferable to characterise the resistance to heat transfer through the temperature difference, although a robust definition of a time-dependent bulk temperature needs to be established from first principles. In applications where a comparison with an actual steady flow is not required, the degree of non-linearity may give some indication of heat transfer effectiveness [106].

While a hydrodynamically- and thermally-developed sinusoidally-pulsating flow has been the primary focus, it is hoped that the generalised analyses of the local time-dependent mechanisms will permit extension to more complex geometries and flow rate modulations. For example, simple transients such as impulsive changes in heat flux or wall temperature [161] constitute generalisations of the periodic-steady state where the variables interact based on continuous periodic changes. Similarly, the case of a time-varying inlet temperature under a steady flow [105] can give insights into the behaviour of a time-varying bulk temperature that results from an unsteady flow. In the same manner, it is hoped that the behaviour of heat transfer under laminar fully-developed sinusoidal pulsations can give insights into more complex heat transfer scenarios by identifying how the velocity and temperature fields are affected by superimposed unsteadiness on a local time-dependent basis.

Chapter 10

Conclusions

This study has characterised the behaviour of hydrodynamically- and thermally-developed sinusoidal pulsations in a rectangular channel geometry using a combination of complementary analytical, experimental and numerical techniques. The complete data sets provided by the theoretical models compensate for the expensive nature of experiments while the lack of complexity offered by analytical theory is addressed by the experimental and numerical analyses. To simplify the problem, hydrodynamic behaviour was initially decoupled to investigate the underlying mechanics that may lead to a change in heat transfer performance. The interdependencies of the velocity and temperature fields were subsequently demonstrated, and a theory linking the wall shear stress with convective heat flux was developed. With a theoretical framework in place, the heat transfer performance of a pulsating flow liquid-cooling flow loop was measured and analysed.

Separate hydrodynamic and thermal experimental test rigs have been designed and constructed that facilitate the measurement of hydrodynamically- and thermally-developed sinusoidal pulsations. The measurements of the velocity field over the range $1.4 \leq Wo \leq 7.0$ using particle image velocimetry (PIV) constitute the first local time-dependent measurements in a two-dimensional vessel to the author's knowledge. Furthermore, the accuracy of the wall shear stress measurements compares favourably with existing results in pipes. As an interesting aside, the phenomenon of off-wall reversal has been observed experimentally. The local time-dependent wall temperature and convective heat flux measurements – taken using infrared thermography (IRT) at a frequency of $Wo = 1.76$ – are the first of a pulsating

or oscillating incompressible flow in a heated vessel, to the best of the author's knowledge. The maximum instantaneous enhancement of the convective heat flux is approximately 1% of the heat flux generated in the thin foil. However, this is small compared to the instantaneous enhancements that may be achieved with thick-walled heaters, according to theory. Reasonable agreement with the newly-derived analytical solution to the 2-D energy equation and an existing 1-D conjugate solution has been demonstrated by the thermal measurements. Good agreement was found between the experimental velocity data and the new representations of the solutions to the momentum equation, which decompose the parameters into local amplitude and phase values. This facilitates the shift to a flow rate-fixed model, reduces computational expense and gives added insight into the evolution of inertial features. The analytical solutions of Chapter 3 add to the short list of complete thermo-fluidic solutions of common engineering flows. To the best of the author's knowledge, the solution to the energy equation constitutes the first in two dimensions. Hence, an analytical framework has been developed that permits the inspection of coupled hydrodynamic and thermal behaviour on a local and time-dependent basis.

Many of the novelties described above have filled gaps in the literature that were identified (see Section 2.3) after the comprehensive review of Chapter 2. Furthermore, analysis of the data has led to an increased understanding of the coupling between the velocity and temperature fields and underlying mechanisms. Pulsations affect the bulk temperature and wall temperature gradient through displacement. The wall shear stress is an important thermal indicator that may predict the enhanced temperature gradients at the wall for realistic boundary conditions. Under the ideal constant heat flux boundary condition, heat transfer to the fluid is invariant. The convective heat flux is closely tied with the wall shear stress profile for the case of constant temperature. For the realistic case of a finite wall thermal resistance, the capacitive and lateral conduction terms distort the heat flux profile from the wall shear stress profile.

The fundamental question of this thesis has concerned the enhancement of heat transfer using flow pulsation. It is found that pulsation acts to reduce time- and space-averaged heat transfer for the case of a unidirectional, hydrodynamically- and thermally-developed flow with flow reversal precluded and negligible axial temperature gradient fluctuations, axial conduction and viscous heating. However, time intervals and local regions of heat

transfer enhancement have been predicted and measured. The bulk temperature oscillates with twice the pulsation frequency such that the impedance may be intermittently enhanced and reduced during a cycle, with an overall time-averaged reduction. The wall heat flux is both enhanced and diminished during a cycle with a time-average of zero. The thermal performance improves with increasing frequency and flow rate amplitude, though the pressure gradient may increase substantially. In the thermally-developing region, the spatial variation of the axial temperature gradient may result in regions of time-averaged enhancement. Hence, it may be possible to optimise heat transfer on a time- or space-averaged basis using tailored flow rate pulsations or channel geometries.

10.1 Future Work

This research has concluded that time- and space-averaged heat transfer is reduced in the hydrodynamically- and thermally-developed region for the case of sinusoidal pulsations. In general, future work should move towards greater flow complexity through the time-dependent behaviour of the flow rate pulsations and the channel geometry. The author has explored a number of different avenues of research that were not included in this thesis. As concluded in Chapter 10, sinusoidal pulsations (without bulk-mean flow reversal) are found to reduce time- and space-averaged heat transfer in the hydrodynamically- and thermally-developed region. However, time intervals and local regions of heat transfer enhancement have been predicted and measured. Careful investigation of the time-dependent behaviour of the mechanisms of heat transfer enhancement may provide insight into flow rate pulsations that enhance heat transfer on an overall time-averaged basis. Analysis of the thermal performance in the presence of spatial variations of the axial temperature gradient may give insight into the optimisation of heat transfer in the thermally-developing region and complex channel geometries.

10.1.1 Flow Rate Pulsations

The instantaneous behaviour of the wall heat flux is given by Figure 7.16, while an illustrative example of the instantaneous temperature difference is plotted in Figure 7.13. To establish

the exact time-dependent behaviour of impedance, the instantaneous definition of bulk temperature needs to be derived in a robust manner, analogous to that of the time-averaged quantity [29]. The wall heat flux is enhanced over the half-cycle $\pi/2 - 3\pi/2$, where the flow rate decreases from its maximum value to its minimum value. In general, intervals over which the time-averaged wall heat flux is increased relative to the time-averaged temperature difference will result in a time-averaged heat transfer enhancement over the interval. If possible, flow rate pulsations should be tailored to mimic the characteristics of the intervals that enhance heat transfer. The time-dependent flow rate can be decomposed into a sum of sinusoidal functions using a Fourier series, and solutions to the velocity and temperature fields obtained using the same analytical techniques described in Chapter 3.

Flow rate pulsations that experience bulk mean flow reversal $Q_A/Q_0 > 1$ appear to achieve the highest enhancements [16, 88]. It has also been proposed that modulation of the flow rate either above or below its initial value leads to opposing effects on time-averaged heat transfer, with the enhancement and reduction over the half-cycles cancelling for pseudo-sinusoidal pulsations [30]. Modulation of the flow rate below its initial value was found to enhance heat transfer by up to 40%. Figure 2.19 illustrates the flow rate pulsations that were found to enhance heat transfer, which resemble a truncated sine waves that could be generated by a vibrating element and check valves. Persoons et al. [16] found that the inherent pulsations generated using a piezoelectric element, vibrating membrane and valves enhanced heat transfer by as much as 40% in minichannel heat sinks at low Reynolds numbers. Thus, it may be possible to exploit the flow rates delivered by commercially-available micropumps to deliver heat transfer enhancement in electronics and photonics cooling applications.

The gear pump used in the current research cannot generate pulsations that experience negative flow rate. Furthermore, valves cannot be used to truncate a universally-positive flow rate. With this in mind, an oscillating piston pump was designed and manufactured as pictured in Figure 10.1. The McLennan 34HSX-108 stepper motor reaches up to 25 Hz with a resolution of up to 20000 steps per revolution. The Applied Motion ST5-Q-NN drive and encoder has the ability to accelerate and decelerate the motor for portions of the revolution, such that a large and highly-controlled variety of flow rate pulsations could be generated. The rotary motion of the stepper motor is converted into linear oscillatory motion of a piston diaphragm using a Scotch yoke mechanism. The flow generated by the piston pump was

measured by the author in an empty rectangular channel using PIV; however, the amplitudes of the measured velocity oscillations were about 8% lower than that predicted by theory at $Wo = 3.1$, perhaps due to discrepancies in the bore of the cylinder, the stroke of the piston or the angular frequency of the motor.

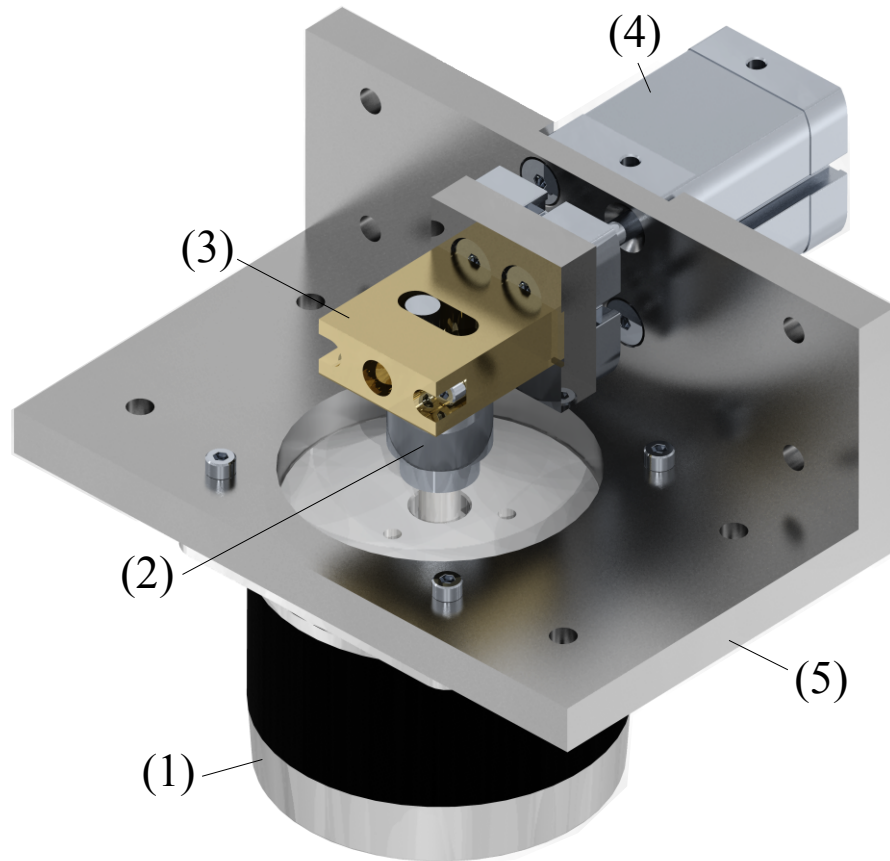


Figure 10.1: Model of the piston pump, containing (1) stepper motor, (2) crank, (3) sliding yoke, (4) piston-cylinder and (5) support.

10.1.2 Channel Geometry and Developing Flow

Changes in heat transfer result from the displacement of fluid in the presence of a temperature gradient. With a temperature gradient that is uniform in time and space (i.e. a hydrodynamically- and thermally-developed flow), this research has shown that time-averaged heat transfer is reduced. However, the variations in the entry region may cause local regions of time-averaged enhancement [29, 74]. The phases of temperature and velocity

determine heat transfer augmentation, which may be positive in the thermally-developing region [106]. Thermally-developing flow was touched upon during the study of the axial temperature gradient in Section 7.2.2. However, an analysis of the time-averaged Nusselt number enhancement with axial length was not performed and it may be possible to choose a channel length that experiences a space-averaged enhancement. In a tapered geometry, the asymmetry of oscillatory velocity profiles during accelerative and decelerative half-cycles may cause bidirectional drift, where fluid particles near the walls drift to the wider end and particles in the core towards the narrower end [162]. The resulting axial transport of a concentration is either greater than or less than the straight vessel, dependent on the frequency and amplitude parameters [163]. Hence, the numerical model – which has been validated in the fully-developed region – can be utilised to investigate the entry region as well as more complex flow geometries, which are currently beyond the reach of exact solutions.

Bibliography

- [1] L. Wilson, “International technology roadmap for semiconductors (ITRS),” *Semiconductor Industry Association*, 2013.
- [2] S. V. Garimella, T. Persoons, J. Weibel, and L. Yeh, “Technological drivers in data centers and telecom systems: Multiscale thermal, electrical, and energy management,” *Applied Energy*, vol. 107, pp. 66–80, 2013.
- [3] R. Enright, S. Lei, K. Nolan, I. Mathews, A. Shen, G. Levaufre, R. Frizzell, G. Duan, and D. Hernon, “A vision for thermally integrated photonics systems,” *Bell Labs Technical Journal*, vol. 19, pp. 31–45, 2014.
- [4] R. W. Tkach, “Scaling optical communications for the next decade and beyond,” *Bell Labs Technical Journal*, vol. 14, no. 4, pp. 3–9, 2010.
- [5] N. Jeffers, J. Stafford, K. Nolan, B. Donnelly, R. Enright, J. Punch, A. Waddell, L. Erlich, J. O’Connor, A. Sexton, R. Blythman, and D. Hernon, “Microfluidic cooling of photonic integrated circuits (PICs),” in *4th European Conference on Microfluidics, Limerick, Ireland*, 2014.
- [6] D. B. Tuckerman and R. F. W. Pease, “High-performance heat sinking for VLSI,” *Electron Device Letters, IEEE*, vol. 2, no. 5, pp. 126–129, 1981.
- [7] B. Agostini, M. Fabbri, J. E. Park, L. Wojtan, J. R. Thome, and B. Michel, “State of the art of high heat flux cooling technologies,” *Heat Transfer Engineering*, vol. 28, no. 4, pp. 258–281, 2007.
- [8] S. G. Kandlikar, “Heat transfer mechanisms during flow boiling in microchannels,”

- in *ASME 2003 1st International Conference on Microchannels and Minichannels*, pp. 33–46, American Society of Mechanical Engineers, 2003.
- [9] J. Wei, “Hybrid cooling technology for large-scale computing systems: From back to the future,” in *Proceedings of ASME InterPACK*, 2011.
- [10] E. G. Colgan, B. Furman, M. Gaynes, W. S. Graham, N. C. LaBianca, J. H. Magerlein, R. J. Polastre, M. B. Rothwell, R. Bezama, R. Choudhary, *et al.*, “A practical implementation of silicon microchannel coolers for high power chips,” *IEEE Transactions on Components and Packaging Technologies*, vol. 30, no. 2, pp. 218–225, 2007.
- [11] W. Spencer, W. T. Corbett, L. Dominguez, and B. D. Shafer, “An electronically controlled piezoelectric insulin pump and valves,” *IEEE Transactions on Sonics and Ultrasonics*, vol. 25, no. 3, pp. 153–156, 1978.
- [12] V. Singhal, S. V. Garimella, and A. Raman, “Microscale pumping technologies for microchannel cooling systems,” *Applied Mechanics Reviews*, vol. 57, no. 3, pp. 191–221, 2004.
- [13] R. Bodén, M. Lehto, U. Simu, G. Thornell, K. Hjort, and J.-Å. Schweitz, “A polymeric paraffin actuated high-pressure micropump,” *Sensors and Actuators A: Physical*, vol. 127, no. 1, pp. 88–93, 2006.
- [14] N.-T. Nguyen and X. Huang, “Development of a peristaltic pump in printed circuit boards,” *Journal of Micromechatronics*, vol. 3, no. 1, pp. 1–13, 2005.
- [15] D. J. Laser and J. G. Santiago, “A review of micropumps,” *Journal of Micromechanics and Microengineering*, vol. 14, no. 6, p. R35, 2004.
- [16] T. Persoons, T. Saenen, T. Van Oevelen, and M. Baelmans, “Effect of flow pulsation on the heat transfer performance of a minichannel heat sink,” *Journal of Heat Transfer*, vol. 134, no. 9, p. 091702, 2012.
- [17] S. V. Garimella, V. Singhal, and D. Liu, “On-chip thermal management with microchannel heat sinks and integrated micropumps,” *Proceedings of the IEEE*, vol. 94, no. 8, pp. 1534–1548, 2006.

- [18] R. Wälchli, R. Linderman, T. Brunschwiler, U. Kloter, H. Rothuizen, N. Bieri, D. Poulikakos, and B. Michel, “Radially oscillating flow hybrid cooling system for low profile electronics applications,” in *Semiconductor Thermal Measurement and Management Symposium, 2008. 24th Annual IEEE*, pp. 142–148, IEEE, 2008.
- [19] R. Wälchli, T. Brunschwiler, B. Michel, and D. Poulikakos, “Self-contained, oscillating flow liquid cooling system for thin form factor high performance electronics,” *Journal of Heat Transfer*, vol. 132, no. 5, p. 051401, 2010.
- [20] T. Walsh, K. Yang, V. Nee, and Q. Liao, “Forced convection cooling in microelectronic cabinets via oscillatory flow techniques,” *Experimental Thermal and Fluid Science*, vol. 7, no. 2, p. 140, 1993.
- [21] U. H. Kurzweg and L. Zhao, “Heat transfer by high-frequency oscillations: A new hydrodynamic technique for achieving large effective thermal conductivities,” *Physics of Fluids*, vol. 27, no. 11, pp. 2624–2627, 1984.
- [22] U. H. Kurzweg, “Heat transfer device for the transport of large conduction flux without net mass transfer,” 1986. US Patent No. 4590993.
- [23] R. H. Keil and M. H. I. Baird, “Enhancement of heat transfer by flow pulsation,” *Industrial & Engineering Chemistry Process Design and Development*, vol. 10, no. 4, pp. 473–478, 1971.
- [24] W. Augustin and M. Bohnet, “Influence of pulsating flow on fouling behaviour,” in *Proceedings of the Engineering Foundation Conference on Mitigation of Heat Exchanger Fouling and its Economic and Environmental Implications, Banff, Canada, 1999*.
- [25] W. L. Van Nostrand, S. H. Leach, and J. L. Haluska, “Economic penalties associated with the fouling of refinery heat transfer equipment,” *Fouling of Heat Transfer Equipment*, pp. 619–643, 1981.
- [26] C. Lelièvre, P. Legentilhomme, C. Gaucher, J. Legrand, C. Faille, and T. Bénézech, “Cleaning in place: Effect of local wall shear stress variation on bacterial removal from

- stainless steel equipment,” *Chemical Engineering Science*, vol. 57, no. 8, pp. 1287–1297, 2002.
- [27] W. Augustin and M. Bohnet, “Influence of a pulsating flow on fouling behavior of heat transfer surfaces,” *Chemie Ingenieur Technik*, vol. 73, no. 9, pp. 1139–1144, 2001.
- [28] C. R. Gillham, P. J. Fryer, A. P. M. Hasting, and D. I. Wilson, “Enhanced cleaning of whey protein soils using pulsed flows,” *Journal of Food Engineering*, vol. 46, no. 3, pp. 199–209, 2000.
- [29] H. N. Hemida, M. N. Sabry, A. Abdel-Rahim, and H. Mansour, “Theoretical analysis of heat transfer in laminar pulsating flow,” *International Journal of Heat and Mass transfer*, vol. 45, no. 8, pp. 1767–1780, 2002.
- [30] G. J. Brereton and Y. Jiang, “Convective heat transfer in unsteady laminar parallel flows,” *Physics of Fluids*, vol. 18, no. 10, p. 103602, 2006.
- [31] C. Fan and B. T. Chao, “Unsteady, laminar, incompressible flow through rectangular ducts,” *Zeitschrift für angewandte Mathematik und Physik (ZAMP)*, vol. 16, no. 3, pp. 351–360, 1965.
- [32] S. Uchida, “The pulsating viscous flow superposed on the steady laminar motion of incompressible fluid in a circular pipe,” *Zeitschrift für Angewandte Mathematik und Physik (ZAMP)*, vol. 7, no. 5, pp. 403–422, 1956.
- [33] H. Ito, “Theory of laminar flow through a pipe with non-steady pressure gradients,” *Proceedings of the Institute of High Speed Mechanics*, p. 163, 1953.
- [34] R. Siegel and M. Perlmutter, “Heat transfer for pulsating laminar duct flow,” *Journal of Heat Transfer*, vol. 84, no. 2, pp. 111–122, 1962.
- [35] M. Faghri, K. Javdani, and A. Faghri, “Heat transfer with laminar pulsating flow in a pipe,” *Letters in Heat and Mass Transfer*, vol. 6, no. 4, pp. 259–270, 1979.
- [36] G. G. Stokes, “On the effect of the internal friction of fluids on the motion of pendulums,” *Transactions of the Cambridge Philosophical Society*, vol. 9, p. 8, 1851.

- [37] F. M. White and I. Corfield, *Viscous Fluid Flow*, vol. 2. McGraw-Hill New York, 1991.
- [38] J. R. Womersley, "Method for the calculation of velocity, rate of flow and viscous drag in arteries when the pressure gradient is known," *Journal of Physiology*, vol. 127, no. 3, pp. 553–563, 1955.
- [39] L. Shemer, I. Wygnanski, and E. Kit, "Pulsating flow in a pipe," *Journal of Fluid Mechanics*, vol. 153, pp. 313–337, 1985.
- [40] D. Holmes and J. Vermeulen, "Velocity profiles in ducts with rectangular cross sections," *Chemical Engineering Science*, vol. 23, no. 7, pp. 717–722, 1968.
- [41] E. G. Richardson, "The amplitude of sound waves in resonators," *Proceedings of the Physical Society*, vol. 40, no. 1, p. 206, 1927.
- [42] E. G. Richardson and E. Tyler, "The transverse velocity gradient near the mouths of pipes in which an alternating or continuous flow of air is established," *Proceedings of the Physical Society*, vol. 42, no. 1, p. 1, 1929.
- [43] T. Sexl, "Über den von E. G. Richardson entdeckten 'Annulareffekt'," *Zeitschrift für Physik*, vol. 61, no. 5-6, pp. 349–362, 1930.
- [44] R. G. Linford and N. W. Ryan, "Pulsatile flow in rigid tubes," *Journal of Applied Physiology*, vol. 20, no. 5, pp. 1078–1082, 1965.
- [45] D. Hershey and G. Song, "Friction factors and pressure drop for sinusoidal laminar flow of water and blood in rigid tubes," *AIChE Journal*, vol. 13, no. 3, pp. 491–496, 1967.
- [46] J. Harris, G. Peev, and W. L. Wilkinson, "Velocity profiles in laminar oscillatory flow in tubes," *Journal of Physics E: Scientific Instruments*, vol. 2, no. 11, p. 913, 1969.
- [47] T. Muto and K. Nakane, "Unsteady flow in circular tube: Velocity distribution of pulsating flow," *Bulletin of JSME*, vol. 23, no. 186, pp. 1990–1996, 1980.

- [48] E. B. Denison and W. H. Stevenson, "Oscillatory flow measurements with a directionally sensitive laser velocimeter," *Review of Scientific Instruments*, vol. 41, no. 10, pp. 1475–1478, 1970.
- [49] E. B. Denison, W. H. Stevenson, and R. W. Fox, "Pulsating laminar flow measurements with a directionally sensitive laser velocimeter," *AIChE Journal*, vol. 17, no. 4, pp. 781–787, 1971.
- [50] S. Einav and S. L. Lee, "Migration in an oscillatory flow of a laminar suspension measured by laser anemometry," *Experiments in Fluids*, vol. 6, no. 4, pp. 273–279, 1988.
- [51] D. M. Eckmann and J. B. Grotberg, "Experiments on transition to turbulence in oscillatory pipe flow," *Journal of Fluid Mechanics*, vol. 222, pp. 329–350, 1991.
- [52] M. Clamen and P. Minton, "An experimental investigation of flow in an oscillating pipe," *Journal of Fluid Mechanics*, vol. 81, no. 03, pp. 421–431, 1977.
- [53] B. Ünsal, S. Ray, F. Durst, and Ö. Ertunç, "Pulsating laminar pipe flows with sinusoidal mass flux variations," *Fluid Dynamics Research*, vol. 37, no. 5, pp. 317–333, 2005.
- [54] F. Durst, U. Heim, B. Ünsal, and G. Kullik, "Mass flow rate control system for time-dependent laminar and turbulent flow investigations," *Measurement Science and Technology*, vol. 14, no. 7, p. 893, 2003.
- [55] S. Ray, B. Ünsal, F. Durst, Ö. Ertunc, and O. A. Bayoumi, "Mass flow rate controlled fully developed laminar pulsating pipe flows," *Journal of Fluids Engineering*, vol. 127, no. 3, pp. 405–418, 2005.
- [56] K. Haddad, Ö. Ertunç, M. Mishra, and A. Delgado, "Pulsating laminar fully developed channel and pipe flows," *Physical Review E*, vol. 81, no. 1, p. 016303, 2010.
- [57] P. E. Hughes and T. V. How, "Pulsatile velocity distribution and wall shear rate measurement using pulsed doppler ultrasound," *Journal of Biomechanics*, vol. 27, no. 1, pp. 103–110, 1994.

- [58] M. Ojha, R. L. Hummel, S. C. Cobbold, and K. W. Johnston, "Development and evaluation of a high resolution photochromic dye method for pulsatile flow studies," *Journal of Physics E: Scientific Instruments*, vol. 21, no. 10, p. 998, 1988.
- [59] T. S. Zhao and P. Cheng, "The friction coefficient of a fully developed laminar reciprocating flow in a circular pipe," *International Journal of Heat and Fluid Flow*, vol. 17, no. 2, pp. 167–172, 1996.
- [60] M. Ohmi, M. Iguchi, and T. Usui, "Flow pattern and frictional losses in pulsating pipe flow: Part 5, wall shear stress and flow pattern in a laminar flow," *Bulletin of JSME*, vol. 24, no. 187, pp. 75–81, 1981.
- [61] T. E. Inc., "SDMP320 piezoelectric micropump," 2008. <http://www.takasago-fluidics.com>.
- [62] G. Taylor, "Dispersion of soluble matter in solvent flowing slowly through a tube," in *Proceedings of the Royal Society of London A: Mathematical, Physical and Engineering Sciences*, vol. 219, pp. 186–203, 1953.
- [63] P. C. Chatwin, "The approach to normality of the concentration distribution of a solute in a solvent flowing along a straight pipe," *Journal of Fluid Mechanics*, vol. 43, no. 2, pp. 321–352, 1970.
- [64] P. C. Chatwin, "On the longitudinal dispersion of passive contaminant in oscillatory flows in tubes," *Journal of Fluid Mechanics*, vol. 71, no. 03, pp. 513–527, 1975.
- [65] E. J. Watson, "Diffusion in oscillatory pipe flow," *J. Fluid Mech.*, vol. 133, pp. 233–244, 1983.
- [66] R. Smith, "Contaminant dispersion in oscillatory flows," *Journal of Fluid Mechanics*, vol. 114, pp. 379–398, 1982.
- [67] C. H. Joshi, R. D. Kamm, J. M. Drazen, and A. S. Slutsky, "An experimental study of gas exchange in laminar oscillatory flow," *Journal of Fluid Mechanics*, vol. 133, pp. 245–254, 1983.

- [68] M. J. Jaeger and U. H. Kurzweg, "Determination of the longitudinal dispersion coefficient in flows subjected to high-frequency oscillations," *Physics of Fluids*, vol. 26, no. 6, pp. 1380–1382, 1983.
- [69] U. H. Kurzweg, "Enhanced heat conduction in oscillating viscous flows within parallel-plate channels," *Journal of Fluid Mechanics*, vol. 156, pp. 291–300, 1985.
- [70] J. G. Zhang and U. H. Kurzweg, "Numerical simulation of time-dependent heat transfer in oscillating pipe flow," *Journal of Thermophysics and Heat Transfer*, vol. 5, no. 3, pp. 401–406, 1991.
- [71] O. Mamoru and K. Akira, "Lumped-parameter modeling of heat transfer enhanced by sinusoidal motion of fluid," *International Journal of Heat and Mass Transfer*, vol. 34, no. 12, pp. 3083–3095, 1991.
- [72] D. Lee, S. Park, and S. Ro, "Heat transfer in the thermally developing region of a laminar oscillating pipe flow," *Cryogenics*, vol. 38, no. 6, pp. 585–594, 1998.
- [73] R. Siegel, "Influence of oscillation-induced diffusion on heat transfer in a uniformly heated channel," *J. Heat Transfer*, vol. 109, no. 1, pp. 244–247, 1987.
- [74] S. Y. Kim, B. H. Kang, and J. M. Hyun, "Heat transfer in the thermally developing region of a pulsating channel flow," *International Journal of Heat and Mass Transfer*, vol. 36, no. 17, pp. 4257–4266, 1993.
- [75] H. Cho and J. Hyun, "Numerical solutions of pulsating flow and heat transfer characteristics in a pipe," *International Journal of Heat and Fluid Flow*, vol. 11, no. 4, pp. 321–330, 1990.
- [76] H. Cho and J. Hyun, "Motion and heat transfer in the blasius flow containing a pulsating component," *International Journal of Heat and Fluid Flow*, vol. 10, no. 4, pp. 349–357, 1989.
- [77] T. Moschandreou and M. Zamir, "Heat transfer in a tube with pulsating flow and constant heat flux," *International Journal of Heat and Mass Transfer*, vol. 40, no. 10, pp. 2461–2466, 1997.

- [78] D. A. Nield and A. V. Kuznetsov, "Forced convection with laminar pulsating flow in a channel or tube," *International Journal of Thermal Sciences*, vol. 46, no. 6, pp. 551–560, 2007.
- [79] D. Gedeon, "Mean-parameter modeling of oscillating flow," *Journal of Heat Transfer*, vol. 108, no. 3, pp. 513–518, 1986.
- [80] Z. Yu, X. Mao, and A. J. Jaworski, "Experimental study of heat transfer in oscillatory gas flow inside a parallel-plate channel with imposed axial temperature gradient," *International Journal of Heat and Mass Transfer*, vol. 77, pp. 1023–1032, 2014.
- [81] Q. D. Liao, K. T. Yang, and V. W. Nee, "An analysis of conjugate heat transfer from a heated wall in a channel with zero-mean oscillatory flow for small oscillatory flow Reynolds numbers," *International Journal of Heat and Mass Transfer*, vol. 37, pp. 415–423, 1994.
- [82] L. Shi, X. Mao, and A. J. Jaworski, "Application of planar laser-induced fluorescence measurement techniques to study the heat transfer characteristics of parallel-plate heat exchangers in thermoacoustic devices," *Measurement Science and Technology*, vol. 21, no. 11, p. 115405, 2010.
- [83] T. Zhao and P. Cheng, "A numerical solution of laminar forced convection in a heated pipe subjected to a reciprocating flow," *International Journal of Heat and Mass Transfer*, vol. 38, no. 16, pp. 3011–3022, 1995.
- [84] T. S. Zhao and P. Cheng, "Oscillatory heat transfer in a pipe subjected to a laminar reciprocating flow," *Journal of Heat Transfer*, vol. 118, no. 3, pp. 592–597, 1996.
- [85] C. Sert and A. Beskok, "Numerical simulation of reciprocating flow forced convection in two-dimensional channels," *Journal of Heat Transfer*, vol. 125, no. 3, pp. 403–412, 2003.
- [86] R. D. Patel, J. J. McFeeley, and K. R. Jolls, "Wall mass transfer in laminar pulsatile flow in a tube," *AIChE Journal*, vol. 21, no. 2, pp. 259–267, 1975.

- [87] T. J. Pedley, "On the forced heat transfer from a hot film embedded in the wall in two-dimensional unsteady flow," *Journal of Fluid Mechanics*, vol. 55, no. 2, pp. 329–357, 1972.
- [88] S. K. Gupta, T. R. D. Patel, and R. C. Ackerberg, "Wall heat/mass transfer in pulsatile flow," *Chemical Engineering Science*, vol. 37, no. 12, pp. 1727–1739, 1982.
- [89] O. I. Craciunescu and S. T. Clegg, "Pulsatile blood flow effects on temperature distribution and heat transfer in rigid vessels," *Journal of Biomechanical Engineering*, vol. 123, no. 5, pp. 500–505, 2001.
- [90] R. Blythman, T. Persoons, N. Jeffers, K. P. Nolan, and D. B. Murray, "Localised dynamics of laminar pulsatile flow in a rectangular channel," *International Journal of Heat and Fluid Flow*, vol. 66, pp. 8–17, 2017.
- [91] W. M. Kays, M. E. Crawford, and B. Weigand, *Convective Heat and Mass Transfer*. Tata McGraw-Hill Education, 2012.
- [92] R. K. Shah and A. L. London, *Advances in Heat Transfer*, vol. 1. Academic Press, 1978.
- [93] L. Rosenhead, *Laminar Boundary Layers*. Clarendon Press Gloucestershire, UK, 1963.
- [94] B. R. Morton, "The generation and decay of vorticity," *Geophysical & Astrophysical Fluid Dynamics*, vol. 28, no. 3-4, pp. 277–308, 1984.
- [95] R. Siegel, "Heat transfer for laminar flow in ducts with arbitrary time variations in wall temperature," *Journal of Applied Mechanics*, vol. 27, no. 2, pp. 241–249, 1960.
- [96] S. X. Gao and J. P. Hartnett, "Analytical Nusselt number predictions for slug flow in rectangular duct," *International Communications in Heat and Mass Transfer*, vol. 20, no. 5, 1993.
- [97] G. L. Morini, "Thermal characteristics of slug flow in rectangular ducts," *International Journal of Thermal Sciences*, vol. 38, no. 2, pp. 148–159, 1999.

- [98] M. Spiga and G. L. Morini, “Nusselt numbers in laminar flow for H₂ boundary conditions,” *International Journal of Heat and Mass Transfer*, vol. 39, no. 6, pp. 1165–1174, 1996.
- [99] R. Siegel and J. M. Savino, “An analytical solution of the effect of peripheral wall conduction on laminar forced convection in rectangular channels,” *Journal of Heat Transfer*, vol. 87, no. 1, pp. 59–66, 1965.
- [100] J. M. Savino and R. Siegel, “Extension of an analysis of peripheral wall conduction effects for laminar forced convection in thin-walled rectangular channels,” tech. rep., Lewis Research Center, National Aeronautics and Space Administration, 1965.
- [101] J. M. Savino and R. Siegel, “Laminar forced convection in rectangular channels with unequal heat addition on adjacent sides,” *International Journal of Heat and Mass Transfer*, vol. 7, no. 7, pp. 733–741, 1964.
- [102] Z. Guo and H. J. Sung, “Analysis of the Nusselt number in pulsating pipe flow,” *International Journal of Heat and Mass Transfer*, vol. 40, no. 10, pp. 2486–2489, 1997.
- [103] J. W. Rose, “Heat-transfer coefficients, wilson plots and accuracy of thermal measurements,” *Experimental Thermal and Fluid Science*, vol. 28, no. 2, pp. 77–86, 2004.
- [104] F. P. Incropera, A. S. Lavine, T. L. Bergman, and D. P. DeWitt, *Fundamentals of Heat and Mass Transfer*. Wiley, 2007.
- [105] E. M. Sparrow and F. N. De Farias, “Unsteady heat transfer in ducts with time-varying inlet temperature and participating walls,” *International Journal of Heat and Mass Transfer*, vol. 11, no. 5, pp. 837–853, 1968.
- [106] R. Mathie, *Unsteady and Conjugate Heat Transfer in Convective-Conductive Systems*. PhD thesis, Imperial College London, 2012.
- [107] Y. B. Zudin, *Theory of Periodic Conjugate Heat Transfer*. Springer, 2007.

- [108] A. Berson, M. Michard, and P. Blanc-Benon, “Measurement of acoustic velocity in the stack of a thermoacoustic refrigerator using particle image velocimetry,” *Heat and Mass Transfer*, vol. 44, no. 8, pp. 1015–1023, 2008.
- [109] X. Mao and A. J. Jaworski, “Application of particle image velocimetry measurement techniques to study turbulence characteristics of oscillatory flows around parallel-plate structures in thermoacoustic devices,” *Measurement Science and Technology*, vol. 21, no. 3, p. 035403, 2010.
- [110] D. Quosdorf, M. Brede, A. Leder, D. Lootz, H. Martin, and K.-P. Schmitz, “Micro-Particle-Image-Velocimetry zur Bestimmung der Geschwindigkeiten in einem Koronargefäß mit Stent,” *tm-Technisches Messen Plattform für Methoden, Systeme und Anwendungen der Messtechnik*, vol. 78, no. 5, pp. 239–245, 2011.
- [111] S. A. Self, “Focusing of spherical Gaussian beams,” *Applied Optics*, vol. 22, no. 5, pp. 658–661, 1983.
- [112] P. van Walree, “VWDOF calculator (version 2.1),” 2002 – 2016.
- [113] C. Meola and G. M. Carlomagno, “Recent advances in the use of infrared thermography,” *Measurement Science and Technology*, vol. 15, no. 9, p. R27, 2004.
- [114] D. B. Donoghue, *Bubble impingement and the mechanisms of heat transfer enhancement*. PhD thesis, Trinity College Dublin, 2014.
- [115] R. O’Reilly Meehan, *Flow structures in and heat transfer enhancement in the wakes of sliding bubbles*. PhD thesis, Trinity College Dublin, 2016.
- [116] M. J. Gibbons, *Electrospray cooling and droplet evaporation*. PhD thesis, Trinity College Dublin, 2016.
- [117] A. Mosyak, E. Pogrebnyak, and G. Hetsroni, “Effect of constant heat flux boundary condition on wall temperature fluctuations,” *Journal of Heat Transfer*, vol. 123, no. 2, pp. 213–218, 2001.

- [118] O. Raghu and J. Philip, "Thermal properties of paint coatings on different backings using a scanning photo acoustic technique," *Measurement Science and Technology*, vol. 17, no. 11, p. 2945, 2006.
- [119] P. Kieruj, D. Przystacki, and T. Chwalczuk, "Determination of emissivity coefficient of heat-resistant super alloys and cemented carbide," *Archives of Mechanical Technology and Materials*, vol. 36, no. 1, pp. 30–34, 2016.
- [120] J. Stafford, E. Walsh, and V. Egan, "Characterizing convective heat transfer using infrared thermography and the heated-thin-foil technique," *Measurement Science and Technology*, vol. 20, no. 10, p. 105401, 2009.
- [121] Crystran, "Crystran: materials." [http://http://www.crystran.co.uk/optical-materials/sapphire-al2o3](http://www.crystran.co.uk/optical-materials/sapphire-al2o3), 2012. [Online; accessed 08-September-2014].
- [122] M. Ochs, T. Horbach, A. Schulz, R. Koch, and H. J. Bauer, "A novel calibration method for an infrared thermography system applied to heat transfer experiments," *Measurement Science Technology*, vol. 20, no. 7, p. 075103, 2009.
- [123] F. Durst, S. Ray, B. Ünsal, and O. A. Bayoumi, "The development lengths of laminar pipe and channel flows," *Journal of Fluids Engineering*, vol. 127, no. 6, pp. 1154–1160, 2005.
- [124] S. Ray, B. Ünsal, and F. Durst, "Development length of sinusoidally pulsating laminar pipe flows in moderate and high Reynolds number regimes," *International Journal of Heat and Fluid Flow*, vol. 37, pp. 167–176, 2012.
- [125] R. Moissis, *The secondary flow in rectangular ducts*. PhD thesis, Massachusetts Institute of Technology, 1957.
- [126] S. H. Maslen, "Transverse velocities in fully developed flows," *Quarterly of Applied Mathematics*, vol. 16, no. 2, pp. 173–175, 1958.
- [127] S. I. Sergeev, "Fluid oscillations in pipes at moderate Reynolds numbers," *Fluid Dynamics*, vol. 1, no. 1, pp. 121–122, 1966.

- [128] M. Raffel, C. E. Willert, S. Wereley, and J. Kompenhans, *Particle Image Velocimetry: A Practical Guide*. Springer, 2013.
- [129] M. Spiga and G. L. Morini, “The developing Nusselt numbers for slug flow in rectangular ducts,” *International Journal of Heat and Mass Transfer*, vol. 41, no. 18, pp. 2799–2807, 1998.
- [130] J. L. M. Hensen and A. E. Nakhi, “Fourier and Biot numbers and the accuracy of conduction modelling,” in *Proceedings of BEP Conference*, pp. 247–256, 1994.
- [131] E. Nogueira, J. Pereira, M. Baesso, and A. Bento, “Study of layered and defective amorphous solids by means of thermal wave method,” *Journal of Non-crystalline Solids*, vol. 318, no. 3, pp. 314–321, 2003.
- [132] A. Bejan, *Convection Heat Transfer*. John Wiley & Sons, 2013.
- [133] H. W. Coleman and W. G. Steele, *Experimentation, Validation, and Uncertainty Analysis for Engineers*. John Wiley & Sons, 2009.
- [134] International Organization for Standardization (ISO), *Guide to the Expression of Uncertainty in Measurement*. ISO Geneva, 1993.
- [135] C. E. Willert and M. Gharib, “Digital particle image velocimetry,” *Experiments in Fluids*, vol. 10, no. 4, pp. 181–193, 1991.
- [136] J. J. Charonko and P. P. Vlachos, “Estimation of uncertainty bounds for individual particle image velocimetry measurements from cross-correlation peak ratio,” *Measurement Science and Technology*, vol. 24, no. 6, p. 065301, 2013.
- [137] R. D. Keane and R. J. Adrian, “Optimization of particle image velocimeters,” in *Proceedings of SPIE-the International Society for Optical Engineering*, vol. 1404, pp. 139–159, 1990.
- [138] R. D. Keane and R. J. Adrian, “Theory of cross-correlation analysis of PIV images,” *Applied Scientific Research*, vol. 49, no. 3, pp. 191–215, 1992.

- [139] J. Westerweel, *Digital Particle Image Velocimetry - Theory and Application*. Delft University Press, 1993.
- [140] J. Westerweel, D. Dabiri, and M. Gharib, “The effect of a discrete window offset on the accuracy of cross-correlation analysis of digital piv recordings,” *Experiments in Fluids*, vol. 23, no. 1, pp. 20–28, 1997.
- [141] M. Stanislas, K. Okamoto, C. J. Kähler, and J. Westerweel, “Main results of the second international PIV challenge,” *Experiments in Fluids*, vol. 39, no. 2, pp. 170–191, 2005.
- [142] V 20 Committee, “Standard for verification and validation in computational fluid dynamics and heat transfer,” *American Society of Mechanical Engineers, New York*, 2009.
- [143] H. W. Coleman and F. Stem, “Uncertainties and cfd code validation,” *Journal of Fluids Engineering*, vol. 119, pp. 795–803, 1997.
- [144] J. H. Kim, T. W. Simon, and R. Viskanta, “Journal of heat transfer policy on reporting uncertainties in experimental measurements and results,” *Journal of Heat Transfer*, vol. 115, no. 1, pp. 5–6, 1993.
- [145] M. Knapp-Corders and B. McKeeman, “Improvements to tic and toc functions for measuring absolute elapsed time performance in matlab,” 2011.
- [146] G. E. Box, G. M. Jenkins, G. C. Reinsel, and G. M. Ljung, *Time Series Analysis: Forecasting and Control*. John Wiley & Sons, 2015.
- [147] L. Kirkup and R. B. Frenkel, *An Introduction to Uncertainty in Measurement*. Cambridge University Press, 2006.
- [148] A. Barletta, “Fully developed mixed convection and flow reversal in a vertical rectangular duct with uniform wall heat flux,” *International Journal of Heat and Mass Transfer*, vol. 45, no. 3, pp. 641–654, 2002.
- [149] A. Pozzi and R. Tognaccini, “Thermo-fluid dynamics of the unsteady channel flow,” *European Journal of Mechanics-B/Fluids*, vol. 28, no. 2, pp. 299–308, 2009.

- [150] S. Alimohammadi, D. B. Murray, and T. Persoons, “On the numerical–experimental analysis and scaling of convective heat transfer to pulsating impinging jets,” *International Journal of Thermal Sciences*, vol. 98, pp. 296–311, 2015.
- [151] S. Alimohammadi, E. Fanning, T. Persoons, and D. B. Murray, “Characterization of flow vectoring phenomenon in adjacent synthetic jets using CFD and PIV,” *Computers and Fluids*, vol. 140, pp. 232–246, 2016.
- [152] ANSYS Inc., “ANSYS CFX-solver theory guide,” 2009. Release 12.1.
- [153] E. R. G. Eckert and G. M. Low, “Temperature distribution in internally heated walls of heat exchangers composed of noncircular flow passages,” tech. rep., National Advisory Committee for Aeronautics, 1951.
- [154] J. Nikuradse, “Geschwindigkeitsverteilung in Turbulenten Stromungen,” *Zeitschrift-VDI*, vol. 70, 1926.
- [155] J. Nikuradse, “Untersuchungen über turbulente Strömungen in nicht kreisförmigen Rohren,” *Ingenieur-Archiv*, vol. 1, no. 3, pp. 306–332, 1930.
- [156] E. F. Adiutori, “Origins of the heat transfer coefficient,” *Mechanical Engineering-CIME*, vol. 112, no. 8, pp. 46–51, 1990.
- [157] I. Newton, “A scale of the degrees of heat,” *Philosophical Transactions of the Royal Society of London*, 1701.
- [158] J. B. J. Fourier, *The Analytical Theory of Heat*. The University Press, 1878.
- [159] E. F. Adiutori, *The New Heat Transfer*. Ventuno Press, 1974.
- [160] A. Degiovanni and B. Remy, “An alternative to heat transfer coefficient: A relevant model of heat transfer between a developed fluid flow and a non-isothermal wall in the transient regime,” *International Journal of Thermal Sciences*, vol. 102, pp. 62–77, 2016.
- [161] M. Rebay and J. Padet, “Laminar boundary-layer flow over a semi-infinite plate impulsively heated or cooled,” *European Physical Journal of Applied Physics*, vol. 7, no. 3, pp. 263–269, 1999.

- [162] D. P. Gaver and J. B. Grotberg, "An experimental investigation of oscillating flow in a tapered channel," *Journal of Fluid Mechanics*, vol. 172, pp. 47–61, 1986.
- [163] D. A. Godleski and J. B. Grotberg, "Convection-diffusion interaction for oscillatory flow in a tapered tube," *Journal of Biomechanical Engineering*, vol. 110, no. 4, pp. 283–291, 1988.

Appendix A

A.1 Solutions for Flow Rate and Wall Shear Stress

The flow rate is given by:

$$Q' = \Re(\psi_Q e^{iWo^2 t}) \quad (1a)$$

$$\psi_u = -\frac{64ab\nabla p_A}{\pi^4} \sum_{m=1,3,\dots}^{\infty} \sum_{n=1,3,\dots}^{\infty} \frac{1}{m^2 n^2} \frac{1}{\beta_{mn} + iWo^2} \quad (1b)$$

and the dimensional wall shear stress at $\hat{z} = [0, \hat{b}]$ is:

$$\hat{\tau}'_{zx} = \Re(\psi_{\hat{\tau}_{zx}} e^{i\omega \hat{t}}) \quad (2a)$$

$$\psi_{\hat{\tau}_{zx}} = -\frac{16\nu\nabla \hat{p}_A}{\hat{b}\pi} \sum_{m=1,3,\dots}^{\infty} \sum_{n=1,3,\dots}^{\infty} \frac{\sin(\frac{m\pi \hat{y}}{\hat{a}})}{m} \frac{1}{\nu\beta_{mn} + i\omega} \quad (2b)$$

The mean over the wall is determined using $\psi_{\langle \hat{\tau}_{zx} \rangle} = (1/\hat{a}) \int_0^{\hat{a}} \psi_{\hat{\tau}_{zx}} \partial \hat{y}$. The mean over the entire perimeter is the weighted mean of the individual wall averages $\psi_{\langle \hat{\tau} \rangle} = (\hat{a}\psi_{\langle \hat{\tau}_{zx} \rangle} + \hat{b}\psi_{\langle \hat{\tau}_{yx} \rangle})/(\hat{a} + \hat{b})$. As with velocity, the above equations represent the steady solution with $\nabla p_A = \nabla p_0$, $\psi_Q = Q_0$ and $\psi_{\hat{\tau}_{zx}} = \hat{\tau}_{zx,0}$ if $Wo = 0$ and $\omega = 0$.

A.2 Solution for Steady Temperature Profile

The solution of Spiga and Morini [98], reorganised in terms of the non-dimensionalised variable of Equation 3.4, may be described as a sum of five distinct terms, with four accounting

for the effects of prescribed heat transfer to the channel at each boundary and one applying the effects of advection. Using the non-dimensionalised parameters of Equation 3.4, the steady temperature profile is given by:

$$\begin{aligned}\theta_0(x,y,z) = & \frac{a}{\pi^2} \sum_{j=1}^{\infty} \frac{(-1)^j d_2 + d_1}{j^2} \cos\left(\frac{j\pi y}{a}\right) \\ & + \frac{b}{\pi^2} \sum_{k=1}^{\infty} \frac{(-1)^k d_4 + d_3}{k^2} \cos\left(\frac{k\pi z}{b}\right) \\ & + \frac{\partial \theta_0}{\partial x} \sum_{j=0,2,\dots}^{\infty} \sum_{k=0,2,\dots}^{\infty} A_{jk,0} \Phi_2\end{aligned}\quad (3)$$

with:

$$A_{jk,0} = \begin{cases} x & j = 0, k = 0 \\ \frac{128\nabla p_0 Pr}{\pi^4} \sum_{m=1,3,\dots}^{\infty} \sum_{n=1,3,\dots}^{\infty} \frac{1}{\beta_{mn} \beta_{jk} (j^2 - m^2)(k^2 - n^2)} & j = 0, k \neq 0 \text{ or } k = 0 \\ \frac{256\nabla p_0 Pr}{\pi^4} \sum_{m=1,3,\dots}^{\infty} \sum_{n=1,3,\dots}^{\infty} \frac{1}{\beta_{mn} \beta_{jk} (j^2 - m^2)(k^2 - n^2)} & j \neq 0, k \neq 0 \end{cases} \quad (4)$$

The values of the binary constants d indicate the unique version of heating (see Table 3.3). An energy balance gives $\partial \theta_0 / \partial x = c / Pr$ where $c = L / (2a + 2b)$ is the heated fraction of the cross-sectional perimeter.

A.3 1-D Parallel Plates Solution for Oscillatory Temperature Profile

The solutions for velocity and temperature in a parallel plate channel are given by Kurzweg [69]. For convenience, the origin is maintained at the mid-channel height $-(b/2 + w) \leq z \leq (b/2 + w)$ and the results subsequently shifted in space to match the origin of the 2-D solution. Using the same non-dimensionalisations as Section 3.1.3, the velocity under an

oscillating pressure gradient $p' = \Re(\nabla p_A e^{iWo^2 t})$ is given by:

$$u'(z) = \Re(\psi_u e^{iWo^2 t}) \quad (5a)$$

$$\psi_u = -i \frac{\nabla p_A}{Wo^2} \left[\frac{\cosh(\sqrt{i} Wo z)}{\cosh(\sqrt{i} Wo/2)} - 1 \right] \quad (5b)$$

The oscillating temperature profiles in the fluid $-b/2 \leq z \leq b/2$ and foil $-(b/2 + w) \leq z \leq -b/2$ are given by:

$$\theta'_f(z) = \Re(\psi_{\theta,f} e^{iWo^2 t}) \quad (6a)$$

$$\theta'_s(z) = \Re(\psi_{\theta,s} e^{iWo^2 t}) \quad (6b)$$

$$\psi_{\theta,f} = \Phi_f \cdot \cosh(\sqrt{iPr} Wo z) + \frac{\nabla p_A}{Wo^4 Pr (Pr - 1)} + \frac{1}{Wo^2 (Pr - 1)} \cdot \psi_u \quad (6c)$$

$$\psi_{\theta,s} = \Phi_s \cdot \cosh[\sqrt{i\sigma Pr} Wo (z + 1/2 + w)] \quad (6d)$$

with the constants given by:

$$\Phi_f = - \frac{\nabla p_A}{Wo^4 Pr (Pr - 1) \cosh(\sqrt{iPr} Wo/2)} \cdot \frac{\kappa \sqrt{Pr} \tanh(\sqrt{i} Wo/2) + \sqrt{\sigma} \tanh(\sqrt{i\sigma Pr} Wo w_s)}{\kappa \tanh(\sqrt{iPr} Wo/2) + \sqrt{\sigma} \tanh(\sqrt{i\sigma Pr} Wo w_s)} \quad (7a)$$

$$\Phi_s = \frac{1}{\cosh(\sqrt{i\sigma Pr} Wo w_s)} \left[\Phi_f \cdot \cosh(\sqrt{iPr} Wo/2) + \frac{\nabla p_A}{Wo^4 Pr (Pr - 1)} \right] \quad (7b)$$

and $\kappa = k_f/k_s$, $\sigma = \alpha_f/\alpha_s$, $w_s = 2\hat{w}_s/D_h$. The constant temperature boundary condition is given by $k_s \rightarrow \infty$ while the constant heat flux boundary condition corresponds to $k_s \rightarrow 0$. The slope at the wall is $(\Psi_{\partial\theta_f/\partial z})|_{z=-b/2}$. The mean temperature in the fluid is $\Psi_{\langle\theta_f\rangle} = (1/b) \int_{-b/2}^{b/2} \psi_{\theta,f} dz$. The complex Nusselt number is similar to that defined by Gedeon [79], but with variable wall thickness (such that the wall may have constant temperature but a low thermal mass):

$$Nu_m = -2 \frac{(\Psi_{\partial\theta_f/\partial z})|_{z=-b/2}}{\Psi_{\theta_w} - \Psi_{\langle\theta_f\rangle}} \quad (8)$$

While not presented in this thesis, the unsteady conjugate problem in a parallel plate geometry has been solved by the author for the case of top and bottom walls with differing thicknesses and thermal conductivities (as experienced in the experimental setup). However, it is found that the solution is approximately symmetric if the bottom wall is thin, the top wall has low thermal conductivity and the outer edges of the walls are insulated. Hence, the solution of Kurzweg [69] is used for simplicity.